Development of UV filters through solvothermal synthesis and evaluation of their potential in skincare applications

Simran Channa

Submitted in accordance with the requirements for the degree of Doctor of Philosophy.

The University of Leeds

School of Chemistry

May 2022

Contains commercially sensitive information.

The candidate confirms that the work submitted is her own and that appropriate credit has been given where reference has been made to the work of others.

This copy has been supplied on the understanding that it is copyright material and that no quotation from the thesis may be published without proper acknowledgement.

Acknowledgments

I would like to express my endless thanks to my primary supervisor, Dr Natalia Sergeeva, for her support, expertise, encouragement, and all the guidance she has given me throughout this project. I'm also extremely grateful to my industrial supervisor Bhaven Chavan, for the insight he has given me into the personal care industry and for all the technical knowledge he has shared. Thanks also to Croda and EPSRC for their sponsorship and funding.

Many thanks to Dr Alexander Kulak for his expertise with SEM imaging and EDX analysis throughout this work. I am also very grateful to Dr Zabeada Aslam for carrying out TEM and EDS analysis in Chapter 2. Thanks also go to Mohammad Shalbaf from Croda's formulation team who carried out the formulation and *in vitro* SPF tests. I would also like thank my second supervisor Dr Christine Bosch, for allowing me to utilise the School of Food Science and Nutrition facilities, and Ganwarige Fernando for advising me on the DPPH assay protocol.

Special thanks to the Natalia Sergeeva group and all of Lab 3.14 (past and present) for their ongoing support and friendship. I would also like to thank the School of Chemistry, namely Dr Christopher Pask and David Fogarty for their kindness, knowledge, and willingness to help.

I am thankful to all my family for their love and support and wish to show particular appreciation to my parents for teaching me the value of hard work, perseverance, and resilience. Finally, an extra special thanks to my fantastic friends, whose support and encouragement throughout this PhD never wavered.

Abstract

Regulatory limitations of TiO_2 and ZnO (≤ 25 % in sunscreen formulations) means the UV protection they can supply alone is limited. Carbon dots are desirable in many fields as they have good UV absorption, water solubility, ease of preparation, biocompatibility, and small size. Though, their use as UV filters in sunscreen formulations is largely unexplored. This thesis investigates carbon dots as potential active components in sunscreens and for the structural advancement of known UV filters: TiO_2 and ZnO, during their synthesis.

A series of carbon dots was prepared. Based on preliminary screening of UV data; three compounds made from precursors vanillin, ethanolamine, urea, and citric acid were deemed good candidates, and are referred to as VanCitCD, EthCitCD and UreCitCD, respectively. These were characterised by FT-IR, TEM, and Fluorescence spectroscopy. The radical scavenging activity using DPPH assay was studied for all carbon dots, and VanCitCD, UreCitCD and EthCitCD were the most effective. EthCitCD and UreCitCD, were most promising overall, and were carried forward for formulation and SPF testing. UreCitCD improved the SPF at higher loadings in two formulations, while EthCitCD was effective in one at a lower loading. There are currently no sunscreens that utilise carbon dots in this manner, so this previously untapped area, may be a useful advancement in the sun care industry.

Subsequently, TiO_2 and ZnO, were grown in the presence of carbon dots, through hydrothermal reactions, to investigate the impact on their morphology, crystallinity, and optical properties. Current literature investigates the inclusion of carbon dots after the preparation of the metal oxides; therefore, this area is largely unknown.

For TiO_2, 6.25 % inclusion of three selected carbon dots led to an improvement in the UV-vis absorption of the composites and enhanced the stability of the suspension. Lastly, the carbon dots successfully controlled the morphology of ZnO and through growth with EthCitCD, broad attenuation was achieved in the HEVL region.

Contents

Table of Figures

Summary of Tables

Abbreviations

UV	Ultraviolet
Vis	Visible
IR	Infrared
CFCs	Chlorofluorocarbons
NIR	Near infrared
MIR	Mid infrared
FIR	Far infrared
DNA	Deoxyribonucleic acid
RNA	Ribonucleic acid
ROS	Reactive oxygen species
MAPK	Mitogen-activated protein kinases
MMP-1	Matrix metalloproteinase 1
TIMP-1	TIMP metallopeptidase inhibitor 1
HEVL	High energy visible light
PABA	*para*-aminobenzoic acid
FDA	Food and Drug Administration
IC	Internal conversion
ISC	Intersystem crossing
VR	Vibrational relaxation
EC	European Commission
SCCS	Scientific Committee on Consumer Safety
EU	European Union
ECHA	European Chemicals Agency
REACH	Registration, Evaluation, Authorisation and Restriction of Chemicals
SVHCs	Substances of very high concern
CMR	Carcinogenic, mutagenic and reprotoxic
SPF	Sun protection factor
PL	Photoluminescence
FT-IR	Fourier-transform infrared spectroscopy
XRD	X-Ray diffraction

TEM	Transmission electron microscopy
EDS	Energy dispersive spectroscopy
GQDs	Graphene quantum dots
CQDs	Carbon quantum dots
CNDs	Carbon nanodots
PDs	Polymer dots
2D	2-Dimensional
CDs	Carbon dots
3D	3-Dimensional
QY	Quantum yield
N-doped	Nitrogen-doped
O-doped	Oxygen-doped
sol-gel	Solution-gelation
PVA	Polyvinyl acetate
EthCitCD	Ethanolamine and citric acid carbon dots
UreCitCD	Urea and citric acid carbon dots
AdeCitCD	Adenine and citric acid carbon dots
GlyCitCD	Glycerol and citric acid carbon dots
VanCitCD	Vanillin and citric acid carbon dots
GluCitCD	Glucose and citric acid carbon dots
SucCitCD	Sucrose and citric acid carbon dots
EthTarCD	Ethanolamine and tartronic acid carbon dots
AdeTarCD	Adenine and tartronic acid carbon dots
CA	Citric acid
DPPH	1,1-diphenyl-2-picrylhydrazyl
MeOH	Methanol
RSA	Radical scavenging activity
ISO	International Standardisation Organisation
NS	Not significant
XT-300	XT-300 10 % TiO_2
ATR	Attenuated total reflectance
SEM	Scanning electron microscopy
HF	Hydrofluoric acid

$BMIMBF_4$	1-butyl-3-methylimidazolium tetrafluoroborate
TTIP	Titanium (IV) isopropoxide
AcOH	Acetic acid
TiO_2-CD	Titanium dioxide-carbon dot
HRTEM	High resolution transmission electron microscopy
FESEM	Field emission scanning electron microscopy

1. Introduction

1.1. Skin: structure, function, and protection

The skin is the largest human organ and has three key functions: protection, regulation and sensation (1). As the primary shield for most of the body, skin provides the first defence against external injury, microorganisms, and radiation (1-3). Moreover, as a regulatory organ its other responsibilities include maintaining body temperature and regulating fluid levels to prevent dehydration (3-5). Furthermore, its vast network of nerve cells enables the skin to detect and relay environmental changes, thus providing sensory information (6). By providing an interface between the outside world and the inner organism, the skin takes the brunt of environmental exposure, which it is designed to withstand to an extent (4). However, it is still vulnerable to damage and as its role is crucial to the human body, it is evidently worthy of protection.

The skin has an intricate structure of tissues to facilitate its complex functions which can be divided into three main layers: the epidermis, the dermis and the subcutaneous tissue or hypodermis, as displayed in Figure 1.1 (1, 7).

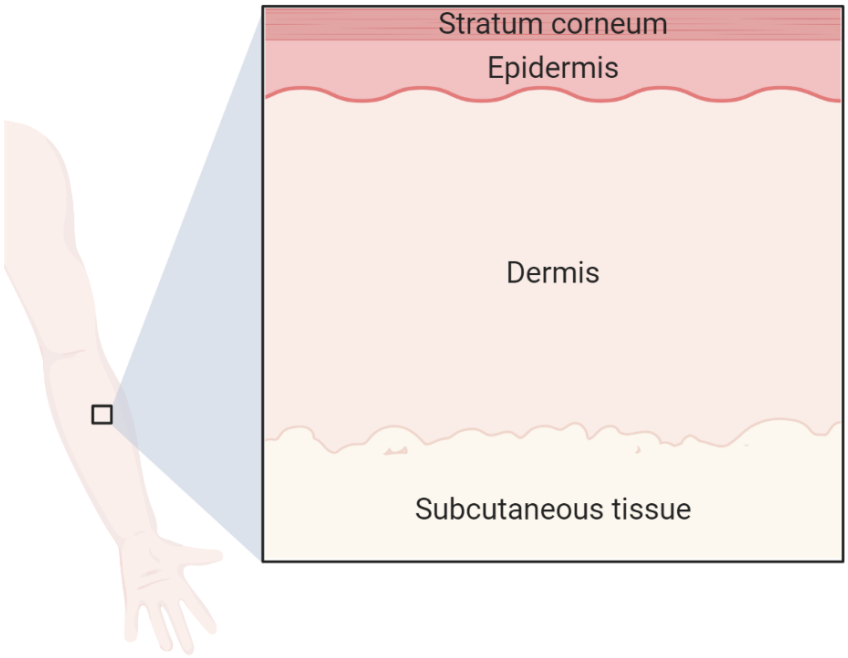

Figure 1.1: Illustration of skin structure, made with BioRender.com (1, 7)

The epidermis acts as the interface between the organism and its environment, and thus the barrier functions of the skin are predominantly limited to this area (2, 8). It is layered as follows: stratum corneum, granular layer, spinous layer and basal layer (1, 8). Keratinocytes, cells abundant in proteins such as keratin, make up approximately 95 % of this region (2, 9). Melanocytes, Langerhans cells and Merkel cells constitute the remainder of cells found within the epidermis (2, 9). Melanocytes are found at the bottom of the epidermis in the basal layer. They are responsible for synthesising melanin *[1]* which is a pigment produced naturally in the body that is capable of providing the skin with some protection from ultraviolet (UV) damage (2).

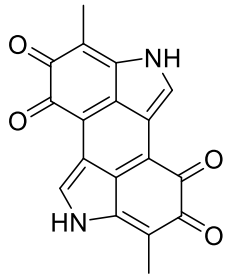

[1]

The dermis is featured below the epidermis and with a thickness of 1-2 mm, it forms a major part of skin (8, 9). Collagen, elastin, dermal fibroblasts and glycosaminoglycans are all found in this region, which collectively form the extracellular matrix (9). Collagen and elastin are both proteins that contribute to the strength and flexibility of the skin. In modern-day cosmetics, their preservation is sought after to maintain a typically “youthful” appearance of skin that is associated with minimal wrinkles. Relative to the epidermis, the dermis is highly vascular and houses the sweat glands, adipose cells (fat cells) and white blood cells (9).

The deepest layer of the skin is the hypodermis or the subcutaneous tissue. This is mainly made up of body fat for insulation and protection, as well as connective tissues. The function of this layer is predominantly to protect internal organs from damage by shock or changes in temperature.

With an overview of the skin’s basic structure, and the function of each layer, we can better understand the impact that natural sunlight has on it and what exactly we are protecting when we use products like sunscreens.

1.1.1. Natural sunlight

The skin itself is susceptible to environmental exposure such as solar radiation and pollution (10). Natural sunlight is comprised of three key components: ultraviolet (UV) light, visible (vis) light and infrared (IR) radiation (11). This refers to three energy bands in the electromagnetic spectrum (Figure 1.2), whereby energy increases from IR to vis to UV, while wavelength decreases in the same order (11).

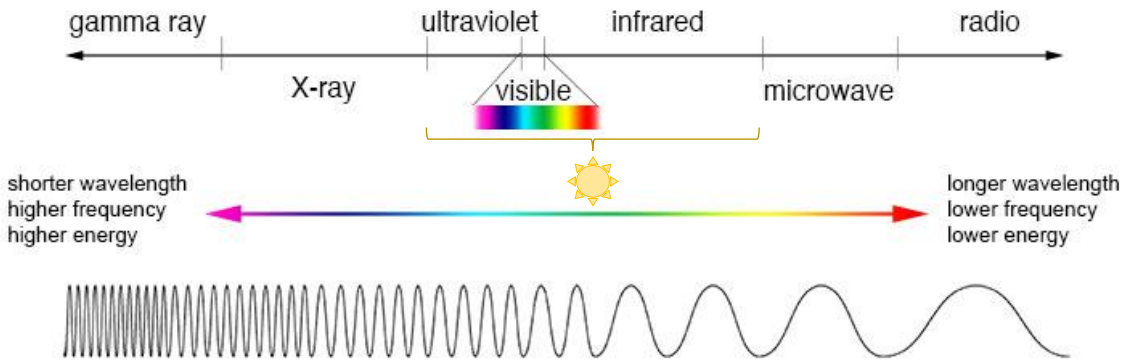

Figure 1.2: Relationship of energy, wavelength, and frequency in the electromagnetic spectrum, reproduced from (12) with copyright permission.

The relationship between wavelength and frequency can be described by the following equation:

Equation 1.1

$$\lambda = \frac{c}{\nu}$$

where: λ is wavelength (nm)

c is the speed of light (a constant of 299,792,458 m/s)

ν is frequency (Hz or s^{-1}) (13)

In quantum theory, the Planck-Einstein relation describes the energy of a photon as:

Equation 1.2

$$E = h\nu$$

where: *E* is energy (J)

h = constant of proportionality (Planck's constant of 6.626 x 10^{-34} J s)

ν is frequency (Hz or s^{-1}) (13)

Knowing the relationship between wavelength and frequency, as in Equation 1.1, the following equation can be derived, which shows that wavelength is inversely proportional to energy:

Equation 1.3

$$E = \frac{hc}{\lambda}$$

where: *E* is energy (J)

h = constant of proportionality (Planck's constant of 6.626 x 10^{-34} J s)

λ is wavelength (nm)

c is the speed of light (a constant of 299,792,458 m/s) (13)

The wavelength is important as it also indicates how far each type of radiation can penetrate the skin, which will be detailed later in this section. It should be noted that although the sun emits significantly more IR (54 % of its energy) compared to UV (7 %), the photon energy of UV radiation is greater (11).

1.1.2. UV radiation

UV light is subdivided into UVA, UVB and UVC radiation corresponding to 315 nm – 400 nm, 280 nm – 315 nm and 200 nm – 280 nm, respectively (14). The ozone layer in the Earth's atmosphere absorbs all UVC radiation and approximately 90 % of UVB radiation, it therefore plays an important role in shielding the Earth as UVC (with the shortest wavelength) has the highest energy, and therefore is most damaging. UVA is generally not absorbed and so its transmission to Earth is not hindered (15). Of the

three types of UV radiation, UVA penetrates the skin the furthest, as shown in Figure 1.3 (16).

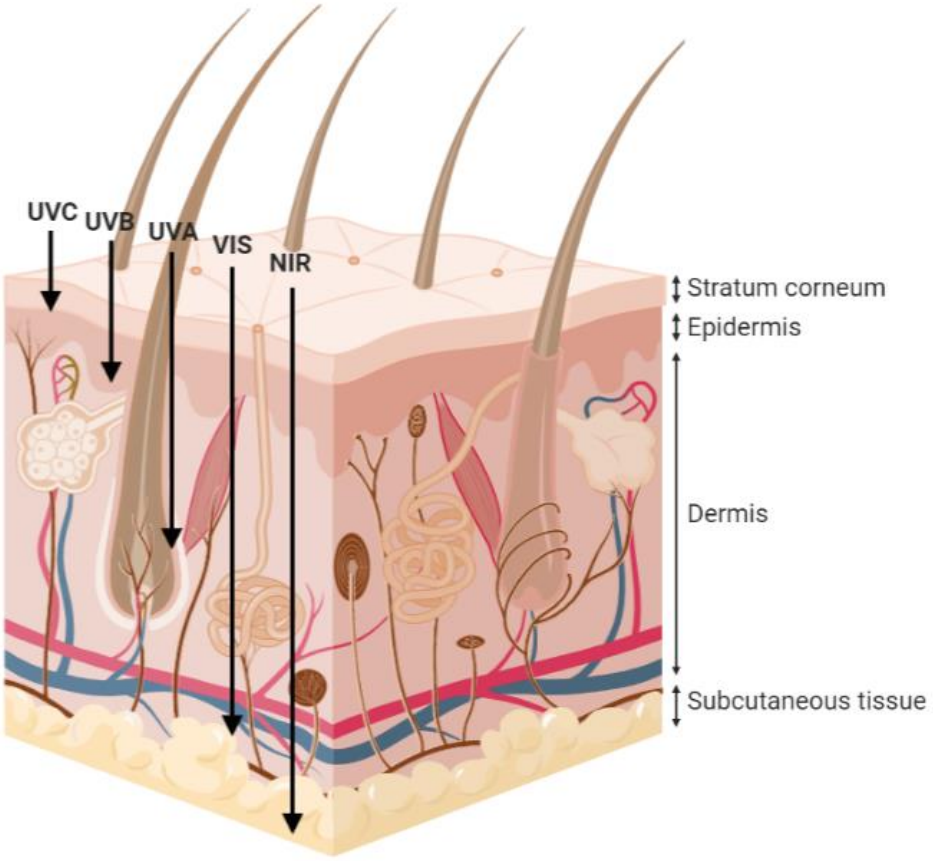

Figure 1.3: Pictorial representation of the depth at which solar light penetrates the skin. Adapted from B. Kaur (16), with BioRender.com.

The ozone layer is vulnerable to depletion from anthropological activities. Such an example would be the release of chlorofluorocarbons (CFCs) into the atmosphere through refrigeration and air conditioning systems (17). In 1974, it was proposed that such compounds were breaking down in the stratosphere and releasing atoms such as chlorine (Cl) which could destroy ozone molecules (O_3) (18). As a direct consequence of the weakened ozone layer, the transmission of UVB radiation to the surface of the Earth increased (19), and an increase in certain skin cancers, eye cataracts and immune deficiency disorders was reported (20). The threat to human health was severe so governments over the world agreed to phase out such ozone-depleting substances in the late 1980s and the international treaty “The Montreal Protocol” was signed (20).

1.1.3. Benefits of UV radiation

The absorption of UV radiation for the purpose of cutaneous vitamin D synthesis demonstrates one of the health benefits of exposing the skin to natural sunlight (21). Vitamin D is an important hormone in the body, tasked with the regulation of calcium absorption and, coupled with the parathyroid hormone, is responsible for bone mineralisation (22). A deficiency in vitamin D can be incapacitating as it can lead to diseases such as osteoporosis and osteomalacia, both of which weaken the bones (22, 23). The production of vitamin D within the body relies on UVB radiation, while UVA is ineffective in its synthesis (23).

Figure 1.4 shows the synthesis of vitamin D (24, 25). On exposure to sunlight, UVB radiation penetrates the epidermis of the skin and homolytically cleaves the C-C bond in provitamin D3 [a] to form previtamin D3 [b]. Thermal isomerisation because of body temperature, then forms vitamin D3 [d]. Alternatively, previtamin D3 is photolyzed to form tachysterol [d] and lumisterol [e] (24, 26). While it is important to maintain appropriate levels of vitamin D, it is argued that the dangers of prolonged sun exposure, like UV-induced erythema, development of skin cancer and accelerate skin ageing (10), outweigh the benefit of self-producing vitamin D over using supplements.

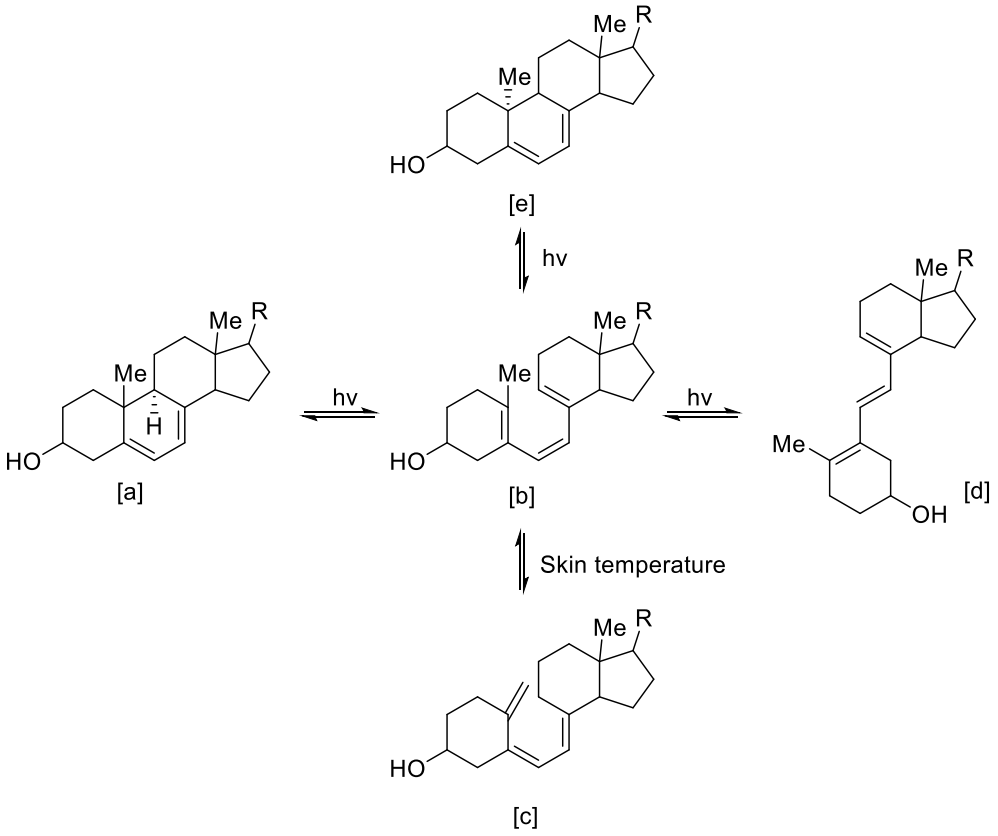

Figure 1.4: Synthesis of vitamin D where R = C_9H_{17} or C_8H_{17} for vitamin D2 or vitamin D3 series, respectively. [a] Provitamin D (7-dehydrocholesterol), [b] Previtamin D, [c] Vitamin D, [d] Tachysterol, [e] Lumisterol

1.1.4. Visible light

Visible light includes wavelengths of 400 to 700 nm (27). It can penetrate the skin more deeply than UV to depths of 90 - 750 µm as outlined in Figure 1.3 (27). Some dermal conditions benefit from this property, and visible light lasers can be used as a form of treatment. However, there is also evidence that visible light can stimulate long-lasting pigmentation in those with dark skin, and erythema in light-skinned individuals not too dissimilar to the effects of UVB exposure (27).

1.1.5. Infrared radiation

IR radiation corresponds to wavelengths between 760 nm and 1 mm. As this covers a vast range, it is typically divided into three smaller subsections. This includes IRA or near-IR (NIR) which refers to 760 nm - 1440 nm, IRB or mid-IR (MIR) which consists of 1440 nm - 3000 nm and finally IRC or far-IR (FIR) which corresponds to 3000 nm – 1 mm (11, 28, 29). More than half of the radiation emitted by the sun falls into the IR

region of the electromagnetic spectrum (11). There are also artificial sources of infrared radiation which can be used for therapeutic purposes such as treatment for rheumatoid arthritis (11). IRA makes up approximately 30 % of total solar energy and is capable of evenly penetrating deep within the layers of the skin, without generating a noticeable increase in temperature on the surface of the skin (30).

1.2. Solar damage

1.2.1. Absorption of harmful UVR

Skin cell studies, both *in vivo* and *in vitro*, have revealed molecular and structural damage because of exposure to UV light. Upon contact with skin, UV radiation is partially reflected and partially absorbed by the layers within the skin. Melanin, DNA, RNA, proteins, urocanic acid and aromatic amino acids such as tyrosine and tryptophan, are among some of the chromophores present in the skin that are capable of absorbing UV radiation (31). The absorption of UV radiation prompts a complicated process of chemical reactions, which in turn can lead to the production of reactive oxygen species (ROS) (15).

UVB radiation has the ability to cause DNA damage both directly and indirectly, through the production of dimers of DNA bases and through the formation of free radicals respectively (15). Mutations can occur as a result of both scenarios and typically, these are repaired by defence systems within the body. Those that are unrecoverable undergo apoptosis, essentially cell death, to prevent the multiplication of the mutated cell (15). However, if these mechanisms of protection and cellular repair are inadequate, a mutation can develop into a malignant tumour (32). It is in this manner that overexposure to UV radiation can lead to cancer.

UVA radiation, while sometimes considered a lesser concern than UVB, can also damage DNA directly and indirectly. Predominantly, this is through irradiation of molecular oxygen to produce ROS (15). In addition, erythema, more commonly known as sunburn, is achieved through over-exposure to UVB radiation and is indicated through reddening of the skin (33).

1.2.2. Reactive oxygen species

The skin is vulnerable to solar and environmental damage, due to direct and often constant exposure. Solar radiation can induce the production of free radicals and ROS within the body, via penetration of the skin. Together, these are encased under the term ROS (see Figure 1.5) (34, 35). Free radicals can be thought of as fragments of molecules or chemical species with a single unpaired electron (34). ROS are important for living organisms, for example phagocytes store free radicals to fight invading pathogens with them (36), which makes up an important aspect of immune response.

ROS are produced and broken down by all aerobic organisms, to maintain normal cell function. However, if this process occurs excessively, the cell enters a state of oxidative stress. In this condition, oxidants and antioxidants are no longer in balance and the levels of ROS present in the cell increase on the whole (35). If oxidative stress is severe, it can damage cell membranes, lipoproteins and DNA, and in some cases lead to gene mutations and cancer, as outlined in Figure 1.5 (34). Typically, ROS pose little danger provided the cellular defence mechanisms, including enzymatic and non-enzymatic antioxidant defences and repair processes, are efficiently able to limit the damage they can cause. However, as the body ages, the efficiency of these internal defence and repair mechanisms decline, thus increasing the risk of harm from ROS (34).

UVA and UVB radiation can cause extensive damage on a cellular level, directly and indirectly. The next section will focus on some existing UV filters that provide a protective barrier between the skin and harmful UV light.

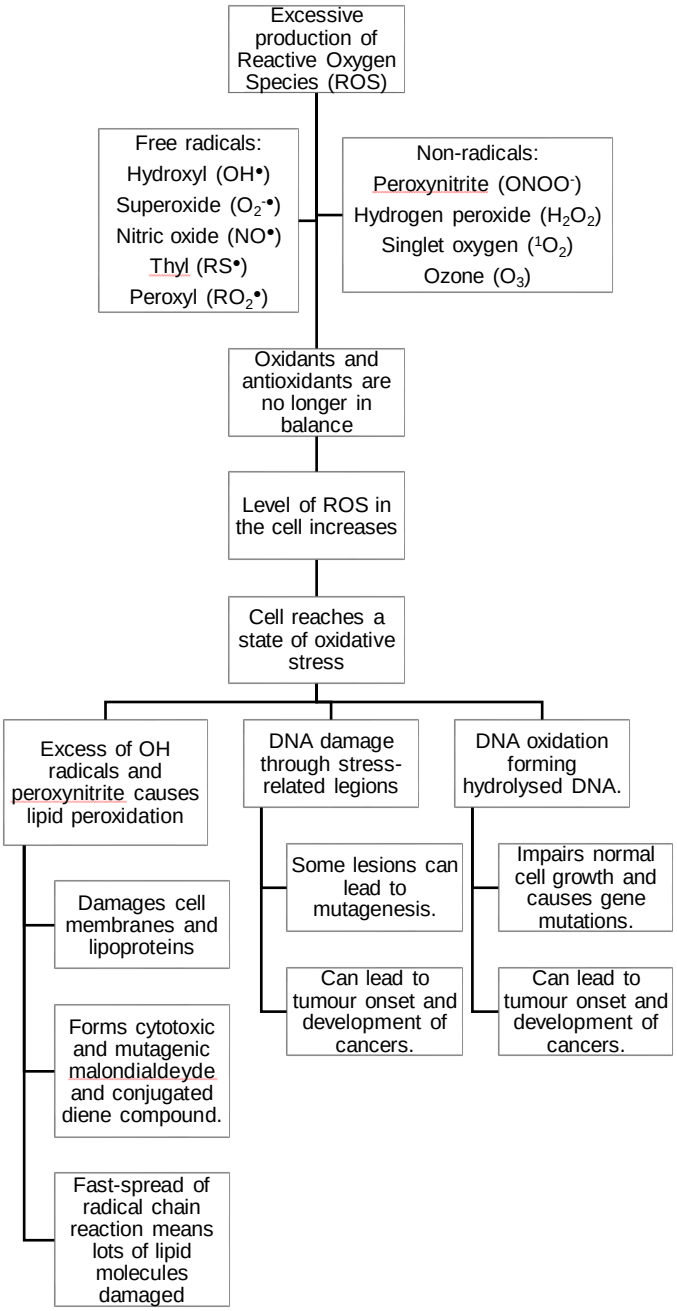

Figure 1.5: Possible outcomes of excessive ROS production in cells (36).

1.2.3. Damage from NIR

Photoageing in reference to the skin, describes the changes that become evident alongside chronological ageing (37). These typically include the production of prominent wrinkles, reduction in skin elasticity, as well as irregular skin pigmentation and impairment of skin barrier functions (11, 37). There is evidence to suggest that

IRA radiation has the ability to induce biological responses when absorbed by the skin which can lead to the breakdown of collagen, and signs of photoageing (28).

Mitogen-activated protein kinases (MAPKs), which participate in multiple important cell activities such as differentiation, movement, division, and death, have been shown to be activated by IRA radiation (28, 38). This can provoke the production of ROS in mitochondria, which originate from the mitochondrial electron transfer chain (39). The resulting signalling response leads to an increased production of matrix metalloproteinase (MMP-1) which can break down type-1 and type-3 collagen, and elastic fibres, through proteolysis (40). The breakdown of these elements is synonymous with ageing skin and thus, IRA is deemed to have a role in photoageing of skin (28, 41). Additionally, the production of the tissue specific inhibitor of MMP-1, known as TIMP-1, is not encouraged in the same manner. Thus, the imbalance of the two is also thought to emphasise clinical symptoms of ageing such as a loss of skin elasticity as well as wrinkle formation (28).

To summarise, natural sunlight is beneficial to the body through processes like the generation of vitamin D *in vivo.* However, the damage that can be caused to the skin has also been detailed and is more difficult to undo. From this, it is evident that the skin should be well-protected from solar exposure in order to maintain a healthy lifestyle.

1.3. Sunscreens: photoprotection with organic and inorganic filters

The discovery of UV rays by Ritter in 1801 was crucial in developing our understanding of photodamage and photoprotection (42). However, phenomena such as sunburn was still misunderstood and believed to be due to heat damage. It was not until 1820 when Englishman Sir Everard Home exposed one hand to the sun and shielded the other with black fabric, that he observed sunburn on the exposed hand despite the covered hand registering a higher temperature on the thermometer (43). This was confirmed by Widmark, of Sweden, who published experimental evidence of UV-induced erythema, in 1889 (44). Despite this, confusion over the damaging impact of UV radiation continued as late as 1900.

Presently, the negative impact of UV radiation and the emerging knowledge of the effects of HEVL and NIR, are more understood. With this, the personal care industry developed sunscreens, using various optical filters, to create skin protection products that are accessible for consumers. The definition of a sunscreen in Europe, is a cosmetic product that contains inorganic or organic UV filters, also known as physical or chemical filters (which describes their active mechanism), to reflect and/or scatter UVR or to absorb it (45). Such products are often formulated into creams, lotions, or gels, offering variety to the consumer. Ideally, a sunscreen will meet the requirements outlined in Table 1.1, although it is rare that a product will meet them all.

Table 1.1: Sunscreen specifications (45)

An ideal sunscreen should:
✓ Enable broad spectrum protection against UVA and UVB, also HEVL and NIR ✓ Utilise both chemical and physical filters for optimum protection ✓ Some protection against environmental pollution ✓ Good stability under high temperatures and intense sunlight (other cosmetics tend not to be subject to such harsh testing) ✓ Formulations are not irritant to the skin ✓ Possible degradation products should not be irritant to the skin ✓ Neither the formulation nor degradation products should be able to penetrate the skin and be absorbed systemically ✓ Should be easy to formulate with ✓ Should not harm living organisms or the environment ✓ Feel and colour should be pleasing to the consumer

1.3.1. Topical photoprotection

Topical protection of the skin is a popular and effective method used to counter solar radiation. However, it is noted that ROS can still form as a result of other stimuli, such as smoking (37). Topical protection generally works by absorption or scattering of the targeted radiation (see Figure 1.6). Sunscreens are an example of an existing consumer product that works in this manner and targets UV radiation. Sunscreens are cosmetic products designed to protect the consumer from harmful solar radiation, including UVA, UVB, high energy visible light (HEVL) and IR. Typically, the formulation

will include the active compound, designed to shield the skin through absorption, scattering, or a combination – in the case of UV protection this will often be a UV filter. In addition, further components are included such as preservatives, fragrances and emulsifiers to improve the longevity and appeal of the product (16).

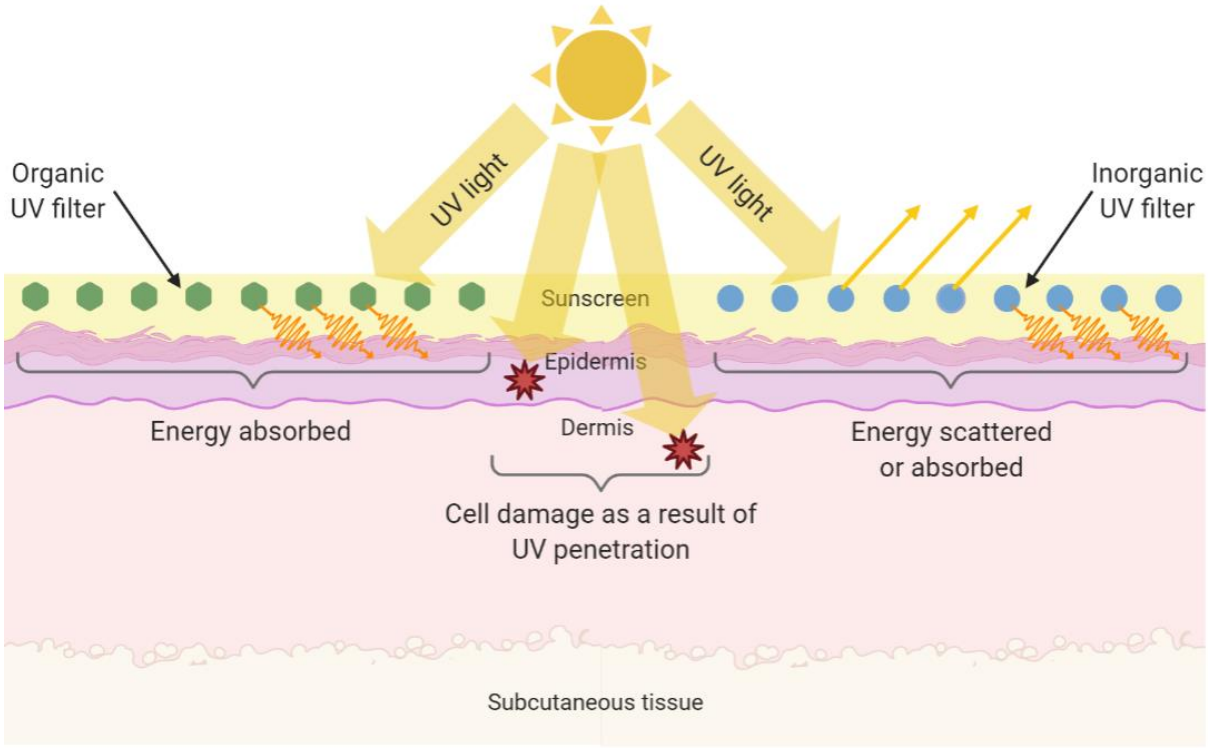

Figure 1.6: The interaction of UV light with UV filters in a layer of sunscreen on the skin, made using BioRender.com

Inorganic sunscreens typically contain zinc oxide and titanium dioxide. They are often opaque and thick creams that can effectively protect from UVA and UVB radiation through scattering and absorption of UV light (21). In contrast, chemical sunscreens work solely by absorbing UVA and UVB radiation. They can contain multiple active ingredients such as *para*-aminobenzoic acid (PABA) and oxybenzone, combined with additives to stabilise the formulation (16, 46). In comparison to inorganic formulations, the chemical kind are not easily washed off. However, it is questioned whether chemical sunscreens can potentially be absorbed into the systemic circulation and induce toxic effects (16). This is one of the reasons it is important to consider the toxicity of compounds when developing novel consumer skincare products.

HEVL resides in the violet-blue band of the electromagnetic spectrum (400–500 nm). Sources of such light include sunlight, flat digital mobile phone displays, computers,

and televisions. A fractionated vegetable derived melanin compound sold as Liposhield™ HEV Melanin from Vantage Specialty Ingredient, Inc is an example of a topical defence against HEVL (47). It prevents harmful HEVL from penetrating the skin through specific absorption, while allowing inoffensive visible light to pass through (16).

Furthermore, a combination of red, yellow, and black iron oxides, alongside zinc oxide, has been shown to protect from HEVL somewhat, by Bernstein *et al* (48). Iron oxides are considered to be inactive ingredients meaning they are not FDA-approved UV filters, in a sunscreen formulation (49). As each iron oxide has a different light attenuation profile (see Figure 1.7) they combined these, with zinc oxide and titanium dioxide, in various formulations to find 71.9 % - 85.6 % attenuation between 415 and 465 nm, while the products with no filters showed no significant HEVL attenuation. From Figure 1.7, HEVL attenuation by TiO_2 is insignificant, while ZnO can attenuate up to 450 nm. Therefore, the inclusion of iron oxides into the formulation and their combination with ZnO and TiO_2 is likely to be causing this increase in attenuation.

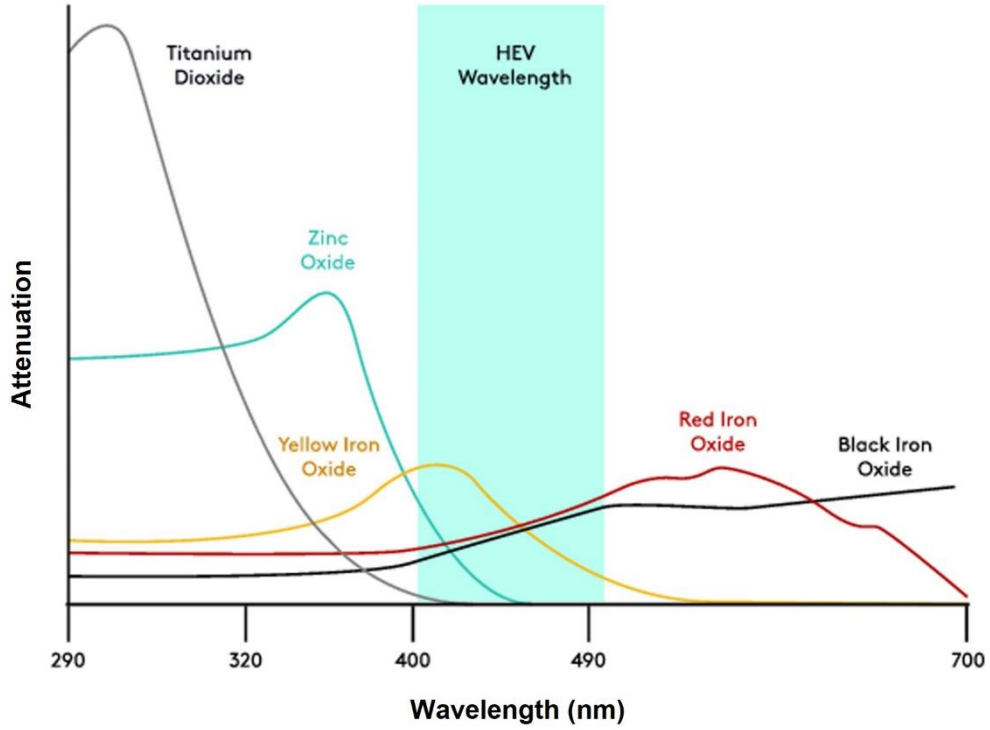

Figure 1.7: Light attenuation for inorganic filters. Reproduced from Bernstein *et al.* (48) with copyright permission.

As stated earlier, IR radiation can lead to ROS production and cutaneous changes within the skin. Specifically, IR radiation targets mitochondria and causes the increased production of matrix metalloproteinase-1 (MMP-1) which is an enzyme that degrades collagen. It is thought that the topical application of antioxidants, such as coenzyme Q derivatives which target mitochondria specifically, can provide photoprotection from IR radiation (50).

1.3.2. Mechanisms of UV attenuation

There are three mechanisms of UV attenuation in sunscreens: absorption, scattering and reflection (backward scattering); with absorption and scattering being the two fundamental ways in which electromagnetic radiation interacts with matter (51).

Scattering occurs when the separation of positive and negative electrical charges within a molecule or particle forms an electric dipole, which oscillates with the frequency of radiation it is exposed to (51). These oscillating dipoles then emit radiation of the initial frequency in diverse directions, which then dissipates in the incident direction, and this is known as scattering. In this case the radiation itself does not have resonance frequencies with the energy transitions of the molecule and so energy transfer does not occur (51).

For absorption, the energy transition of the molecule and the exciting radiation resonate, which allows energy to be transferred to the molecule (51). When a photon of UV light is absorbed by an organic molecule, an electronic transition can take place; the molecule is excited from the electronic ground state (S_0) to an excited state (S_n). From here, the energy absorbed can be dissipated in several ways: vibrational relaxations, non-radiative pathways (by internal conversion (IC) $S_n \rightarrow S_0$ or $T_n \rightarrow S_0$ and/or intersystem crossing (ISC) or $S_n \rightarrow T_n$) and radiative pathways (photoluminescence) (51).

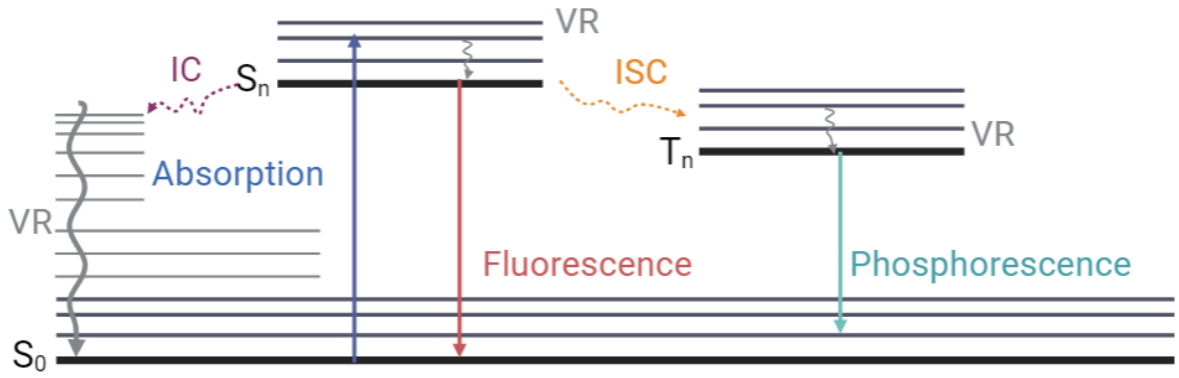

Figure 1.8: A Jablonski diagram to show the possible pathways once UV light is absorbed in a molecule. VR is vibrational relaxation; IC is internal conversion and ISC is intersystem crossing. Made with BioRender.

Inorganic UV filters like TiO_2 and ZnO function by both absorption and scattering mechanisms. Both materials are semiconductors, and their bulk crystals have large bandgaps, meaning the energy required to promote an electron from the valence band to the conduction band is high. Here, this corresponds to a wavelength of 380–420 nm. The particle size influences the bandgap energy, so that as the particle size decreases the bandgap energy increases. The mechanism of light attenuation applied will depend on the particle size. A larger particle size will mean scattering is preferred over absorption, while for nano-sized materials (often used in sunscreens), absorption is the dominating process (51).

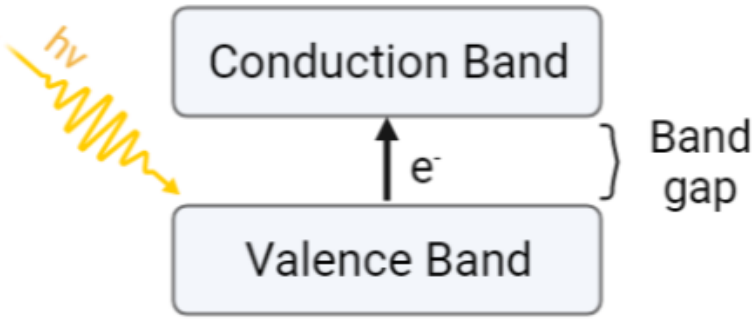

Figure 1.9: Promotion of an electron from the valence band to the conduction band, in a semiconductor (51).

1.3.3. Common UV filters in sunscreens and their challenges

1.3.3.1. Titanium dioxide

Titanium dioxide (TiO_2) is a metal oxide that can be found as three crystalline polymorphs: anatase, rutile and brookite. Its high refractive index (2.4), stability and the fact it is insoluble in water, allows it to be used as a pigment first and foremost (52). In addition to a colourant, it can also be used as a UV filter in cosmetic products, at a maximum of 25 % of the formulation, and is authorised under entry 27 of Annex VI and entry 143 of Annex IV to Regulation (EC) No. 1223/2009[1] (53). Early sunscreen formulations containing titanium dioxide often had a thick consistency, did not blend easily with the skin, and produced a white layer due to its high refractive index (54). These properties formed a physical barrier and shielded the skin from UV light, acting as an effective filter by means of scattering and reflection. However, these same characteristics made it an unappealing cosmetic. The FDA (Food and Drug Administration) enabled nanoparticles to be used in sunscreens in 1999 (54). The advantage of using nanoparticles in such formulations, is that their size makes them more transparent, have improved texture which blends with the skin more effectively and produce a less viscous formula (54). However, there has been some uncertainty as to whether they are safe to be used on the skin, due to potential for systemic absorption, and whether they are hazardous in the wider environment as possible bioaccumulates.

The safety of nano-TiO_2 as a UV filter in sunscreens was reviewed by the Scientific Committee on Consumer Safety (SCCS) and in 2013 it was concluded that this material was safe to be applied to healthy or sunburnt human skin (53). However, in a separate Opinion, the SCCS showed concern for the safety of nano-TiO_2 in spray products particularly, because of risk of exposure to TiO_2 nanoparticles by inhalation. Following the receipt of industrial data, the SCCS deemed TiO_2 to be safe in spray personal care products, at a lower concentration of up to 5.5 % (53). At this lower

1 This Regulation outlines the rules a cosmetic product must comply with to be appropriate to market and ensures protection of human health as well as the function of the internal market. It defines a cosmetic product as “any substance or mixture intended to be placed in contact with the external parts of the human body (epidermis, hair system, nails, lips, and external genital organs) or with the teeth and the mucous membranes of the oral cavity with a view exclusively or mainly to cleaning them, perfuming them, changing their appearance, protecting them, keeping them in good condition or correcting body odours”.

percentage, the remainder of the formulation may have to compensate with additional filters and booster compounds, to reach the same SPF rating as a cream, which could be costly. There is potential for improvement here, for example by replacing existing nano-TiO_2 in sprays with biocompatible alternatives.

Additionally, titanium dioxide is known to form free radicals such as superoxide and hydroxyl radicals, when irradiated with UVA and UVB light, through its involvement in electron transfer reactions (55). Withstanding UV exposure is inherent for an active ingredient in a sunscreen, therefore sunscreen formulations often contain additives like antioxidants and radical scavengers, to supress any highly reactive radicals that are produced and form less dangerous products (56). This in turn prevents damage to biomaterials by free radicals and ROS (55). Minimising ROS contact on the skin, created within the sunscreen formulation, can be achieved by incorporating heavy metals (V and Ce) or antioxidants to combat the ROS, or alternatively by coating with silica. Both methods have their drawbacks. The inclusion of heavy metals and antioxidants may present toxicological issues and reduced transparency, while coating with silica is aesthetically undesirable for sunscreens as its high refractive index can compromise the transparency of the applied formulation (57).

To summarise, TiO_2 is a very effective UV filter due to its high refractive index and low cost, however as a component in sunscreens, it is not without limitations. As a suspected carcinogen by inhalation, its percentage inclusion in formulation is capped and it is also prone to forming damaging ROS under UV light. From this perspective, production of alternative UV filters is desirable.

1.3.3.2. Zinc Oxide

Zinc oxide is another physical UV filter, often used in sunscreens. As a metal oxide and semiconductor, like TiO_2, it shares many of the same physical properties. Similarly, it is considered a carcinogen by inhalation. For this reason, the usage of zinc oxide and its nano equivalent, is limited to 25 % in formulation, except in applications where lung exposure is a concern (i.e., sprays). It must meet the criteria outlined by the EU commission, which states it is not to be used in such applications (58). Specifically for nano-ZnO the material must have a purity of ≥ 96 % and any impurities present should be CO_2 and water, anything else should be less than 1 % in total (58). The nanomaterial should have a wurtzite crystalline structure and appear as clusters

of rods, stars or isometric shapes (58). Additionally, its water solubility should be less than 50 mg/L (58).

ZnO is capable of broad-spectrum UV protection and can attenuate wavelengths up to 450 nm which enables it to offer some HEVL protection. However, as Figure 1.7 shows, attenuation at these wavelengths is weak. Due to the criteria outlined by the European Commission and the restrictions placed on ZnO, extending its absorption to the visible light region while meeting the regulations, is a challenging feat.

1.3.3.3. Avobenzone

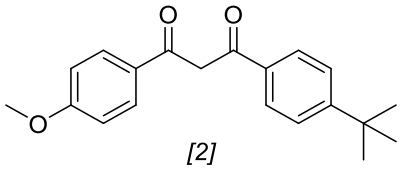

[2]

Avobenzone *[2]* is a typical UVA filter, with the trade name Parsol® 1789. It was patented in 1973 and approved by the EU and FDA in 1978 and 1988, respectively (51). It is currently approved for worldwide use but was discovered to be unstable when exposed to UV light. As a photoprotector, this was not only detrimental to its efficacy but also, it formed argyglyoxals and benzils as it degraded, of which photoallergenic and cytotoxic reactions can be attributed to (59).

Octocrylene *[3]*, capable of quenching triplet state of avobenzone, is also an effective way to stabilise it (51). However, the recent Opinion from the SCCS states that octocrylene may be potentially disruptive to the endocrine system and should be used at concentrations of no more than 10 % (60). Its environmental impact is also in question.

Several photostabilisers were used in synergy with avobenzone, to mitigate its degradation: Mexoryl SX, Corapan® and butyloctyl salicylate, to name a few (61). Additionally, antioxidants have been studied for their ability to stabilise photodegradation of avobenzone, by quenching ROS formed. Afonso *et al* investigated vitamin C, vitamin E and ubiquinone, for this use (62). They found ubiquinone to be the most effective photostabiliser for avobenzone, though vitamin C and E showed promise.

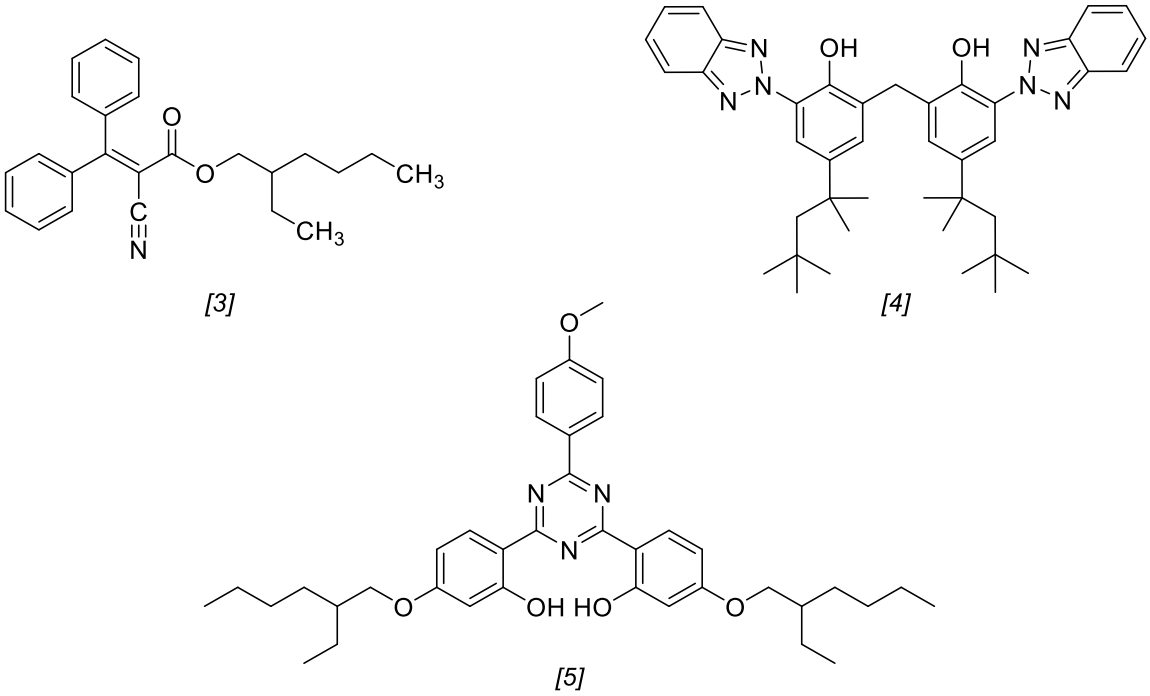

Figure 1.10: Common stabilisers of avobenzone: octocrylene *[3]*, bisoctrizole *[4]* and bemotrizinol *[5]*.

Bisoctrizole *[4]* and bemotrizinol *[5]* are UV filters that are both also used in conjunction with avobenzone, for stability (Figure 1.10). Bisoctrizole (Tinosorb® M) consists of colourless organic microfine particles that absorb, reflect and scatter UV light and is available as a 50 % aqueous dispersion. Bemotrizinol (Tinosorb® S) on the other hand is oil soluble for high water resistance and can be used in partnership with other organic and inorganic filters. It is also highly photostable, a broad-spectrum UV filter and meets the necessary safety requirements.

The example of avobenzone showcases the importance of maintaining stability in a sunscreen formulation, and its lack of stability is one of its key limitations. Ideally the UV filter itself would be stable as well as able to attenuate UV light, without degradation. However, where this is not possible antioxidants and other photostabilisers can be incorporated.

1.3.3.4. Oxybenzone

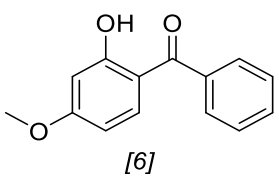

[6]

Oxybenzone *[6]* is an organic, UVA filter, with an absorption range of 270–350 nm (63). It is a benzophenone compound, grouped within the class of aromatic ketones, and was approved by the FDA for use in sunscreens in the early 1980s (63). However, it is controversial in the field of personal care because some studies showed it to be systemically absorbed (64) which raised the question of its toxicity to humans (65). Further to this, oxybenzone was identified in many water sources and has proved stubborn to remove by existing wastewater treatment plants. While industrial runoff was one of the culprits of this, it is believed the use of sunscreens and cosmetics that contain oxybenzone, add to the problem – for example oxybenzone can be washed off into open water sources or in the shower, and can be excreted in urine which also finds its way back into the environment. It is now thought to be a threat to coral reefs, through activation of coral viruses which in turn leads to oxidative stress, discharge of symbiotic algae (which are coloured and responsible for providing energy to coral) and finally bleaching of the coral, as proposed by Danovaro *et al* (66). As of 2021, Hawaii passed legislation which banned the unprescribed use of oxybenzone (and octinoxate) to offer some protection to the coral reefs[2].

Additionally, concentrations are regulated to 6 % in sunscreen and cosmetic formulations in the US, while this was recently reduced to 2.2 % in Europe (67). Japan and Australia have an upper limit of 5 % and 10 % respectively (67). As the effects of the likes of oxybenzone become more widely understood, it is likely to become more restricted as a consequence. The need for alternative UV filters that are biocompatible, biodegradable, all whilst maintaining their efficacy, is increasingly apparent.

In this section, topical photoprotection, mechanisms of UV attenuation and some existing UV filters have been explored. Throughout the project, UV attenuation was often the first form of evaluation for the optical properties of new materials formed. Therefore, it was important to gain an understanding of the mechanisms on a molecular level. Additionally, investigating the challenges of common UV filters like avobenzone and titanium dioxide helps to establish where there is room for improvement. There is a drive for biocompatible, biodegradable, cheap materials that

[2] It is also banned in several Caribbean islands like Aruba and Bonaire, as well as Palau, The Marshall Islands, Thailand, the Northern Mariana Islands, and the US Virgin Islands.

are capable of broad-spectrum protection, stretching into the visible region, that must also be photostable. Currently, no existing UV filter meets all these demands all while following the regulations outlined later in the chapter.

1.4. Natural antioxidants to combat ROS

Antioxidants are radical scavengers which aim to protect molecular targets once ROS, such as excited singlet oxygen, have been formed (68). Typically, an antioxidant molecule can counteract several free radicals and thus reduce the risk of oxidative damage to cells (69). Antioxidants can be both enzymatic and non-enzymatic (35).

Vitamin E and vitamin C are among the non-enzymatic antioxidants assisting photoprotection in the body (70). It is known that an increase in antioxidants can help to improve radical scavenging capability within the body, and thus prevent the harmful effects of ROS. Antioxidants can be found in many foods, and it is believed their concentration within the body can be increased with dietary changes in favour of foods rich in antioxidants.

Polyphenols, found in plants, are a class of antioxidants which include phenols *[7]*, phenolic acids *[8]* and flavonoids *[9]* (71). Generally, they have hydroxyl groups capable of hydrogen transfer for the purpose of reducing free radicals (69). Such compounds can be found in both red and white wine, green and black tea, as well as various fruits and vegetables (69). The consumption of foods rich in antioxidants is one method that is currently being used to counter the production of ROS. In addition, aromatic rings on flavonoids enable them to absorb UV radiation in the range of 200 nm to 400 nm. Therefore, if topically applied to the skin, they could also attenuate UV light (21).

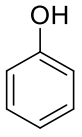

[7]

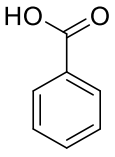

[8]

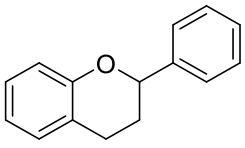

[9]

Antioxidants are common additives in sunscreen formulations and often work in synergy with physical filters like titanium dioxide and zinc oxide. Therefore, it is

valuable to gain an insight to how some of their common classes like polyphenols, which are capable of counteracting ROS.

1.5. Regulations within the cosmetics industry

Sunscreens are considered a cosmetic product. To ensure the safety, efficacy, and security of the product, for use within the public, regulations are put in place in the cosmetics industry, and many other industries alike.

The Food and Drug Administration (FDA) is responsible for this in the US. As part of the Department of Health and Human Services, it serves to protect public health and is responsible for regulating the safety, efficacy and security of human and veterinary drugs, cosmetics, food supply, radiative products, biological products, and medical devices (72).

The European Commission provides a similar service for those countries in the European Union. It implements EU Commission, Regulation (EC) No. 1223/2009 which is a European legislation for finished cosmetics products.[3] Within this regulation, Annex VI outlines a list of 45 UV filters that are allowed in cosmetic products including titanium dioxide (rutile and anatase) as well as zinc oxide (73). It is applied nationally, and all member states are bound by these regulations. After the UK exited the EU on January 1st, 2021, the EU Cosmetics Regulation was no longer applicable there so the UK Cosmetics Regulation was established in its place. Both regulations are in alignment and have no significant differences to date.

As the project is based in the UK, we will be focussing predominantly on European regulations as these are the most applicable. ECHA is the European Chemicals Agency. Within ECHA, various legislature exists to regulate the chemicals used within the EU. One important legislation is Regulation (EC) No. 1907/2006, also known as the REACH Regulation (Registration, Evaluation, Authorisation and Restriction of Chemicals), which in short aims to protect human health and the environment, from threats of chemical hazards, while also encouraging a competitive chemicals industry.

[3] This was last updated on 01/10/2021.

Additionally, REACH advocates for reducing the testing of hazardous substances on animals, through alternative methods (74).

ECHA publishes a Candidate List of Substances of Very High Concern (SVHCs). This is part of the authorisation process, which aims to gradually replace SVHCs by less dangerous substances or better technologies. A substance might be proposed to be recognised as a SVHC if it is: carcinogen, mutagenic, toxic for reproduction (CMR) in accordance with Regulation (EC) No 1272/2008 of the European Parliament and of the Council (75), bioaccumulative or very persistent, to name a few reasons. After a 45-day consultation, if a substance is identified as a SVHC it is placed on the Candidate List. Suppliers of such substances have an immediate responsibility to supply safety information such as SDS, how to use the substance safely and to notify ECHA if the article they produce contains more than 1 tonne per producer or importer per year at greater than 0.1 % concentration (w/w) (76).

1.5.1. Recent changes to Regulation (EC) 1223/2009

Furthermore, EU allowed UV Filters: Annex VI, Regulation 1223/2009/EC on Cosmetic Products, as corrected by Corrigendum to Commission Regulation (EU) 2021/850, contains relevant changes to regulations concerning titanium dioxide (77).

Commission Delegation Regulation (EU) 2020/217, to be put in place from October 1, 2021, states that those substances that have been identified as CMR substances should be removed from cosmetic products from the same date. Specifically, it refers to titanium dioxide in powder form, with ≥ 1 % of particles with aerodynamic diameter of ≤ 10 μm being classified as ‘Carcinogen Category 2 (inhalation)’ (77).

Titanium dioxide is allowed for use as a colourant (entry 143 of Annex IV to Regulation (EC) No 1223/2009), as a UV filter in its nano form ≤ 25 % concentration (entries 27 and 27a of Annex VI to Regulation (EC) No 1223/2009) but should not be used in applications that might lead to lung exposure. As an important component in cosmetic products, an exception was requested in January 2020 leading to the Scientific Community on Consumer Safety (SCCS) adopting an opinion on the matter. It was concluded that titanium dioxide in loose powder form, was safe for use in face products in a concentration of ≤ 25 % and in aerosol spray hair products ≤ 1.4 % (for consumer use) and ≤ 1.1 % (for professional use). With regards to the use of titanium dioxide (nano) as a UV filter, entry 27a of Annex VI to Regulation (EC) No 1223/2009 already

states that it should not be used where inhalation is a risk and could lead to lung exposure (77).

1.5.2. Regulations for methods of sunscreen evaluation

There are two main ways to assess a sunscreen's ability to protect from solar radiation. The first is its Sun Protection Factor (SPF), which is a number assigned to each product that describes the level of exposure that can be endured before skin erythema occurs. The notion of an SPF factor was developed over decades in the 20th Century by Ellinger (1934), Schulze (1956) and finally popularised by Grieter (1978), through a growing need to evaluate the protection of sunscreens (78). When the industry recommended amount (2 mg/cm^2) (79) of SPF 30 sunscreen is applied, for example, it will take 30 times longer to cause skin erythema than it would for unprotected skin. However, SPF refers to the efficacy of a UVB filter, rather than UVA or broad-spectrum filters (79).

Therefore, the second assessment must refer to UVA protection in a sunscreen. This is much more difficult to standardise because, unlike SPF for UVB, the endpoint is not erythema and in reality, UVA protection can be calculated based on different endpoints, which can cause variation in the protection factor (78). Boots UK Limited developed a UVA star rating system in 1992, which ranged from 0 to 5 (80). It describes the percentage of UVA radiation absorbed in comparison to UVB radiation, with five stars offering the best protection against UVA rays. The minimum recommended star rating is four. While sunscreens with four stars are very close to the ideal protection of UVA and UVB, it is important to declare their limitations. No sunscreen product can filter all UV radiation and therefore should not claim to or mislead consumers into thinking the sunscreen gives total protection (79).

It was important to gain an understanding of the recent changes to Regulations in the Cosmetics Industry and the way in which sunscreens are evaluated, as ultimately any alternative UV filters produced will aim to be incorporated into such formulations.

1.6. Project aims

The overarching aim of the project is to develop alternative UV filters and evaluate them for use in personal care applications, with a focus on sunscreens.

Sunscreens contain multiple components: physical and chemical UV filters, antioxidants, stabilisers and more. Regulatory limitations of TiO_2 and ZnO, ≤ 25 % in sunscreen formulations, means the UV protection they can solely supply is limited. They are often used in conjunction with chemical filters like avobenzone which can have photostability issues, and oxybenzone which has been found to be environmentally damaging. Alternative materials are therefore sought after.

Carbon dots have a number of desirable properties that make them suitable alternative candidates. This includes good UV absorption, ease of preparation, biocompatibility, and small size. These properties make them applicable to a wide range of fields, though their use as UV filters in sunscreen formulations has not yet been explored.

This project aims to investigate the preparation of carbon dots and evaluate their potential for use as alternative UV filters or UV boosters within personal care formulations, with a focus on sunscreens, in collaboration with Croda. It intends to examine the more environmentally sound hydrothermal synthesis as a viable means for the preparation of carbon dots from small organic molecules, in a friendly solvent (water), and consider the capability of the reactions to be scaled up for use in industry.

Moreover, it aims to explore the inclusion of carbon dots into the solvothermal reactions of known UV filters, TiO_2 and ZnO, to investigate the impact on their morphology, crystallinity, and optical properties. This area is largely unexplored, therefore the aim was to uncover improvements in the optical properties of these materials, by a facile, solvothermal preparation.

2. Investigation of carbon dots as UV-vis filters

2.1. Introduction

Carbon dots can be described as distinct, sphere-like nanoparticles, 10 nm or smaller in size (81-84) and are classed among carbon nanomaterials such as: buckminsterfullerene (C60); single and multi-walled carbon nanotubes; nanodiamonds; carbon nanofibres and graphene (85). They typically consist of a carbon core adorned with carboxylic acid functional groups on the surface (Figure 2.1) (84, 86). This functionality enables excellent water solubility, in contrast to macroscopic carbon which is typically a black material that is insoluble in water. With abundant carboxylic acid groups, they are suitable for further functionalisation with a variety of organic, inorganic, polymeric and biological species (84). Carbon dots (CDs) have intriguing optical properties such as size and excitation wavelength dependent photoluminescence (87). Amongst these characteristics they are also biocompatible, photochemically stable, generally have low toxicity and have several quick, cheap synthetic routes (88). Their exceptional characteristics, coupled with their facile syntheses, demonstrate perhaps why this nanomaterial is pursued so widely in current research, in fields such as: bioimaging; sensing; photovoltaics and medicine (88).

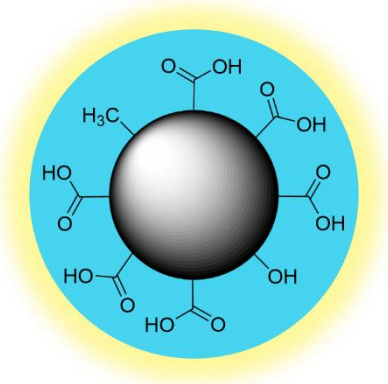

Figure 2.1: Depiction of carbon dots with carboxylic acid functionality as adapted from Baker *et al.* (84)

An adjustable and strong fluorescence emission was the initial attraction of carbon dots for many researchers. It was thought that they would be good candidates to

replace quantum dots (nanoscale semiconductor crystals with optical and electronic properties owed to their size), which are often used in biosensing and bioimaging applications because of their fluorescent nature. However, their use in biological applications is limited by the toxicity of the heavy metals used to prepare them. On the other hand, carbon dots are non-toxic, biocompatible, cheap to produce and chemically inert, all while maintaining good fluorescence. This makes them an attractive alternative particularly in applications where toxicity is a concern (85).

2.1.1. Synthesis of carbon dots

In the first instance, carbon dots were isolated during preparative electrophoresis (a type of purification) of single-walled carbon nanotubes by Xu *et al* (2004) (81). Then in 2006, they were produced by laser ablation of graphite powder and cement (89). In the literature, carbon dots are often characterised by UV-vis absorption spectroscopy, photoluminescence (PL) spectroscopy, FT-IR, XRD, TEM and EDS (90).

Now there are a variety of other ways in which carbon dots, also known as carbon nanodots (CNDs), can be prepared. These can be divided into “top-down” and “bottom-up” strategies, as outlined in Figure 2.2, and can also lead to the formation of graphene quantum dots (GQDs) and polymer dots (PDs).

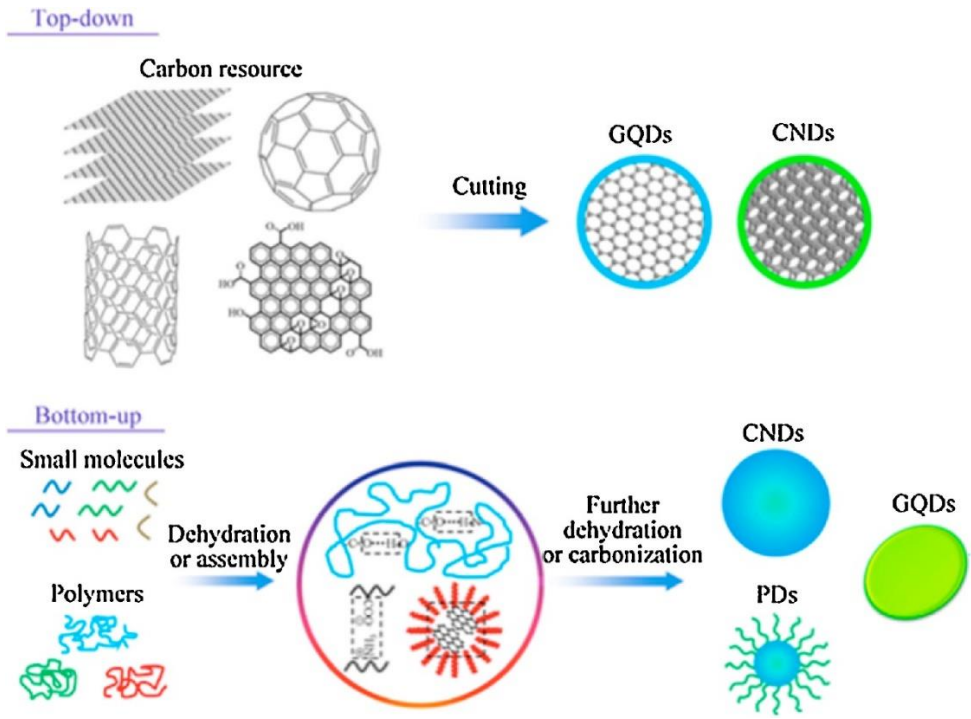

Figure 2.2: A schematic to show top-down and bottom-up carbon dot synthesis. Reproduced from (91) with copyright permission.

2.1.1.1. Top-down methods

Top-down methods such as chemical exfoliation, arc-discharge, and laser ablation, typically involve the exfoliation and cutting of macroscopic carbon, like carbon black or graphite powder, to obtain 2D nanoparticulate graphene quantum dots (92). These approaches often use harsh reaction conditions, expensive materials, and equipment, have long processing times, and do not enable good control of particle size (93).

Chemical ablation involves using strong oxidising acids to carbonise small organic molecules, which are then divided into smaller sheets through controlled oxidation. Albeit one of the most accessible synthetics methods to prepare carbon dots, according to Wang *et al.* chemical ablation relies on harsh conditions and is a multi-step process which does not enable good control of particle size.

Electrochemical methods of carbon dot synthesis typically use the “top-down” approach, which involves the chemical cutting of bulk carbon materials such as graphite. However, this process is non-selective, resulting in carbon dots of a broad range of sizes which then require additional separation to achieve uniformity, and additionally such CDs exhibit limited photoluminescence (< 10 %) (94).

A material that is attached to a solid (or less commonly a liquid) can be removed from the surface if irradiated with a laser, in a process known as laser ablation. To produce carbon nanoparticles, Hu *et al.* suspended carbon materials in organic solvent and irradiated this with a laser of wavelength 1.064 µm. It was reported that the synthesis and surface modification of the carbon dots occurred concurrently. Thus, this one-step approach was able to produce fluorescent carbon nanoparticles. By varying the organic solvent in the reaction, the surface of the carbon nanoparticles could be manipulated to emit light of a specific wavelength (95).

2.1.1.2. Bottom-up methods

In contrast, bottom-up approaches like microwave synthesis, hydrothermal and solvothermal reactions, plasma treatment and chemical vapour deposition yield 3D, quasispherical, carbon dots (92) through the polymerisation of molecular precursors like citric acid and glucose. These reactions typically produce fewer defects and allow good control of the size and surface properties of carbon dots.

Microwave synthesis uses microwave radiation to achieve pyrolysis of organic compounds and provides the homogenous, fast heating that is necessary to form luminescent carbon dots of a uniform size (96).The procedure is quick, generally low-cost and is deemed a ‘green’ synthetic route. Using a microwave heating process, Pires *et al* prepared carbon dots from raw cashew gum, which showed good biocompatibility and low cytotoxicity, enabling them to be used in live-cell imaging (97).

Hydrothermal and solvothermal syntheses utilise an autoclave reactor in which the reactants are sealed, allowing the reaction to take place under high pressure and relatively low temperature. Hydrothermal procedures are carried out in water, while solvothermal procedures are carried out in an alternative solvent. Generally, these provide non-toxic, low-cost, and ‘green’ synthetic routes to produce carbon dots. An organic precursor is required to undergo hydrothermal carbonisation, which means many sources can be suitable reactants, and waste food products are often used, such as onion waste (98). Other natural sources include plant leaves (99, 100), orange juice (101), oats (102), potato (103), milk (104) and waste biomass (105) which have all been reportedly used to make carbon dots. Owed to its versatile reactants, there are many examples of carbon dots prepared by the hydrothermal method (93).

2.1.1.3. Scale up

Hydrothermal synthesis can also be done on a large scale, though it requires much greater capacity autoclaves, which may pose somewhat of a limitation. However, once invested in, this would result in large-scale facile hydrothermal synthesis. Wu *et al.* reported the use of a 10 L autoclave to synthesise homogeneous lamellar morphology boehmite from aluminium nitrate and urea (106).

2.1.1.4. Doping Carbon Dots

There are methods of surface modification that can be employed to improve the specificity of carbon dots, as well as the fluorescence quantum yield. Fluorescence QY can range between 0 and 1 where a higher value gives a stronger fluorescence signal and brighter fluorophore. It is the ratio of photons absorbed to photons emitted. Doping with heteroatoms; such as nitrogen, during the preparation of carbon dots is one of the methods (107). The inclusion of atoms other than carbon and oxygen has been known to enhance the photoluminescence properties of the material (107).

Mangosteen pulp and pulp-free lemon juice are among some natural sources that have been carbonised to obtain N-doped carbon dots with a nitrogen content of 3.16 % and 15 % respectively. In these cases the nitrogen was utilised solely from the biomass (88). Additionally, Nescafe instant coffee powder was found to produce carbon dots with a nitrogen content of 7.8 %, by Jiang *et al.* (108) These had been formed simply by combining hot water and coffee powder, and extracted by centrifugation and filtration (88). The fact that carbon dots are present in regularly consumed goods such as instant coffee, supports the non-toxic and biocompatible qualities of this material. Additionally, natural proteins such as *Bombyx mori* silk were used in the hydrothermal preparation of carbon dots, treated at 180^{o}C. Their intrinsically high nitrogen content (18 %) made them desirable for producing N-doped carbon dots (88).

Gholinejad *et al.* selected vanillin as a precursor because it is an abundant, cheap, and natural resource. Also, as it bears formyl groups, it could be subsequently used to modify Fe_3O_4 nanoparticles, which in turn could assist reduction of Pd(II) to Pd(0). They dissolved vanillin in ethanol and heated to 180 °C for 12 h, utilising the solvothermal method to produce carbon dots that fluoresced at 413 nm when excited at 350 nm (109). The UV-vis spectrum was not presented in this paper, though it could be inferred that the CDs absorbed at 350 nm from the fluorescence data.

2.1.2. Carbon dots derived from citric acid

As previously stated, a wide variety of carbon sources are used to prepare carbon dots, though citric acid has become one of the most prevalent in the literature. Owed to its three reactive carboxyl groups, it can support sufficient dehydration, carbonisation, and interaction with doping agents (110). In this effect, citrate-based CDs can form with citric acid alone and alongside small organic molecules like urea and amino acids.

It is understood that citrate-based CDs are made up of polydisperse structures like small molecules, oligomers, polymer chains, polymer clusters and carbon cores (110). The research of Song *et al.* supports this. They synthesised carbon dots from citric acid and ethylenediamine (140 °C), separated the components by column chromatography on silica and obtained five fluorescent batches which they characterised. Batch one was found to be fluorescent 5-oxo-1,2,3,5-tetrahydroimidazo[1,2-a]pyridine-8-carboxylic acid (IPCA) while batches two and three

mainly consisted of oligomers and batches four and five were nanosized carbon cores formed from monomer polymerisation and carbonisation of citric acid (111). They believed that the polymer clusters and carbon cores were able to improve the water solubility and stability of IPCA through electrostatic interactions and ultimately, the various components that make up the carbon dot solutions were in synergy (111).

2.1.3. Carbon dots as UV filters

Carbon dots tend to exhibit strong UV absorption due to the sp^2, π-conjugated skeleton. Often, an absorption band is present at 250–300 nm which corresponds to the π–π* transition of aromatic C=C bonds (112, 113). Surface functional groups are also understood to contribute to the absorption properties of carbons dots (114) with amino groups reportedly encouraging a red-shift in absorption (115).

There are many examples in the literature, where carbon dots have been used as sensors (90, 116-118), but their use in a UV-shielding capacity, is less well-studied. Gan *et al.* reported the use of carbon dots to develop composite materials with the ability of UV filtering and light conversion, for use in energy-saving buildings (119). They formed a composite film of fluorescent red, cellulose nanocrystals and carbon dots made from lignin and phenylenediamine. Lignin was dissolved in sulfuric acid, before it was heated at 200 °C for 10 h, and then dialysed for purification, to form carbon dots. The sulfuric acid served to catalyse the carbonisation of lignin during the reaction while phenylenediamine acted as an auxiliary agent (119). The conjugated structure of the resultant carbon dots enabled the absorption of UV light and had a long-wavelength emission of 623 nm when excited at 395 nm. This made it a promising energy-saving building material.

Xie *et al.* heated citric acid and N-(2-aminoethyl)-3-aminopropyl-trimethoxysilane in water, in an autoclave for 12 h at 180 °C (120). This produced organosilane-functionalised carbon dots. Using a sol-gel method, the CDs were used to dope Ormosil gel glass at various loading concentrations (Figure 2.3). The increasing strength of the blue emission shown suggests that doping with CDs enabled effective conversion of UV light to blue light. Thus, the resultant hybrid materials were found to

be capable of shielding harmful UV light, and could have applications in optical materials (120).

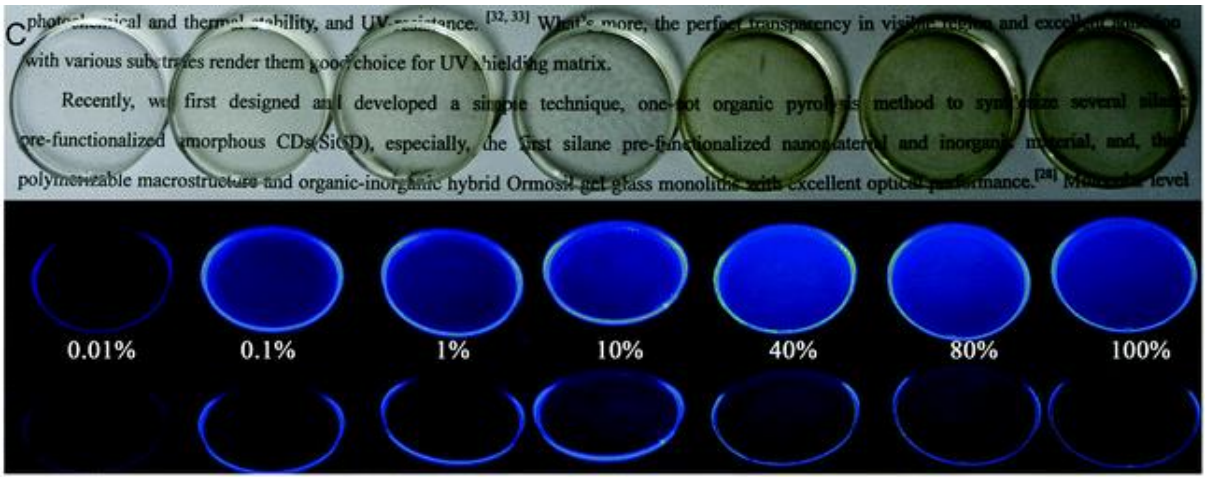

Figure 2.3: Photographs of Ormosil gel glass doped with various ratios of CDs under visible light, 365 nm illumination and 254 nm illumination (top - bottom). Reproduced from (120) with copyright permission.

Park *et al.* have demonstrated the use of carbon dots in films, to block UV and blue light, for the purpose of eye protection (121). The absorptive nature of carbon dots means that their use as a filter in a film is unaffected by the angle of light. They reported the formation of carbon dots from acetone and water, heated to 150 °C for 10 h. The carbon dots were filtered and dialysed for purification by separating large and small molecules by diffusion, through a membrane with a specific molecular weight cut-off. Dialysis is typically used to separate carbon dots from any unreacted precursors or small molecules. They exhibited two intense absorption peaks at 242 nm and 296 nm, which corresponded to π-π* transition of C=C bonds and n-π* transition of C=O bonds, respectively. The PL spectra showed excitation-dependent emissions. When excited between 380–520 nm the emission peaks redshifted from 450 nm to 560 nm. They compared the UV and blue blocking capabilities of the carbon dot films with a commercial blue filter and showed them to be higher.

2.1.3.1. Carbon dots in personal care

The personal care industry is enormous and consists of a range of products used to clean, enhance, and protect the human body. Generally, such products are applied topically to areas such as the skin, hair, nails, and teeth, to improve their aesthetic. Inescapably, the toxicity of such products is scrutinised. It is therefore important for their ingredients to be non-toxic and biocompatible, as well as to look and feel

appealing to the consumer. The environmental impact of the product must also be considered, including the synthetic routes used to form the components of the formulation as well as the influence these might have on the environment if released.

To date, there is little research on the preparation and inclusion of carbon dots in cosmetic formulations. In 2019, after the start of this project, Hu *et al.* proposed their carbon dots had potential to be used in personal care products like sunscreens (122). They used the hydrothermal method to prepare carbon dots from citric acid and a nitrogen source: urea, glycine and N,N'-bis(2-aminoethyl)-1,3-propanediamine. They achieved full-band UV absorbing materials by adapting the functional groups present on the carbon dot surface. Each reaction was carried out in water, except when N,N'-bis(2-aminoethyl)-1,3-propanediamine was used as the nitrogen source, ethylene glycol (29 %) was required. The reactions were heated to 200 ˚C for 5 hours and cooled naturally. A water phase needle (0.22 µm) was used to filter the products, followed by 24 h dialysis (Mw 1000), drying under vacuum at 70 ˚C, and finally freeze-drying of the resultant viscous products to obtain solid carbon dots. By incorporating the carbon dots into PVA films, they were able to show promise as UV absorbers for the purpose of skin protection and also demonstrated some anti-ageing properties (122).

Investigations into the use of *Dunaliella salina* (a unicellular, micro-algae) as a carbon dot precursor, were carried out by Chatzimitakos *et al* (2020), to enhance the *in vitro* SPF of sunscreen (123). Through heating the dried algal biomass in a crucible at 250 °C for 2 h in an oven, a black powder was obtained which was ultrasonicated with water for 5 minutes. The fluorescent supernatant was collected and filtered to obtain carbon dots. The UV-vis spectrum shows a weak shoulder at 270 nm which may be attributed to C=O n-π* and π-π* transitions or aromatic C=C π-π* transitions. Fluorescence emission was excitation-dependent, with a maximum recorded at 470 nm when excited at 380 nm. These CDs were compared with the *in vitro* SPF properties of citric acid-based carbon dots, made when citric acid was heated to 200 °C for 3 h in an oven, and dispersed in water. While both materials were able to enhance the SPF, the algae-base carbon dots proved more effective and exhibited negligible cytotoxicity to eukaryotic cells.

Jian *et al.* presented a simple dry heating method used to produce carbon quantum dots from spermidine, to act as effective antibacterial agents in eye drop formulations used to treat bacterial keratitis. They were found to be effective against several types of bacteria such as: *Staphylococcus aureus and Pseudomonas aeruginosa,* as well as *methicillin-resistant S. aureus* which is resistant to many drugs (124).

2.2. Aim

The popularity of carbon dots as a research area is highlighted by the vast array of literature on the topic. Using the Web of Science database there were 1390 reviews about carbon dots, prior to 2018. To date, there are 3638 reviews on the subject (84, 85, 89), and many more articles, which gives an indication of the level of intrigue surrounding this topic. Due to the broad range of properties, carbon dots have found use in many biological applications (125) such as cell imaging (126), as well as in energy conversion and storage devices (127), photocatalysis (128) and fluorescent ink (129). Their ability to absorb UV and visible light, biocompatibility, ease of synthesis and more, make them well suited to use as solar filters in products like sunscreens. However, just a handful of studies have considered carbon dots for use in this application (122, 123).

This chapter aims to investigate the facile preparation of carbon dots from small organic molecules, using a hydrothermal method, with a variety of reaction conditions, to optimise the broad-spectrum light attenuation. The subsequent materials will be evaluated for their potential in Croda's sunscreen formulations as UV boosters, which aim to increase the UV blocking power of sunscreens in cooperation with a main active ingredient.

2.3. Strategy and development of carbon dots

As demonstrated in Section 2.1, a variety of precursors can be used to prepare carbon dots. In this work, nine variations of carbon dots were prepared by hydrothermal synthesis, using precursors [1-7] in Figure 2.4, with citric acid or tartronic acid.

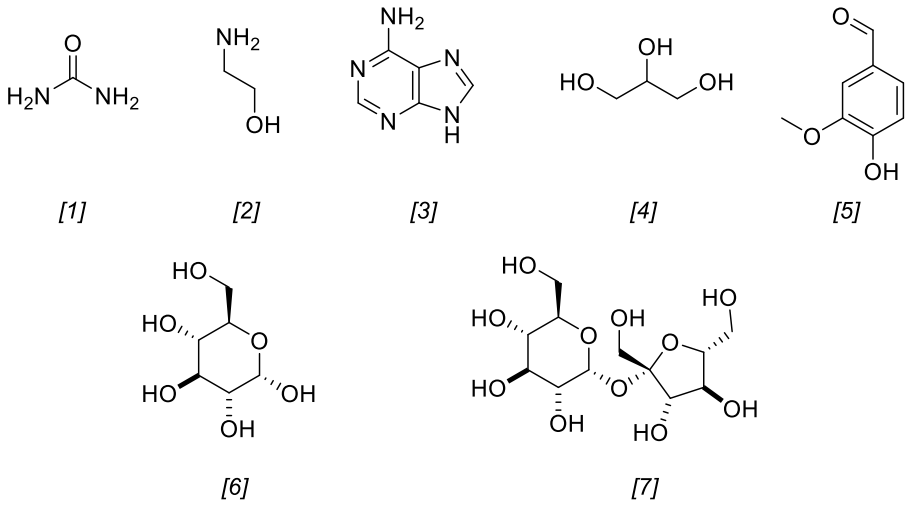

Figure 2.4: Selected precursors for carbon dots reactions: urea, ethanolamine, adenine, glycerol, vanillin, glucose, and sucrose [1-7], respectively.

With multiple carboxyl groups, citric acid and tartronic acid should interact easily with the dopants (chosen precursors) and were therefore used to facilitate the dehydration and carbonisation of the reactants (30). It is known that the absorption characteristics of carbon dots are impacted by the type of surface groups, the size of the π-conjugated system and the O/N content in the carbon core (130). Glycerol, vanillin, sucrose, and glucose are largely carbon-based with oxygenated functional groups, making them suited to the carbonisation process as well as able to impart -OH functionality to the carbon dots. Urea, ethanolamine, and adenine were employed as a nitrogen source in the reaction, which is known to extend the absorption towards the visible region. The use of O- and N-dopants were chosen on the premise that their non-bonding electrons may encourage n - π* transitions in the carbon dots (114, 115). These have a lower energy gap than π - π* transition and so they absorb longer wavelength radiation. The aromaticity of sucrose, glucose, vanillin, and adenine may also extend the absorption of the carbon dots towards the visible region, by forming more elaborate conjugate systems. The extension of the π system reduces the energy gap for π - π* transitions (131). With these precursors, a selection of O-doped and N-doped carbon dots were synthesised.

A simple preparation was derived from a procedure by Zhu *et al.* (132) and is outlined in Figure 2.5. Here, citric acid and an organic precursor [1-7] were dissolved in water and heated for 5 h at 200 °C, to form a coloured solution of carbon dots. Tartronic acid and precursors [2-3] were also investigated under the same reaction conditions.

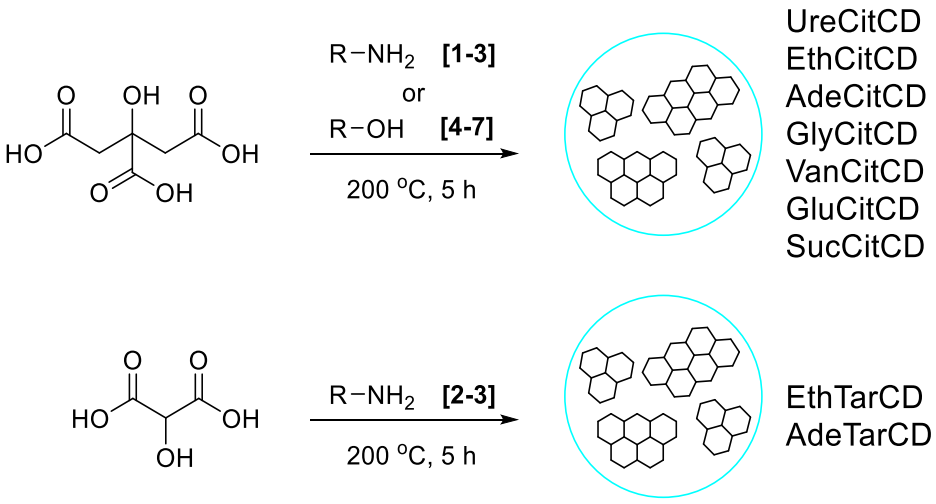

Figure 2.5: Summary of carbon dot synthesis

Several reactions were carried out to explore the effect of varying the reaction time, solvent, and molar ratios of precursors on the carbon dots absorption wavelength. These are outlined in

Table 2.1. At this early stage in the research, the initial UV-vis and fluorescence exhibited under the table-top UV lamp were used as first indicators that carbon dots had been formed. The products varied from orange – brown solutions which were well aligned with what was described in the literature.

Table 2.1: Summary of carbon dot preparations and their corresponding UV absorptions.

Preparations of EthCitCD					
Citric acid	**Ethanolamine**	**Solvent**	**Conditions**	**Absorption (nm)**	**Dried mass (mg/ mL)**
1.02 g, 5.2 mmol	280 µL, 4.7 mmol	H_2O (10 mL)	5 h, 200 °C	320, 365 (shoulder)	87.1
2.0162 g, 10.4 mmol	280 µL, 4.7 mmol	H_2O (10 mL)	5 h, 200 °C	319, 352 (shoulder)	-
2.0202 g, 10.4 mmol	280 µL, 4.7 mmol	EtOH (10 mL)	5 h, 200 °C	346	-
0.1957 g, 1 mmol	60 µL, 1 mmol	H_2O (10 mL)	5 h, 200 °C	320	19.5
0.5876 g, 3 mmol	180 µL, 3 mmol	H_2O (10 mL)	5 h, 200 °C	320, 369 (shoulder)	51.6
0.9634 g, 5 mmol	310 µL, 5 mmol	H_2O (10 mL)	5 h, 200 °C	320, 369 (shoulder)	83.6
Preparations of UreCitCD					
Citric acid	**Urea**	**Solvent**	**Conditions**	**Absorption (nm)**	**Dried mass (mg/ mL)**
1.0105 g, 5.2 mmol	0.2889 g, 4.7 mmol	H_2O (10 mL)	5 h, 200 °C	226 (shoulder), 331	27.4
0.765 g, 4 mmol	2.55 g, 40 mmol	H_2O (20 mL)	24 h, 200 °C	259 (shoulder), 328	-
Preparations of VanCitCD					
Citric acid	**Vanillin**	**Solvent**	**Conditions**	**Absorption (nm)**	**Dried mass (mg/ mL)**
1.0033 g, 5.2 mmol	0.7074 g, 4.7 mmol	H_2O (10 mL)	5 h, 200 °C	204, 225 (shoulder), 280, 312, 357 (shoulder)	-
1.0171 g, 5.2 mmol	0.7261 g, 4.7 mmol	EtOH (10 mL)	5 h, 200 °C	204, 230, 279, 309	-
1.0235 g, 5.2 mmol	0.6986 g, 4.7 mmol	H_2O (10 mL)	24 h, 200 °C	202, 228, 279, 308	54.7
1.0081 g, 5.2 mmol	0.1966 g, 1.3 mmol	H_2O (10 mL)	5 h, 200 °C	202, 227, 279, 308	-
1.0038 g, 5.2 mmol	0.3993 g, 2.6 mmol	H_2O (10 mL)	5 h, 200 °C	203, 229, 279, 309	-
Preparations of GlyCitCD					
Citric acid	**Glycerol**	**Solvent**	**Conditions**	**Absorption (nm)**	**Dried mass (mg/ mL)**
1.0239 g, 5.2 mmol	340 µL, 4.7 mmol	H_2O (10 mL)	5 h, 200 °C	200	92.0

Preparations of SucCitCD					
Citric acid	**Sucrose**	**Solvent**	**Conditions**	**Absorption**	**Dried mass (mg/ mL)**
1.0090 g, 5.2 mmol	1.6216 g, 4.7 mmol	H_2O (10 mL)	5 h, 200 °C	202, 290 (shoulder)	93.3
Preparations of GluCitCD					
Citric acid	**Glucose**	**Solvent**	**Conditions**	**Absorption**	**Dried mass**
1.0052 g, 5.2 mmol	0.8378 g, 4.7 mmol	H_2O (10 mL)	5 h, 200 °C	204, 288 (shoulder)	82.7
Preparations of AdeCitCD					
Citric acid	**Adenine**	**Solvent**	**Conditions**	**Absorption**	**Dried mass**
0.9609 g, 0.005 mol	0.6737 g, 0.005 mol	H_2O (10 mL)	5 h, 200 °C	200, 259	-
Preparations of AdeTarCD					
Tartronic acid	**Adenine**	**Solvent**	**Conditions**	**Absorption**	**Dried mass**
0.6039 g, 0.005 mol	0.6785 g, 0.005 mol	H_2O (10 mL)	5 h, 200 °C	201, 260	-
Preparations of EthTarCD					
Tartronic acid	**Ethanolamine**	**Solvent**	**Conditions**	**Absorption**	**Dried mass**
0.6089 g, 0.005 mol	300 µL, 0.005 mol	H_2O (10 mL)	5 h, 200 °C	264–350 (weak shoulder)	66.8

UV-vis spectroscopy was used, first and foremost, to determine how capable each material was at filtering light by absorption with a particular focus on UVA, UVB and HEVL. As the concentration of the neat carbon dots was unknown, each solution was freeze-dried to remove water, weighed, and redispersed in water so that UV-vis spectra could be measured at known mg/ mL, and compared.

UV-vis spectra of the starting precursors and those of the final materials were also used to monitor the progress of the reaction. Those with the most favourable optical properties, namely absorption of UVA and UVB were chosen and carried forward for further analysis. This strategy is depicted in the flow chart in Figure 2.6.

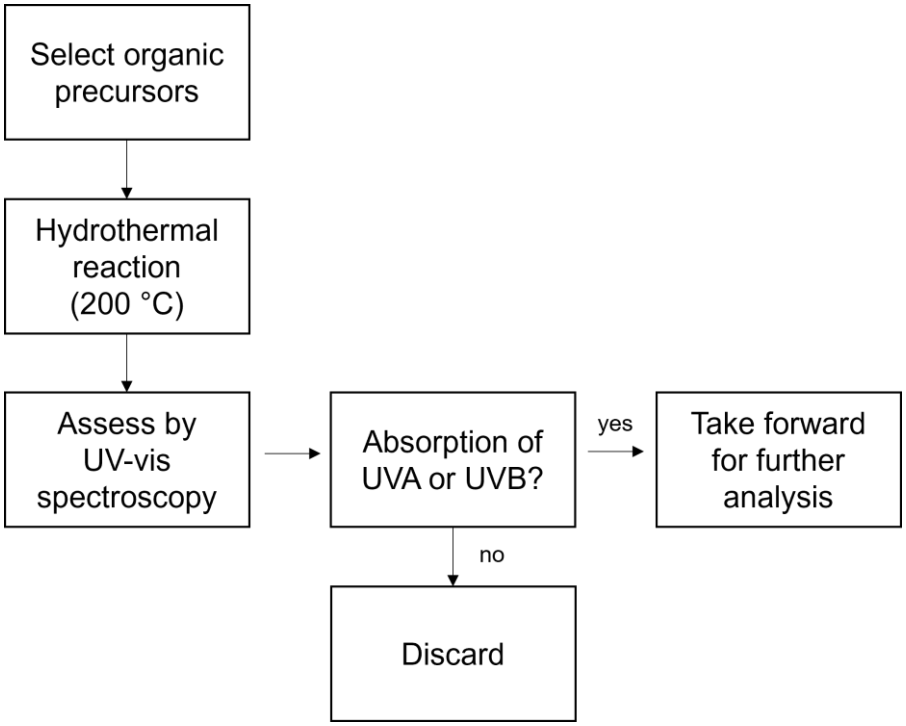

Figure 2.6: A flow chart to show the initial assessment of the carbon dots by UV-vis spectroscopy.

2.4. Initial UV assessment

UV spectroscopic analysis was carried out as an initial assessment of the material's efficiency as a UV blocker.

2.4.1. O-Doped carbon dots

Carbon dots formed from O-containing glucose, glycerol, sucrose, and vanillin, in combination with citric acid, are shown in Figure 2.7. Samples of interest for sunscreen applications should absorb in either the UVA and UVB regions, as indicated in Figure 2.7, or broadly across both. VanCitCD shows a broad absorption across the UVC region (200 nm, 225 nm) and UVB region (280 nm, 312 nm). These could be attributed to a combination of π–π* transitions of carbon dots with extended π systems and n-π* transitions due to the inclusion of non-bonding O electrons. The carbon dots may vary in length of conjugation, which might explain the broad absorption peaks. The remainder of the carbon dot samples (GluCitCD, SucCitCD, and GlyCitCD) showed broad UVC absorption but were not effective in the desired regions (UVB or UVA).

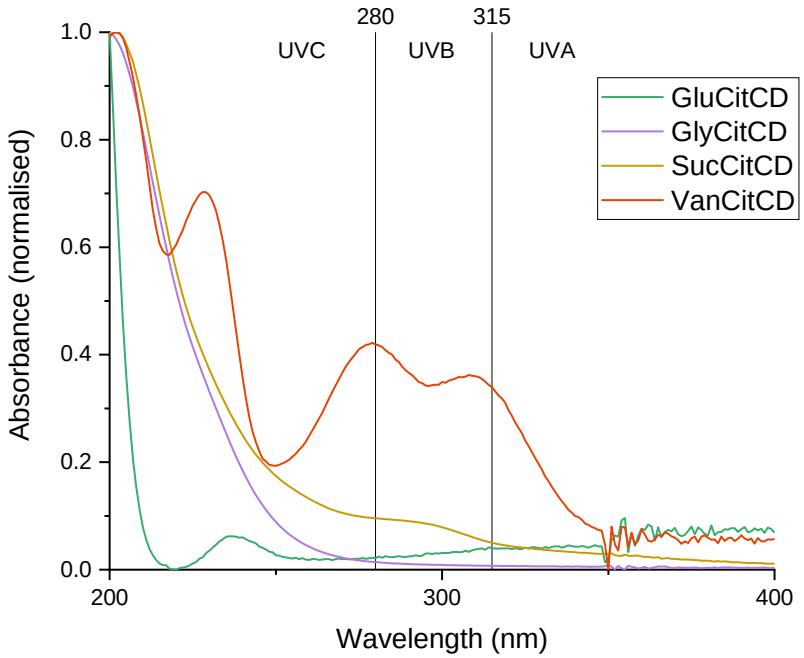

Figure 2.7: UV-vis spectra of O-doped carbon dots, measured at concentration of 0.003 % v/v.

This may suggest that, when paired with citric acid, the resultant π conjugate systems were shorter than vanillin. It is possible that the abundance of -OH groups in sucrose, glucose and glycerol may be reacting with multiple carboxylic acid groups on citric acid, through condensation reactions, and potentially hindering the formation of longer-chain polymers through earlier termination of the polymerisation. The ratio of O=C-OH to -OH of citric acid and dopant could be investigated further to optimise the conjugation, for example a 2: 1 ratio yield of citric acid to sucrose might encourage more conjugation as more carboxyl groups will be available for condensation reactions with O-H.

Overall, the UV profile of carbon dots formed from vanillin and citric acid (VanCitCD) appears to be the most encouraging for use as a UV filter and will be carried forward for further characterisation and assessment. The remaining O-doped carbon dots were disregarded on account of their less-than-optimal UV profiles.

2.4.2. N-doped carbon dots

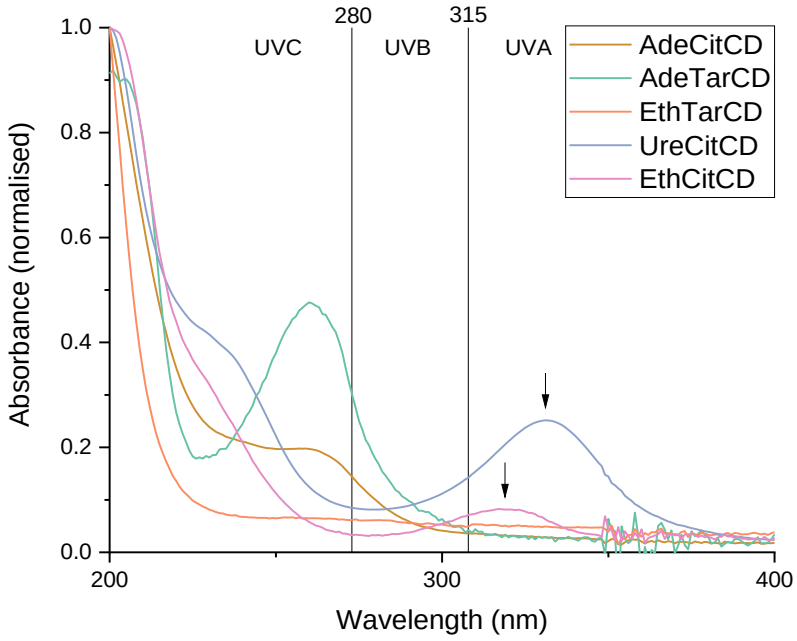

Figure 2.8: UV-vis spectra of N-doped carbon dots measured at concentration of 0.003 % v/v.

The UV profiles of N-doped carbon dots, using adenine, ethanolamine, and urea, coupled with citric acid and tartronic acid, are shown in Figure 2.8. The boundaries of UVA, UVB and UVC are clearly indicated, with 280 nm and above being the region of interest, for UV-filtering sunscreen applications. There are two clear contenders with absorption peaks in the UVA region: EthCitCD (320 nm) and UreCitCD (331 nm), which may be attributed to lower energy n-π* transitions that are associated with non-bonding heteroatoms in C=O or C=N bonds or π-π* transitions of C=C bonds due to extension of the conjugate system through polymerisation (130). Both these materials do not absorb UVB light but broadly absorb in the UVC region (which is filtered by the ozone layer and therefore not applicable). They are promising candidates, although they would not class as broad-spectrum filters based on their lack of UVB absorption.

In contrast, the absorption peaks of EthTarCD, AdeTarCD and AdeCitCD were mainly constrained to the UVC region. Though, AdeTarCD showed a strong absorption at 260 nm, that extended into the UVB region to 315 nm and AdeCitCD had a shoulder at 263 nm that extended into the UVB to 300 nm. It is possible that the smaller sized tartronic acid, with fewer carboxyl groups than citric acid, is less effective at facilitating

condensation of adenine and ethanolamine. With this, shorted conjugate structures might be formed, leading to higher energy electronic transitions and shorter wavelength absorption. Additionally, during synthesis it was noted that adenine did not fully dissolve in the solvent which may have hindered the reaction.

After 1 week, the AdeCitCD and AdeTarCD samples appeared to be contaminated by a growth, on the lining of the glass and the surface of the solution. This was purely observational and without subculturing and further identification tests, it was not possible to know what species of fungi had contaminated the sample. Both products had shown blue fluorescence under a table-top UV lamp at 365 nm, however this was repeated following the observed growths, and the products no longer fluoresced, which suggested degradation of the carbon dots, possibly due to the contaminants. It is possible that these samples were contaminated, and the adenine-based solution provided an optimum medium for fungal growth as adenine has previously been used to provide nutrients in yeast growth media (133).

Overall, the combinations of ethanolamine/adenine with tartronic acid did not produce carbon dots with viable absorption profiles for use in sunscreens. However, ethanolamine when coupled with citric acid, showed promise (UVA absorption) while AdeCitCD did not. From this, it could be inferred that the use of tartronic acid as the backbone of the carbon dots was not as effective as citric acid. Adenine shows a strong absorption near the UVC/UVB border which could potentially be improved with a more appropriate solvent to solubilise adenine in the reaction. UreCitCD and EthCitCD appear to be the most favourable of the N-doped candidates and were continued for further characterisation and testing. As explained in the strategy in Figure 2.6, the remainder (AdeCitCD, AdeTarCD and EthTarCD) were not taken any further as their fundamental UV profiles were undesirable for sunscreen applications, though they were consistent with what has been found in the literature for carbon dots (strong absorption in the range of 200-400 nm, with a tail in the visible range) (130).

2.5. EthCitCD investigations

2.5.1. Characterisation

The hydrothermal reactions of ethanolamine and citric acid yielded carbon dots with desirable UV profiles. In this section, EthCitCD will be characterised by FT-IR, TEM and fluorescence spectroscopy.

2.5.1.1. FT-IR spectroscopy

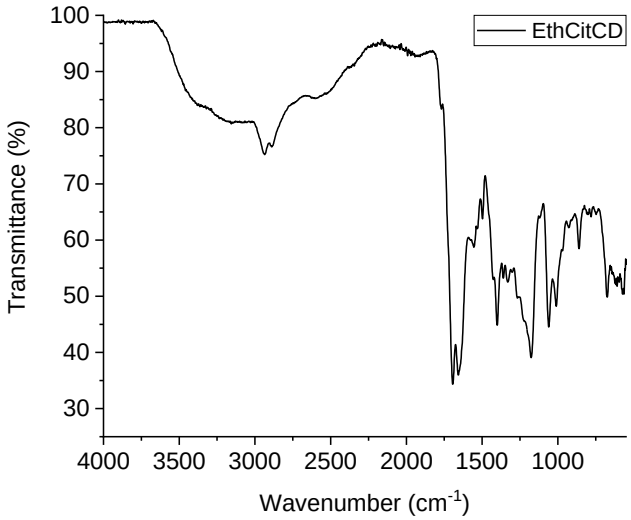

Figure 2.9: FT-IR spectrum and corresponding table of assignments, for EthCitCD.

The FT-IR spectrum of EthCitCD (Figure 2.9) can be used to decipher which functional groups are present in the freeze-dried material and give an indication of whether the reaction went as expected.

Table 2.2: FT-IR assignments for EthCitCD

Material	Assignment	Wavenumber (cm^{-1})
EthCitCD	O-H, N-H stretch	3650 - 2250
	C-H stretch (alkene)	2936
	C-H stretch (alkane)	2889
	C=O carboxylic acid	1769
	C=O stretch (primary amide)	1697
	C=C stretch, C=N stretch, N-H bend	1676-1592
	C-H bend, O-H bend	1480-1326
	C-O stretch alkyl aryl ether	1270
	C-N stretch	1179
	C-O stretch alkyl aryl ether	1062

The peak at 1697 cm^{-1} would suggest the presence of C=O amide stretch, while the absorption band from 1676 – 1592 cm^{-1} may indicate the C=N stretch and N-H in-plane bend, overlapped with C=C stretch. The formation of the amide may indicate condensation reactions between carboxylic acid groups (citric acid) and amino groups (ethanolamine). Additionally, the carboxylic acid C=O stretch is weak at 1769 cm^{-1} which also alludes to its involvement in condensation reactions. The presence of C=C and C=N may suggest conjugated structures have formed. Absorption peaks between 1270 cm^{-1} and 1062 cm^{-1} correspond to stretching vibrations of =C-O-C and C-N and suggest ether and amine linkages are present.

Therefore, using FT-IR it has been established that the carbon dots predominantly consist of conjugate structures with amide bonds and ether linkages, as well as carbonyl, hydroxy and amino groups. These are in line with what would be expected for carbon dots (134). Amino-functionalised and conjugated structures also fit well with the UV properties shown in Figure 2.8.

2.5.1.2. TEM

For analysis by Transmission Electron Microscopy (TEM), the samples were deposited onto a holey carbon grid as nanoparticles tend to cling near the holes due to Van der Waals forces. Typically, the holey carbon grid is hydrophobic, so it was plasma cleaned, to make it slightly hydrophilic to help to retain the carbon dots. EthCitCD was sonicated for around 20 min to make sure it was well dispersed, before adding two drops onto the carbon grid. This was dried and then transferred into the sample holder. The sample was put into the outer chamber under a vacuum for 5 minutes to reach the same vacuum state as the inner chamber, before it was fully inserted for analysis.

In Figure 2.10A-B the nanoparticles are shown collected near the holes of the carbon grid, because of Van der Waals forces between themselves and the plasma-cleaned, slightly hydrophilic surface of the carbon grid. The hydrothermal reaction of ethanolamine and citric acid resulted in carbon dots with an average particle size of 1.6 nm. The particle size of carbon dots varies considerably in the literature, with the type of synthesis, precursors and their concentrations and reaction conditions. For example, Kim *et al.* reported 10–15 nm carbon dots by oxidative carbonisation at 90 °C from the same precursors (135), while Sinclair *et al.* used a pyrolysis method to obtain 13 nm carbon dots (136). In comparison, using this hydrothermal method, the particle

size has been reduced significantly, with uniformity intact, and is in line with other hydrothermal syntheses of N-doped CDs such as cellulose with ethylenediamine (diameter 3.2 nm) (137). However, Li *et al.* described the formation of 13.7 nm diameter carbon dots from citric acid (2 g) and ethanolamine (25 mL) at 180 °C for 4 h (138). This suggests that the high content of ethanolamine might lead to greater surface functionality and so increase the diameter, while in EthCitCD, the amount of organic dopant is relatively low by comparison, which may be responsible for the smaller nanoparticles. As a result of the smaller size, a shift may be apparent in the optical properties.

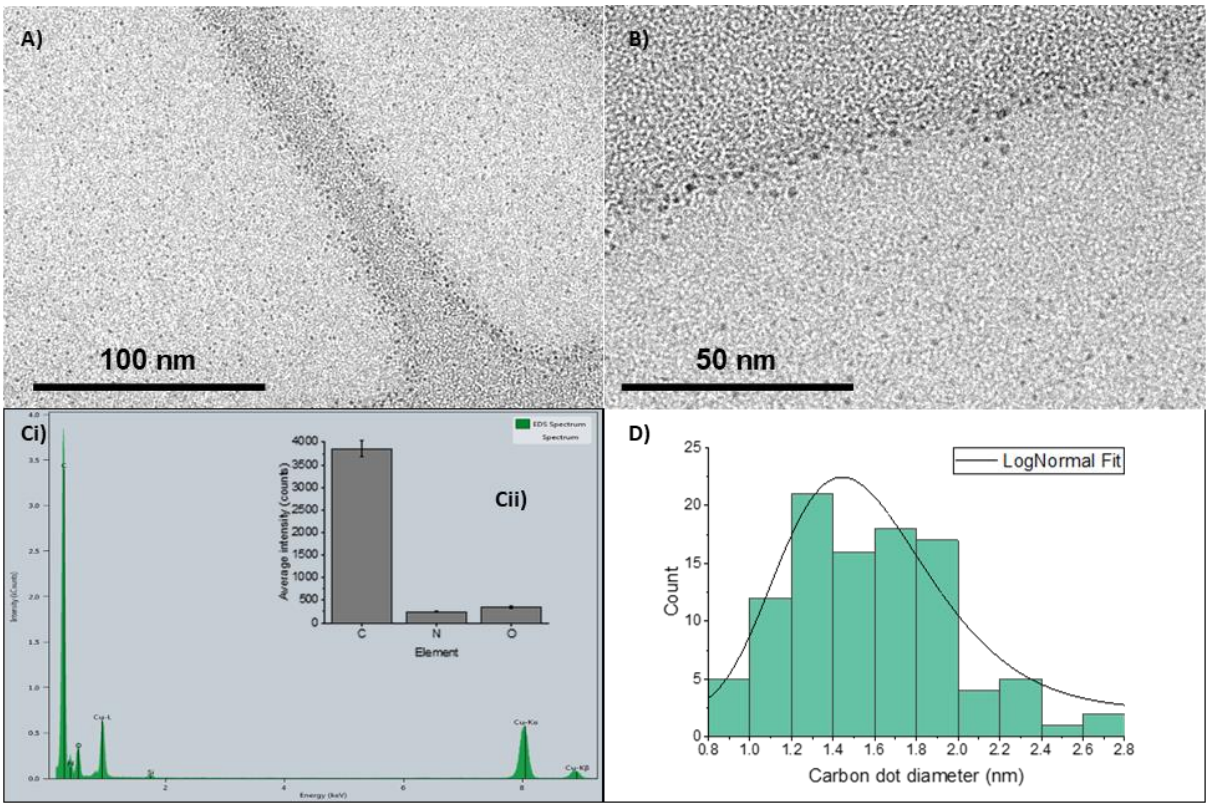

Figure 2.10: A-B) TEM images of EthCitCD at 100 nm and 50 nm scales, respectively, Ci) EDS analysis, Cii) average intensity of C, N and O over 5 sample areas and D) particle size distribution (n=100)

Using Energy Dispersive Spectroscopy (EDS) alongside TEM, the elemental composition of the nanoparticles was investigated. Five EDS data sets were generated from different sites in the sample, to improve the statistical relevance of the data, reliability and ensure the sample was well-represented. EDS confirmed the presence of C, N and O, as well as Cu and Si which are often present in the grid. It is not possible to use the intensity of the EDS peaks quantitatively, since the carbon signal is likely a

combination of carbon in the sample and from the carbon grid support, and therefore cannot be differentiated (139). However, EDS confirms that the carbon dots do not contain any foreign impurities and that they have been successfully doped with nitrogen, which supports the FT-IR results.

Overall, TEM and EDS analysis confirm that N-doped spherical carbon dots (diameter 0.8-2.8 nm) have been formed, with a narrow size distribution. With this, the hydrothermal method displays good control over particle size.

2.5.1.3. Fluorescence spectroscopy

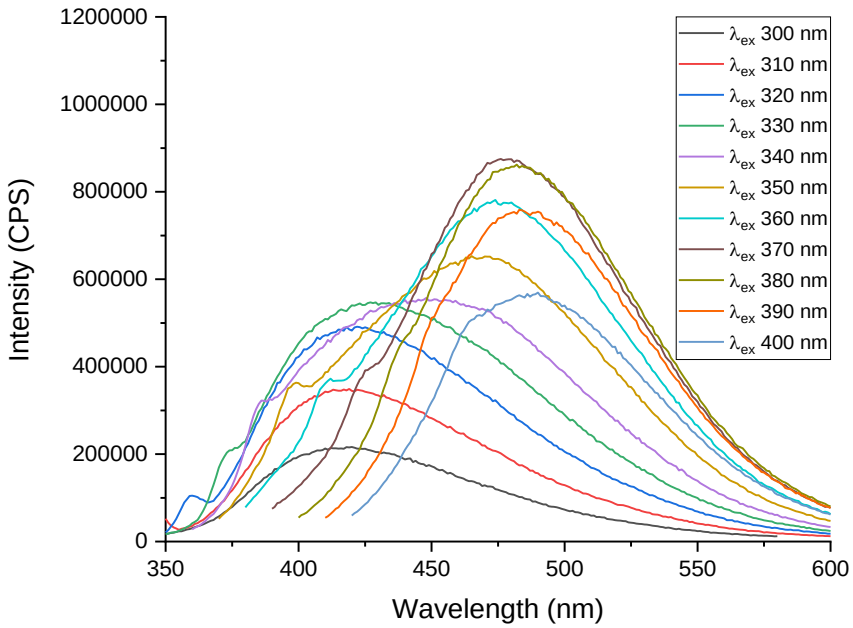

Figure 2.11: Fluorescence spectra of EthCitCD when excited between 300-400 nm, in 10 nm increments (measured at concentration of 0.003 % v/v).

EthCitCD demonstrate excitation-dependent fluorescence emission (Figure 2.11) which is a characteristic found in many reported carbon dots. As the excitation wavelength increased in 10 nm increments between 300 and 400 nm, the emission peak was shown to red-shift (416 nm–488 nm). Additionally, a rise and fall in intensity is distinct, with the maximum emission peak reading at 479 nm, with an excitation wavelength of 370 nm. In comparison to the larger (13.7 nm) carbon dots synthesised by Li *et al.* with maximum emission at 460 nm (ex 370 nm) (138), EthCitCD are significantly red-shifted by 19 nm when excited at 370 nm, which may indicate the

influence of smaller particle size on fluorescence or differences in surface functional groups.

According to the literature, the excitation-dependent emission of carbon dots is not well understood. Due to the variations in functional groups on the surface of the carbon dots and the length of the π conjugate systems, there is likely to be a multitude of molecular electronic transitions that can occur when the carbon dots are excited. These electronic transitions have different probabilities of occurring at different excitation wavelengths. It is therefore possible that a particular transition may dominate at a particular excitation wavelength, which can lead to the observed excitation-dependent emissions (140).

2.5.1.4. Size exclusion chromatography

Size exclusion chromatography has previously been used to separate carbon dots, as they are typically mixtures of varying sizes. To investigate the role of particle size in the optical properties seen, size exclusion chromatography of EthCitCD was carried out and the fractions monitored by UV-vis and fluorescence spectroscopies.

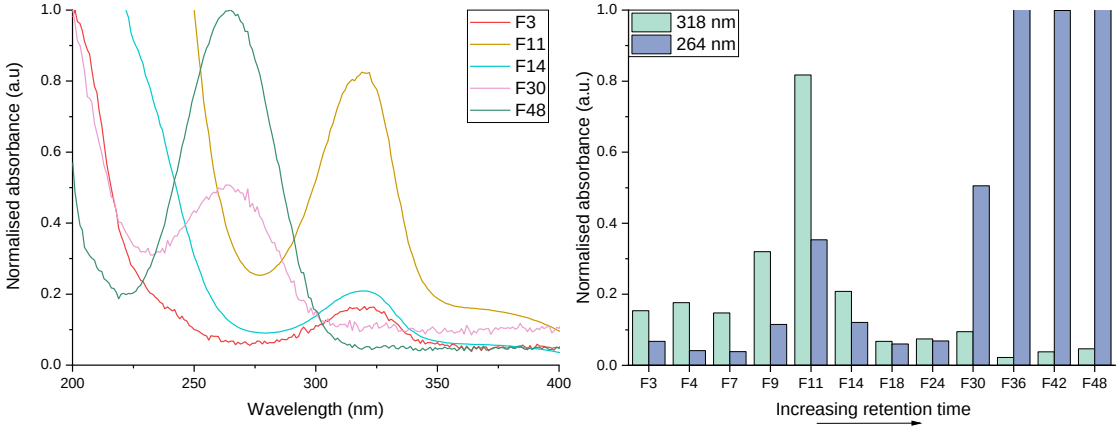

Figure 2.12: Analysis of UV profiles for various fractions from the size exclusion column of EthCitCD (measured at concentrations of 3.2 %)

The principle of size exclusion chromatography is based on the larger particles eluting from the column first, followed by the smaller particles which take longer to pass through various channels and pores in the Sephadex medium. As the fractions of EthCitCD were eluted, two distinct changes were shown in the UV spectra. As the

retention time increases, the rise and fall of absorption at 318 nm is evident, followed by the increase in absorption at 264 nm.

Figure 2.12 shows the normalised absorbance at 264 nm and 318 nm in each fraction, alongside the UV spectra themselves. Thus, it can be inferred that the absorption peak at 318 nm may be due to larger carbon dots with more developed conjugate systems or that are more functionalised. The fluorescence spectra for F11, F30 and F48 fractions are shown in Appendix 2.1 as these fractions exhibited significant changes in their UV profiles. The fluorescence spectra once again show excitation-dependent emissions, though from fraction 30 and beyond, the PL intensity substantially decreases. This, coupled with the UV data, suggests the earlier fractions might contain the carbon dots (as they fluoresce strongly), while the later fractions corresponding to the 264 nm UV absorption might be a mixture of reaction intermediates with some smaller carbon dots, as their fluorescence is low but apparent. The variation in fluorescence emissions, and the excitation-dependent emissions suggest that a mixture of carbon dots is responsible for the UV absorption at 318 nm. Due to the narrow particle size distribution, gathered from the TEM images, it is likely that the carbon dots have eluted together, and it was not possible to separate them with this column. It did, however, allow us to get a better understanding of the carbon dots optical properties.

2.5.2. Controlling reaction conditions

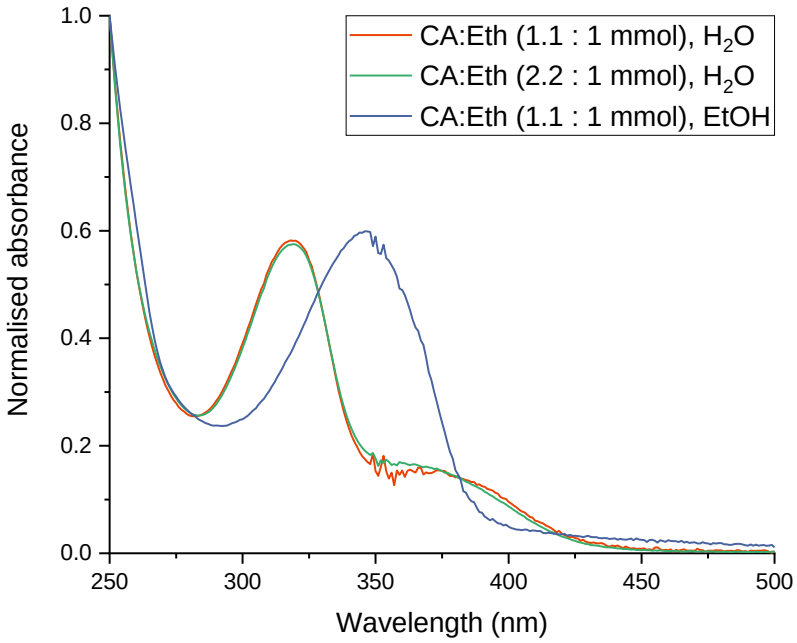

Figure 2.13: UV-vis spectrum of EthCitCD where citric acid (CA): ethanolamine (Eth) molar ratios and solvent were varied as follows: 1) 1.1: 1 mmol, water; 2) 2.2: 1 mmol, water; 3) 1.1: 1 mmol, ethanol, measured at concentrations of 0.003 % v/v, in water and ethanol for 3). All three reactions took place at 200 °C, 5 h.

The molar ratio of citric acid (CA) to ethanolamine was doubled from 1.1 mmol: 1 mmol to 2.2 mmol: 1 mmol, to investigate how increasing citric acid might affect the UV profile. The spectra were normalised by dividing spectra by the max absorbance so that any shift in absorption wavelength could be easily compared (Figure 2.13). Both spectra have the same absorbance of 319 nm and mimic a similar shoulder between 360 nm and 400 nm. This would suggest that the presence of amino groups from ethanolamine must be influencing the UV-vis profile rather than citric acid. The use of ethanol as a solvent over water, caused a significant bathochromic shift in the absorption peak. Ethanol itself has been used as a carbon source in the formation of carbon dots, reported by Wang *et al.* (141) therefore it might be acting as an alternative carbon and oxygen source here, causing structural deviations and a shift in the spectra.

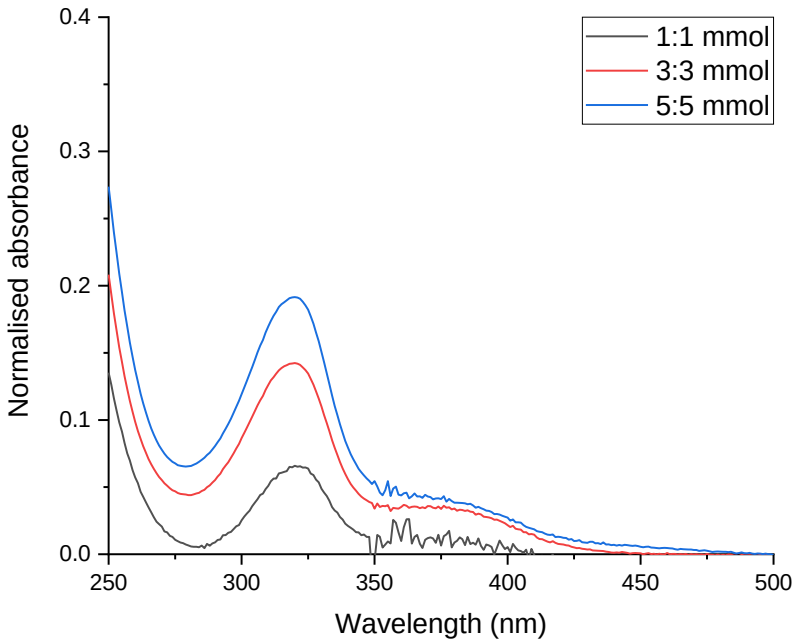

Figure 2.14: UV-vis spectra (250 nm–500 nm) of EthCitCD where the amount of ethanolamine and citric acid was changed. Citric acid: ethanolamine (1:1 mmol; 3:3 mmol, 5:5 mmol) measured at concentrations of 0.003 % v/v, in water.

Here, the amount of ethanolamine and citric acid in the reactions were systematically increased, (1:1 mmol; 3:3 mmol, 5:5 mmol) but the ratios were kept at 1:1. The UV-vis spectra were normalised by dividing the spectra by the max absorbance (Figure 2.14). In each, a defined absorption at 319 nm was shown, which is likely due to the presence of amino groups (due to lower energy n-π* transitions) as deciphered from the spectra in Figure 2.13. The absorbance intensity increases with the amount of precursors and a shift is not observed, which tells us that the reaction is highly reproducible and the intensity of the peak at 319 nm is related to both the citric acid and ethanolamine parameters, as opposed to just one or the other. It indicates that condensation reactions between these precursors contribute significantly to the subsequent optical properties.

2.6. UreCitCD investigations

2.6.1. Characterisation

The hydrothermal reactions of urea and citric acid showed the carbon dots had desirable UV profiles. In this section, UreCitCD will be characterised by FT-IR, TEM, and fluorescence spectroscopy.

2.6.1.1. FT-IR spectroscopy

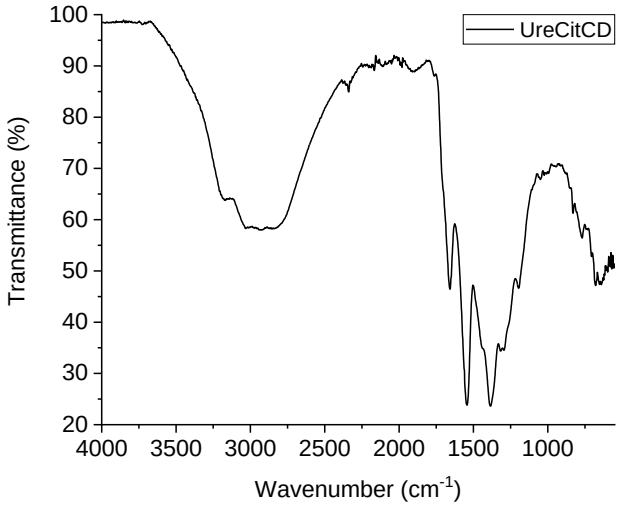

Figure 2.15: FT-IR spectrum for UreCitCD.

The FT-IR spectrum in Figure 2.15 can be used to decipher which functional groups are present on the surface of carbon dots.

Table 2.3: Assignments for FT-IR spectra of UreCitCD

Material	Assignment	Wavenumber (cm^{-1})
UreCitCD	O-H, N-H stretch	3638–2412
	C-H stretch	2929
	C=O stretch	1666
	C=C stretch, C=N stretch, N-H bend	1626–1504
	C-H bend, O-H bend, C-N stretch	1475–1310
	C-O stretch	1288
	C-N stretch	1189

As per the assignment table, the broad band from 3666–2259 cm^{-1} indicates stretching vibration of O-H and in-plane bending vibration of N-H. The absorption bands at 1657 cm^{-1}, 1626–1504 cm^{-1} and 1314 cm^{-1} are consistent with C=O stretch, N-H bend and C-N stretch and suggest the detection of amide bonds, which might indicate the

condensation reaction of citric acid and urea has occurred, as expected; C-H stretching and bending bands were also observed at 3038 cm^{-1}, 2855 cm^{-1} and 1385 cm^{-1}. Also, the presence of C=C and C=N stretching bands at 1626 cm^{-1}–1510 cm^{-1}, which overlap with the N-H bend, may suggest a conjugated structure has formed. Overall, the FT-IR spectrum confirms that hydroxy, amino and carboxyl groups, functionalise the carbon dots and it is likely that the base structure of the material contains amide linkages due to the condensation reaction of citric acid and urea. The FT-IR spectrum is consistent with urea-derived carbon dots in the literature (142).

2.6.1.2. TEM

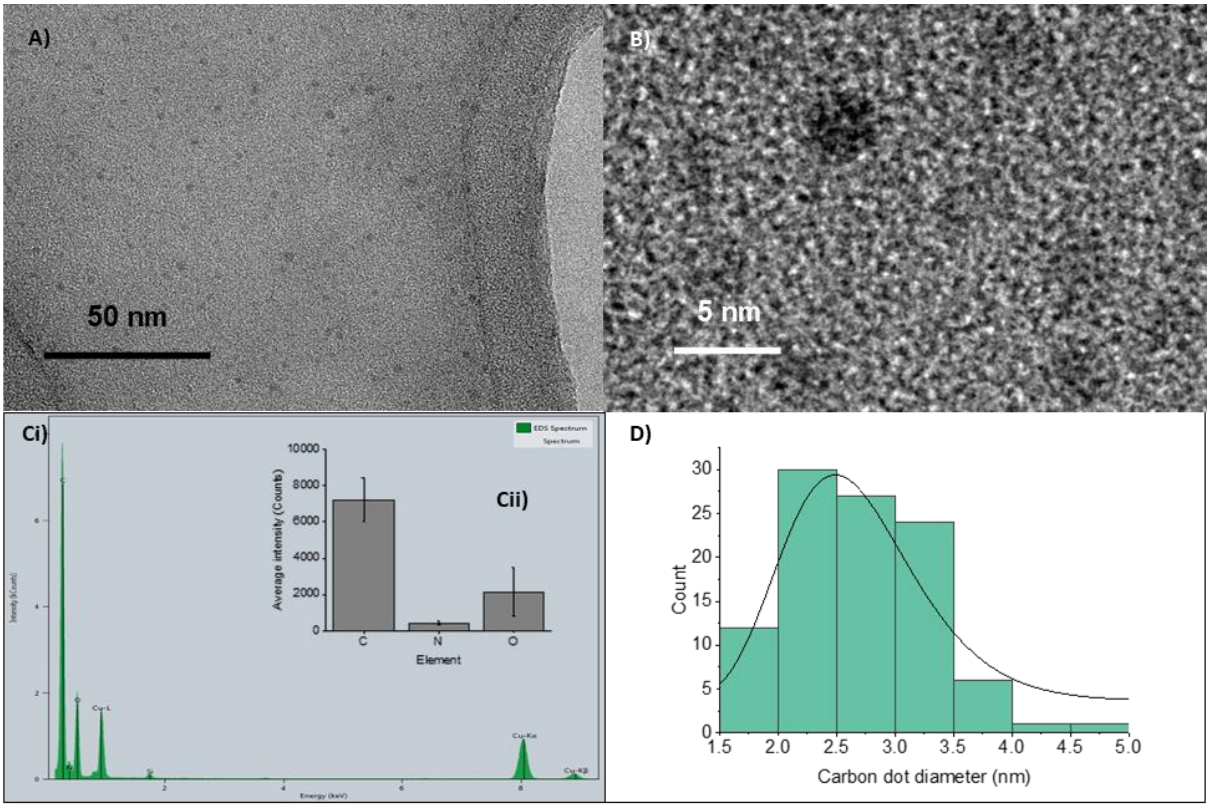

Figure 2.16: A-B) TEM images of UreCitCD at 50 nm and 5 nm scales, respectively, Ci) EDS analysis, Cii) average intensity of C, N and O over 4 sample areas and D) particle size distribution (n=100)

Following the hydrothermal reaction of urea and citric acid, the TEM images in Figure 2.16A-B portray well-dispersed carbon dots with a narrow particle size range of 1.5 - 5 nm and an average size of 2.7 nm. In contrast to EthCitCD, these are larger which may be due to the bulkier nature of urea with double the amino content. They are in good alignment with similar hydrothermal reactions of carbon dots in the literature, like

Huang *et al.* who produced urea-doped CDs with an average size of 3.5 nm and size range of 1- 6 nm (142).

In these TEM measurements a graphene oxide grid was used instead of a carbon grid, to try and get better contrast, though this was to little avail. EDS analysis confirmed the presence of C, N and O, as was expected. Comparing EDS of EthCitCD and UreCitCD, the latter might be expected to show double the nitrogen content as the urea precursor contains two -NH_2 groups. However, EDS does not show this. As the particles are evidently better dispersed in UreCitCD the same number of particles are not being investigated "per EDS capture" because they were not clustered together on screen as in EthCitCD, therefore these results cannot be quantitively compared. However, EDS does ascertain that nitrogen is present in both and overall, UreCitCD formed slightly larger nanoparticles which is likely to impact its optical properties.

2.6.1.3. Fluorescence spectroscopy

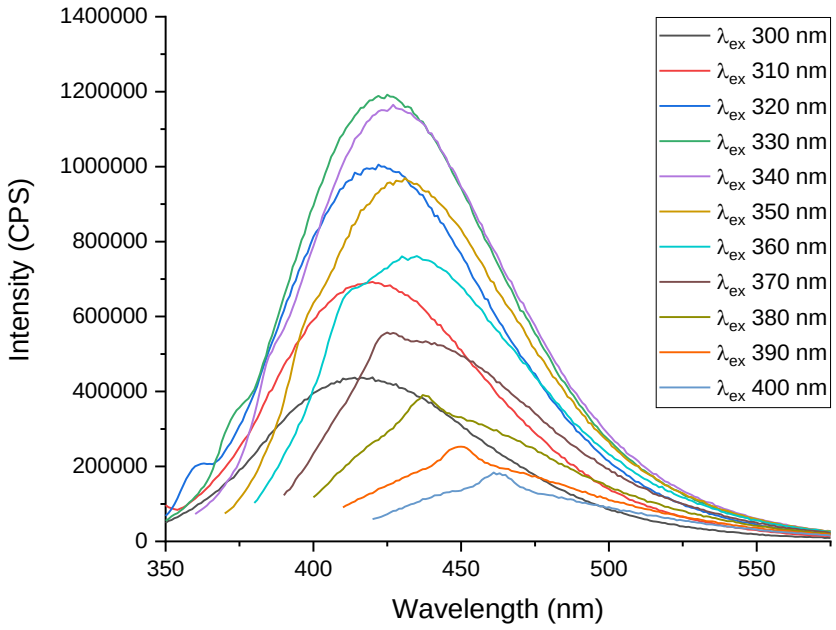

Figure 2.17: Fluorescence spectra of UreCitCD when excited between 300 – 400 nm, in 10 nm increments measured at concentrations of 0.003 % v/v.

UreCitCD displayed the excitation-dependent fluorescence emission phenomenon that is so commonly seen in carbon dots (Figure 2.17). The sample was excited at 300–400 nm in 10 nm increments and the resultant emission spectra was shown to red-shift and ranged from 415 nm to 462 nm. The intensity of the emissions increased

over this range, with a maximum at 424 nm when excited at 330 nm. In contrast, Huang *et al.* urea-doped carbon dots showed maximum emission at 525 nm, when excited at 430 nm (142). The reported sizes are similar, so this large shift in emission wavelength may instead be due to surface passivation owed to urea plus an alternative carbon source.

2.6.2. Controlling reaction conditions

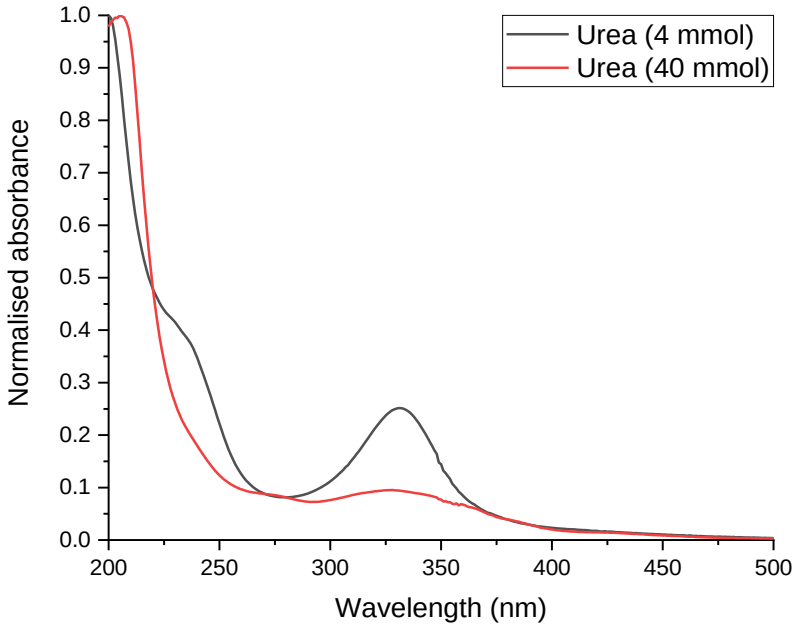

Figure 2.18: UV-vis spectrum of UreCitCD where citric acid (CA): urea molar ratio was increased from 1: 0.9 to 1: 10 mmol, measured at concentrations of 0.003 % v/v. Both reactions took place at 200 °C, 5 h.

The molar ratio of citric acid and urea was increased from 1: 0.9 to 1: 10, respectively. By increasing the proportion of urea in the reaction by a factor of 10, the nitrogen content was significantly raised. It was thought that this would lead to a bathochromic shift in the UV profile (Figure 2.18), by increasing the amino functionality of the carbon dots. However, the lower energy n–π* transitions that correspond to non-bonding electrons of heteroatoms, like nitrogen, are likely causing the absorption peak at 331 nm. This does shift minimally, hypsochromically by 3 nm at a 1: 10 ratio. It is possible that the lack of abundance of citric acid carboxyl groups, hinders the surface passivation of the carbon dots. Therefore, it can be inferred that a more similar ratio

of citric acid to urea, rather than an excess of nitrogen, is optimal for carbon dot formation and more effectively absorbs UVA radiation.

2.7. VanCitCD

2.7.1. Characterisation

In addition to UV spectroscopy shown earlier in the chapter, VanCitCD were characterised by FT-IR spectroscopy and fluorescence spectroscopy.

2.7.1.1. FT-IR spectroscopy

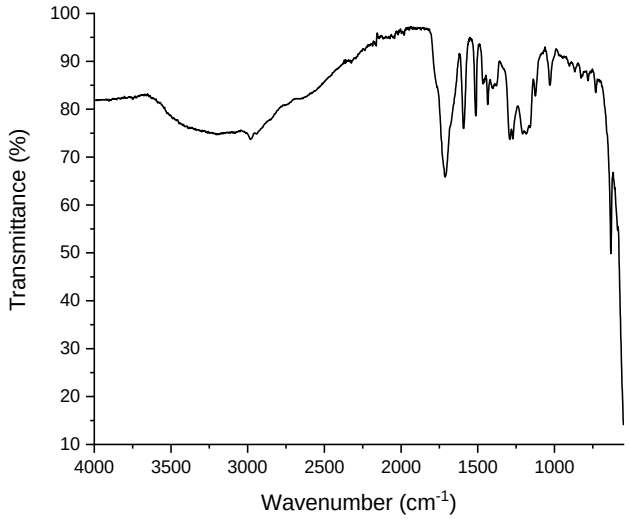

Figure 2.19: FT-IR spectra of VanCitCD

The FT-IR spectrum of VanCitCD (Figure 2.19) was used to distinguish the functional groups on the surface of carbon dots. The corresponding assignments are shown in Table 2.4.

Table 2.4: Assignments for FT-IR spectrum of VanCitCD

Material	Assignment	Wavenumber (cm^{-1})
VanCitCD	O-H, C-H stretch	3635 - 2409
	C=O stretch	1713
	C=C stretch (cyclic alkene)	1594
	N-O stretch	1513
	C-H bend, O-H bend	1437 - 1364
	C-O stretch, C-N stretch	1339 - 1246
	C-O stretch	1038

As shown in the FT-IR spectrum (Figure 2.19), the broad band centred at 3173 cm^{-1} is consistent with hydroxyl stretching vibrations, while the strong absorption at 1713 cm^{-1} corresponds to C=O stretching band and 1594 cm^{-1} can be assigned to the C=C stretching vibration in the aromatic ring. C-H bend and O-H bend (1437 – 1364 cm^{-1}), C-O stretch and C-N stretch (1339 – 1246 cm^{-1}) and C-O stretch (1038 cm^{-1}) were also found. These bands indicate carboxyl and hydroxyl functionalised carbon dots. Additionally, the C=O and C=C stretches, suggest a conjugated π system might make up the carbon dot skeleton.

EDS would have offered additional elemental analysis to support the FT-IR data. While TEM would have given some indication of the particle size and structure of the carbon dots. However, TEM/EDS are expensive to run and therefore could not be carried out for this sample.

2.7.1.2. Fluorescence spectroscopy

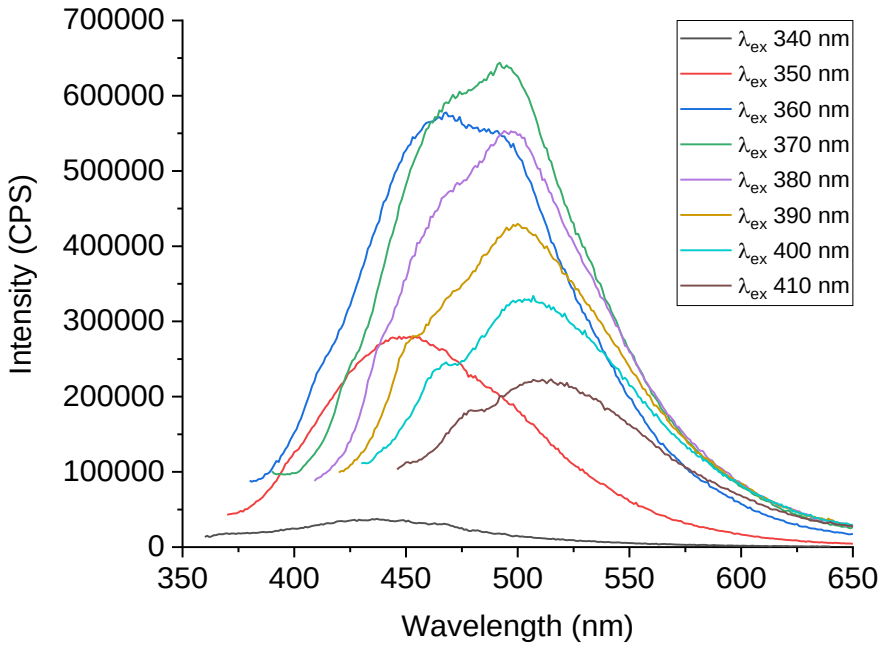

Figure 2.20: Fluorescence spectra of VanCitCD when excited between 340 nm - 410 nm, in 10 nm increments, measured at concentrations of 0.003 % v/v.

The known feature of excitation-dependent fluorescence emissions in carbon dots, meant that fluorescence spectroscopy could also be used to allude to the formation of carbon dots, as well as give information on their PL properties. Figure 2.20 shows that, when excited at 340–410 nm at 10 nm increments, the PL emission red-shifts from

447 to 512 nm. The O-doped nature of the dots appear to red-shift all emission wavelengths, and when excited at 350 nm and 410 nm, the shift in emission spectra is large (65 nm). Additionally, a double peak is evident which is indicative of two groups of similar-sized carbon dots, which can be excited at different wavelengths. It could therefore be speculated that the doubling of the emission band at excitation wavelengths > 360 nm suggests the presence of the O-CDs of varied size as the PL emission depends on the size of CDs. Additionally, due to the highly functionalised surfaces (as indicated by FT-IR), a variety of molecular electronic transitions are expected when the carbon dots are excited. These can be excited by different excitation energies, leading to variation in the emission spectra (140).

The fluorescence spectra therefore insinuate the reaction has formed carbon dots with highly functionalised structures, that must vary in surface groups and size, in order to generate excitation-dependent emissions.

2.7.2. Controlling reaction conditions

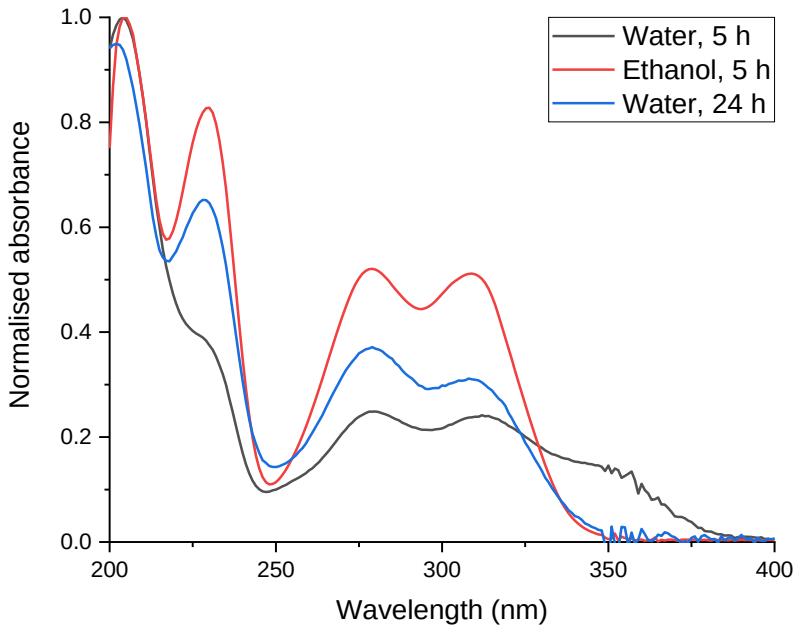

Figure 2.21: UV-vis spectra of VanCitCD when the solvent and reaction time was varied. Each sample was measured at concentrations of 0.003 % v/v, in water. Ratio of citric acid: vanillin was 5.2 mmol: 4.7 mmol at 200 °C in: 1) water (10 mL), 5 h; 2) ethanol (10 mL), 5 h and 3) water (10 mL), 24 h.

Citric acid and vanillin underwent hydrothermal synthesis at a ratio of 1: 0.9, for 5 h in water as per the standard procedure outlined. However, vanillin was found to only be partially soluble in water therefore its suitability for hydrothermal synthesis was questioned. As shown in the UV-vis profile for VanCitCD (water, 5 h) it has two overlapping peaks in the UVB region, at 280 nm and 312 nm, which is very similar to that of vanillin itself. This would suggest that the n–π* electronic transitions may have been maintained and carbonyl groups are still present after the reaction. This in turn indicates that the resultant carbon dots are functionalised with carbonyl groups. Although, there is an additional shoulder at 357 nm which indicates the new material is capable of absorbing UVA light as well. In the UVC region, VanCitCD (water, 5 h) absorbs at 204 nm with a shoulder at 225 nm, which in vanillin is a sharp peak at 232 nm. This indicates a change in the structure of vanillin.

VanCitCD (water, 24 h) where the reaction time was extended to 24 h, showed a similar UV-vis profile to the 5 h reaction. However, what was a shoulder at 225 nm in the 5 h reaction has become a more distinct peak at 228 nm after 24 h. However, further absorption in the UVC region is not a very useful quality from a sun-care perspective. While the wavelength of light absorbed in the UVB region is very similar irrespective of the length of the reaction, VanCitCD (water, 24h) absorbs at a lower intensity at 308 nm than its equivalent peak in the 5h reaction.

It was found that vanillin was not completely soluble in water, so the reaction was repeated in ethanol for 5 h. VanCitCD (ethanol, 5 h) most closely resembled the starting material, although the peak at 230 nm was of a lower intensity than for vanillin itself. Overall, the UV-vis profiles of the carbon dots are very similar to that of the starting materials (Appendix 2.2), particularly vanillin, which suggests that vanillin may not be an ideal precursor for this reaction. With that, further characterisation of the material may not be needed.

2.8. Radical scavenging activity

All the carbon dots, including those that were not effective UV filters, were assessed for their radical scavenging activity by DPPH assay. Only AdeCitCD and AdeTarCD were not tested as these carbon dots were unstable and not deemed viable for further analysis.

1,1-diphenyl-2-picrylhydrazyl (DPPH) is a stable free radical which lies at the heart of a very common assay used to measure the radical scavenging ability of antioxidants. Its characteristically deep violet colour is a result of electron delocalisation over the molecule, and it has an absorption maximum at 517 nm. In its nonradical form, DPPH is pale yellow, therefore it can be used as an indicator of a compound's radical scavenging capabilities as a colour change towards pale yellow suggests that the radical has been scavenged (143). The mechanism is detailed in Scheme 1, where AH represents a proton-donating antioxidant.

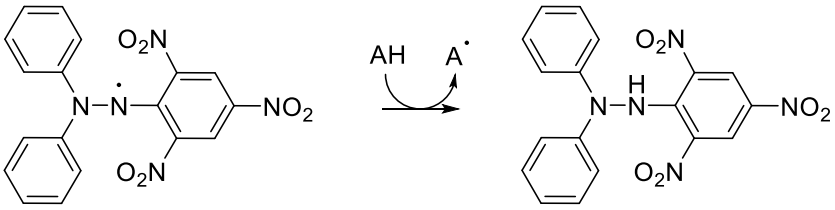

Scheme 1: Mechanism of radical scavenging between DPPH and an antioxidant (AH)

Procedures for DPPH assays vary considerably. The concentration of DPPH used ranged from 22.5 μM to 250 μM and incubation time varied between 5 minutes and an hour (144). The solvent and pH were also seen to differ between protocols (144).

In this research, 0.1 M DPPH solution was used and the 96 well plate was incubated for 30 minutes. In each well there was 20 μL of sample and 200 μL of DPPH or MeOH. This was done in duplicate. For the carbon dots samples, seven dilutions were made up in water with the following percentages of carbon dots: 10 %, 20 %, 30 %, 40 %, 50 %, 60 %, 70 %, and a standard was run with no carbon dots.

For the most promising candidates, their reaction precursors were also assessed. For the starting materials, the concentration of their stock solutions matched their concentration in the reaction. Therefore, they should give the maximum percentage radical scavenging activity (% RSA) if all the starting materials were to have remained unreacted after the hydrothermal reaction. The DPPH assay was also carried out on the starting materials in their reaction pairs, to see if their unreacted combinations could act as antioxidants. The % radical scavenging activity (% RSA) was calculated using Equation 2.1.

Equation 2.1

$$\%\ Radical\ Scavenging\ Activity = \left[\frac{(A_0 - A_n)}{A_0}\right] \times 100$$

When:

A_0 = DPPH abs at 517 nm (average)

A_n = [A_s - A_b]

A_s = Sample + DPPH abs at 517 nm

A_b = Sample + MeOH abs at 517 nm (background)

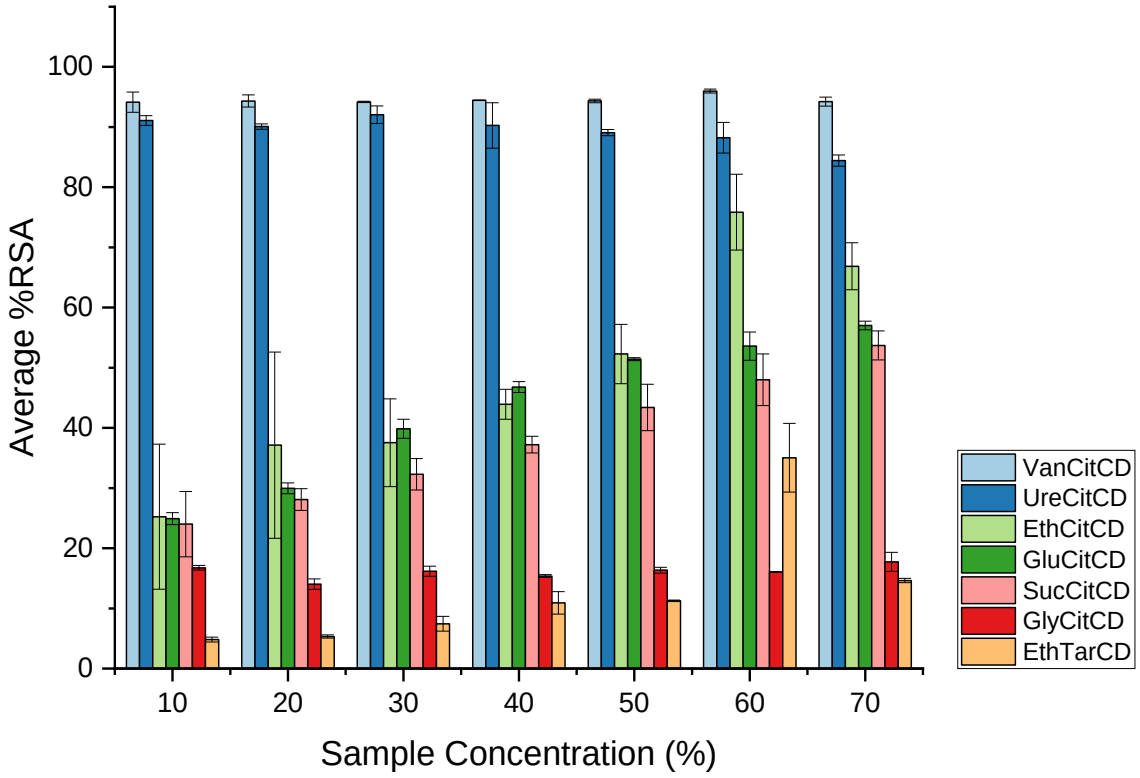

Figure 2.22: Average % RSA of the prepared carbon dots, at seven dilutions given as a percentage of carbon dots in the overall sample. A concentration range of 10 % - 70 % carbon dots was investigated.

Figure 2.22 shows an overview of the average % radical scavenging activity of seven variations of carbon dots that were prepared. The neat carbon dot solution (as produced in the reaction) was used as the initial stock solution for each carbon dot variant. As each reaction had taken place with the same molar ratio of precursors, under the same conditions, use of the neat stock solution allowed the carbon dots to be compared.

As it is expected that there is some variation in the precise structure of the carbon dots, which remains undetermined, it is difficult to know the exact concentration of each solution of carbon dots. By freeze-drying 1 mL of each neat carbon dot solution and weighing the subsequent mass once the solvent was removed, a mass per mL was obtained which is outlined in Appendix 2.3. The intention is to understand the behaviour of the carbon dots in their neat form; therefore, it is not necessary to align the concentrations (mg/mL) in order to study radical scavenging activity.

In Figure 2.22, VanCitCD shows the strongest radical scavenging activity of all the carbon dots analysed, reaching 95 % RSA at the lowest concentration (10 %). It maintained this as the percentage of carbon dots in the sample increased. UreCitCD also exhibited a high % RSA, reaching 91 % at the lowest concentration and reducing slightly in activity as the concentration increased.

As the concentration of EthCitCD increases, the % RSA steadily increases to 76 % before falling slightly at the highest concentration. GluCitCD and SucCitCD exhibit similar trends in % RSA, both increasing with concentration, however GluCitCD performs slightly better. Both GlyCitCD and EthTarCD are the least active. GlyCitCD maintains a low % RSA below 20 % throughout, while EthTarCD has very low activity to begin with, but this increases steadily with concentration, peaking at 36 % before falling again at the highest concentration.

VanCitCD, UreCitCD and EthCitCD displayed the highest percentage radical scavenging activity of all the carbon dots. To get a greater understanding of this, the DPPH assay was performed with starting materials: vanillin, ethanolamine, urea, and citric acid, to determine the RSA of the precursors, both in their reaction pairs and separately.

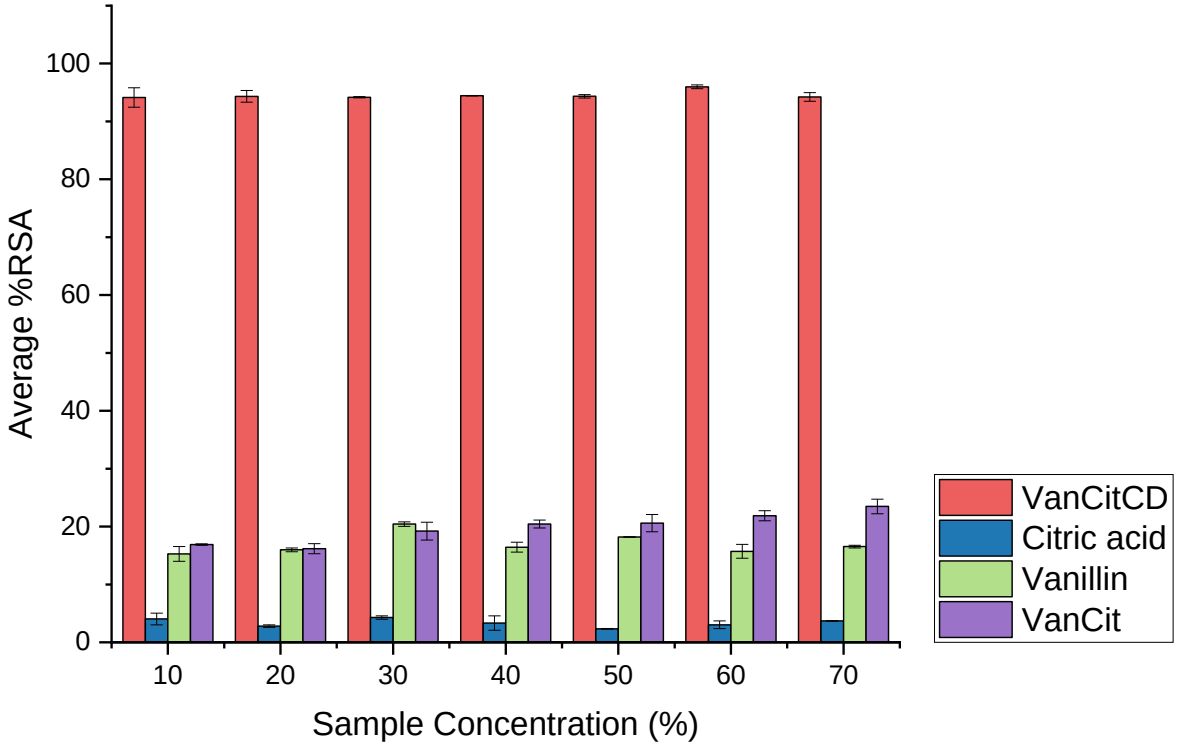

Figure 2.23: Percentage RSA of VanCitCD and its starting materials; combined and separated. A concentration range of 10 % - 70 % was investigated.

The DPPH assay showed that both vanillin and citric acid, displayed very low radical scavenging activity (Figure 2.23). Citric acid maintains <10 % RSA regardless of concentration, while vanillin reaches a maximum of 20 % RSA and fluctuates slightly as the concentration increases. Evidently, the radical scavenging activity of VanCitCD, which maintains > 95 % RSA, is significantly better than the starting materials on their own. The hydroxyl groups adorning VanCitCDs are capable of hydrogen donation which, as described in Scheme 1, can scavenge the DPPH radical. In essence, VanCitCD behave as an antioxidant.

VanCit, which describes the combination of vanillin and citric acid at room temperature, is also much lower than VanCitCD, reaching a maximum of 24 % RSA. The stock solution concentration for the starting materials, both combined and separate, was as it would be in the reaction. Therefore, the result of the DPPH assay should indicate the maximum % RSA if all the starting material remained unreacted at the end of the reaction. VanCitCD shows superior radical scavenging activity compared to its combined starting materials, also.

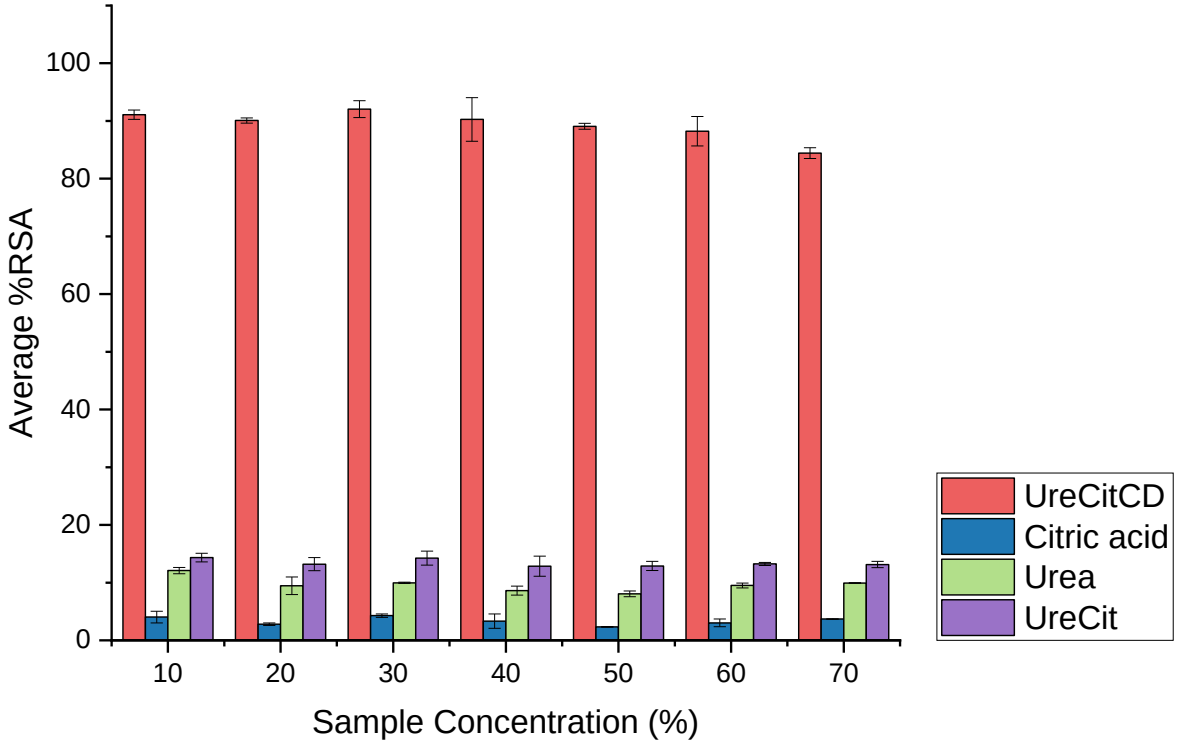

Figure 2.24: Percentage RSA of UreCitCD and starting materials, combined and separate. A concentration range of 10 % - 70 % was investigated.

Figure 2.24 shows that UreCitCD achieves 91 % RSA at a low concentration, and while the RSA drops slightly as the concentration increases, it is still very high in comparison to urea (maximum of 12 %) and citric acid (<10 %). The combination of urea and citric acid (UreCit) has a marginally better RSA than the separated starting materials, staying at 15 % with some fluctuation. UreCitCD has been shown to have amino and hydroxyl functional groups, by FT-IR, which are capable of H-donation to scavenge the DPPH radical. Owed to the small surface area of the carbon dots, the abundance of such groups may be enhancing their radical scavenging properties as there are lots of available H-donating groups.

Overall, the carbon dots have an enhanced radical scavenging activity in comparison to their starting materials. This, coupled with absorbing UV light, make this material well-suited for sunscreens.

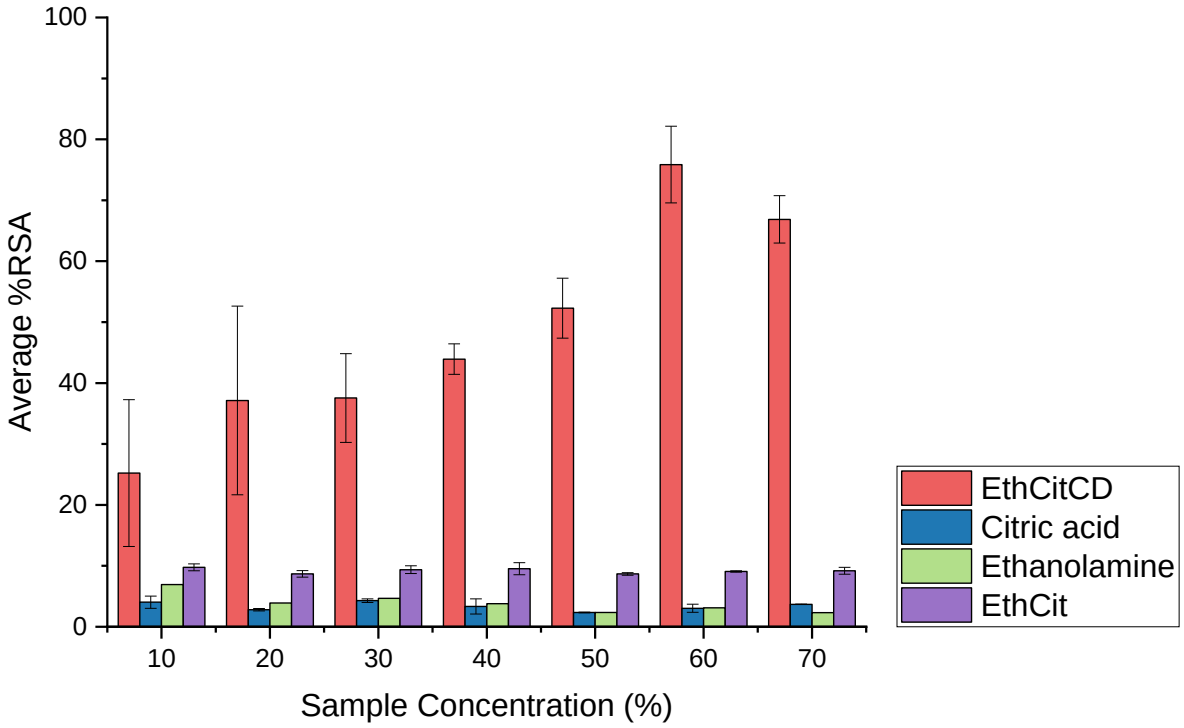

Figure 2.25: Percentage RSA of EthCitCD and starting materials, ethanolamine, and citric acid. A concentration range of 10 % - 70 % was investigated.

As seen in Figure 2.25, ethanolamine and citric acid both show a very low RSA at < 7 %. Together, they achieved 10 % RSA, which is still significantly lower than EthCitCD which reached 76 % at its peak. Like UreCitCD, hydroxyl and amino functional groups have been shown to be present in EthCitCD, by FT-IR. Additionally, the very small size range of 0.8–2.8 nm, could mean there are many of these groups available for H-donation and hence, radical scavenging. This, in combination with the absorption of UVA and UVB radiation, makes EthCitCD highly desirable from a sun-care perspective.

Overall, VanCitCD, UreCitCD and EthCitCD appear to be promising radical scavengers. In combination with the UV-absorbing properties of these carbon dots, the DPPH assays give evidence that they also act as antioxidants, which showcases another advantageous characteristic that would be useful in a sunscreen.

2.9. Formulation studies

2.9.1. Photostability of carbon dots

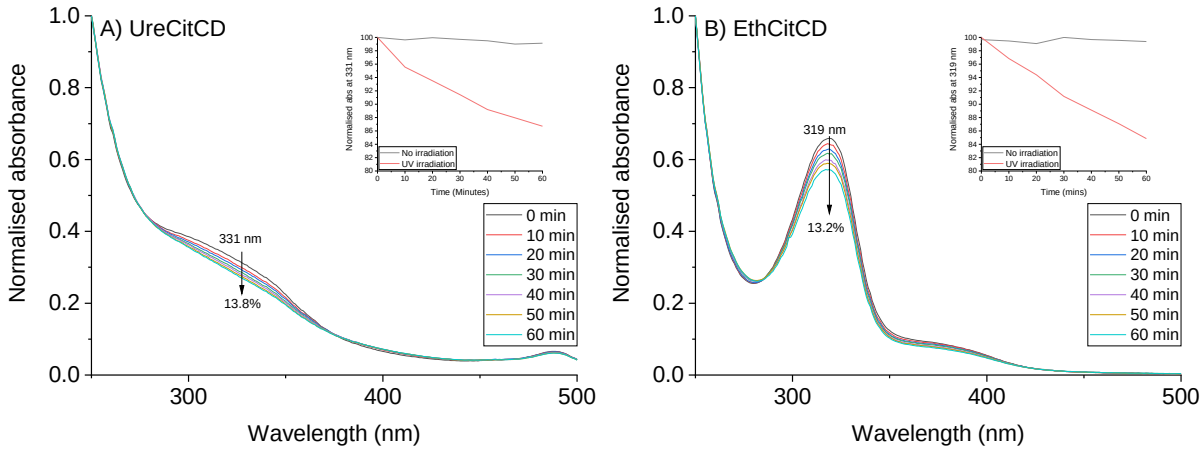

Figure 2.26: A) UV-vis spectra of UreCitCD taken over 60 minutes at 10-minute intervals, under UV radiation. Inset shows absorbance at 331 nm over time. B) UV-vis spectra of EthCitCD taken over 60 minutes at 10-minute intervals, under UV radiation. Inset shows absorbance at 319 nm over time.

The photostability of UV filters for use in sunscreens is important, as by nature, the filters will be exposed to solar light and any degradation as a result, may impact the effectiveness of the formulation. Additionally, it can impact the shelf life and packaging of a product, so it is important to gauge. To give an indication of photostability of two types of carbon dots (EthCitCD and UreCitCD) each sample was irradiated with UV light and a UV-vis spectra was taken every 10 minutes for 60 minutes. The UV light was used to mimic UV radiation from solar exposure. The absorbance in the UVA region was monitored for both, as any changes in this may impact the performance of the UV filter in formulation. For UreCitCD, at 331 nm, the absorbance fell by 13.8 % in 1 h while for EthCitCD, at 319 nm, the absorbance fell by 13.2 %. This indicates that there may be some degradation on intense exposure to UV light. The inset images compare absorbance over time, with UV and no irradiation. This clearly shows some degradation of the carbon dots.

These studies have shown that EthCitCD and UreCitCD may be partially photosensitive under intense UV light. However, their behaviour in formulation may differ therefore their stability should be tested using Croda's in-house protocol.

2.9.2. Scaling up carbon dots

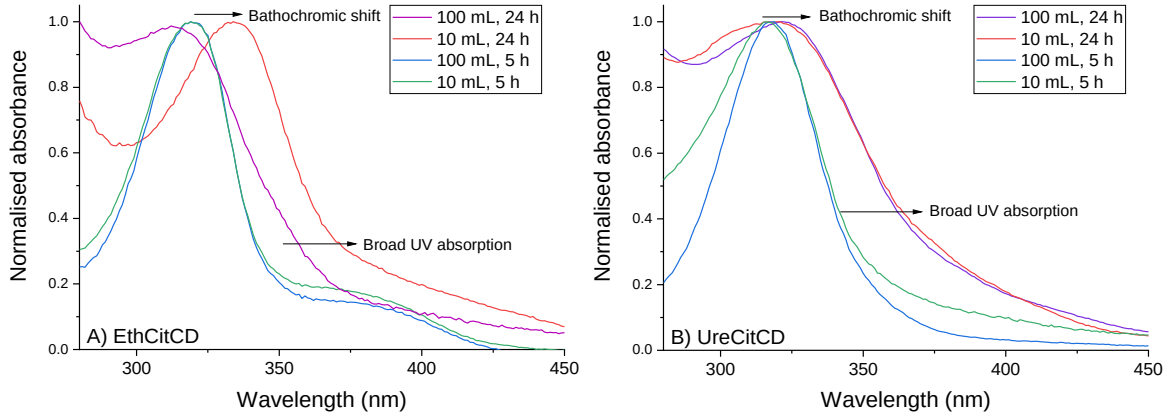

Figure 2.27: UV-vis of EthCitCD (A) and UreCitCD (B) scaled up to 100 mL reactions, compared with 10 mL reactions

Formulation testing is typically done on a larger scale; therefore, it was necessary to scale-up the most effective carbon dot reactions: EthCitCD and UreCitCD. The largest autoclave available was suitable for a 100 mL reaction, so the protocol stated previously was scaled up by a factor of 10. Figure 2.27 shows the UV-HEVL profiles of each carbon dot reaction at a 10 mL scale and a 100 mL scale, for 5 h and 24 h respectively.

For EthCitCD, the 5 h reaction on 100 mL scale shows excellent reproducibility, when compared with the 10 mL scale, with absorption at 319 nm. A longer reaction time of 24 h was investigated on a 100 mL scale, and 10 mL scale for comparison. The 10 mL reaction exhibited a bathochromic shift in absorption to 334 nm, and a broad absorption from 350–450 nm. This suggests that with a longer reaction time, a longer conjugate system is capable of forming, extending the absorption into the visible region. The equivalent reaction (100 mL, 24 h) demonstrated a slight hypsochromic shift (312 nm) relative to the 5 h reaction but showed a broad absorption across the UV and HEVL regions. Again, the broad absorption towards the HEVL region may be indicative of longer π systems forming with the lengthier reaction time. Following this, both reactions were deemed good candidates for formulation testing.

For UreCitCD, the 5 h reactions on a 10 mL and 100 mL scale showed good reproducibility, with absorption peaks centred at 317 nm. The 100 mL reaction produced a narrow absorption band at 5 h which varied slightly from the 10 mL scale, suggesting the carbon dots might be slightly more uniform in profile. For comparison,

a 24 h reaction time was studied for the UreCitCD reaction on a 10 mL and 100 mL scale. There was a bathochromic shift in the absorption peak to 320 nm, and significant broadening from 350–450 nm compared to the 5 h reaction. Again, this supports the notion that a longer reaction time may lead to the extension of the conjugate system in the carbon dots. With this, both the 5 h and 24 h reactions were considered as worthwhile candidates for formulation testing, and both showed good reproducibility when scaled up.

From this, it was concluded that both EthCitCD and UreCitCD could be scaled up with good reproducibility, when compared to the original reaction, as analysed by UV-vis spectroscopy. All four of the 100 mL reactions were therefore selected for formulation testing, however due to time constraints two reactions needed to be prioritised. With this in mind, the scale up reactions at 24 h were prioritised, due to their broad-spectrum absorption.

2.9.3. Formulations and *in vitro* SPF

To investigate the *in vitro* SPF, the most effective carbon dots candidates were chosen and incorporated into Croda sunscreen formulations. Here, two suitable oil/water base formulations, with a wide pH tolerance to accommodate both CD solutions, were chosen: Brij S2 and S721 (pH 2-13) and Crodafos CES (pH 2-12), abbreviated to Brij and CES, respectively. The active ingredient in these formulations is XT-300 (TiO_2 10 % active) which is a dispersion of large titanium dioxide particles, coated in alumina and stearic acid and dispersed in caprylic/capric triglyceride and polyhydroxystearic acid. Typically, per 1 % active of XT-300, an SPF of 2-3 units is expected. The average boost per 1 % active ingredient is used as an internal metric within Croda, as a measure of how the booster in question, compares to the UV filter.

EthCitCD and UreCitCD were chosen as the two best candidates for initial formulation studies as they showed good UV and visible light absorption, even at low concentrations. While VanCitCD was also a very promising option, as showcased by the UV-vis spectra, the use of 20 % ethanol to dissolve the vanillin precursor meant the reaction was not done in pure water. So, with the intention of adding it to the water phase of the formulation, it was not deemed suitable as it would make the formulation unstable.

In vitro SPF testing is a preliminary study, used to determine the spectral transmittance of a sunscreen on a substrate, using a single beam of UV light. It is an industry standard technique. Croda used an adaptation of the ISO 24443:2019 method to calculate the SPF. 200 mL of carbon dots were supplied (neat) for *in vitro* SPF testing. Therefore, to derive the mass/mL in each sample, an aliquot was freeze-dried and weighed. EthCitCD contained 0.0685 g/mL or 13.7 g/200 mL, while UreCitCD contained 0.0575 g/mL or 11.5 g/200 mL. First, 5 % and 10 % inclusion of each CD solution was investigated in the two base formulations, with no added UV filter. This was to investigate the SPF of the materials on their own, in formulation, as to be applicable as a UV booster in a formulation, the materials must not show SPF on their own. Then, alongside Croda's XT-300 UV filter, 5 % and 10 % of each active ingredient were incorporated into formulation.

The previous formulations added the same w/w % of 5 and 10 %, which corresponded to 0.343 g and 0.685 g for EthCitCD, and 0.288 g and 0.575 g for UreCitCD, respectively. Therefore, to remove the variable of a change in mass and increase the loading, 2.5 g of each carbon dot solution was added into a separate formulation. This corresponded to 36.5 % and 43.5 % (w/w %) for EthCitCD and UreCitCD, respectively.

Each formulation was tested in 3 batches with 5 runs. Using a T-Test, the significant difference of the means was calculated for each sample that generated a higher SPF than that of the filter on its own. In Appendix 2.4 and Appendix 2.5, the statistical significance (P) is shown for Crodafos CES and Brij formulations, respectively, where $P<0.05$ = ✶, $P<0.01$ = ✶✶, $P<0.001$ = ✶✶✶ and $P>0.05$ is not significant (NS).

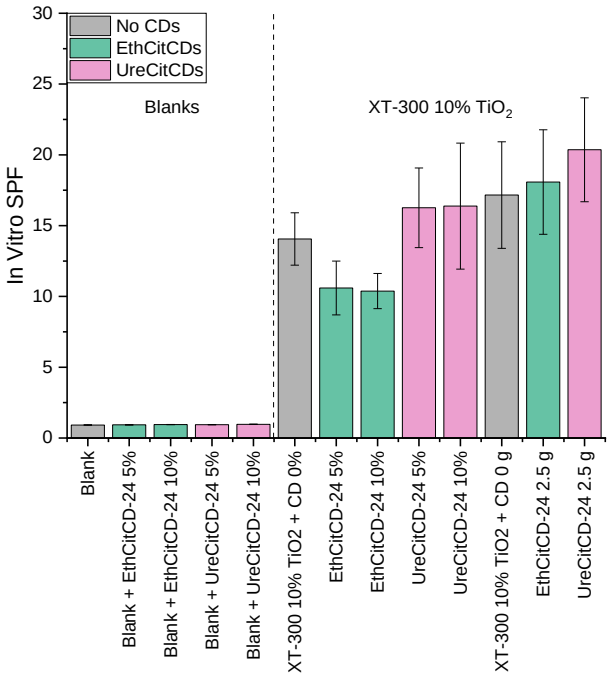

Figure 2.28: In vitro SPF of EthCitCD and UreCitCD in Crodafos CES formulation at 5 %, 10 % and 2.5 g inclusions.

For the CES formulation, the *in vitro* SPF is outlined in Figure 2.28. A blank measurement was taken, without any added UV filter or carbon dots, which confirmed that the formulation on its own had an SPF of less than 1. EthCitCD-24 (5 % and 10 %) and UreCitCD-24 (5 % and 10 %) were combined into four separate formulations, none of which contained the XT-300 UV filter. The *in vitro* SPF for each was less than 1, therefore on their own the carbon dots did not contribute to an increase in SPF.

XT-300 10 % TiO_2 (abb. XT-300) is one of Croda's TiO_2-based UV filters. Here, it was incorporated into the formulation alone to act as a control experiment and achieved an SPF of 14.06. Combining the UV filter and EthCitCD (5 % and 10 %), the SPF of the formulation decreased to 10.60 and 10.38, respectively. However, when 5 % and 10 % of UreCitCD was combined with the UV filter in formulation, SPF values of 16.26 and 16.38 were reached, respectively. For the CES formulation, the lower loading of UreCitCD (5 %) was statistically significant (P=0.017) while the 10 % equivalent was not.

At a higher loading of 2.5 g each, EthCitCD-loaded formulation reached an SPF of 18.08 (P>0.05), while UreCitCD-loaded formulation achieved 20.36 (P=0.025). Of the

two, the formulation with UreCitCD (2.5 g) loading was statistically significant, and therefore was the more promising candidate for further *in vivo* SPF testing. Neither material was able to increase SPF alone, which suggests their UV filtering ability works in synergy with the XT-300 UV filter. Also, it means the materials could be marketed at UV boosters further down the line (as it has been shown they do not act as a UV filter on their own).

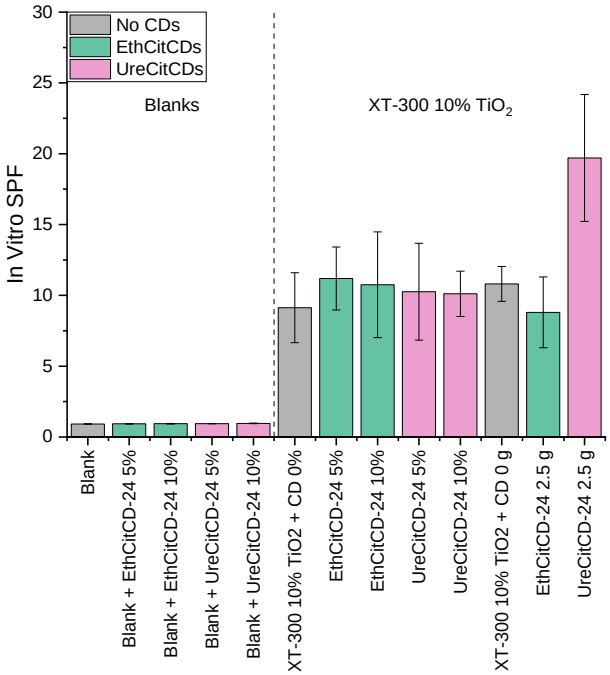

Figure 2.29: In vitro SPF of EthCitCD and UreCitCD in Brij formulation at 5 %, 10 % and 2.5 g inclusions.

Figure 2.29 outlines the *in vitro* SPF studies for Brij formulation. As for the previous formulation, a blank measurement was taken with no UV filter and no carbon dots, achieving an SPF <1, which showed the other components of the formulation were not UV active. Each of the carbon dots, EthCitCD and UreCitCD, were added to formulation at 5 % and 10 %, with no UV filter, and achieved an SPF of less than 1. This suggested that the carbon dots alone do not act as UV filters in formulation, at these w/w percentages. As a control experiment, XT-300 was incorporated into the formulation alone and achieved an SPF of 9.13. On addition of 5 % and 10 % EthCitCD, the formulation reached SPF 11.19 and 10.75, respectively. While, with the

inclusion of 5 % and 10 % UreCitCD, SPF values of 10.26 and 10.11 were obtained, though only EthCitCD (5 %) showed statistical significance.

As stated in the previous section, these formulations used the same w/w % of 5 % and 10 %, which corresponded to 0.343 g and 0.685 g for EthCitCD, and 0.288 g and 0.575 g for UreCitCD, respectively. To counter the effect of a change in mass and simultaneously increase the loading, 2.5 g of EthCitCD and UreCitCD were added to respective formulations. This attained a lower SPF of 8.8 for EthCitCD, though $P>0.05$, and increased the SPF to 19.70 for UreCitCD, where $P < 0.001$, consequently only the latter was statistically significant. UreCitCD showed promise as a UV booster at higher loading (2.5 g), while EthCitCD showed some potential at 5 % loading, and had a particularly high “average unit boost per 1 g active” of 6. Therefore, both materials are worthy of further *in vivo* SPF analysis.

It is interesting that the carbon dots do not appear to improve the SPF of the formulation on their own. Though, when used in combination with the XT-300 UV filter, they are able to significantly boost the SPF, particularly for UreCitCD 2.5 g loading. This would imply there is synergy between the TiO_2 UV filter and the carbon dots. XT-300 has a stearic acid coating which could be forming electrostatic interactions with carbon dots within the formulation. This may be facilitating electronic interactions between TiO_2 and the carbon dots, which could be improving light absorption in the UV region, increasing the SPF. Additionally, the additional electrostatic interactions, in combination with the small size of the carbon dots, may be enhancing the crosslinking within the film, reducing the transmission of light, leading to an improvement in SPF.

For the moment, this is speculatory. Further experiments such as varying the concentration of carbon dots within the formulation, would help to gain an understanding of their role and their impact on the SPF. Transient absorption spectroscopy could be used to better understand the energy transfer processes that are occurring between the TiO_2 filter and carbon dots. Additional experiments such as viscosity of the formulation as well as studying the thickness and mechanical properties of the film, may also be useful.

2.9.4. Summary

Through *in vitro* SPF analysis, UreCitCD and EthCitCD have been demonstrated as good UV booster candidates, and function in synergy with a TiO_2-based UV filter, in

formulation. UreCitCD showed promise in both CES and Brij formulations at a higher loading of 2.5 g, while EthCitCD was more effective at 5 % loading in Brij formulation. Additionally, the materials were commended for their ease-of-use and stability during the making of the formulations, all of which are important characteristics in a UV booster.

Further analysis, such as *in vivo* SPF testing, would be the necessary next step, which studies the erythemal response of the skin when exposed to UV radiation. Such investigations are carried out by an external company at a cost of around €5,200 for four samples, which unfortunately was not within the budget of this project. However, the groundwork has been carried out, and these carbon dots remain good candidates for UV boosters within Croda formulations, pending further testing.

2.10. Conclusion

In this chapter, several types of carbon dots have been prepared by a facile synthetic route. Using the strategy outlined in Section 2.3, the carbon dots underwent an initial assessment of their UV absorption properties, to ascertain which might have potential as UV filters for use in sunscreen applications. From this, three promising candidates were obtained: EthCitCD, UreCitCD and VanCitCD, made from citric acid and ethanolamine, urea, and vanillin, respectively.

To confirm the formation of carbon dots and understand the optical properties better, further characterisation was carried out through FT-IR, TEM, EDS, and fluorescence spectroscopy. FT-IR determined that EthCitCD and UreCitCD were functionalised with hydroxyl, amino and carboxyl groups. The presence of nitrogen was also confirmed through EDS analysis. For VanCitCD, hydroxyl and carboxyl functional groups were evident from FT-IR. TEM showed the narrow particle size distribution of both EthCitCD (0.8 - 2.8 nm) and UreCitCD (1.5 - 5 nm) which indicated this hydrothermal protocol controlled the particle size well. The fluorescence spectra for all three showed excitation-dependent emissions which is a common phenomenon for carbon dots. Overall, the characterisation techniques confirmed the formation of carbon dots.

The radical scavenging activity for all carbon dots was studied as, alongside good UV properties, radical scavengers in a sunscreen formulation would be highly beneficial to quench any radicals produced by other components like titanium dioxide for

example. With this, VanCitCD, UreCitCD and EthCitCD showed the most promising RSA. However, as VanCitCD was prepared in 20 % ethanol, it was not taken forward further for studies in formulation, as it would make them unstable.

The photostability of EthCitCD and UreCitCD were explored, and it was found that they showed some photosensitivity and further analysis of the formulation photostability would be needed. The carbon dots were successfully scaled up by a factor of 10, demonstrating promise for scale-up on an industrial level. Finally, *in vitro* SPF analysis was carried out in two different formulations with the chosen carbon dots. Both candidates were demonstrated as good UV boosters, working in synergy with the existing TiO_2 filter in the formulation. UreCitCD was effective in CES and Brij formulations at a higher loading of 2.5 g, while EthCitCD showed better promise at 5 % loading in Brij formulation. *In vivo* SPF testing followed by toxicity and stability tests would be the necessary next steps to taking these materials forward in sun-care products. The additional feature of effective radical scavenging activity, shown by EthCitCD and UreCitCD, may give it dual application in other skincare products as an antioxidant, with UV filtering capabilities.

2.11. Experimental

2.11.1. Characterisation techniques

Infrared spectra (IR) were obtained from solid phases using a Bruker Alpha Platinum ATR FTIR spectrometer with vibrational frequencies (cm^{-1}). The electronic absorption spectra were recorded using a Cary 100 UV-Vis scanning spectrophotometer. Spectrophotometric experiments to assess the photostability of the materials were carried out using a Cary 50 UV-Vis spectrophotometer controlled at 20 °C by a single cell Peltier accessory, while Xenon lamps were used as the UV light source. The fluorescence spectra were recorded on a FluoroMax-3 spectrofluorometer. Transmission electron microscopic (TEM) analysis was carried out using the FEI Titan Themis Cubed operated at 80 kV. Samples were prepared by sonication and then drop casting onto holey carbon TEM grids or graphene oxide TEM grids (as indicated). The Shimadzu 3600 Plus Spectrophotometer with an integrating sphere (ISR 240A) with an NPC 603A large compartment sample attachment was used to measure SPF following an adaptation of the ISO 24443:2019 method.

2.11.2. Reagents

Alfa Aesar supplied citric acid (99+ %), vanillin (99 %), and adenine (99 %). Ethanolamine (99+ %), 1,1-diphenyl-2-picrylhydrazyl, Sephadex G-50, urea (99.5+ %) and glycerol (99.5+ %) was provided by Sigma-Aldrich. Fluka Analytical supplied tartronic acid (97+ %). Fischer Scientific provided sucrose while D(+)-glucose anhydrous was supplied by Scientific Laboratory Supplies. Ethanol was supplied by VWR chemicals.

2.11.3. Methods

2.11.3.1. EthCitCD

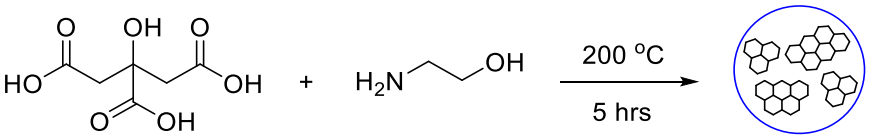

Citric acid (1.0413 g, 5.2 mmol) and ethanolamine (280 µL, 4.7 mmol) were dissolved in water (10 mL) after stirring for 5 minutes. The mixture was poured into a Teflon liner, which was sealed in a hydrothermal autoclave reactor. Finally, this was placed in an oven at 200 °C for 5 hours. The neat reaction mixture was collected. In this case, a yellowed suspension was obtained. Under the UV lamp, blue emission was evident when excited at 365 nm.

The following reactions were carried out using the same protocol, parameters such as solvent were changed (Table 2.5). Each was analysed by UV-vis and exhibited blue emission when excited at 365 nm under a UV lamp.

Table 2.5: Variations in reaction conditions for EthCitCD

Citric acid	Ethanolamine	Solvent	Conditions	Dried mass (mg/ mL)
2.0162 g, 10.4 mmol	280 µL, 4.7 mmol	H_2O (10 mL)	5 h, 200 °C	-
2.0202 g, 10.4 mmol	280 µL, 4.7 mmol	EtOH (10 mL)	5 h, 200 °C	-
0.1957 g, 1 mmol	60 µL, 1 mmol	H_2O (10 mL)	5 h, 200 °C	19.5
0.5876 g, 3 mmol	180 µL, 3 mmol	H_2O (10 mL)	5 h, 200 °C	51.6
0.9634 g, 5 mmol	310 µL, 5 mmol	H_2O (10 mL)	5 h, 200 °C	83.6
9.9940 g, 52 mmol	2.8 mL, 47 mmol	H_2O (100 mL)	5 h, 200 °C	-
10.0105 g, 52 mmol	2.8 mL, 47 mmol	H_2O (100 mL)	24 h, 200 °C	-
1.0067 g, 5.2 mmol	280 µL, 4.7 mmol	H_2O (10 mL)	24 h, 200 °C	-

2.11.3.2. UreCitCD

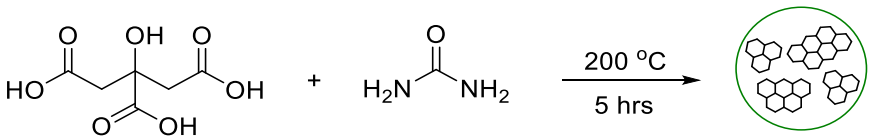

Citric acid (1.0105 g, 5.2 mmol) and urea (0.2889 g, 4.7 mmol) were dissolved in water (10 mL) after stirring for 5 minutes in a glass vial. The mixture was poured into a Teflon liner, which was sealed in a hydrothermal autoclave reactor. Finally, this was placed in the new oven at 200 °C for 5 hours and the neat reaction mixture was collected. Under the UV lamp, blue emission was evident when excited at 365 nm. 1 mL of product was freeze dried and produced a dried mass of 27.4 mg.

The following reactions were carried out using the same protocol, parameters such as solvent were changed (Table 2.6). Each was analysed by UV-vis and exhibited blue emission when excited at 365 nm under a UV lamp.

Table 2.6: Variations in reaction conditions for UreCitCD

Citric acid	Urea	Solvent	Conditions	Dried mass (mg/ mL)
0.765 g, 4 mmol	2.55 g, 40 mmol	H_2O (20 mL)	24 h, 200 °C	-
9.9410 g, 52 mmol	2.8868 g, 47 mmol	H_2O (100 mL)	5 h, 200 °C	-
9.9677 g, 52 mmol	2.8818 g, 47 mmol	H_2O (100 mL)	24 h, 200 °C	57.5
1.0033 g, 5.2 mmol	0.2891 g 4.7 mmol	H_2O (10 mL)	24 h, 200 °C	-

2.11.3.3. VanCitCD

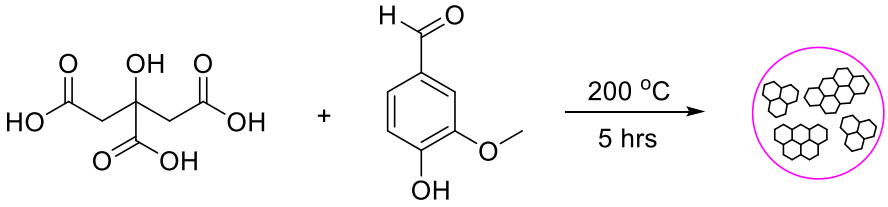

Citric acid (1.0033 g, 5.2 mmol) and vanillin (0.7074 g, 4.7 mmol) were mixed in water (10 mL) and vanillin was partially dissolved after stirring for 5 minutes. The mixture was poured into a Teflon liner, which was sealed in a hydrothermal autoclave reactor. Finally, this was placed in an oven at 200 °C for 5 hours. The neat reaction mixture was collected. In this case, sticky residue remained at the bottom of the Teflon liner and the suspension was collected. Under the UV lamp, blue emission was evident when excited at 365 nm.

The following reactions were carried out using the same protocol, parameters such as solvent were changed (Table 2.7). Each was analysed by UV-vis and exhibited blue emission when excited at 365 nm under a UV lamp.

Table 2.7: Variations in reaction conditions for VanCitCD

Citric acid	Vanillin	Solvent	Conditions	Dried mass (mg/ mL)
1.0171 g, 5.2 mmol	0.7261 g, 4.7 mmol	Ethanol (10 mL)	5 h, 200 °C	-
1.0235 g, 5.2 mmol	0.6986 g, 4.7 mmol	Water (10 mL)	24 h, 200 °C	54.7
1.0081 g, 5.2 mmol	0.1966 g, 1.3 mmol	Water (10 mL)	5 h, 200 °C	-
(1.0038 g, 5.2 mmol)	0.3993 g, 2.6 mmol	Water (10 mL)	5 h, 200 °C	-

2.11.3.4. GlyCitCD

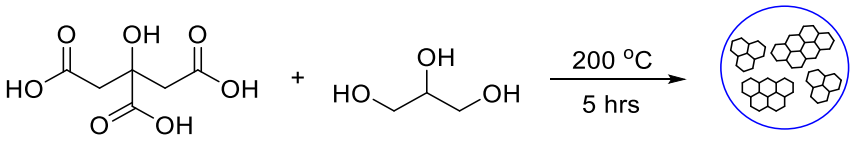

Citric acid (1.0239 g, 5.2 mmol) and glycerol (0.34 mL, 4.7 mmol) were dissolved in water (10 mL) after stirring for 5 minutes. The mixture was poured into a Teflon liner, which was sealed in a hydrothermal autoclave reactor. Finally, this was placed in an oven at 200 °C for 5 hours. The neat reaction mixture was collected. 1 mL of product was freeze dried and produced a dried mass of 92.0 mg.

2.11.3.5. SucCitCD

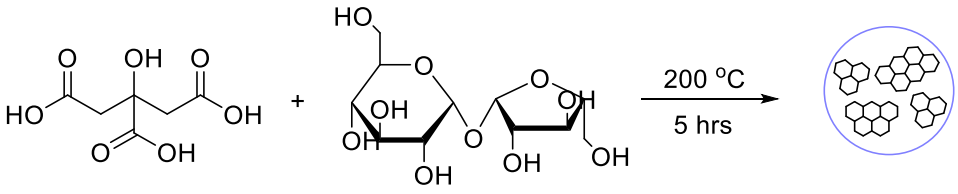

Citric acid (1.0090 g, 5.2 mmol) and sucrose (1.6216 g, 4.7 mmol) were dissolved in water (10 mL) by stirring at 40 °C. The mixture was poured into a Teflon liner, which was sealed in a hydrothermal autoclave reactor. Finally, this was placed in an oven at 200 °C for 5 hours. The neat reaction mixture was collected. Freeze dried 1 mL to give a dried mass of 93.3 mg.

2.11.3.6. GluCitCD

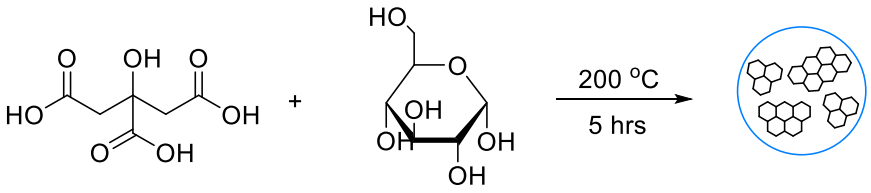

Citric acid (1.0052 g, 5.2 mmol) and glucose (0.8378 g, 4.7 mmol) were dissolved in water (10 mL) by stirring at 40 °C. The mixture was poured into a Teflon liner, which was sealed in a hydrothermal autoclave reactor. Finally, this was placed in an oven at 200 °C for 5 hours. The neat reaction mixture was collected. Freeze dried 1 mL to give a dried mass of 82.7 mg.

2.11.3.7. AdeCitCD

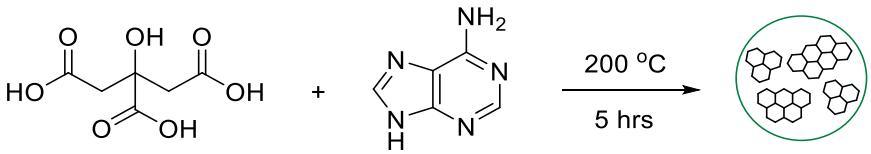

Citric acid (0.9609 g, 0.005 mol) and adenine (0.6737 g, 0.005 mol) were mixed in water (10 mL), adenine did not dissolve fully. The mixture was poured into a Teflon liner, which was sealed in a hydrothermal autoclave reactor. Finally, this was placed in an oven at 200 °C for 5 hours. The neat reaction mixture was collected – a bright orange solution with some solid particulates, registering at pH 4. The product exhibited blue fluorescence under a UV lamp at 365 nm. The product was seemingly unstable as it turned brown after one week and blue fluorescence at 365 nm was no longer visible.

2.11.3.8. AdeTarCD

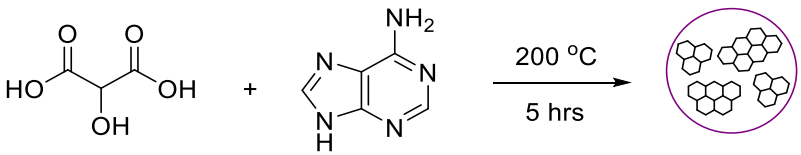

Tartronic acid (0.6039 g, 0.005 mol) and adenine (0.6785 g, 0.005 mol) were mixed in water (10 mL), adenine did not dissolve fully. The mixture was poured into a glass vial which was placed in a Teflon liner and sealed in a hydrothermal autoclave reactor. Finally, this was placed in an oven at 200 °C for 5 hours. The neat reaction mixture was collected – a yellow/green solution with some solid particulates, registering at

pH 4. The product exhibited blue fluorescence under a UV lamp at 365 nm. The product was seemingly unstable as it turned brown after one week; formed a white growth on the surface of the solution and vial; and blue fluorescence at 365 nm was no longer visible.

2.11.3.9. EthTarCD

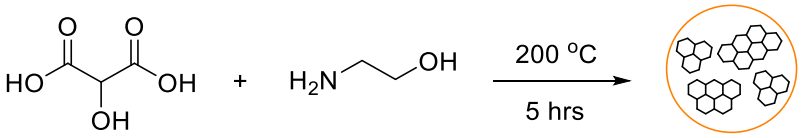

Tartronic acid (0.6089 g, 0.005 mol) and ethanolamine (0.30 mL, 0.005 mol) were dissolved in water (10 mL). The mixture was poured into a Teflon liner and sealed in a hydrothermal autoclave reactor. Finally, this was placed in an oven at 200 °C for 5 hours. The neat reaction mixture was collected – a transparent, yellow solution registering at pH 5. The product exhibited blue fluorescence under the UV lamp at 365 nm. After one week the carbon dots appeared to be stable, the colour had remained the same, there was no precipitate and blue fluorescence at 365 nm was maintained. Freeze dried 1 mL to give a dried mass of 66.8 mg.

2.11.3.10. Size exclusion column

The Sephadex size exclusion column was prepared as follows: Sephadex G-50 (2 g) was dissolved in hot water (100 mL). Once expanded, it was washed with deionised water and the column was filled. This was washed through with water before use. Carbon dots (5 mL) were freeze-dried, redispersed into water (1 mL), and loaded onto the column. Water was used as the mobile phase and various fractions were collected, and their fluorescence monitored with a table-top UV lamp. Subsequently, the fractions were monitored by UV and fluorescence spectroscopy.

2.11.3.11. DPPH assay

Seven dilutions were made up in water, of each carbon dot sample, with the following percentages of carbon dots: 10 %, 20 %, 30 %, 40 %, 50 %, 60 %, 70 %, and a standard was run with no carbon dots. 20 µL of each dilution was added into the wells of a 96 well plate, this was done in triplicate. Methanol (200 µL) was added into one complete set, while 0.1M DPPH solution (200 µL) was added into the remaining two complete sets. All of this was done in the dark as DPPH is light sensitive. The plate

was placed into the Tecan reader, absorbance scans were taken at 0 minutes, followed by a 30-minute incubation period at room temperature, and then a second absorbance scan. The radical scavenging activity was calculated.

2.11.3.12. Crodafos CES formulation

Keltrol CG-RD (Xanthan gum), Veegum Pure (magnesium aluminium silicate) and Pricerine 9091 (glycerin) were mixed. Water and Titriplex III (disodium EDTA) were added with stirring. This was heated to 75 °C, to make up the water phase. The oil phase components were then combined: Crodafos™ CES (Cetearyl Alcohol (and) Dicetyl Phosphate (and) Ceteth-10 Phosphate), Crodamol™ CAP (Cetearyl Ethylhexanoate (and) Isopropyl Myristate), Crodamol™ ISIS (Isostearyl Isostearate), Crodamol™ IPM (Isopropyl Myristate) and Crodamol™ GTCC (Caprylic/Capric Triglyceride), and heated to 75 °C. Solaveil XT-300 was added to the oil phase with stirring and briefly re-heated to 75 °C. The oil phase was added to the water phase with stirring and homogenised at 10000 rpm for 1 min/100 g. When the temperature fell below 40 °C, Euxyl PE 9091 was stirred in.

2.11.3.13. Brij Formulation

Deionised Water, Pricerine 9091 (Glycerin), Veegum Ultra (magnesium aluminium silicate) and Keltrol CG-SFT (xanthan gum) were combined and heated to 80 – 85 °C. This made up the water phase. Brij S2, Brij S721, Arlamol HD, Arlamol PS15E, Crodamol IPM and XT-300 (48.5 % Active TiO_2) at 10 % were combined and heated to 80 – 85 °C. This made up the oil phase. The oil phase was added to the water phase slowly, with vigorous stirring. The mixture was homogenised at 10000 rpm for 1 min/100 g. When the temperature dropped below 40 °C Euxyl PE 9091 was stirred in.

2.12. Appendices

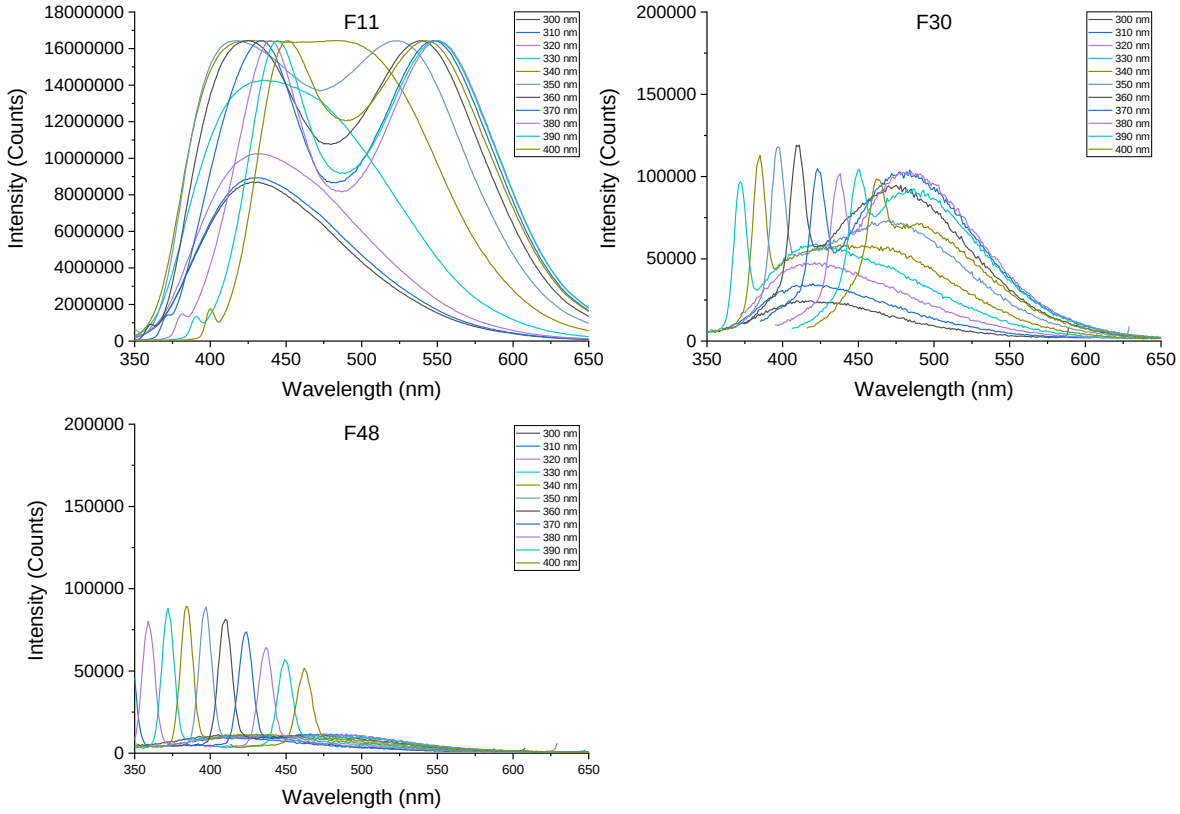

Appendix 2.1: Fluorescence spectra of F11, F30 and F48. Note the different Y scale for F11. Measured at concentrations of 3.2 % v/v.

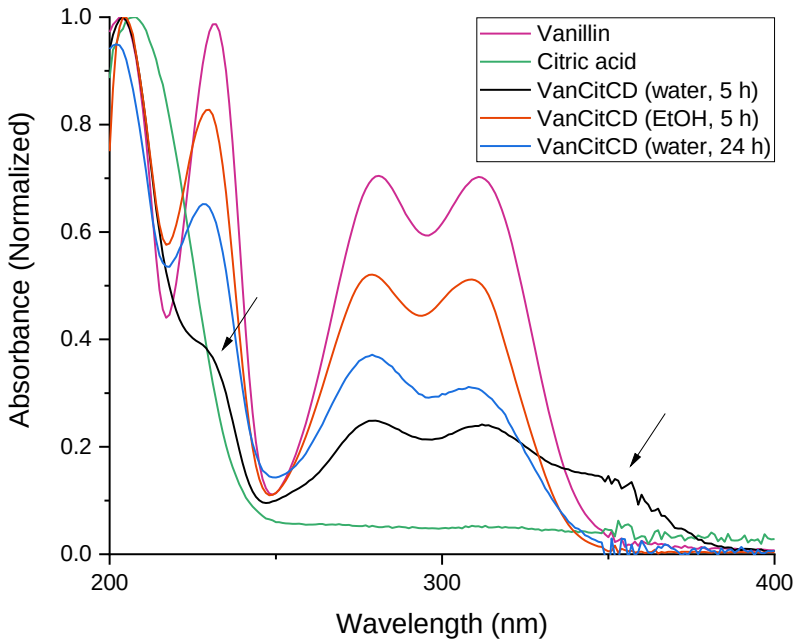

Appendix 2.2: UV-vis of VanCitCD (water for 5 h, water for 24 h and ethanol for 5 h) alongside precursors vanillin and citric acid. Measured at concentrations of 0.003 % v/v.

Carbon dots	Concentration (mg/mL)
VanCitCD	110.2
UreCitCD	27.4
EthCitCD	87.1
GluCitCD	82.7
SucCitCD	93.3
GlyCitCD	92.0
EthTarCD	66.8

Appendix 2.3: Concentration (mg/mL) of neat carbon dot solution

	Formulation	Average	STDEV	Average unit boost per 1 g active	Average % boost	Student T Test / Two tailed / Unpaired)	
Blanks	Blank no filter no EthCitCd-24 or UreCitCd-24	0.9186667	0.0155226	N/A	N/A	N/A	N/A
	Blank no filter + EthCitCd-24 (0.3425g)	0.9346667	0.0112546	N/A	N/A	0.0031401	✶✶
	Blank no filter EthCitCd-24 (0.685g)	0.9513333	0.0099043	N/A	N/A	1.818E-07	✶✶✶
	Blank no filter + UreCitCd-24 (0.2875g)	0.9413333	0.010601	N/A	N/A	6.83E-05	✶✶✶
	Blank no filter no UreCitCd-24 (0.575g)	0.9666667	0.0089974	N/A	N/A	4.369E-11	✶✶✶
XT-300 10 % TiO_2	Control (XT-300 10 % TiO2)	14.061333	1.8462892	N/A	N/A	N/A	N/A
	EthCitCd-24 (0.3425g)	10.602	1.8983421	-10.10024	24.61 %↓	2.357E-05	✶✶✶
	EthCitCd-24 (0.685g)	10.376667	1.2363233	-5.379075	26.17 %↓	5.918E-07	✶✶✶
	UreCitCd-24 (0.2875g)	16.259333	2.8093326	7.6452174	0.1565	0.0172221	✶
	UreCitCd-24 (0.575g)	16.379333	4.4464022	4.0313043	0.165	0.0727372	NS
	Control (XT-300 10 % TiO2)	17.159333	3.7631853	N/A	N/A		
	EthCitCd-24 (2.5g)	18.081333	3.6853666	0.3688	0.0536	0.5033694	NS
	UreCitCd-24 (2.5g)	20.364	3.6731162	1.2818667	0.1865	0.0254642	✶

Appendix 2.4: In vitro SPF for Crodafos CES formulations incorporating EthCitCD and UreCitCD. T-Test was used to determine statistical significance, where P<0.05 = ✶, P<0.01 = ✶✶, P<0.001 = ✶✶✶ and P>0.05 is not significant (NS)

	Formulation	Average	STDEV	Average unit boost per 1 g active	Average % boost	Student T Test / Two tailed / Unpaired)	
Blanks	**Blank no filter no EthCitCd-24 or UreCitCd-24**	0.918	0.010142	N/A	N/A	N/A	N/A
	Blank no filter + EthCitCd-24 (0.3425g)	0.928667	0.014075	N/A	N/A	0.024287	✶
	Blank no filter EthCitCd-24 (0.685g)	0.944667	0.016417	N/A	N/A	1.06E-05	✶✶✶
	Blank no filter + UreCitCd-24 (0.2875g)	0.942667	0.011629	N/A	N/A	1.1E-06	✶✶✶
	Blank no filter no UreCitCd-24 (0.575g)	0.962	0.016125	N/A	N/A	1.06E-09	✶✶✶
XT-300 10 % TiO_2	**Control (XT-300 10 % TiO2)**	9.134	2.473279	N/A	N/A		N/A
	EthCitCd-24 (0.3425g)	11.19	2.22335	6.00292	0.2256	0.023589	✶
	EthCitCd-24 (0.685g)	10.75	3.734618	2.359124	0.1774	0.173315	NS
	UreCitCd-24 (0.2875g)	10.264	3.418623	3.930435	0.1238	0.308516	NS
	UreCitCd-24 (0.575g)	10.112	1.597749	1.70087	0.1073	0.208838	NS
	Control (XT-300 10 % TiO2)	10.812	1.230413		N/A		
	EthCitCd-24 (2.5g)	8.800667	2.500633	-0.80453	18.09 %↓	N/A	N/A
	UreCitCd-24 (2.5g)	19.70067	4.481894	3.555467	0.8224	4.57E-08	✶✶✶

Appendix 2.5: In vitro SPF for Brij formulations incorporating EthCitCD and UreCitCD. T-Test was used to determine statistical significance, where P<0.05 = ✶, P<0.01 = ✶✶, P<0.001 = ✶✶✶ and P>0.05 is not significant

3. Investigations of titanium dioxide

3.1. Introduction

Titanium dioxide (TiO_2) is a white, inorganic material with exceptional physicochemical characteristics like biocompatibility, whitening capability, photocatalysis, corrosion-resistance, optical performance, and electrical properties (145, 146). TiO_2 has vast applications, leading to more than 5 million tonnes produced, per year, globally (147). In bulk, meaning at a particle size > 100 nm, it has a high refractive index and poor solubility, making it well-suited for use as a pigment (148) in many consumer products like paint (149) and paper (148). As an extremely white and bright material, it is often incorporated into products to enhance these features. As a UV filter, it is also added to ceramics and plastics to impart UV-blocking capabilities to the materials (148). In medicine, titanium dioxide can also be used in implanted biomaterials. While, in the food industry, it acts as a white colourant labelled E171 (150).

The cosmetics and personal care industry incorporates approximately 1300 tonnes of titanium dioxide into its products as colourants in toothpastes (151) or eye shadows, and as a UV filter in sunscreen formulations (152). As well as having the ability to absorb and scatter UV light, it also boasts chemically stability, is non-toxic and biocompatible (153), all of which are attributes that are highly desirable in the personal care field. The properties of titanium dioxide are largely influenced by particle size and geometry, therefore, the physicochemical properties of nano sized TiO_2 (< 100 nm) can vary significantly from the bulk (154). For example, TiO_2 nanoparticles are transparent in appearance as they do not reflect visible light, though they are still capable of UV absorption. The opacity of bulk TiO_2 sunscreen formulations is typically considered aesthetically displeasing to consumers, therefore nanoparticulate TiO_2 was introduced into formulations for a transparent appearance.

Among these features, TiO_2 is also a semiconductor with catalytic properties (153). Its semiconducting properties ultimately give it the ability to offer UV protection. It is classed as an intrinsic N-type semiconductor due to the oxygen vacancies in its lattice (155). It has a band gap energy that corresponds to 387 nm for anatase and 405 nm for rutile, which means that light of these wavelengths and below is capable of exciting

electrons from the valence band to the conduction band (155). In a sunscreen formulation, TiO_2 can absorb UV radiation, which in turn promotes electrons from its valence band to its conduction band, leaving behind holes in the valence band as shown in Equation 3.1 (156). The holes and the excited electrons can either recombine or participate in redox reactions that can form ROS like hydroxyl radicals and superoxide (Equation 3.2 and Equation 3.3).

Equation 3.1

$$TiO_2 + hv \rightarrow (e_{CB}^- + H_{VB}^+)\, TiO_2$$

Equation 3.2

$$H_{VB}^+ + H_2O \rightarrow H^+ + \cdot OH$$

Equation 3.3

$$e_{CB}^- + O_2 \rightarrow O_2^{\cdot -} \rightarrow\rightarrow\rightarrow H_2O_2$$

In the introductory chapter, the damage that ROS can cause such as initiating oxidative stress which can lead to DNA damage, was discussed. As a result, the risk of ROS production must be mitigated when titanium dioxide is used in sunscreens, with the incorporation of antioxidants and radical scavengers, in the formulation or coated on to TiO_2 itself (155).

3.1.1. Crystal structure

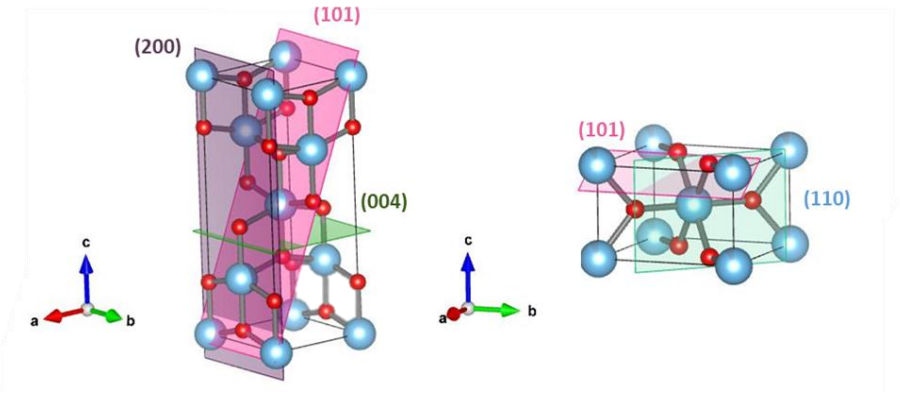

Figure 3.1: Crystal structure of anatase (left) showing planes (101), (200) and (004), and rutile (right) showing planes (101) and (110). Ti atoms are blue and O atoms are red. Made using Vesta software.

Anatase, rutile and brookite are the three main polymorphs of titanium dioxide, of which anatase and rutile have a tetragonal structure (shown in Figure 3.1), while brookite has orthorhombic structure (156). The lattice parameters of anatase are as follows: a = 3.785 Å, c= 9.514 Å, a = b, space group I 41/a m d (157). For rutile, the lattice parameters are a = 4.594 Å, c = 2.958 Å, a = b, space group P42/mnm (157). Generally, anatase is considered more photoactive forming free radicals as a result (156) and so is usually used in photocatalysis applications (156). Rutile, on the other hand, is a more effective light scatterer and therefore better applied to pigments (156). Typically, anatase is the more stable phase for nanoparticles below 11 nm in size, while rutile is more stable at particle sizes above 35 nm (158).

3.1.2. Synthesis of TiO_2

Some of the synthetic methods for the formation of TiO_2 nanomaterials have been summarised by Chen *et al.* including: sol-gel, hydrothermal, solvothermal, direct oxidation, chemical and physical vapour deposition, electrodeposition, sonochemical and microwave (159), and with them various morphologies like nanoparticles, nanorods and nanotubes are produced (159).

Hydrothermal synthesis is generally considered to be a facile route to producing highly crystalline materials under mild reaction conditions of low temperature and relatively short reaction times (160). It allows greater control over particle size and morphology, and can produce homogeneous results (160). Typically, a titanium alkoxide is dissolved in an organic solvent, in order to control hydrolysis and prepare uniform TiO_2 colloids (161). The hydrothermal treatment that follows, typically leads to formation of pure anatase. This section will outline a few examples of hydrothermal preparations of TiO_2.

Hydrothermal synthesis allows for a variety of different morphologies of TiO_2 to occur. Yu *et al.* utilised hydrofluoric acid to control the shape of anatase TiO_2, based on the work of Yang *et al.* (162), and produced nanosheets with exposed (001) facets for use in dye-sensitized solar cells (163). Scanning Electron Microscopy (SEM) and Transmission Electron Microscopy (TEM) images taken from their 2010 paper can be seen in Figure 3.2. TEM image (B) indicates that the lattice spacing parallel to top and bottom facets is 0.235 nm, which can be assigned to the (001) anatase planes, thereby confirming the exposure of the (001) facets during this crystal growth.

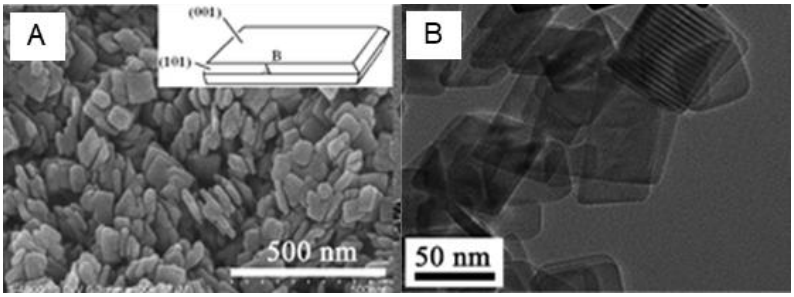

Figure 3.2: SEM (A) and TEM (B) images of TiO_2 nanosheets. Reproduced from the research of Yu *et al.* with copyright permission.

Su *et al.* demonstrated the influence of hydrothermal reaction time on the transformation of anatase to rutile, at two temperatures: 150 °C and 200 °C (160). First, they created a sol using titanium (IV) n-butoxide in isopropyl alcohol as a TiO_2 precursor, acetylacetone to control reaction kinetics and used dilute i-propanolic solution to avoid strong hydrolysis. After washing the titanium oxyhydroxide white precipitate with water, nitric acid was added dropwise to form a clear sol, which was heated to reflux at 85 °C for 8h. The sol underwent hydrothermal treatment at 150 °C and 200 °C for various durations. At both temperatures, the anatase phase is apparent in the initial growth stages of TiO_2 and extending the heating duration encourages the transformation from anatase to rutile. They suggest that the transformation may be initiated by the formation of rutile nuclei on the anatase (112) phase, leading to the growth of rutile crystallites in preference over anatase (160).

3.1.2.1. Growth mechanism

Prathan *et al.* proposed the following growth mechanism for the formation of TiO_2 nanorods, through a hydrothermal synthesis of titanium (IV) butoxide in diluted hydrochloric acid (164). As $Ti(OBu)_4$ reacts with water, Ti uses its vacant d-orbitals to accept O lone pairs and as Ti-O bonds are formed, the coordination number of Ti^{4+} increases from 4 to 6. The now six-fold structure reaches high pressure and form octahedra which finally precipitates into crystals on combination. Condensation reactions facilitate the agglomeration of the octahedra, through corner and edge sharing. Under acidic conditions, Ti-OH is easily protonated ($Ti\text{-}OH_2^+$) allowing facile combination with other OH^- groups on TiO_6 octahedra. The elimination of water in the dehydration reaction, then forms Ti-O-Ti bridges. More acidic conditions will favour the hydrolysis and dehydration reactions, and high temperatures are necessary for crystal growth to progress. Though, anatase phase forms preferentially under mildly acidic

conditions due to its lower surface energy. The reaction can be written as follows, where $Ti(OR)_4$ is titanium alkoxide precursor (165):

$$Ti(OR)_4 + 4H_2O \rightarrow Ti(OH)_4 + 4ROH \textit{ (hydrolysis)}$$

$$Ti(OH)_4 \rightarrow TiO_2 + 2H_2O \textit{ (dehydration)}$$

3.1.2.2. Control of facet growth

During crystal growth, often the surfaces with higher reactivities are quickly reduced to minimise the surface energy (166). In TiO_2 for example, the (101) facet dominates most anatase crystals as it is the most thermodynamically stable, while the (001) facet is far more reactive and often supressed. Typically facets with a greater percentage of uncoordinated atoms, are more reactive, such is the case with (001) compared to (101) in TiO_2 (167). Therefore, by exposing more reactive facets, there is potential to improve the photoreactive properties, so control over the facets produced was sought after.

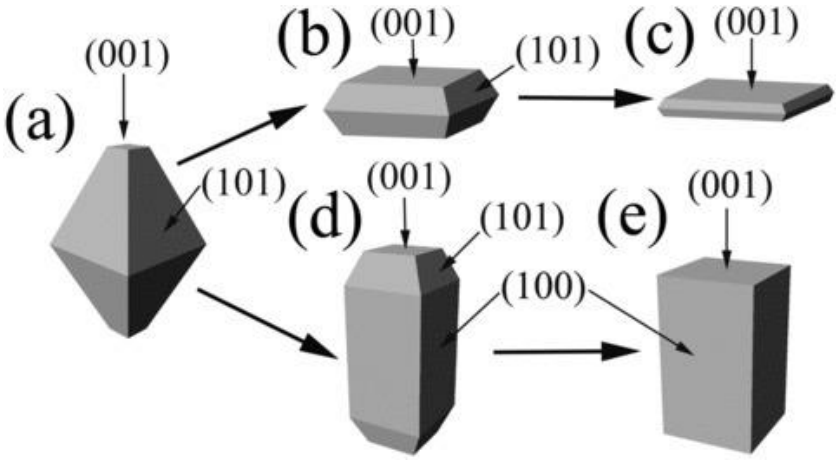

Figure 3.3: Representations of anatase shapes: a) slightly truncated tetragonal bipyramid, b) truncated tetragonal bipyramid, c) square sheet, d) elongated truncated tetragonal bipyramid and e) tetragonal cuboid. Reproduced from (168) with copyright permission.

Zhao *et al.* presented the schematic drawings shown in Figure 3.3 which describe various anatase morphologies, with different exposed facets (168). The slightly truncated tetragonal bipyramid (a) has a dominating (101) facet that accounts for 94 % of the total surface, which is considered the “equilibrium shape” by the Wulff construction method. A larger percentage of exposed (001) facets is shown in (b) described as a truncated tetragonal bipyramid, while (c) shows a square sheet where (001) is the dominating facet. The elongated truncated tetragonal bipyramid is shown

in (d) and has a high proportion of lateral (100) facets while (e) shows a tetragonal cuboid of (100) and (101) facets.

Hydrofluoric acid (HF) has been used to control the shape of the TiO_2 crystals and as a capping agent (169). Han *et al.* produced anatase nanosheets, with up to 89 % exposed (001) facets, using a solvothermal route with 47 % hydrofluoric acid as the solvent and tetrabutyl titanate (170). They found that fluorine ions were instrumental in producing the exposed (001) surface, possibly by reducing the surface energy of (001) to lower than that of (101). By increasing the amount of HF acid, the nanosheets increased in size and percentage of exposed (001) surface. At 200 °C for 24 h, $Ti(OBu)_4$ (5 mL), and hydrofluoric acid (0.8 mL) were the optimum conditions for maximum (001) facet exposure (170). Ultimately, by using a facile solvothermal method, they were able to prepare TiO_2 nanosheets with superior photocatalytic efficiency simply by altering the morphology. However, HF is a very corrosive chemical that is not environmentally friendly (169), therefore alternative processes are sought after that allow control over facet formation. Zhao *et al.* used 1-butyl-3-methylimidazolium tetrafluoroborate ([BMIM][BF_4]) as a softer alternative source of fluoride ions, compared to HF (168). The F^- ions were capable of stabilising (001) facets while the $[BMIM]^+$ was found to favourably stabilise the (100) facets, in a capping agent role, leading to nano-cuboidal TiO_2.

Amine compounds are often incorporated into TiO_2 synthesis as they can encourage highly crystalline titanium dioxide with controlled morphology. Amines can act as a bridging ligand, to aid the formation of the Ti-O-Ti backbone in a specific direction and also as a capping agent to prevent the formation in other dimensions (169). Roy *et al.* report the use of diethanolamine to strategically inhibit the growth of (001) facet by preferentially H-bonding (through N-H and O-H) to two exposed O atoms on (001) (169). As depicted in Figure 3.4, their density functional theory (DFT) calculations showed the distance between hydrogens of N-H and O-H in diethanolamine, and O atoms on (001) facet were closely matched (0.46 nm and 0.53 nm, respectively), enabling H-bonding (171). Conversely, the O atoms on (101) facet are 0.28 nm apart, providing ill-suited sites for H-bonding with diethanolamine (171). With this, diethanolamine selectively H-bonds with (001) facet, inhibiting its growth, leaving the facet exposed.

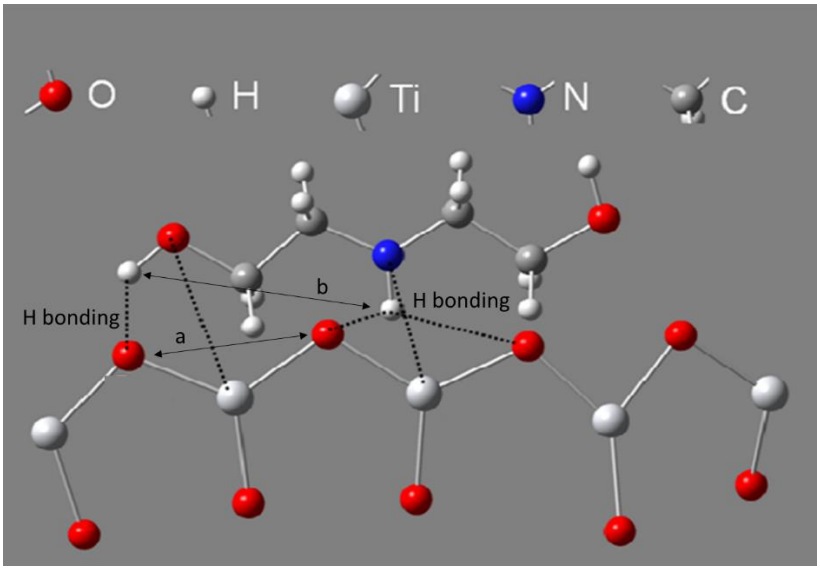

Figure 3.4: The electronic interactions of the (001) facet of TiO_2, with diethanolamine. DFT calculations showed a = 0.53 nm, b = 0.46 nm. Adapted with permission from Roy *et al* (169). Copyright © 2013, American Chemical Society.

3.1.3. TiO_2 with organic dopants

Titanium dioxide has a relatively high band gap energy (approximately 3.2 eV) which corresponds to short-wavelength UV light (172). There are many studies focused on lowering the band gap energy of TiO_2 so that visible light can be used as a stimulus for photocatalysis. Doping is one of the ways in which TiO_2 can be modified to improve its attenuation of visible light. Metals, as well as non-metals such as nitrogen, carbon, fluorine, and sulphur, have been used, however, the focus has previously been to enhance photocatalytic performance (158, 173, 174).

Gosh *et al.* have outlined some of the many applications of modified titania in the environmental and healthcare fields, such as dye degradation, antibacterial activity and medical implants (175), which use its photocatalytic properties. However, there is little research in the literature where carbon doping of TiO_2 is used to improve its properties as a UV filter in sunscreen applications for example or improve its stability in formulation. In 2022, Dai *et al.* produced a review which outlined the role of carbon in titanium dioxide materials (176). The premise of this research was that carbon-based nanomaterials and titanium dioxide may work synergistically for improved photocatalytic performance, through sharing some of the excellent properties of carbon nanomaterials include electronic storage and conductivity, photosensitiser in the visible light range.

The inclusion of carbon into titanium dioxide has been reported to be an effective way to facilitate the absorption of visible light (177). It may do so by forming a carbonaceous species on the surface (177). Additionally, the incorporation of carbon can increase the surface area and provide more reactive sites. The combination of visible light absorption, increased surface area and reactive sites can be used in applications like organic contaminant degradation (177). For example, Shen *et al.* prepared C-doped TiO_2 by calcinating titanium carbide in air, at 350 °C and demonstrated its effectiveness on the degradation of trichloroacetic acid (178).

Doping TiO_2 with nitrogen can reportedly alter properties like refractive index, hardness, electrical conductivity, elastic modulus, and visible light induced photocatalytic activity. Peng *et al.*, for example, formed irregular, spherical N-doped TiO_2 by heating commercial P25 TiO_2, which is a mixture of rutile and anatase, with triethanolamine, in an autoclave for 24 h at 140 °C (134). The resultant N-TiO_2 showed better visible light photoactivity than P25 itself.

3.1.4. Carbon nanoparticles and TiO_2

There has been recent literature interest in the use of carbon quantum dots (CQDs) for surface modification of TiO_2. In 2019, Yan *et al.* reported the preparation of TiO_2-CQDs composites for use as antimicrobial agents (179). Using an electrochemical method, they prepared CQDs using graphite rods. Following this, they combined titanium dioxide with a solution of the CQDs, ethanol and water, then heated the reaction mixture at 140 °C for 4 h. The result was washed with water, dried under vacuum, and formed TiO_2-CQDs with uniform morphologies (ca. 35 nm) and crystallinity maintained. They reported the ability of the CQDs to prevent the titanium dioxide from agglomerating and the composite was found to have superior antibacterial activity.

Safardoust-Hojaghan *et al.* prepared graphene quantum dots (GQDs) from citric acid, ethylene diamine and water using a hydrothermal method, at 180 °C for 8 h (180). P25 TiO_2 was stirred into the resultant aqueous solution of GQDs for 24 h. The average particle size was found to be 65 nm, though the crystallinity was not commented on. The nanocomposite was found to show promising photodegradation abilities towards methylene blue, under UV light, improving the efficiency relative to pure TiO_2.

Ma *et al.* used CQDs to develop a CQDs-dye-TiO_2 complex to develop a high-efficiency photoelectric conversion system (180). They reported that the CQDs could facilitate one-way electron transfer between rhodamine B and titanium dioxide and improved the photoelectric conversion efficiency of the complex sevenfold.

In these examples, the modification of prepared titanium dioxide with carbon nanoparticles is a shared feature. Carbon dots have varied physicochemical properties, among them are excellent optical properties, high stability, abundance of functional groups like amino, hydroxyl and carboxyl groups, electron mobility (130) and a particle size of 1 – 10 nm. After extensive literature research, the impact of carbon dots inclusion into the reaction of TiO_2 itself, has not yet been studied. Owed to their very small particle size and high functionality, it is believed that carbons dots may interfere with the growth of titanium dioxide which may lead to interesting morphologies and resultant optical properties, that can be exploited for use in personal care products like sunscreens.

3.1.5. Aim

Some of the existing methods of altering the properties of TiO_2 have been highlighted, including the incorporation of various forms of carbon. The overview of the literature has demonstrated the tuning of TiO_2 optical properties with non-metals such as carbon and nitrogen is well-explored. The ability of carbon dots to tune the optical properties of TiO_2, either through inclusion or by changing the structural properties (such as morphology) is promising. Though, the incorporation of carbon dots directly into the preparation of titanium dioxide, has not been studied.

The broad aim of this study is to explore what impact carbon dots have on the hydrothermal preparation of TiO_2 with a focus on its structural, morphological, and optical properties. EthCitCD, UreCitCD and VanCitCD from Chapter 2, functionalised with N and O groups, will be used to investigate this. The potential of the resulting materials as sunscreen additives, will be considered.

3.2. Sol-gel investigations

One common way to prepare TiO_2 is through the sol-gel method. Typically, the hydrolysis and polymerisation of the precursors form a colloidal suspension or “sol”.

The metal alkoxide will react in the presence of water, triggering hydrolysis. Subsequently, condensation occurs by elimination of water and the formation of metal oxide linkages, leading to the growth of polymer networks in the liquid sol. Following the completion of polymerisation and the loss of solvent, the liquid sol forms a solid gel phase which, once dried, forms a solid powder. This is often thermally treated by calcination, at high temperatures, to remove any lasting residues (181).

Using a sol-gel method outlined by Ananth *et al.,* TiO_2 was prepared (182). Titanium isopropoxide was added dropwise to an acidified solution of water and isopropanol, which formed a white precipitate. The reaction was stirred at 60 °C for 30 minutes and was then washed with water and methanol to remove any impurities. This reaction was repeated with the addition of EthCitCD solution and formed a yellow solid powder. The colour change indicated possible adsorption of EthCitCD onto TiO_2, which is similar to what Ananth *et al.* found on addition of betanin dye into the sol-gel reaction (182).

3.2.1. Analysis of crystallinity

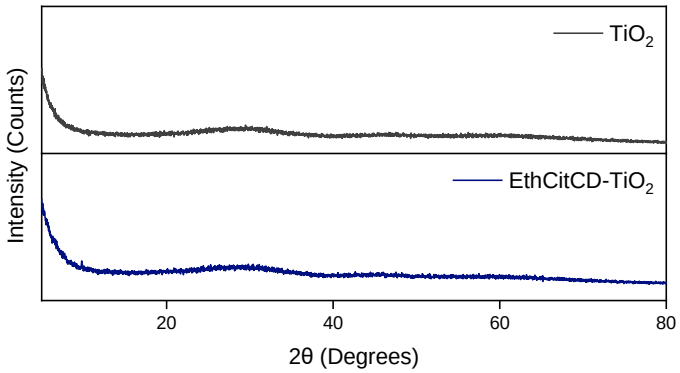

Figure 3.5: XRD patterns of pure TiO_2 and TiO_2 with EthCitCD, prepared by sol-gel route

There were two key analytical checkpoints for these reactions: 1) XRD patterns to determine crystallinity; 2) UV-vis spectra to establish any changes in the attenuation of light. The XRD patterns are shown in Figure 3.5. It is evident from the broad peaks and level of noise, that both materials lack crystallinity. This is because the calcination step was intentionally omitted to reduce the energy consumption of the reaction, and therefore some organic molecules may remain (161). The lack of crystallinity caused two key problems: firstly, crystallinity is a pre-requisite of the use of titanium dioxide in

cosmetic products as outlined in EU Commission, Regulation (EC) No. 1223/2009, Annex VI (53) therefore this sol-gel preparation immediately falls short of this criterion. Secondly, it would be difficult to follow any changes in crystalline structure resulting from the addition of organic additives from Chapter 2.

3.2.2. Analysis of optical properties

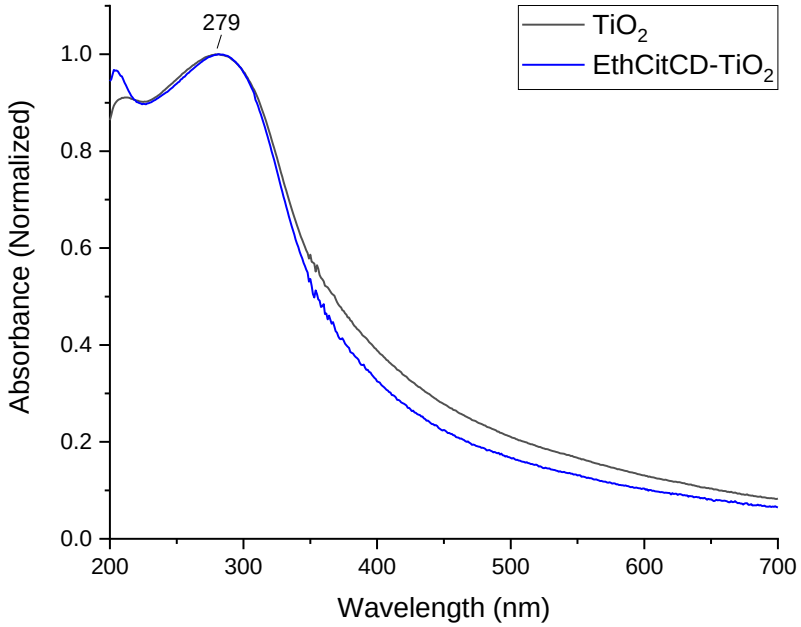

Figure 3.6: UV/vis of TiO_2 and EthCitCD-TiO_2, prepared by sol-gel method, measured at 0.003 % w/v in 60 % EtOH, normalised between 0 and 1.

The UV-vis spectra in Figure 3.6 are very similar. Both have a λ_{max} of 279 nm and a broad attenuation of light that tails into the visible region, suggesting there is little difference in the two materials. With the unpromising optical properties, coupled with the amorphous nature of the materials, it was quickly concluded that this method of synthesis was not an effective way to alter the properties of titanium dioxide.

Attention was turned to the hydrothermal preparation of titanium dioxide which is known for its ability to easily produce highly crystalline material, even when dopants are incorporated.

3.3. Characterisation of TiO_2 with nanoscale organic additives

In this section, the nanoscale organic additives are solutions of carbon dots as prepared and analysed in Chapter 2. EthCitCD, UreCitCD and VanCitCD were selected to be incorporated into the TiO_2 hydrothermal reaction, as they had the most desirable optical properties and showed potential in radical scavenging.

First, pure, crystalline anatase was prepared following a procedure by Yang *et al.* (162), however, the titanium precursor titanium (IV) butoxide was replaced with titanium (IV) isopropoxide as this was readily available in the lab. Water (1.25 mL), acetic acid (20 mL) and 1-butyl-3-methylimidazolium tetrafluoroborate (500 µL) were combined, titanium isopropoxide (500 µL) was added and the mixture was sonicated. It was then heated in a hot oven at 200 °C for 24 h. The white precipitate was collected through centrifugation, washed with water and ethanol, and then dried at 75 °C. The procedure is depicted in Figure 3.7. Going forward the following abbreviations will be used: titanium (IV) isopropoxide (TTIP), 1-butyl-3-methylimidazolium tetrafluoroborate ($BMIMBF_4$), and acetic acid (AcOH).

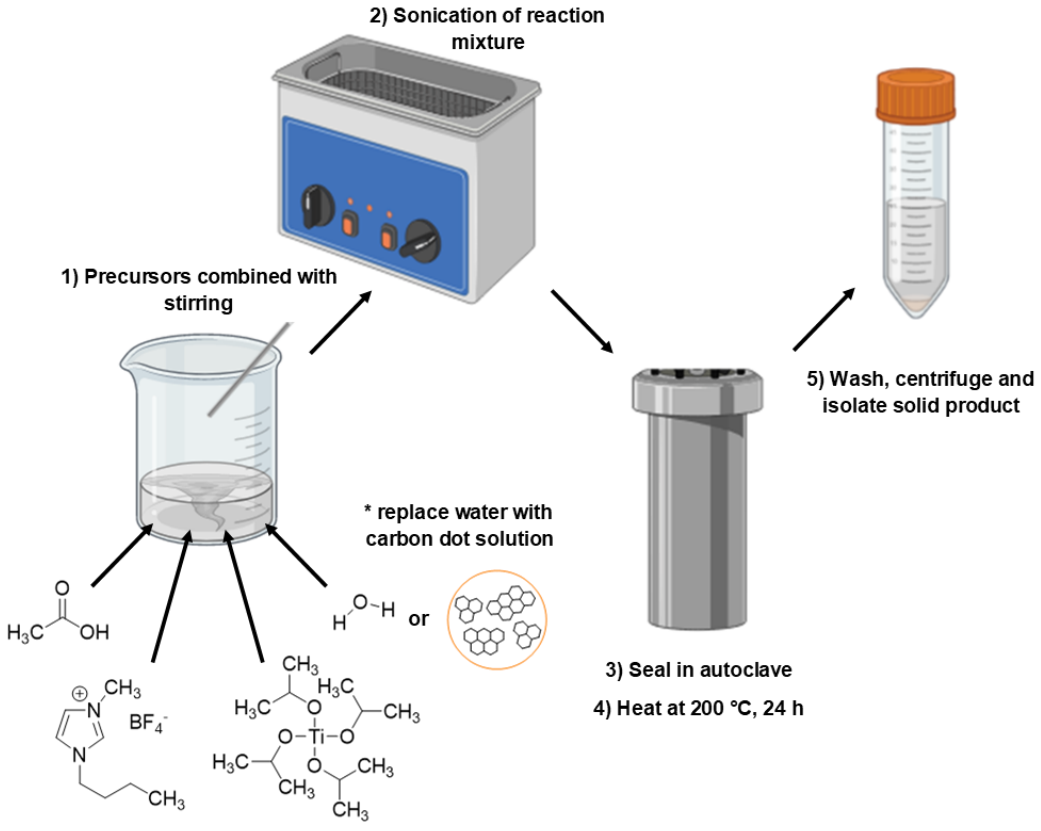

Figure 3.7: A scheme to show the preparation of TiO_2 by hydrothermal synthesis, with and without an organic additive. Made with BioRender.

This reaction was repeated at a duration of 48 h, to determine whether expanding the reaction time would impact the morphology or crystallinity of the product and determine reaction conditions for the subsequent experiments. Appendix 3.1 shows that both 24 h and 48 h reactions produced anatase, and an extended reaction time did not alter the crystallinity or lead to the transformation to rutile. Additionally, as shown in the SEM images in Appendix 3.2, the morphology was consistent with nanocuboids and was sustained from 24 h to 48 h. After discerning there was no significant changes between 24 h and 48 h TiO_2, the subsequent reactions were carried out at a duration of 24 h.

This section will discuss the effect of three nanoscale organic additives: EthCitCD, UreCitCD and VanCitCD, on the structure, morphology, and resultant properties of TiO_2. They have been incorporated as three different percentages of total solvent in the reaction: 50 %, 6.25 % and 0.25 %, and replaced pure water in the reaction as they are all suspended in distilled water.

Water is an important component in this reaction as it facilitates hydrolysis of TTIP and condensation processes. Zhao *et al.* followed a very similar synthetic route and systematically changed the molar ratios of the components: titanium isopropoxide, water, [BMIM][BF_4] and acetic acid to explore how this affected TiO_2 morphology (168). They reported that little water in the reaction formed uniform, nanocuboids, walled by (100) and (001) facets. While, as the water content increased, the length of the nanocuboids became shorter and the aspect ratios also began to decrease. This was justified by more water leading to faster hydrolysis and condensation, in addition to rapid nucleation and growth of anatase nanocrystals. Consequently, smaller nanocuboids would result on account of the accelerated formation of a vast amount of anatase nuclei.

With this, it is known that by changing the percentage of carbon dots in the reaction, the water content will also change. While it is expected that in general, this may decrease the aspect ratio of the TiO_2 nanoparticles it was important to ascertain this in accordance with the percentage of carbon dots. The preparation of pure TiO_2 was therefore carried out with water contents of 50 %, 6.25 % and 0.25 %, as it was necessary to demonstrate the effect of water on its own, in order to compare with the that of the carbon dots.

3.3.1. Pure TiO_2

3.3.1.1. Structural characterisation

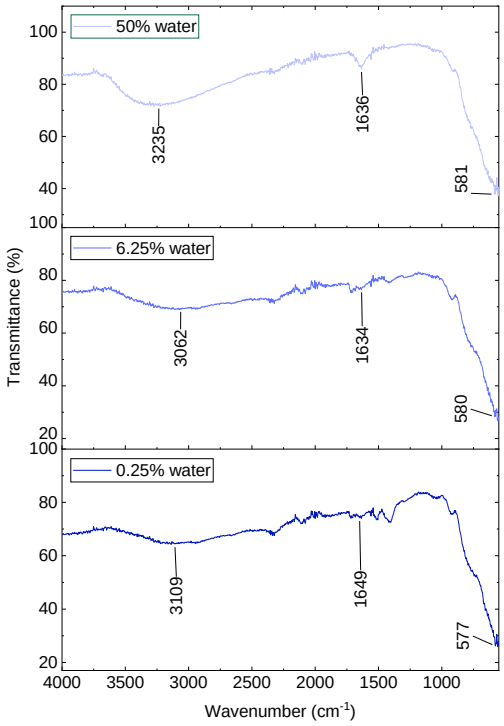

Figure 3.8: FT-IR spectra of pure TiO_2 with 50 %, 6.25 % and 0.25 % water.

Pure TiO_2 was prepared with three different proportions of water and FT-IR analysis was used to determine the success of the reaction (Figure 3.8). The assignments are summarised in Table 3.1.

Table 3.1: FT-IR assignments for pure TiO_2 with 50 %, 6.25 % and 0.25 % water

Material	Assignment	Wavenumber (cm^{-1})
TiO_2 50 % water	O-H stretch	3674 - 2385
	O-H bend	1636
	Ti-O-Ti stretch	875 - 550
	Ti-O stretch	581
TiO_2 6.25 % water	O-H stretch	3656 - 2376
	C=O stretch, C=C stretch, O-H bend	1773 - 1329
	Ti-O-Ti stretch	883 - 550
	Ti-O stretch	580
TiO_2 0.25 % water	O-H stretch	3631- 2368
	C=O stretch, C=C stretch, O-H bend	1749 - 1318
	Ti-O-Ti stretch	892 - 550
	Ti-O stretch	577

At 50 % water, the expected absorption bands for TiO_2 were found: 735 cm^{-1} which can be ascribed to Ti-O-Ti stretching mode and 581 cm^{-1} which can be assigned to Ti-O stretching band, as well as 3235 cm^{-1} (broad) and 1636 cm^{-1} which correspond to the stretching and bending O-H vibrational modes (consistent with moisture in the sample) (183).

At 6.25 % water, the following absorption bands were found: 725 cm^{-1} which corresponds to Ti-O-Ti stretching mode and 580 cm^{-1} which can be ascribed to Ti-O stretching band, and 3062 cm^{-1} (broad) and 1634 cm^{-1} which correspond to the stretching and bending O-H vibrational modes (consistent with moisture in the sample) (183).

At 0.25 % water there is a broad band at 3109 cm^{-1} and a band at 1649 cm^{-1} which correspond to the stretching and bending vibrational modes of O-H (consistent with moisture in the sample), 725 cm^{-1} which corresponds to Ti-O-Ti stretching mode and 577 cm^{-1} which can be ascribed to Ti-O stretching band (183).

Overall, the FT-IR spectra shown in Figure 3.8 show the expected absorption bands for TiO_2, in agreement with literature (183-185), for all three reactions, which would indicate pure TiO_2 has been prepared successfully.

3.3.1.2. Crystallinity and morphology

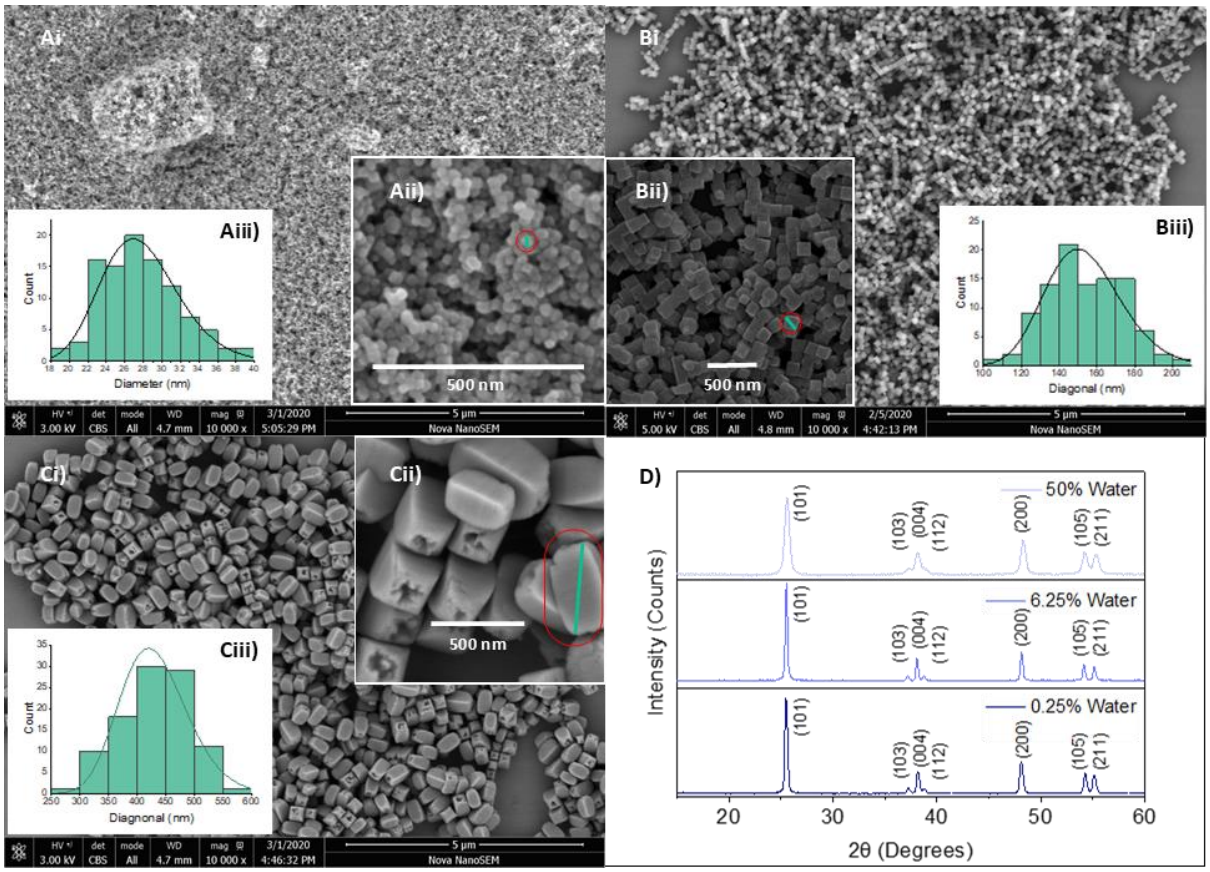

Figure 3.9: SEM images and XRD patterns of pure TiO_2, with varying amounts of water. Ai-ii) 50 % water, Bi-ii) 6.25 % water and Ci-ii) 0.25 % water and D) XRD patterns of pure TiO_2 (50 %, 6.25 % and 0.25 % water). Particle size distribution n=100.

The SEM images of titanium dioxide, prepared with varying water content, are shown in Figure 3.9. The volume ratios of the quaternary system TTIP: $BMIMBF_4$: water: AcOH were varied as follows: 1: 1: 20: 20, 1: 1: 2.5: 40 and 1: 1: 0.1: 40, corresponding to Figure 3.9A-C, respectively. The particle size and morphology varied as the percentage of water in the reaction was changed, though the anatase phase was formed for all, as shown in the XRD patterns (Figure 3.9D).

At low water content, the quaternary system of AcOH, $BMIMBF_4$, water and TTIP, selectively stabilised the (001) and (100) facets, which led to the formation of consistent nanocuboids. The diagonal across the (100) facet was measured as indicated in Figure 3.9Cii, to gather a size distribution of 250–600 nm, averaging at 432 nm. The particle size of TiO_2 decreased significantly as the percentage of water increased. At 6.25 % water (Figure 3.9B), irregularly shaped nanoparticles (cubes with

some spherical tendencies) formed (diagonal length 100–210 nm) with a lower aspect ratio. This supported the notion that through accelerated hydrolysis, condensation, nucleation and growth of anatase, more water leads to faster-forming anatase nuclei and consequently smaller sized particles (168). The highest content of water (50 %) formed sphere-like nanoparticles between 18 and 40 nm in diameter. These are not much larger than the calculated crystallite size (14.2 nm), which represent the smallest, most likely single crystal in the materials. This may suggest crystal growth is not facilitated effectively with high water content.

The XRD patterns of each variation of pure TiO_2 (with 50 %, 6.25 % and 0.25 % water) are shown in Figure 3.9. At 50 % water, diffraction peaks were seen at the following angles (2θ): 25.5°, 37.2°, 38.2°, 38.8°, 48.3°, 54.2°, 55.2° which correspond to (101), (103), (004), (112), (200), (105), (211). At 6.25 % water, the angles (2θ) of the diffraction peaks were: 25.5°, 37.2°, 38.1°, 38.8°, 48.2°, 54.1°, 55.1° which correspond to (101), (103), (004), (112), (200), (105), (211), respectively. At 0.25 % water, diffraction peaks were found at the following angles (2θ): 25.5°, 37.2°, 38.2°, 38.8°, 48.1°, 54.3°, 55.2° which correspond to (101), (103), (004), (112), (200), (105), (211), respectively.

The diffraction patterns of each material are consistent with anatase (JCPDS card no. 21-1272), and the signals were relatively sharp in all three samples which indicated highly crystalline materials. The percentage crystallinity was calculated from the XRD patterns as follows:

Equation 3.4

$$\boldsymbol{Crystallinity} = \frac{\boldsymbol{Area\ of\ crystalline\ peaks}}{\boldsymbol{Area\ of\ all\ peaks\ (crystalline + amorphous)}} \times \mathbf{100}$$

This established that the crystallinity of anatase was 95 %, 89 % and 93 % for water contents of 50 %, 6.25 % and 0.25 %, respectively, and therefore was high in all samples.

The (101) diffraction peak is strongest in all three samples which suggests crystal growth along this plane is consistently predominant - conventional for TiO_2 as the (101) plane is the most thermodynamically stable (166). In all XRD patterns, the (200) reflection has a strong signal compared to typical anatase, due to the orientation of

the TiO_2 nanocuboids during XRD characterisation, which prefer to lie laterally on the (100) facets (168).

The crystallite size can be determined using the Scherrer equation (186):

Equation 3.5

$$D = \frac{k\lambda}{\beta_D \cos\theta}$$

where D is the crystallite size (nm), k is Scherrer's constant (0.90)(187), λ is the x-ray wavelength (0.152 nm), β_D is the full width at half-maximum intensity (radians) and θ is the peak position (radians).

Table 3.2: Crystallite size (nm) of pure TiO_2, calculated using the Scherrer equation.

	Water content		
	50 %	**6.25 %**	**0.25 %**
Crystallite size D (nm)	14.2	31.0	26.4

The crystallite size was calculated for the (101) plane for each material and shows at 6.25 % it is double the size than at 50 %, while at 0.25 % it falls back to 26.4 nm. Generally, the smaller the crystallite size the softer the bulk material.

It should be noted that as the percentage of water increases, broadening of the peaks is evident. This could be due to smaller crystallites, with fewer lattice planes, leading to a reduction in constructive interference and so less defined (broader) peaks. Alternatively, it could be due to elastic distortions or strains in the crystal lattice also known as microstrains, which can contribute to peak broadening or shifts (188).

With this, the d-spacings were calculated using $d_{hkl}=\lambda/(2\sin\theta)$, for TiO_2 with 50 %, 6.25 % and 0.25 % water. They showed no significant variation (see Appendix 3.3), which would indicate that the broadening of the XRD peaks is due to the presence of smaller crystallites.

In this section, the impact of varying water contents from 50 %, 6.25 % and 0.25 % on TiO_2 was analysed by SEM, XRD and FT-IR. In line with what was reported by Zhao *et al.* the crystal growth of anatase was affected by increased amounts of water, as was the morphology (168). Though, this was not found to limit the crystallinity or form defects in the lattice structure. This will enable comparison of pure TiO_2 with the doped

TiO_2-carbon dot (TiO_2-CD) structures, in the subsequent sections, to explore the affect that carbon dots have on morphology, crystal growth and ultimately optical properties.

3.3.1.3. Attenuation of UV and visible light

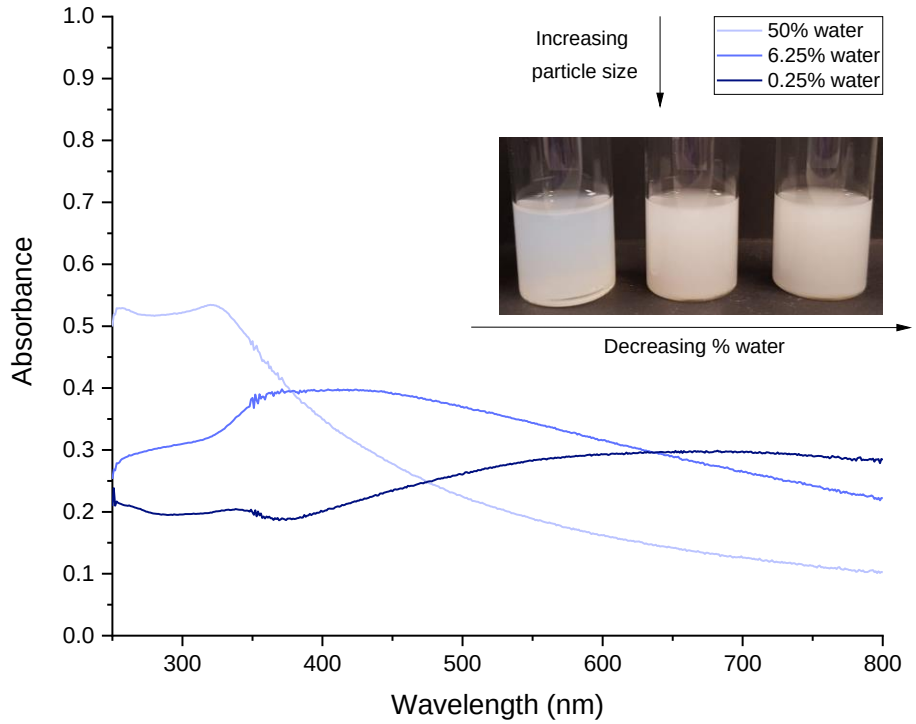

Figure 3.10: UV-vis spectra of TiO_2 suspended in 60 % EtOH [0.025 mg/mL], prepared with 50 %, 6.25 % and 0.25 % water. Inset image shows suspensions of each sample in 60 % EtOH [0.2 mg/mL].

The UV-vis profiles of pure TiO_2, prepared with 50 %, 6.25 % and 0.25 % water, are shown in Figure 3.10, and were measured at a concentration of 0.025 mg/mL in 60 % ethanol. With 50 % water, λ_{max} 325 nm was achieved, followed by a steady, broad decline in absorption intensity over the visible region (400–800 nm). When prepared with 6.25 % water, a broad peak over 350–450 nm can be seen, which again gradually declines as the wavelength increases to 800 nm. Preparation with 0.25 % water has a broad absorption that increases over the visible region, and peaks between 650–750 nm. There is a distinct red shift in the spectra from 50 % > 6.25 % > 0.25 % water which would confirm an increase in particle size. Additionally, a reduction in overall absorption intensity is observed. All samples have been measured at the same concentration (mg/mL). From the SEM images, it is known that the particle size is increasing from 50 % < 6.25 % < 0.25 % water; therefore, it is expected that the scattering efficiency increases as a particle diameter increases while absorption

efficiency decreases. In addition, a visual observation (Figure 3.10 inset) indicates the samples prepared with 0.25 % and 6.25 % water appeared to be more turbid, which may explain the overall reduction in absorption intensity. Overall, this gives an understanding of how an increase in TiO_2 particle size might influence the UV-vis spectra and will aid the interpretation of spectra for TiO_2 grown with organic additives. All samples were measured at the same % w/v.

3.3.2. EthCitCD-TiO_2

3.3.2.1. FT-IR analysis

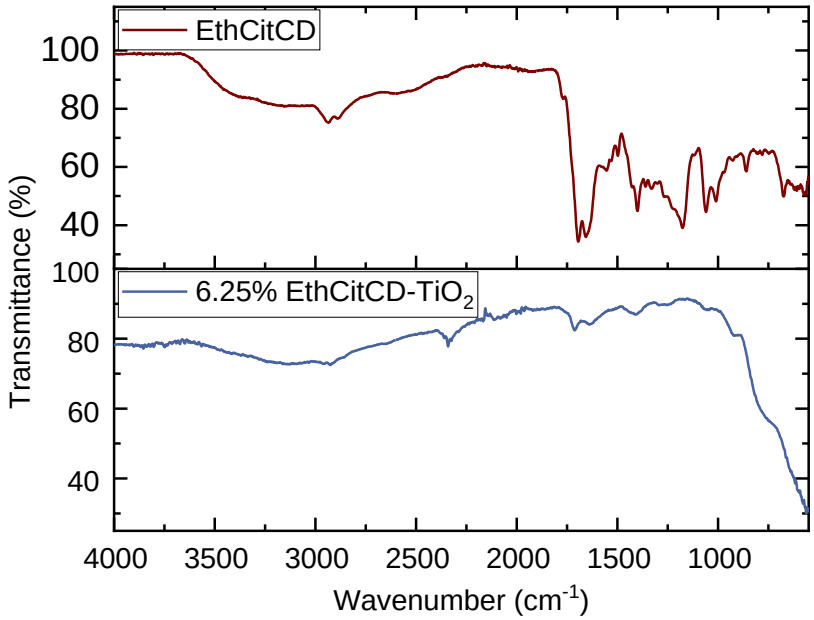

Figure 3.11: FT-IR spectra of EthCitCD and EthCitCD-TiO_2 at 6.25 % inclusion.

Figure 3.11 shows the FT-IR of EthCitCD alongside EthCitCD-TiO_2 made from 6.25 % inclusion of EthCitCD, for comparison. The corresponding assignments are listed in Table 3.3. Due to not enough sample, equivalent FT-IR spectra could not be obtained for 0.25 % and 50 % EthCitCD-TiO_2.

Table 3.3: FT-IR assignments for EthCitCD, EthCitCD-TiO_2 (6.25 %) and pure TiO_2 (6.25 %)

Material	Assignment	Wavenumber (cm^{-1})
EthCitCD	O-H, N-H stretch	3650 - 2250
	C-H stretch (alkene)	2936
	C-H stretch (alkane)	2889
	C=O carboxylic acid	1769
	C=O stretch (primary amide)	1697
	C=C stretch, N-H bend	1676-1592
	C-H bend, O-H bend	1480-1326
	C-O stretch alkyl aryl ether	1270
	C-N stretch	1179
	C-O stretch alkyl aryl ether	1062
6.25 % EthCitCD-TiO_2	O-H, N-H stretch	3681 - 2404
	C-H stretch	2925
	C=O stretch, C=C stretch, O-H bend	1749 – 1544
	C=O stretch	1712
	C=C stretch, N-H bend	1684 - 1483
	C-H, O-H bend	1461 – 1352
	C-O stretch, alkyl aryl ether	1268, 1062
	Ti-O-Ti stretch	888 – 550
	Ti-O stretch	562
6.25 % Pure TiO_2	O-H stretch	3656 - 2376
	O-H bend	1773 - 1329
	Ti-O-Ti stretch	883 – 550
	Ti-O stretch	580

Here, FT-IR spectroscopy was used to ascertain the functional groups present in TiO_2 after hydrothermal preparation alongside the amino, carboxyl and hydroxyl functionalised EthCitCD carbon dots. The new material, EthCitCD-TiO_2, has absorption bands at 883–550 cm^{-1} and 580 cm^{-1} which correspond to Ti-O-Ti and Ti-O stretching bands, respectively. This confirms the presence of the Ti-O-Ti bridge, suggesting polycrystalline TiO_2 (183), as is also shown in the FT-IR spectrum of pure TiO_2. Further to this, the absorption band at 1749–1544 cm^{-1} can be assigned to the C=O stretch, C=C stretch and O-H bend. While bands at 1684–1483 cm^{-1} and 1461–1352 cm^{-1} correspond to the C=C stretch and N-H bend, and the C-H and O-H bends, respectively. These bands, accompanied by the broad O-H/N-H stretch at 3681–2404 cm^{-1}, suggest there are amino, carboxyl and hydroxyl functionalities within EthCitCD-TiO_2 which is in alignment with those present in EthCitCD. Additionally, Energy Dispersive X-Ray (EDX) analysis confirmed the presence of Ti, O, C and N at all three percentage inclusions of EthCitCD, which supports this notion (see Appendix 3.4, Appendix 3.5 and Appendix 3.6).

3.3.2.2. Crystallinity and morphology

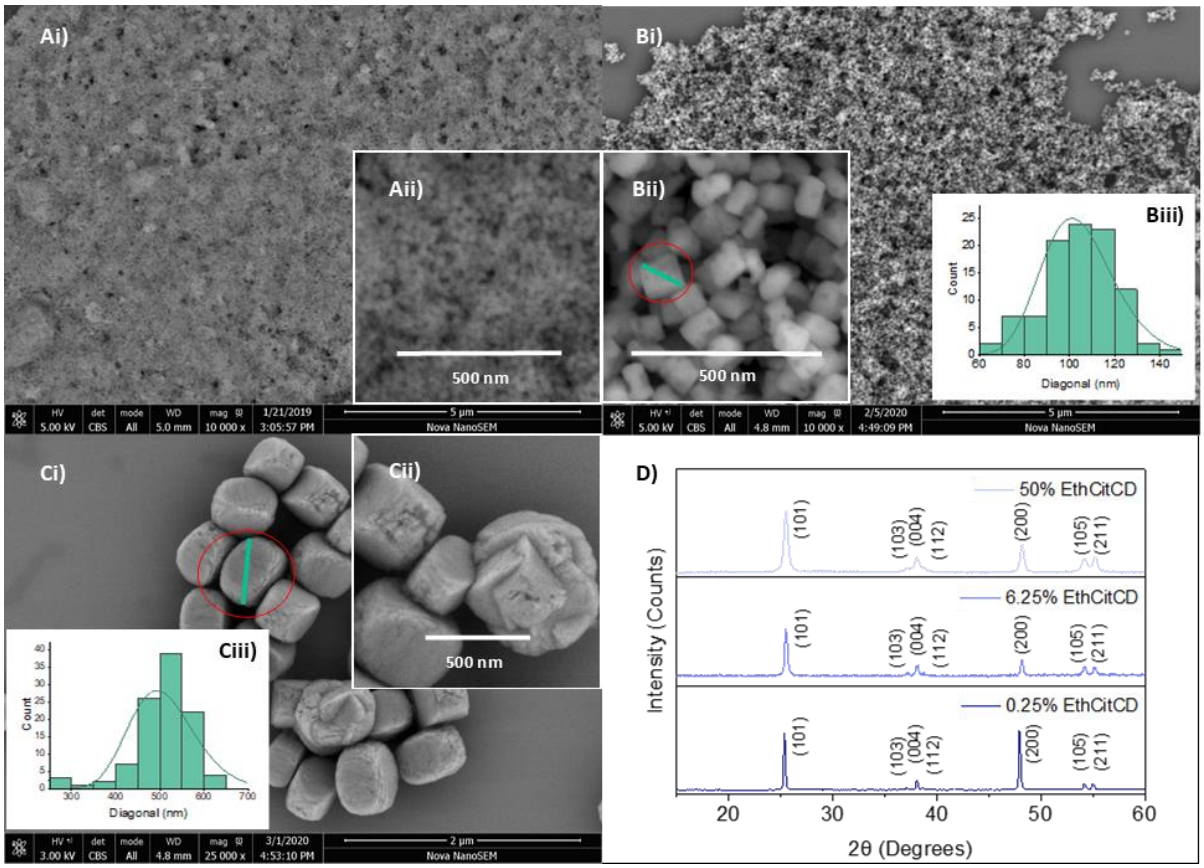

Figure 3.12: SEM images and XRD patterns of EthCitCD-TiO_2, with varying amounts of EthCitCD solution. Ai-ii) 50 % EthCitCD, Bi-ii) 6.25 % EthCitCD and Ci) 0.25 % EthCitCD and D) XRD patterns of EthCitCD-TiO_2 (50 %, 6.25 % and 0.25 % EthCitCD).

Figure 3.12 shows the SEM images of EthCitCD-TiO_2, prepared with 50 %, 6.25 % and 0.25 % EthCitCD solution, in place of distilled water. One of the most striking differences is the dramatic change in particle size, as the percentage of EthCitCD solution changes, which is important as particle size can have a strong impact on the optical properties. Following the research of Zhao *et al.* and our preliminary experiments with pure TiO_2, it is understood that water can lead to rapid nucleation of many nuclei, which in turn can result in smaller nanoparticles. Here, with the addition of EthCitCD, the particle size of EthCitCD-TiO_2 (50 %) was found to be between 16 – 23 nm[4] while pure TiO_2 (50 %) was larger at 18–40 nm. This suggests the inclusion of

[4] The image was not resolved enough to enable an accurate particle size distribution of these nanoparticles; therefore, an approximate range was obtained using ImageJ software (n=10).

carbon dots is reducing the particle size of TiO_2 even further. The amorphous carbon could be inhibiting the grain growth of TiO_2 (189). Alternatively, it could be forming nucleation sites. The nucleation of anatase at this 50 % of carbon dots, must be occurring faster than the crystal growth, which may explain the uniform but minimal crystal growth and little variation in size (165). Using the XRD data, the crystallite size was calculated (Table 3.4). At 50 % EthCitCD inclusion, it was 15.7 nm for (101), which is comparable to the approximate particle size measured, therefore suggesting that during this reaction, the crystal growth is minimal.

Figure 3.12B shows irregular cube-like shapes formed with 6.25 % EthCitCD in contrast to the uniform cubes formed for pure TiO_2 (6.25 % water). This change in uniformity may suggest interaction with carbon dots during the growth of the crystals.

The F^- ions in $BMIMBF_4$ which can stabilise (001) facet and $BMIM^+$ which preferentially adsorbs onto (100) facet resulting in homogeneous structures, may be impeded, otherwise the regular cubes would have formed as in TiO_2 (6.25 %). The small size of the carbon dots (0.8 – 2.8 nm) and their highly functionalised surfaces, may be able to interact with bridging O atoms on (100), with distances of 0.651 and 0.661 nm, according to Liu *et al.* However, the carbon dots might be too large to stabilise the (100) facet by H-bonding, but small enough to impede the access of $BMIM^+$ to do so, leading to non-uniform morphology.

0.25 % Inclusion of EthCitCD produced large (250–700 nm, length), cuboidal structures, though their aspect ratio was lower in comparison to pure TiO_2 (0.25 % water) which may indicate a lower percentage of (100) facets. The low carbon dot content has produced more uniform particles, which is consistent with $BMIMBF_4$ being the dominating stabilising agent once again.

The XRD patterns of each variation of EthCitCD-TiO_2 (with 50 %, 6.25 % and 0.25 % EthCitCD solution) are shown in Figure 3.12D.The XRD patterns are consistent with JCPDS card no. 21-1272 for tetragonal anatase and confirm that the anatase phase was formed in all reactions despite carbon dot inclusions. For 50 % EthCitCD diffraction peaks at angles (2θ): 25.5°, 37.2°, 38.1°, 38.8°, 48.2°, 54.2°, 55.2° were identified, and correspond to planes (101), (103), (004), (112), (200), (105), (211). At 6.25 % EthCitCD inclusion, diffraction peaks were found at the following angles (2θ): 25.5°, 37.1°, 38.2°, 38.8°, 48.2°, 54.2°, 55.2° which are consistent with planes (101),

(103), (004), (112), (200), (105), (211). Finally, at 0.25 %, diffraction peaks were seen at angles (2θ): 25.3°, 37.1°, 38.1°, 38.6°, 47.9°, 54.2°, 55.0° which correspond to planes (101), (103), (004), (112), (200), (105), (211). There is no indication of an amorphous carbon signal, which is possibly due to the low CD content and low intensity of the signal itself. The diffraction peaks and corresponding d-spacings are listed in full in Appendix 3.7.

The crystallite sizes were determined using the Scherrer equation (Equation 3.5), for plane (101) and are shown in Table 3.4.

Table 3.4: Crystallite size of EthCitCD-TiO_2 for plane (101) at 50 %, 6.25 % and 0.25 % inclusion

	EthCitCD content		
	50 %	**6.25 %**	**0.25 %**
Crystallite size D (nm)	15.7	23.0	40.1

The smallest crystallite size was achieved with 50 % inclusion (15.7 nm), followed by 6.25 % (23.0 nm) and 0.25 % (40.1 nm). It was evident, therefore, that by increasing the percentage inclusion of EthCitCD, the crystallite size decreased. This, coupled with the particle size distribution derived from the SEM images, can shed light on the crystal growth habits in each case. A similar particle size and crystallite size may indicate the crystal did not grow much more than the size of its smallest constituent and could suggest the formation of anatase was driven by rapid nucleation.

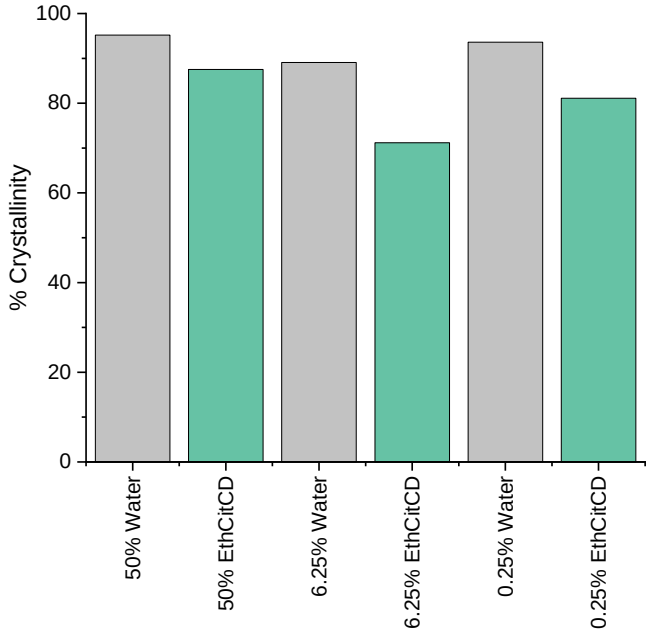

Figure 3.13: Percentage crystallinity of pure TiO_2 and EthCitCD-TiO_2 (50 %, 6.25 % and 0.25 %, respectively).

The signals are relatively sharp in all three patterns, which indicates the materials are crystalline. The percentage crystallinity of each material was calculated using Equation 3.4 and is displayed in Figure 3.13. From this, the crystallinity of EthCitCD-TiO_2 is shown to be lower in comparison to pure TiO_2, which may insinuate the introduction of a dopant. 6.25 % inclusion of EthCitCD is just 71.2 % crystalline which may suggest, at this percentage, doping of carbon dots into TiO_2 was particularly successful. Broadening of the XRD peaks is evident as the percentage of carbon dots increases, and the particle size decreases. Lattice strain can also lead to broadening of XRD peaks because of distortions in the lattice and defects.

The presence of defects in the lattice, also imply C or N may have been incorporated into the lattice and can be indicated by shifts in the XRD pattern. At 50 % EthCitCD inclusion, a diffraction peak (101) and (200) exhibited a shift in $2\theta > 0.1°$. While diffraction peak at (211) showed significant shift in relation to pure TiO_2, for 6.25 % EthCitCD-TiO_2. A shift greater than 0.1° was seen for all diffraction peaks except (004), in EthCitCD-TiO_2 (0.25 %). These shifts may therefore be evidence of C and N inclusion within the TiO_2.

The d-spacings, which describe the distance between planes of atoms, have been calculated for each (hkl) plane and are presented in Appendix 3.7. Deviations in the d-spacings can be indicative of changes in the lattice, often due to the influence of a dopant. A comparison of some of the d-spacings and 2θ° values for pure TiO_2 and TiO_2 with EthCitCD, is shown in Table 3.5, to ascertain whether there were any significant changes in the lattice.

Table 3.5: Comparison of the d-spacings and 2θ° for prominent diffraction planes (101), (004) and (200).

	[50 % EthCitCD]		[6.25 % EthCitCD]		[0.25 % EthCitCD]	
hkl	**2θ°**	**d_{hkl} (Å)**	**2θ°**	**d_{hkl} (Å)**	**2θ°**	**d_{hkl} (Å)**
101	25.475	3.447	25.455	3.450	25.334	3.466
004	38.096	2.329	38.156	2.325	38.076	2.330
200	48.192	1.862	48.172	1.862	47.909	1.872

	[50 % water]		[6.25 % water]		[0.25 % water]	
hkl	**2θ°**	**d_{hkl} (Å)**	**2θ°**	**d_{hkl} (Å)**	**2θ°**	**d_{hkl} (Å)**
101	25.576	3.434	25.516	3.442	25.475	3.447
004	38.177	2.324	38.096	2.329	38.156	2.325
200	48.293	1.858	48.152	1.863	48.111	1.864

Of the three diffraction planes, (101) d-spacing (EthCitCD-TiO_2) deviates the most from pure TiO_2 in all three reactions, and in all cases increases. This could be evidence of a dopant causing lattice strain in the (101) plane.

Overall, the inclusion of EthCitCD carbon dots has led to morphological changes of titanium dioxide, which are particularly evident in 6.25 % EthCitCD-TiO_2 for they are of heterogenous nature. In each case, crystalline anatase has been successfully produced, though the crystallinity shows some variation, likely due to the presence of dopants. There is also some evidence of lattice strain in (101) plane which supports the idea that carbon dots have doped TiO_2 during crystal growth. Interestingly, at the highest addition of EthCitCD, the particle size was extremely small. This will partially be due to the high content of water inducing rapid nucleation (as outlined previously) but could also be due to 0.8-2.8 nm sized carbon dots providing further nucleation sites.

Thus far, the following has been demonstrated: control of particle size, while maintaining good crystallinity of anatase, in the presence of an organic dopant, the

presence of which is evidenced by FT-IR spectroscopy and EDX analysis (Appendix 3.4 - Appendix 3.6). The next section will consider the optical properties of the doped materials.

3.3.2.3. Attenuation of UV and visible light

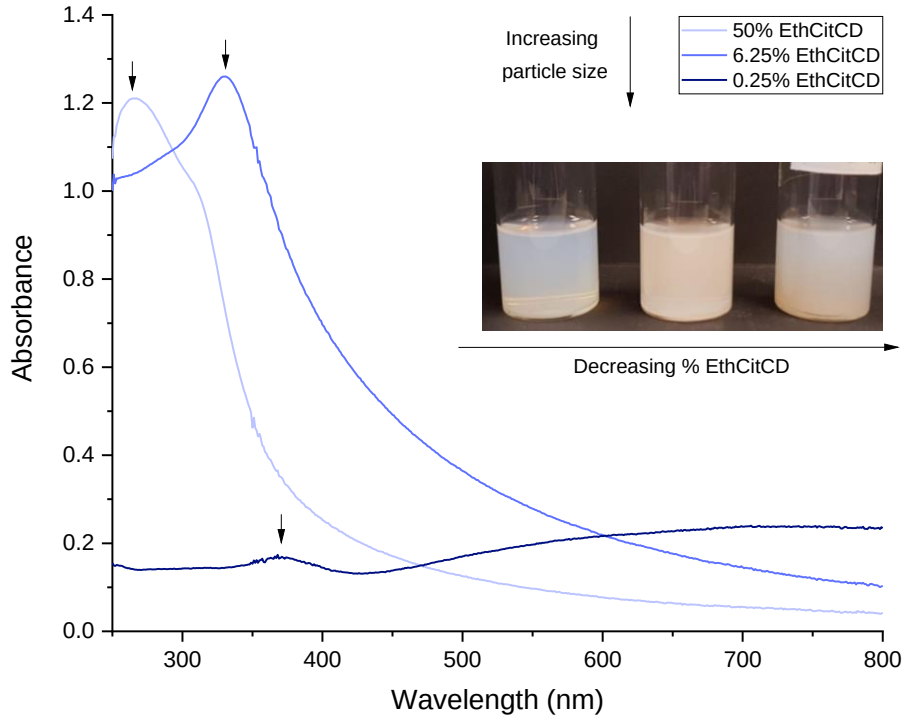

Figure 3.14: UV-vis spectra of EthCitCD-TiO_2 suspended in 60 % EtOH [0.025 mg/mL], grown with 50 %, 6.25 % and 0.25 % EthCitCD. Inset image shows suspensions of each sample in 60 % EtOH [0.2 mg/mL].

Figure 3.14 shows the UV-vis profiles of EthCitCD-TiO_2, prepared with 50 %, 6.25 % and 0.25 % EthCitCD solution, measured at a concentration of 0.025 mg/mL in 60 % ethanol. As shown in Chapter 2, EthCitCD was found to absorb at 320 nm with a secondary peak at 390 nm. When TiO_2 was prepared with 50 % EthCitCD, λ_{max} of 265 nm was achieved, followed by a shoulder at 310 nm which tails into the visible region. At 6.25 % inclusion of EthCitCD, λ_{max} is red-shifted to 330 nm, and has a broad absorption over the visible region. When prepared with 0.25 % EthCitCD, a low intensity absorption was evident at 370 nm followed by a broad peak across the entire visible region.

As was the case for EthCitCD-TiO_2, the effect of particle size should be taken into consideration. EthCitCD-TiO_2 followed the same trend in particle size as pure TiO_2 for the various percentage inclusions which was: 50 % < 6.25 % < 0.25 %, therefore the

red-shift seen in the spectra may once again be attributed to increase in particle size. However, there is a clear increase in UV attenuation for EthCitCD-TiO_2 (50 %) and EthCitCD-TiO_2 (6.25 %) compared to their equivalent pure TiO_2 and given these are the two reactions more heavily doped with EthCitCD it is in line with what was expected. Owed to the differences in the UV-vis spectra of pure TiO_2 and EthCitCD-doped TiO_2, it is unlikely that particle size alone is responsible for the improvement in UV attenuation and suggests the incorporation of these carbon dots may be responsible.

Overall, an inclusion of 6.25 % EthCitCD appears to have the most promising UV-vis profile from a sun-care perspective, with an intense absorption at 330 nm but also broad absorption over UVB, UVA and into the visible region.

3.3.3. UreCitCD-TiO_2

3.3.3.1. FT-IR Analysis

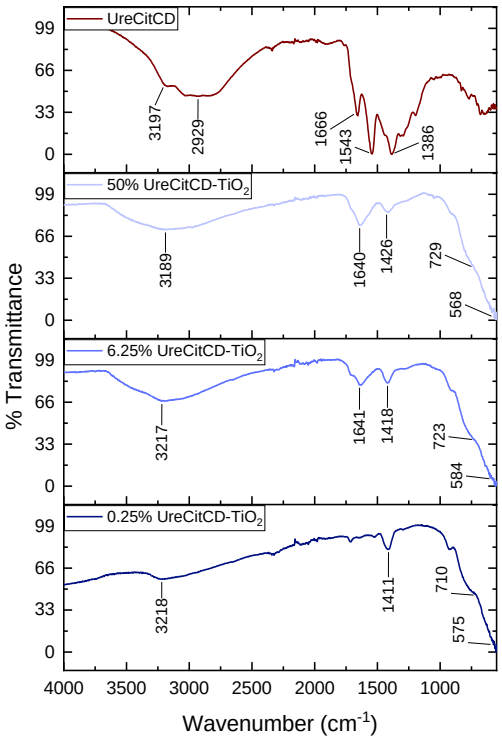

Figure 3.15: FT-IR spectra of UreCitCD and UreCitCD-TiO_2 at 50 %, 6.25 % and 0.25 % inclusions.

Table 3.6: FT-IR assignments for UreCitCD doped TiO_2 at 50 %, 6.25 % and 0.25 % loading.

Material	Assignment	Wavenumber (cm^{-1})
UreCitCD	O-H, N-H stretch	3638 – 2412
	C-H stretch	2929
	C=O stretch	1666
	C=C stretch, N-H bend	1626 – 1504
	C-H bend, O-H bend	1475–1334
	C-O stretch	1288
	C-N stretch	1189
50 % UreCitCD-TiO2	O-H, N-H stretch	3682–2433
	C=O stretch, C=C stretch, N-H bend	1788–1527
	C-H bend, O-H bend	1491–1339
	Ti-O-Ti stretch	891–550
	Ti-O	568
6.25 % UreCitCD-TiO_2	O-H, N-H stretch	3657–2491
	C=O stretch, C=C stretch, N-H bend	1776–1520
	C-H, O-H bend	1485–1357
	Ti-O-Ti stretch	881–550
	Ti-O stretch	584
0.25 % UreCitCD-TiO_2	O-H stretch	3410–2390
	C=O stretch, C=C stretch, N-H bend	1751–1524
	C-H bend, O-H bend	1473–1352
	Ti-O-Ti stretch	884–550
	Ti-O stretch	580

FT-IR analysis of neat UreCitCD and UreCitCD-TiO_2, with 50 %, 6.25 % and 0.25 %, was carried out and normalised between 0 and 100 to counteract the effect of different sample sizes. For comparison, UreCitCD was analysed (fully characterised in Chapter 2). It showed evidence of hydroxyl, carboxyl, and amino functionality (3638 - 2412 cm^{-1}, 1626–1504 cm^{-1} and 1475–1334 cm^{-1}, respectively). The absorption peaks of UreCitCD-TiO_2 compounds show some parallels.

The O-H and N-H stretch is signified by a broad peak in the 3600–2400 cm^{-1} region, for all three composites. Similarly, C=O stretch, C=C stretch and N-H bend can be found in varying intensities between 1780–1520 cm^{-1} for all composites, demonstrating hydroxyl, carboxyl, and amino functionality, which is supported further by the bands in the 1500–1330 cm^{-1} region corresponding to C-H and O-H bends. In each FT-IR spectrum, absorption bands between 880 and 550 cm^{-1} signify the Ti-O-Ti stretch and Ti-O stretch, indicating polycrystalline TiO_2. The C=O stretch centred at 1666 cm^{-1} in UreCitCD is shifted to 1640 cm^{-1} and 1641 cm^{-1} in UreCitCD-TiO_2 (50 %) and UreCitCD-TiO_2 (6.25 %), respectively, which might suggest they are interacting with the metal oxide. The intensity of the bands that indicate the presence of carbon dot

functional groups in the spectra of Figure 3.15, are noticeably reduced as the content of UreCitCD in the reaction is reduced, insinuating they may be correlated.

EDX confirms the presence of Ti, O, N in all three materials, which would indicate the incorporation of UreCitCD, though it only identifies carbon in UreCitCD-TiO_2 (6.25 %) (Appendix 3.8, Appendix 3.9, Appendix 3.10). Contrary to this, FT-IR does indicate the presence of C in UreCitCD-TiO_2 (50 %). The FT-IR spectra considers a larger sample size, while EDX measurement is focussed on a small section of a sample. Therefore, the lack of carbon shown by EDX may be due to the sample area selected for those measurements, while FT-IR may be more representative of the bulk material. EDX could be repeated to confirm this, however as it is used in conjunction with FT-IR, it was not deemed necessary.

3.3.3.2. Crystallinity and morphology

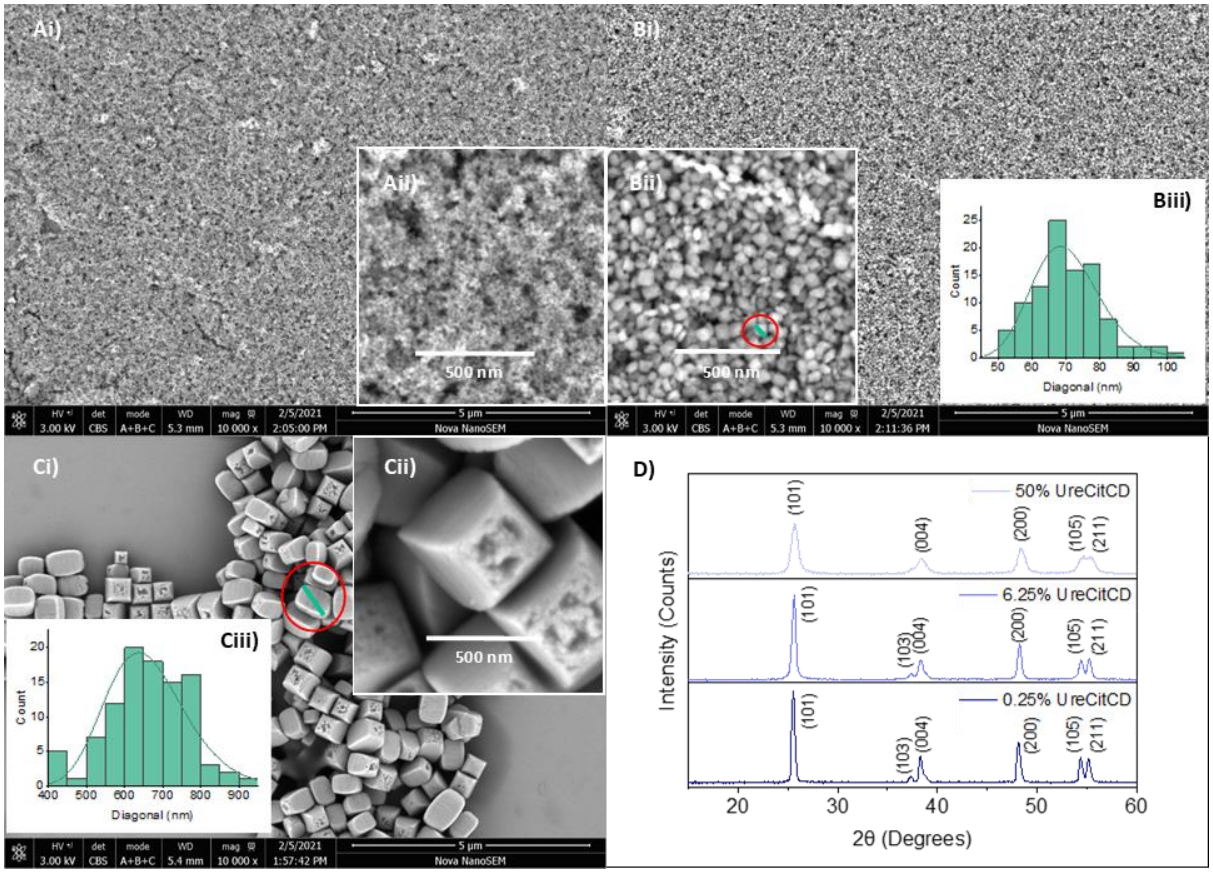

Figure 3.16: SEM images and XRD patterns of UreCitCD-TiO_2, with varying amounts of UreCitCD solution. Ai-ii) 50 % UreCitCD, Bi-ii) 6.25 % UreCitCD and Ci-ii) 0.25 % UreCitCD and D) XRD patterns of UreCitCD -TiO_2 (50 %, 6.25 % and 0.25 % UreCitCD).

The SEM images shown in Figure 3.16 showcase the particle size and morphology of TiO_2 prepared with 50 %, 6.25 % and 0.2 % UreCitCD (A-C respectively). The particle size increases as the percentage of carbon dots in the reaction decrease, which follows the same trend as seen for TiO_2 when water content was varied. However, the particle size of TiO_2 with 50 % UreCitCD is much smaller than pure TiO_2 (50 % water), at 15 nm on average with a range of 11.5 nm – 22.4 nm in diameter[5], which is similar to what was seen for TiO_2 (50 % EthCitCD). At high concentrations of carbon dots, it is possible that carbon is inhibiting the grain growth of TiO_2 (189) or increasing the number of nucleation sites, leading to smaller particles.

With 6.25 % UreCitCD, the particle size increases (70.5 nm on average) but much like for TiO_2 (6.25 % EthCitCD) they are more heterogeneous in structure, with varying cuboidal shapes. The formation of heterogeneous nucleation sites, as a result of carbon dots, is one explanation for the non-uniformity in morphology.

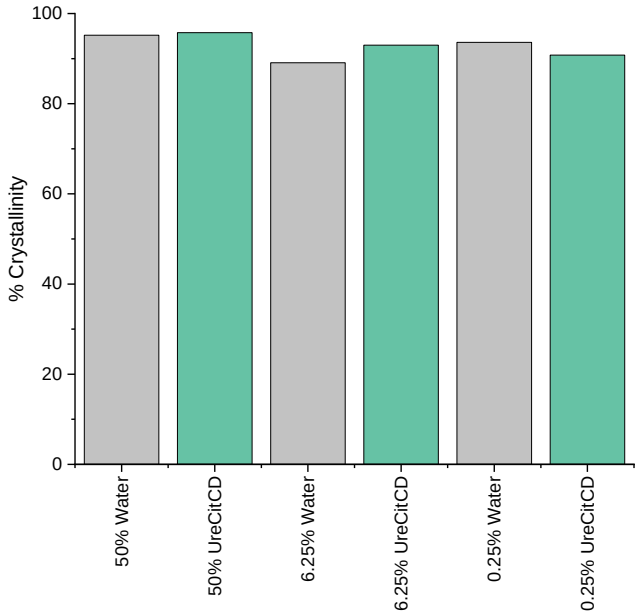

Figure 3.17: Percentage crystallinity of pure TiO_2 vs UreCitCD-TiO_2

With 0.25 % UreCitCD, uniform, nano-cuboid structures are produced (661.7 nm). At this low percentage inclusion, the 1-butyl-3-methylimidazolium tetrafluoroborate may

[5] Particle size was presented as an approximate range and average, as the particles were not resolved enough in the image to measure accurately.

be primarily governing the morphology rather than carbon dots, which might explain the similarities in the doped and pure TiO_2 at this percentage.

The XRD patterns shown in Figure 3.16 confirm the formation of anatase in all three reactions, and from Figure 3.17 the materials appear to be highly crystalline. At 50 % UreCitCD, diffraction peaks were seen at angles (2θ): 25.7°, 38.4°, 48.3°, 54.6°, 55.4° which correspond to (101), (004), (200), (105), (211). When 6.25 % UreCitCD was included, diffraction peaks were found at angles (2θ): 25.6°, 37.3°, 38.3°, 48.3°, 54.4°, 55.2° which correspond to (101), (103), (004), (200), (105), (211). At 0.25 % UreCitCD, diffraction peaks were seen at the following angles (2θ): 25.5°, 37.3°, 38.3°, 48.1°, 54.3°, 55.1° which correspond to (101), (103), (004), (200), (105), (211). Notably, diffraction peak (103) is undistinguishable due to peak broadening of (004) in 50 % UreCitCD-TiO_2, as is (112) diffraction peak in all three materials.

The crystallite sizes were determined using the Scherrer equation (Equation 3.5), for plane (101) and are shown in Table 3.7. The percentage of UreCitCD in the reaction was seen to reduce the crystallite size which was calculated to be 9.3 nm for 50 %, 17.0 nm for 6.25 % and 20.7 nm for 0.25 %. Overall, the crystallite size increased as the percentage of UreCitCD in the reaction decreased.

Table 3.7: Crystallite size of UreCitCD-TiO_2 for plane (101) at 50 %, 6.25 % and 0.25 % inclusion

	UreCitCD content		
	50 %	**6.25 %**	**0.25 %**
Crystallite size D (nm)	9.3	17.0	20.7

There were some shifts in the positions of the diffraction peaks in all three samples. For 50 % UreCitCD-TiO_2, at all diffraction peaks but (200), a shift greater than 0.1° from pure TiO_2 was evident. For 6.25 % UreCitCD-TiO_2 all peaks showed a shift > 0.1° in relation to pure TiO_2. As there was variation in the shifts, it suggested instrumentation error was not responsible. For 0.25 % UreCitCD-TiO_2 just the (004) diffraction peak displayed a deviation > 0.1° from pure TiO_2. To understand whether this was due to lattice strain, d-spacings were calculated (Appendix 3.11). Prominent XRD peaks and d-spacings are displayed in Table 3.8.

Table 3.8: Prominent XRD diffraction peaks of UreCitCD-TiO_2 with d-spacing

	[50 % UreCitCD]		[6.25 % UreCitCD]		[0.25 % UreCitCD]	
hkl	**2θ°**	**d_{hkl} (Å)**	**2θ°**	**d_{hkl} (Å)**	**2θ°**	**d_{hkl} (Å)**
101	25.718	3.415	25.637	3.426	25.516	3.442
004	38.399	2.311	38.278	2.318	38.298	2.317
200	48.273	1.859	48.278	1.858	48.091	1.865

	[50 % water]		[6.25 % water]		[0.25 % water]	
hkl	**2θ°**	**d_{hkl} (Å)**	**2θ°**	**d_{hkl} (Å)**	**2θ°**	**d_{hkl} (Å)**
101	25.576	3.434	25.516	3.442	25.475	3.447
004	38.177	2.324	38.096	2.329	38.156	2.325
200	48.293	1.858	48.152	1.863	48.111	1.864

D-spacings for (101) and (004) shift, mainly at 50 % and 6.25 %, but less so at 0.25 % which is consistent with decreasing loading of carbon dots. The d-spacings for (200) are well aligned with pure TiO_2 which suggests any lattice strain because of carbon dots does not impact this plane.

The addition of carbon dots has led to a loss of uniformity in morphology at 6.25 % loading, and a significant decrease in particle size at 50 % loading. The effect at 0.25 % loading was minimal, though the aspect ratio of the particles decreased. The d-spacings were found to vary mainly at 50 % and 6.25 % loadings, which, in conjunction with FT-IR and EDX analysis, would indicate successful doping of TiO_2.

3.3.3.3. Attenuation of UV and visible light

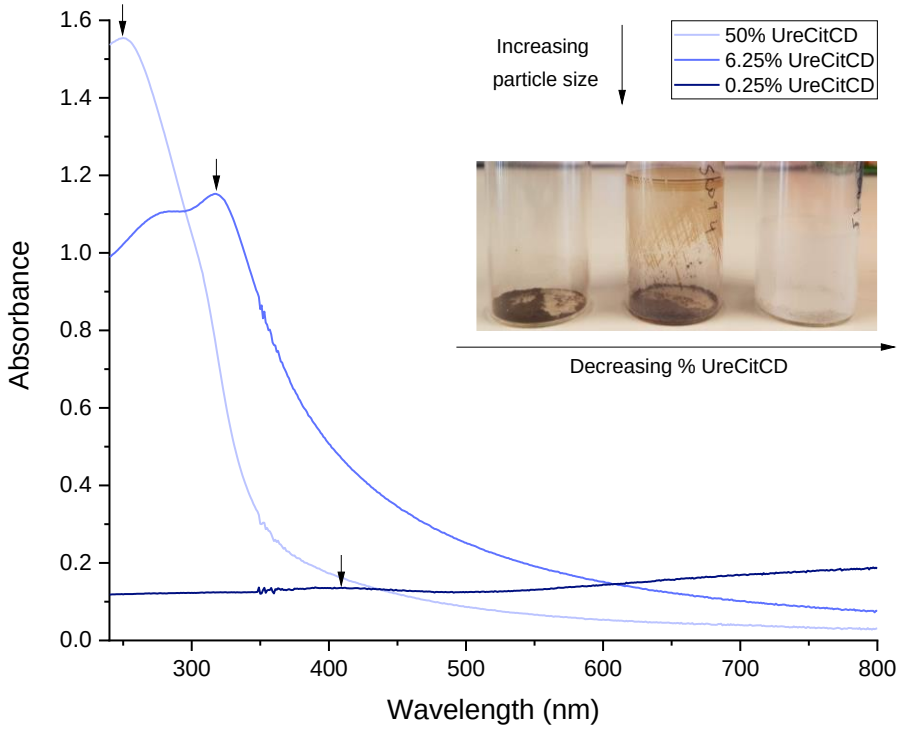

Figure 3.18: UV-vis spectra of UreCitCD-TiO_2 suspended in 60 % EtOH [0.025 mg/mL], grown with 50 %, 6.25 % and 0.25 % UreCitCD. Inset image shows each dried powder sample.

Figure 3.18 shows the UV-vis profiles of UreCitCD-TiO_2, prepared with 50 %, 6.25 % and 0.25 % UreCitCD solution (as characterised in Chapter 2), measured at a concentration of 0.025 mg/mL in 60 % ethanol. UreCitCD absorbs at 330 nm with a shoulder that extends into the visible region. At the highest percentage inclusion of UreCitCD, an intense absorption at 247 nm is seen, with a shoulder at 310 nm. For 6.25 % UreCitCD-TiO_2 an absorption peak at 310 nm is seen, with a shoulder at 290 nm. When the lowest percentage of UreCitCD was added, the UV-vis resembles its equivalent pure TiO_2 sample, although there is an additional broad, low intensity peak at 410 nm.

Through SEM images and particle size analysis, the changing size of the particles is a key difference between samples and one that should be taken into consideration when looking at the optical properties. UreCitCD-TiO_2 followed the same trend in particle size as pure TiO_2 which was: 50 % < 6.25 % < 0.25 %. From this, the red-shift in UV spectra may be attributed to increasing particle size. That being said, the more heavily doped materials (50 % UreCitCD-TiO_2 and 6.25 % UreCitCD-TiO_2) show a

distinct increase in UV attenuation that is not evident in pure TiO_2. This would suggest that particle size alone is not responsible for the improvement in UV attenuation and suggests the integration of carbon dots into the system may contribute.

By comparing the UV spectra of pure TiO_2 with TiO_2 grown alongside UreCitCD, the UV absorption profile has notably improved, particularly for 6.25 % UreCitCD-TiO_2. Therefore, the addition of carbon dots into the system must be contributing to this. It is possible that the presence of the amino, hydroxyl and carboxyl functional groups within the system (as indicated by FT-IR) are improving the UV absorption through lower energy n-π* transitions. Alternatively, the functionalised titanium dioxide might be better dispersed in water than pure TiO_2, and this could be contributing to the improved UV-vis profile. Of the three, an inclusion of 6.25 % UreCitCD has the most favourable UV-vis profile for a UV/HEVL filter as it shows broad-spectrum UV-vis attenuation as well as a more intense peak in UVA region.

3.3.4. VanCitCD-TiO_2

3.3.4.1. FT-IR analysis

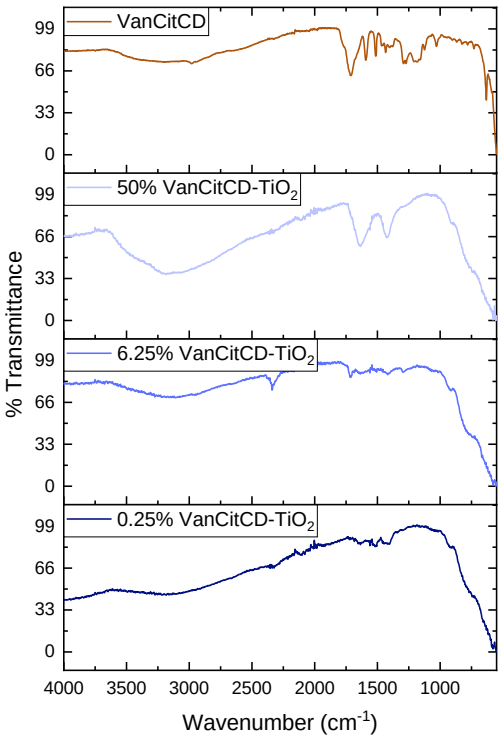

Figure 3.19: FT-IR spectra of VanCitCD and VanCitCD-TiO2 at 50 %, 6.25 % and 0.25 % inclusions.

Table 3.9: FT-IR assignments for VanCitCD doped TiO_2 at 50 %, 6.25 % and 0.25 % loading.

Material	Assignment	Wavenumber (cm^{-1})
VanCitCD	O-H, C-H stretch	3635 - 2409
	C=O stretch	1713
	C=C stretch (cyclic alkene)	1594
	N-O stretch	1513
	C-H bend, O-H bend	1437–1364
	C-O stretch, C-N stretch	1339–1246
	C-O stretch	1038
50 % VanCitCD-TiO2	O-H	3632–2364
	C=O stretch, C=C stretch	1732–1531
	C-H bend, O-H bend, C-O stretch	1506–1213
	Ti-O-Ti stretch	873–550
	Ti-O	578
6.25 % VanCitCD-TiO_2	O-H	3649–2406
	C=O stretch, C=C stretch	1767–1520
	C-H bend, O-H bend	1473–1355
	C-O stretch	1290
	Ti-O-Ti stretch	875–550
	Ti-O	579
0.25 % VanCitCD-TiO_2	O-H	3588–2443
	C=O stretch, C=C stretch	1729–1513
	C-H bend, O-H bend	1457–1356
	Ti-O-Ti stretch	882–550
	Ti-O	588

The FT-IR spectra of VanCitCD-TiO_2 with 50 %, 6.25 % and 0.25 % inclusion are shown in Figure 3.19 alongside the spectrum of VanCitCD on its own, which has been characterised in Chapter 2. In VanCitCD, O-H stretch (3173 cm^{-1}), C=O stretch (1713 cm^{-1}), C=C stretch (1594 cm^{-1}), C-H bend and O-H bend (1437–1364 cm^{-1}), C-O stretch and C-N stretch (1339–1246 cm^{-1}) and C-O stretch (1038 cm^{-1}) indicate carboxyl and hydroxyl functionalised carbon dots.

Having undergone hydrothermal synthesis alongside VanCitCD, with various loadings, the resultant titanium dioxide composites exhibited promising FT-IR spectra that insinuated they had obtained some functionality during the reaction. At each loading, (50 %, 6.25 % and 0.25 %) a broad peak in the 3600–2500 cm^{-1} region was present, which suggest the presence of O-H and C-H stretching bands. Additionally, the C=O and C=C stretching band located between 1780 cm^{-1} and 1530 cm^{-1} was observed, followed by C-H bend, O-H bend, and C-O stretch in the 1500–1200 cm^{-1} region. These bands were apparent in all three materials and were suggestive of carboxyl and hydroxyl functional groups. Further to this, the broad absorption band between

880 cm^{-1} and 550 cm^{-1} can be assigned to the Ti-O stretching modes (184, 185) and Ti-O-Ti bridging stretching vibration (716 cm^{-1}) (183), as is consistent with the literature. The standard spectra of TiO_2 reports the vibration of Ti-O at 463.88 cm^{-1} (183), however, due to the constraints of this FT-IR instrument, 550 cm^{-1} is the limit. The intensity of the hydroxyl and carboxyl absorption bands is shown to decrease in correlation with the loading of the carbon dots.

EDX confirms the presence of Ti, O and C in all three materials (Appendix 3.12 to Appendix 3.14), and N (possibly remaining from the 1-butyl-3-methylimidazolium tetrafluoroborate). This, together with the FT-IR, suggests TiO_2 has obtained some functionality after growth with carbon dots. Which, in turn, may alter the morphology, crystallinity and subsequent optical properties, which will be investigated in the sections to come.

3.3.4.2. Crystallinity and morphology

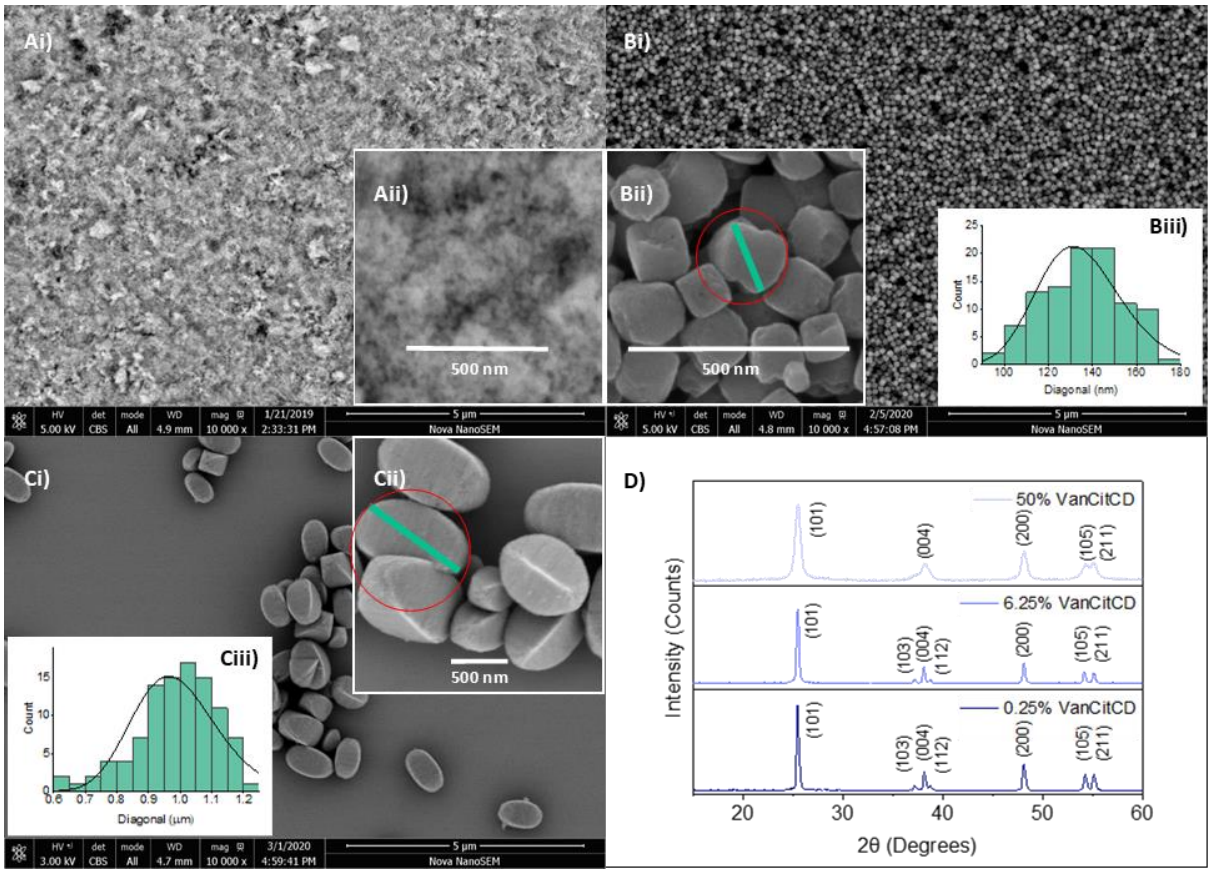

Figure 3.20: SEM images and XRD patterns of VanCitCD-TiO_2, with varying amounts of VanCitCD solution. Ai-ii) 50 % VanCitCD, Bi-ii) 6.25 % VanCitCD and Ci-ii) 0.25 % VanCitCD and D) XRD patterns of VanCitCD-TiO_2 (50 %, 6.25 % and 0.25 % VanCitCD).

Figure 3.20A-C displays the SEM images of VanCitCD-TiO_2 with 50 %, 6.25 % and 0.25 % incorporation of VanCitCD carbon dots, respectively. The particle size increases as the percentage of VanCitCD in the reaction decreases. This is in alignment with what has been observed for reactions of EthCitCD-TiO_2 and UreCitCD-TiO_2. The changes seen in the particle size and morphology must partly be due to the water content in the carbon dots, though the VanCitCD-TiO_2 nanoparticles exhibit some differences in morphology and crystallinity, which suggest the carbon dots may have influenced this as well. For example, the particle size for 50 % VanCitCD-TiO_2 averaged at 21.7 nm (ranging from 14 – 26 nm), while for TiO_2 (50 % water) it ranged from 18 – 40 nm. At high concentrations of carbon dots, carbon may be impeding the grain growth of TiO_2 leading to smaller particles (189). The influence of carbon dots may have provided ample nucleation sites for TiO_2, working in synergy with water, which lead to nanoparticles with even smaller diameters. The size distribution in this case cannot be commented on, as the images were not resolved enough to accurately measure and obtain a reliable size distribution.

Figure 3.20Bii clearly shows cube-shaped particles with an average of 135.2 nm. Though they are not as uniform as pure TiO_2, of the three sets of carbon dots they have produced the most homogeneous sample at 6.25 % inclusion. Without knowing the particle size of VanCitCD from TEM, it is difficult to understand their role in this case. It appears $BMIMBF_4$ has stabilised (100) and (001) facets as it had done in pure TiO_2 which implies that VanCitCD was not inhibiting it. This could be because the carbon dots are larger than they were for EthCitCD and UreCitCD. Alternatively, VanCitCD could be selectively stabilising (100) and (001) facets in synergy with $BMIMBF_4$.

At 0.25 % loading with VanCitCD, the morphology is ellipsoidal. The particles are much larger than for pure TiO_2 with a size range of 0.6 to 1.2 μm and may have formed through stabilisation of (101) facets. At low carbon dot content, control of morphology by $BMIMBF_4$ would be expected, forming large cuboid morphology as seen for reactions with 0.25 % EthCitCD and UreCitCD. This change in shape may therefore be due to stabilisation of (101) facets because of the presence of VanCitCD.

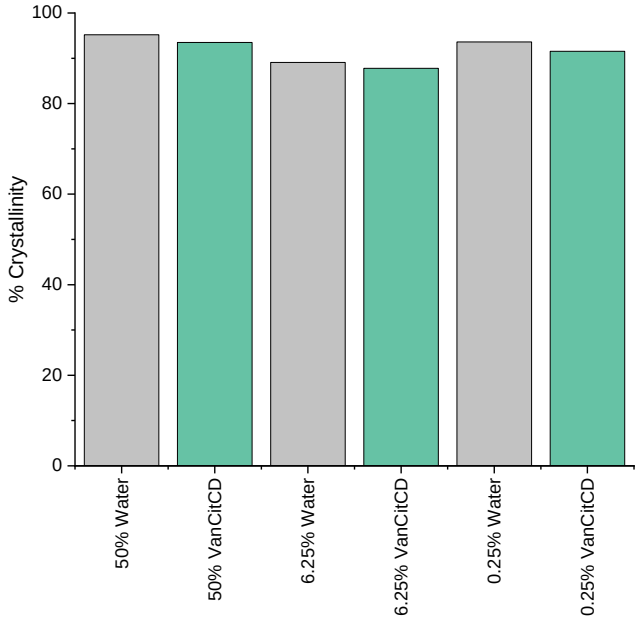

Figure 3.21: Percentage crystallinity of VanCitCD-TiO_2 compared to pure TiO_2

Figure 3.20D shows the XRD patterns of VanCitCD-TiO_2 (with 50 %, 6.25 % and 0.25 % VanCitCD) which are all in line with what is reported in the literature for anatase. The signals are sharp in all patterns which indicates good crystallinity in the materials, as supported in Figure 3.21 which compares the percentage crystallinity to that of pure TiO_2. For 50 % VanCitCD, diffraction peaks were seen at the following angles (2θ): 25.5°, 38.2°, 48.1°, 54.3°, 55.1° which correspond to (101), (004), (200), (105), (211). For 6.25 % VanCitCD, diffraction peaks we found at angles (2θ): 25.5°, 37.1°, 38.1°, 38.8°, 48.1°, 54.1°, 55.1° which correspond to (101), (103), (004), (112), (200), (105), (211). For 0.25 % VanCitCD, diffraction peaks were seen at the following angles (2θ): 25.4°, 37.2°, 38.1°, 38.7°, 48.1°, 54.3°, 55.1°, which correspond to (101), (103), (004), (112), (200), (105) and (211).

Table 3.10: Crystallite size of VanCitCD-TiO_2 for plane (101) at 50 %, 6.25 % and 0.25 % inclusion.

	VanCitCD content		
	50 %	**6.25 %**	**0.25 %**
Crystallite size D (nm)	11.4	27.3	27.1

The crystallite size was calculated using the Scherrer equation (Equation 3.5), for plane (101) for each material (see Table 3.10). It is smallest at 11.4 nm (50 %), while for 6.25 % and 0.25 % inclusions it reaches 27.3 nm and 27.1 nm, respectively.

In VanCitCD-TiO_2 (50 %), diffractions peaks (200) and (211) exhibited a significant shift, in comparison to pure TiO_2 and peak broadening was particularly evident which was likely due to the small crystallite size (11.4 nm). In contrast, 6.25 % and 0.25 % loading of VanCitCD were within 0.1° deviation of pure TiO_2, and so not considered a significant shift. The d-spacings were calculated and are listed in full, in Appendix 3.15, while the data for selected prominent peaks is shown in Table 3.11. There is very little variation in the d-spacings of (101), (004) and (200) for VanCitCD-TiO_2 and pure TiO_2, which tells us the lattice is unlikely to be strained by dopants of VanCitCD.

Table 3.11: Prominent XRD diffraction peaks of VanCitCD-TiO_2 with d-spacing

	[50 % VanCitCD]		**[6.25 % VanCitCD]**		**[0.25 % VanCitCD]**	
hkl	**2θ°**	**d_{hkl} (Å)**	**2θ°**	**d_{hkl} (Å)**	**2θ°**	**d_{hkl} (Å)**
101	25.536	3.439	25.455	3.450	25.435	3.452
004	38.197	2.323	38.116	2.328	38.116	2.328
200	48.071	1.866	48.091	1.865	48.091	1.865

	[50 % water]		**[6.25 % water]**		**[0.25 % water]**	
hkl	**2θ°**	**d_{hkl} (Å)**	**2θ°**	**d_{hkl} (Å)**	**2θ°**	**d_{hkl} (Å)**
101	25.576	3.434	25.516	3.442	25.475	3.447
004	38.177	2.324	38.096	2.329	38.156	2.325
200	48.293	1.858	48.152	1.863	48.111	1.864

Overall, the impact of VanCitCD on the hydrothermal preparation of titanium dioxide has been shown. FT-IR confirms the presence of carboxyl and hydroxyl functional groups, in all materials. This is supported by EDX which shows C, O and Ti are present. At low loading levels, the morphology was well-controlled to form uniform “rugby ball” shaped particles while at higher loadings, homogeneous, nanoparticles (14 – 26 nm) formed. The change in morphology is understood to be due to a combination of water and carbon dots. Although the crystallinity and d-spacings were well maintained in the composites, FT-IR and EDX do suggest the presence of dopants, though it is possible that they are interacting electrostatically and therefore avoid causing lattice strain, thus maintaining the d-spacings. The next steps require consideration of the optical properties.

3.3.4.3. Attenuation of UV and visible light

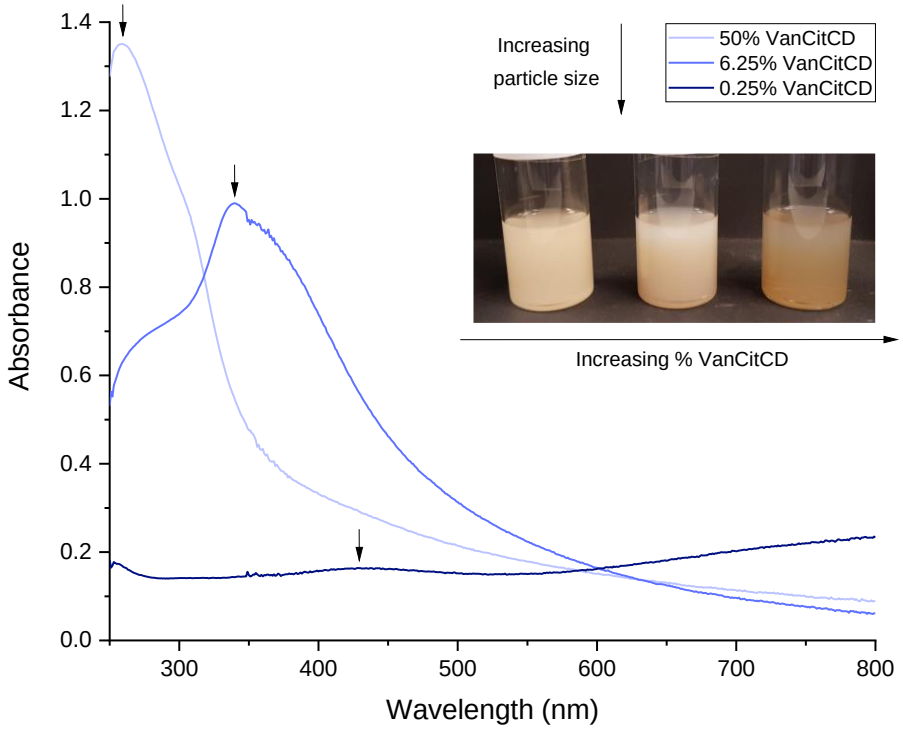

Figure 3.22: UV-vis spectra of VanCitCD-TiO_2 suspended in 60 % EtOH [0.025 mg/mL], grown with 50 %, 6.25 % and 0.25 % VanCitCD. Inset image shows suspensions of each sample in 60 % EtOH [0.2 mg/mL].

Figure 3.22 shows the UV-vis profiles of VanCitCD-TiO_2, prepared with 50 %, 6.25 % and 0.25 % VanCitCD solution (as characterised in Chapter 2), measured at a concentration of 0.025 mg/mL in 60 % ethanol. VanCitCD was found to absorb at 277 nm with a secondary peak at 310 nm. With 50 % VanCitCD inclusion, an intense absorption at 258 nm is seen, with a shoulder at 310 nm, which corresponds closely to VanCitCD, followed by a tail into the visible region which replicates what is seen for TiO_2 with 50 % water. With 6.25 % VanCitCD, there is a clear red-shift in the λ_{max} to 340 nm and a reduction in intensity. This may be due to the combination of particle size effect and the presence of carboxyl and hydroxyl groups from VanCitCD. The UV-vis spectrum for 0.25 % VanCitCD largely resembles pure TiO_2 (0.25 % water) which suggests the variation between ellipsoidal and cuboidal structure may not affect the optical properties drastically.

Overall, the incorporation of carbon dots into the reaction has altered the UV-vis profile significantly. The spectra do appear influenced by the change in particle size, however, through comparison with pure TiO_2 spectra, it was determined that an additional

source is influencing the UV-vis absorption. 6.25 % inclusion of VanCitCD showed the most promising UV-vis profile with broad-spectrum absorption, and an intense peak in the UVA region.

3.3.5. Suspension stability

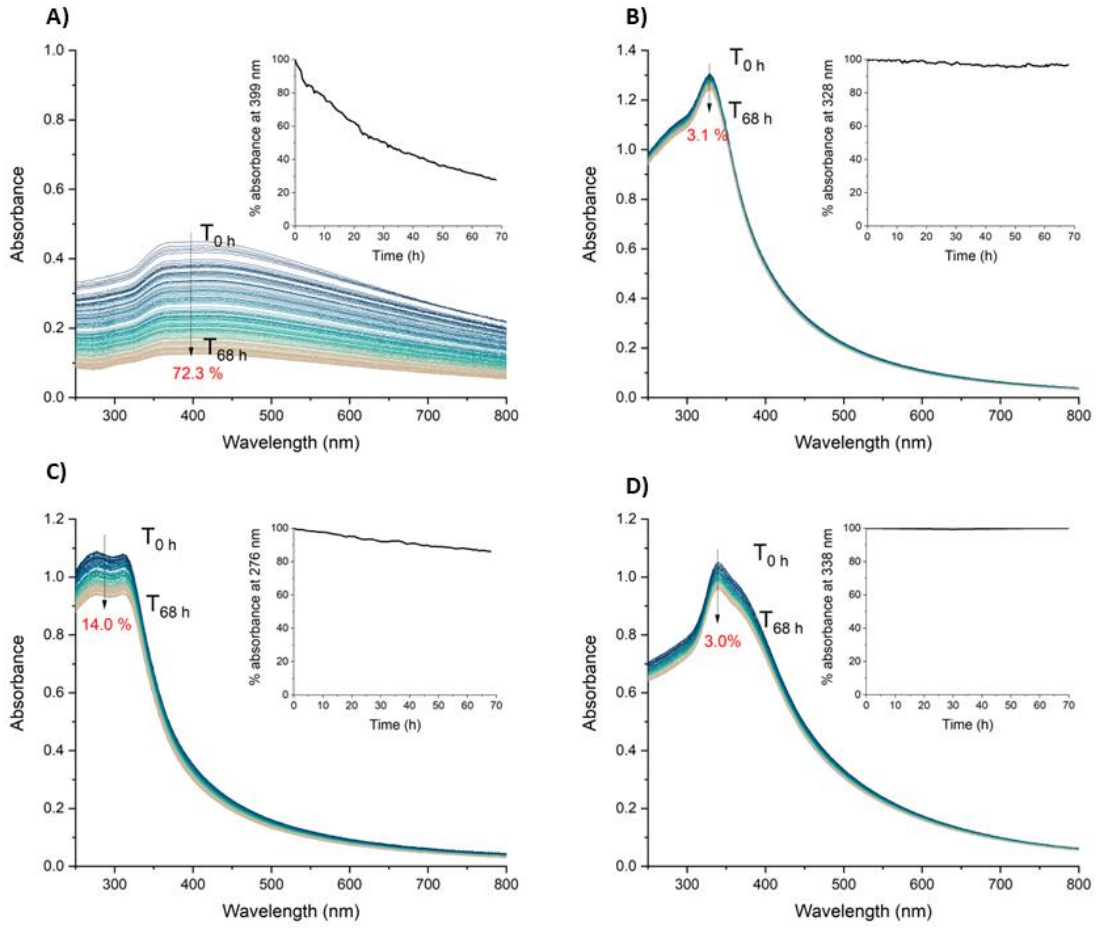

Figure 3.23: UV-vis spectra of: A) Pure TiO_2, B) EthCitCD-TiO_2, C) UreCitCD-TiO_2 and D) VanCitCD-TiO_2 measured every hour for 68 h. The percentage decrease in absorbance is shown in red and the inset graphs show the percentage absorbance at the λ_{max}, by time.

The stability of the CD-TiO_2 suspensions came into question when it was observed that the suspensions of EthCitCD-TiO_2 and VanCitCD-TiO_2 made with 6.25 % carbon dot solution, appeared to be exceptionally stable after 15 weeks of no agitation, when kept at room temperature. Appendix 3.16, Appendix 3.17 and Appendix 3.18 show images of pure TiO_2, EthCitCD-TiO_2 and VanCitCD-TiO_2, suspended in 60 % EtOH at a concentration of 0.2 mg/mL taken 15 weeks apart. Only the materials grown with 6.25 % carbon dot solution remained well suspended after this time, while the rest settled down, including the pure TiO_2 suspensions. Unfortunately, the equivalent

images were not collected for UreCitCD-TiO_2 as these materials were prepared after this study. Following these preliminary experiments, a quantitative way to express the stability was sought.

Since the beam of light in the UV-vis spectrophotometer is stationary, any sedimentation of material over time was likely to cause a change in the absorbance intensity and would therefore be indicated on the UV-vis spectra. Therefore, UV-vis scans over time could be used to investigate the stability of the suspensions. However, the sample could not be agitated once the experiment had started, which posed limitations. As the UV-vis spectrophotometer is a shared instrument, the duration of the experiment corresponded to the maximum out-of-hour usage of the instrument at any one time which was about 68 h (utilising the weekend).

A UV-vis scan (250 nm – 800 nm) was taken every hour for 68 h to monitor any changes in the suspension of the most promising materials: EthCitCD-TiO_2, UreCitCD-TiO_2 and VanCitCD-TiO_2 (6.25 % inclusion), and pure TiO_2 was analysed for comparison. The results are shown in Figure 3.23. The percentage decrease at the λ_{max} was determined for each sample. As is fitting with the observations in Appendix 3.16, Appendix 3.17 and Appendix 3.18, the suspension of pure TiO_2 showed a 72.3 % decrease in absorbance in 68 h. In comparison, EthCitCD-TiO_2, UreCitCD-TiO_2 and VanCitCD-TiO_2 decreased by 3.1 %, 14.0 % and 3.0 % respectively. This might suggest that the carbon dots have imparted functionality during the preparation of TiO_2 and, in conjunction with the particle size, improved the stability of the suspension.

It would be interesting to combine these materials into a Croda Inc. sunscreen formulations and investigate the whether the stability, as well as the UV-vis light attenuation, is improved. As the materials are the anatase polymorph, they are limited by regulations to make up a maximum of 5 % content. If the materials were deemed to have potential, they would also need to be externally assessed for cell toxicity. Due to the impact the Covid-19 pandemic had in Industry and resultant time constraints, it was not possible to study this within this project.

3.4. Conclusion

This chapter has investigated the incorporation of nanoscale organic additives, or more specifically EthCitCD, UreCitCD and VanCitCD carbon dot solutions, from

Chapter 2, into the preparation of titanium dioxide to study the impact on structural, morphological, and optical properties. Having overviewed the literature, this area was somewhat untapped as in the past, more focus has been on using organic dopants such as C and N to alter the properties of prepared titanium dioxide.

The incorporation of three different concentrations of carbon dots were investigated, written as a percentage of overall content these were 50 %, 6.25 % and 0.25 %. FT-IR analysis shows the presence of functional groups that correspond to the carbon dots used, which suggest they have been successfully incorporated into the material. This notion is strengthened by the presence of C, N as well as Ti and O in EDX analysis.

The crystallinity was maintained in all samples as determined by XRD analysis, though as the percentage of carbon dots increased, broadening of the peaks was visible but this may be simply a result of the decrease in particle size.

Each set of reactions followed the same trend for particle size as established by SEM. At the highest percentage content, the smallest particles were produced, and this increased as the percentage of carbon dots was reduced. This might be due to the carbon inhibiting the crystal growth of TiO_2.

The UV-vis attenuation of EthCitCD-TiO_2, UreCitCD-TiO_2 and VanCitCD-TiO_2 improved, and was optimal at 6.25 % inclusion. Each showed a strong UV absorption at 330 nm, 320 nm, and 340 nm respectively, with a broad absorption over the visible region. This was a significant improvement on the equivalent pure TiO_2, and the materials showed promise as a UV-visible light filters.

An assessment of the stability of the suspensions in 60 % ethanol showcased that, at 6.25 % inclusion of carbon dots, the stability of TiO_2 improved for all candidates. Over a period of 68 h, the absorbance of VanCitCD-TiO_2 and EthCitCD-TiO_2 decreased by just 3 %. These materials showed promise as possible additives to improve the stability of formulations like sunscreens, as well as enhance the UV-vis filtering properties.

3.5. Experimental

3.5.1. Characterisation techniques

Infrared (IR) spectra were obtained from solid phases using a Bruker Alpha Platinum ATR FTIR spectrometer with vibrational frequencies (cm^{-1}). The electronic absorption spectra were recorded using a Cary 100 UV-Vis scanning spectrophotometer. Spectrophotometric experiments to assess the suspension stability of the materials were carried out using a Cary 50 UV-Vis spectrophotometer controlled at 20 °C by a single cell Peltier accessory. Samples for scanning electron microscopic (SEM) analysis were dispersed in ethanol, a drop of suspension was cast onto a silicon wafer attached to an SEM stub using copper films. The samples were viewed with a FEI Nova 450 FEG-SEM operating at 3 kV using a CBS detector at various magnifications. X-Ray diffraction (XRD) of the materials were recorded on Bruker D2-Phaser diffractometer using Cu Kα radiation, with a step size of θ = 0.01013° and x-ray wavelength (λ = 0.152 nm). Bragg's law was used to calculate lattice spacings, and Gaussian fitting was used to measure the full width at half maximum (FWHM) of the diffraction peaks.

3.5.2. Materials

Fluorochem supplied 1-butyl-3-methylimidazolium tetrafluoroborate, titanium (IV) isopropoxide, Sigma-Aldrich supplied acetic acid (99–100 %) while Fischer Scientific provided propan-2-ol and nitric acid (70 %).

3.5.3. Sol-gel preparation of titanium dioxide

3.5.3.1. Pure TiO_2

2-propanol (3 mL) and water (50 mL) were stirred. The pH was lowered to pH 2.4 from approximately pH 5.8, with a drop of nitric acid. Titanium isopropoxide (1 mL) was added dropwise, forming a white precipitate on addition. The result was filtered by vacuum through a Buchner funnel and washed with both water (10 mL) and ethanol (10 mL). The white solid was collected and dried in an oven at 50 °C for 24 h. Yield: 0.3142 g.

3.5.3.2. TiO_2 prepared with EthCitCD

EthCitCD (1 mL) was added to a solution of 2-propanol (3 mL) and water (50 mL). With a drop of nitric acid, the pH was reduced to 2.2 and titanium isopropoxide (1 mL) was added dropwise into the reaction. The result was filtered by vacuum through a Buchner funnel and washed with both water (10 mL) and ethanol (10 mL). The pale-yellow solid was collected and dried in an oven at 50 °C for 24 h. Yield: 0.3458 g.

3.5.4. Solvothermal preparation of TiO_2 with organic additives

Each organic additive was included in three different percentages, relative to the volume of acetic acid, while all other factors remained the same. For direct comparison, the percentage of water was varied in the preparation of pure titanium dioxide.

3.5.4.1. Pure TiO_2

Acetic acid (10 mL), 1-butyl-3-methylimidazolium tetrafluoroborate (500 µL), water (10 mL) and titanium (IV) isopropoxide (500 µL) were stirred for 5 minutes and sonicated for 30 seconds. The reactants were sealed in an autoclave and heated in a hot oven, at 200 °C for 24 h. The solid product was decanted, washed with water, sonicated, and centrifuged several times. On the final time, it was washed with ethanol and then left to dry in open air. Yield: 0.0597 g.

This reaction was repeated with the following composition of reactants:

	6.25 % water	**0.25 % water**
Acetic acid	20 mL	20 mL
Water	1.25 mL	50 µL
1-butyl-3-methylimidazolium tetrafluoroborate	500 µL	500 µL
Titanium (IV) isopropoxide	500 µL	500 µL
Yield	**0.1363 g**	**0.0662 g**

3.5.4.2. TiO_2 with EthCitCD

Acetic acid (10 mL), 1-butyl-3-methylimidazolium tetrafluoroborate (500 µL), EthCitCD (10 mL) and titanium (IV) isopropoxide (500 µL) were stirred for 5 minutes and sonicated for 30 seconds. The reactants were sealed in an autoclave and heated in a hot oven, at 200 °C for 24 h. The solid product was decanted, washed with water,

sonicated, and centrifuged several times. On the final time, it was washed with ethanol and then left to dry in open air.

This reaction was repeated with the following composition of reactants:

	6.25 % EthCitCD	**0.25 % EthCitCD**
Acetic acid	20 mL	20 mL
Water	1.25 mL	50 µL
1-butyl-3-methylimidazolium tetrafluoroborate	500 µL	500 µL
Titanium (IV) isopropoxide	500 µL	500 µL
Yield	**0.1157 g**	**0.0345 g**

3.5.4.3. TiO_2 with UreCitCD

Acetic acid (10 mL), 1-butyl-3-methylimidazolium tetrafluoroborate (500 µL), UreCitCD (10 mL) and titanium (IV) isopropoxide (500 µL) were stirred for 5 minutes and sonicated for 30 seconds. The reactants were sealed in an autoclave and heated in a hot oven, at 200 °C for 24 h. The solid product was decanted, washed with water, sonicated, and centrifuged several times. On the final time, it was washed with ethanol and then left to dry in open air. Yield: 0.1293 g

This reaction was repeated with the following composition of reactants:

	6.25 % UreCitCD	**0.25 % UreCitCD**
Acetic acid	20 mL	20 mL
Water	1.25 mL	50 µL
1-butyl-3-methylimidazolium tetrafluoroborate	500 µL	500 µL
Titanium (IV) isopropoxide	500 µL	500 µL
Yield	**0.1242 g**	**0.1154g**

3.5.4.4. TiO_2 with VanCitCD

Acetic acid (10 mL), 1-butyl-3-methylimidazolium tetrafluoroborate (500 µL), VanCitCD (10 mL) and titanium (IV) isopropoxide (500 µL) were stirred for 5 minutes and sonicated for 30 seconds. The reactants were sealed in an autoclave and heated in a hot oven, at 200 °C for 24 h. The solid product was decanted, washed with water, sonicated, and centrifuged several times. On the final time, it was washed with ethanol and then left to dry in open air.

This reaction was repeated with the following composition of reactants:

	6.25 % VanCitCD	0.25 % VanCitCD
Acetic acid	20 mL	20 mL
Water	1.25 mL	50 µL
1-butyl-3-methylimidazolium tetrafluoroborate	500 µL	500 µL
Titanium (IV) isopropoxide	500 µL	500 µL
Yield	**0.1137 g**	**0.1365 g**

3.6. Appendices

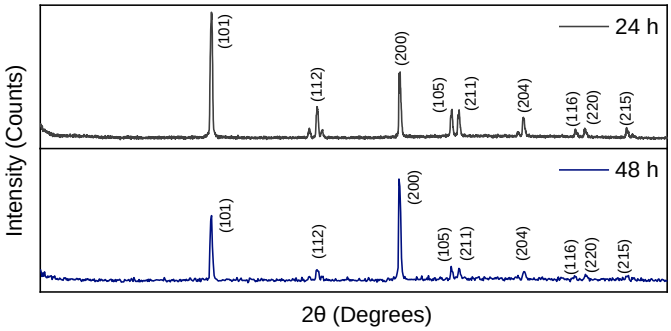

Appendix 3.1: XRD patterns of pure TiO_2 prepared by hydrothermal synthesis at two durations: 24 h and 48 h

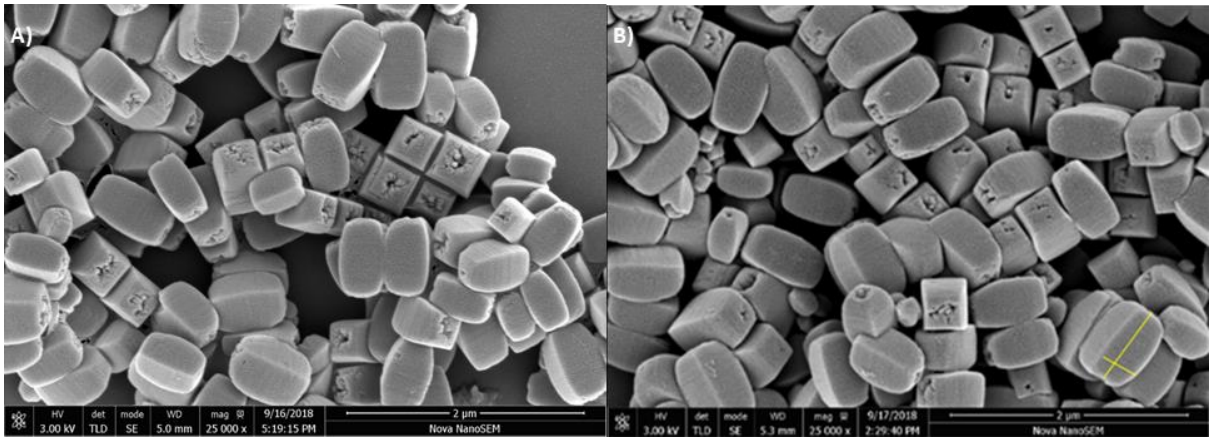

Appendix 3.2: SEM images of pure TiO_2 prepared by hydrothermal synthesis at two durations: A) 24 h and B) 48 h

	[50 % water]		[6.25 % water]		[0.25 % water]	
hkl	**2θ°**	**d_{hkl} (Å)**	**2θ°**	**d_{hkl} (Å)**	**2θ°**	**d_{hkl} (Å)**
101	25.576	3.434	25.516	3.442	25.475	3.447
103	37.228	2.381	37.207	2.382	37.248	2.380
004	38.177	2.324	38.096	2.329	38.156	2.325
112	38.843	2.286	38.762	2.290	38.803	2.288
200	48.293	1.858	48.152	1.863	48.111	1.864
105	54.169	1.669	54.149	1.670	54.270	1.666
211	55.239	1.639	55.118	1.643	55.179	1.641

Appendix 3.3: Calculated d-spacings using $d_{hkl}=\lambda/(2\sin\theta)$, for TiO_2 with 50 %, 6.25 % and 0.25 % water.

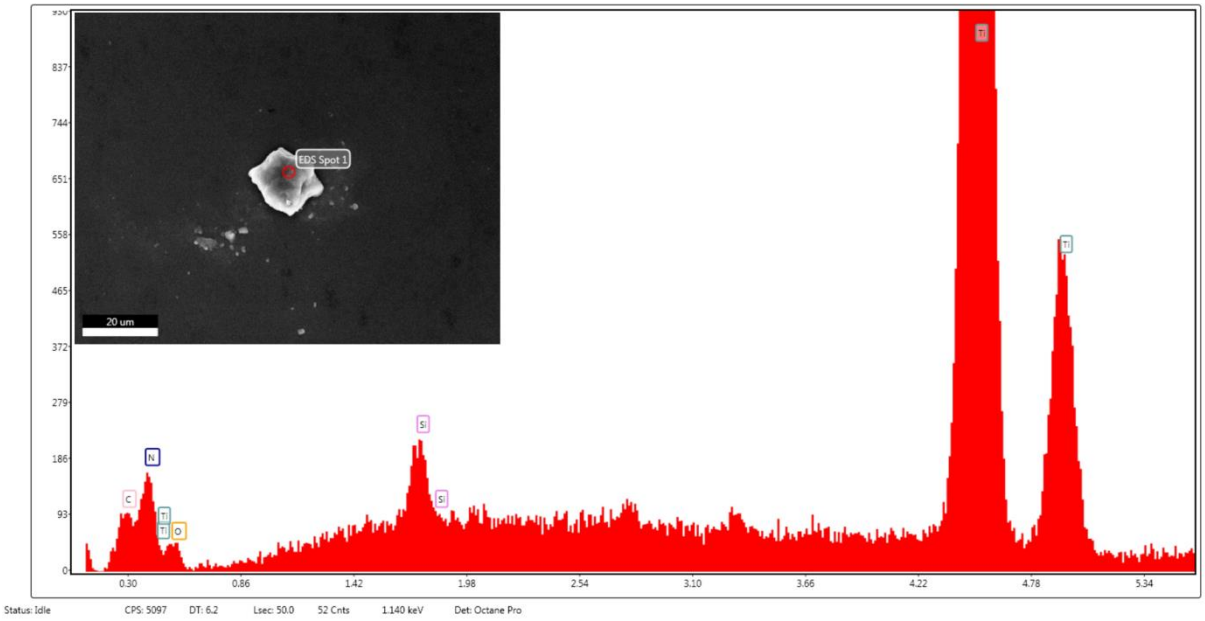

Appendix 3.4: EDX analysis of EthCitCD-TiO_2 (50 %)

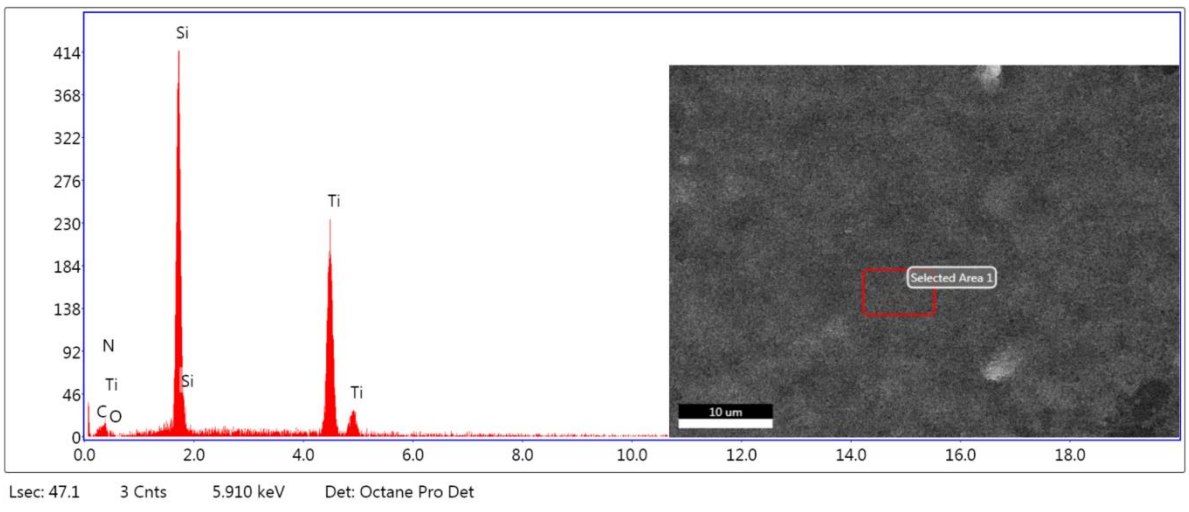

Appendix 3.5: EDX analysis of EthCitCD-TiO_2 (6.25 %)

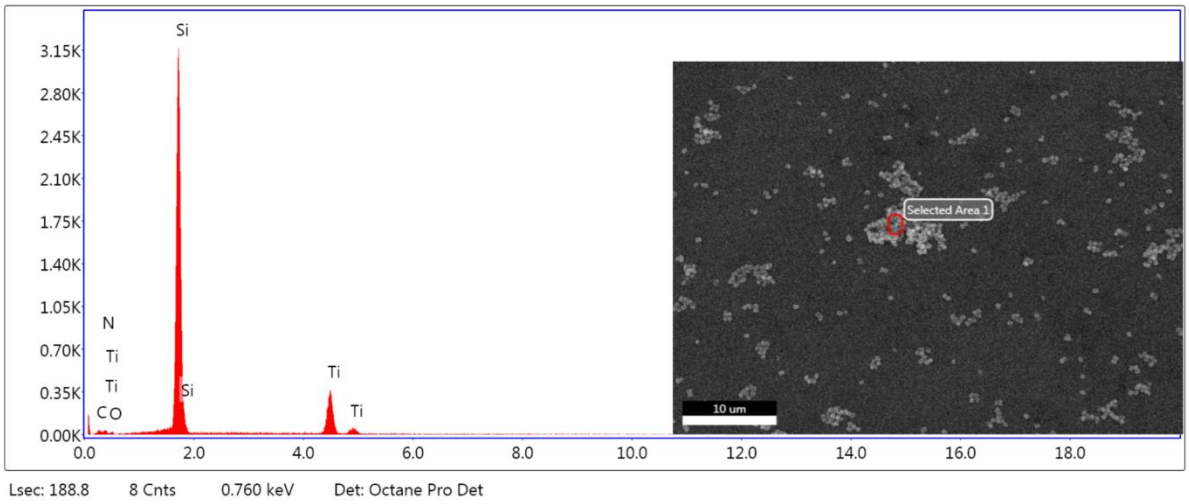

Appendix 3.6: EDX analysis of EthCitCD-TiO_2 (0.25 %)

	[50 % EthCitCD]		[6.25 % EthCitCD]		[0.25 % EthCitCD]	
hkl	**2θ°**	**d_{hkl} (Å)**	**2θ°**	**d_{hkl} (Å)**	**2θ°**	**d_{hkl} (Å)**
101	25.475	3.447	25.455	3.450	25.334	3.466
103	37.228	2.381	37.147	2.386	37.106	2.389
004	38.096	2.329	38.156	2.325	38.076	2.330
112	38.803	2.288	38.823	2.287	38.601	2.299
200	48.192	1.862	48.172	1.862	47.909	1.872
105	54.179	1.669	54.169	1.669	54.169	1.669
211	55.199	1.640	55.239	1.639	54.957	1.647
204	62.872	1.457	62.792	1.459	62.751	1.460
116	69.071	1.341	69.051	1.341	69.051	1.341
220	70.323	1.320	70.222	1.321	70.081	1.324
215	75.230	1.245	75.129	1.247	75.109	1.247

Appendix 3.7: Calculated d-spacings using $d_{hkl}=\lambda/(2\sin\theta)$, for TiO_2 with 50 %, 6.25 % and 0.25 % EthCitCD, where λ = 1.52 Å. 2θ values highlighted in red show > 0.1° deviation from pure TiO_2 equivalent.

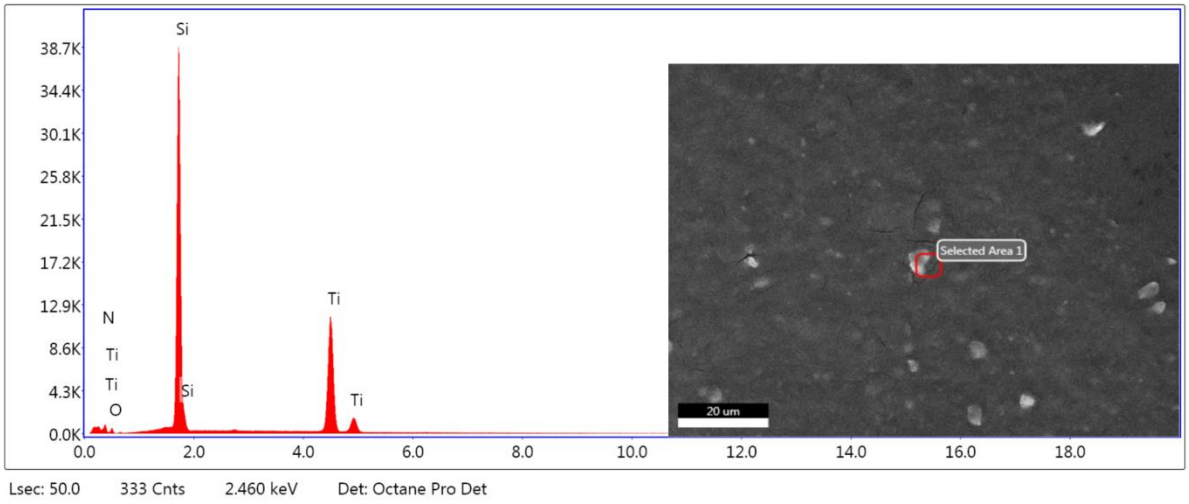

Appendix 3.8: EDX analysis of UreCitCD-TiO_2 (50 %)

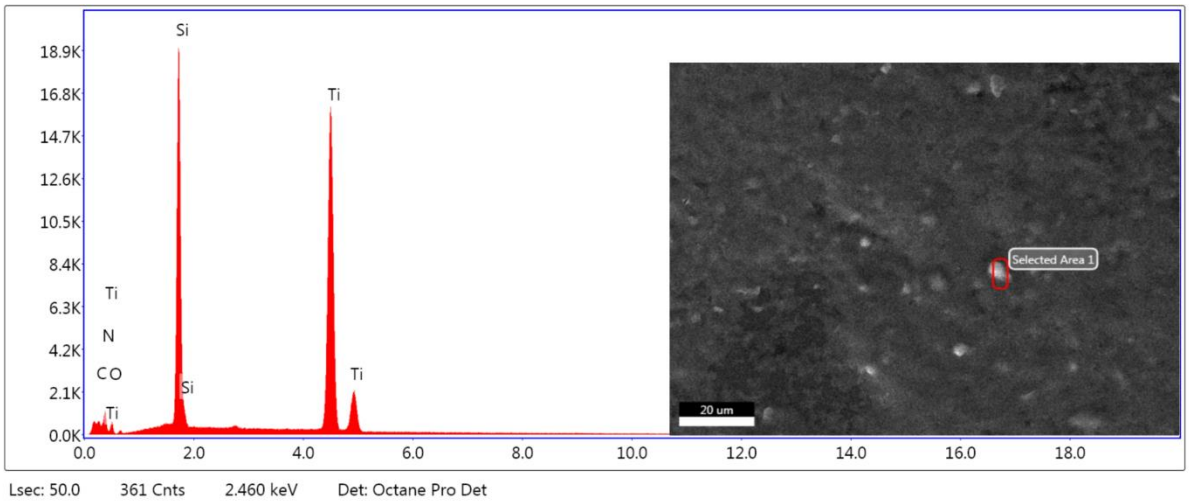

Appendix 3.9: EDX analysis of UreCitCD-TiO_2 (6.25 %)

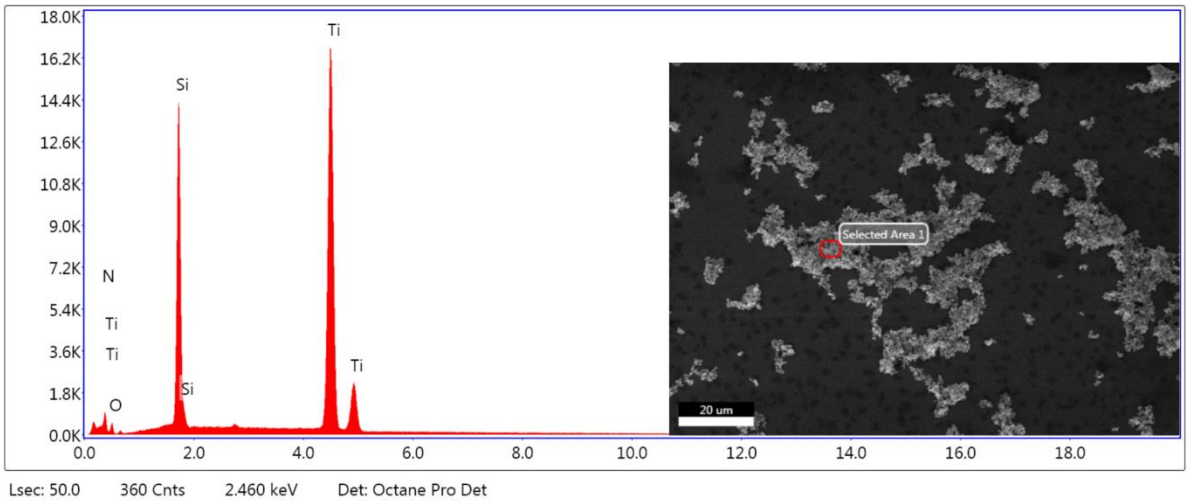

Appendix 3.10: EDX analysis of UreCitCD-TiO_2 (0.25 %)

	[50 % UreCitCD]		[6.25 % UreCitCD]		[0.25 % UreCitCD]	
hkl	**2θ°**	**d_{hkl} (Å)**	**2θ°**	**d_{hkl} (Å)**	**2θ°**	**d_{hkl} (Å)**
101	25.718	3.415	25.637	3.426	25.516	3.442
103	-	-	37.328	2.375	37.288	2.377
004	38.399	2.311	38.278	2.318	38.298	2.317
112	-	-	-	-	-	-
200	48.273	1.859	48.278	1.858	48.091	1.865
105	54.573	1.658	54.351	1.664	54.331	1.665
211	55.441	1.634	55.219	1.640	55.118	1.643
204	63.175	1.451	62.993	1.455	62.913	1.456
116	69.294	1.337	69.334	1.336	69.172	1.339
220	70.566	1.316	70.303	1.320	70.243	1.321
215	75.392	1.243	75.291	1.244	75.230	1.245

Appendix 3.11: Calculated d-spacings using $d_{hkl}=\lambda/(2\sin\theta)$, for TiO_2 with 50 %, 6.25 % and 0.25 % UreCitCD, where λ = 1.52 Å. 2θ values highlighted in red show > 0.1° deviation from pure TiO_2 equivalent.

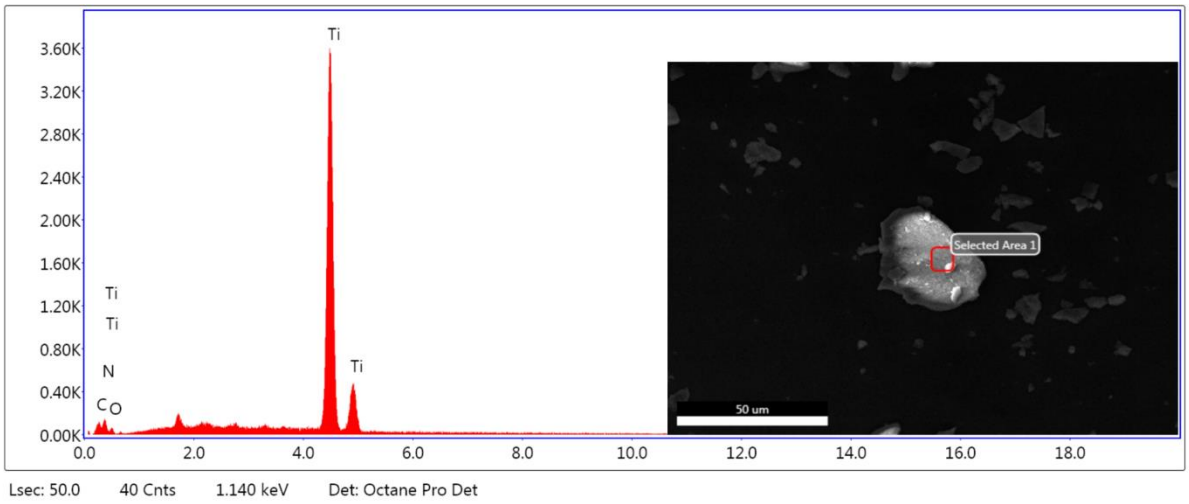

Appendix 3.12: EDX analysis of VanCitCD-TiO_2 (50 %)

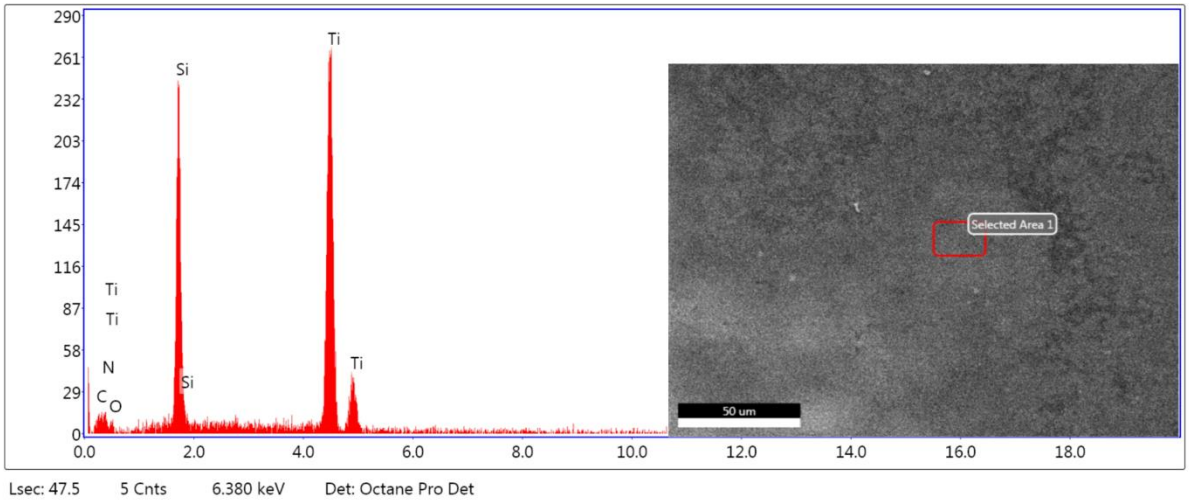

Appendix 3.13: EDX analysis of VanCitCD-TiO_2 (6.25 %)

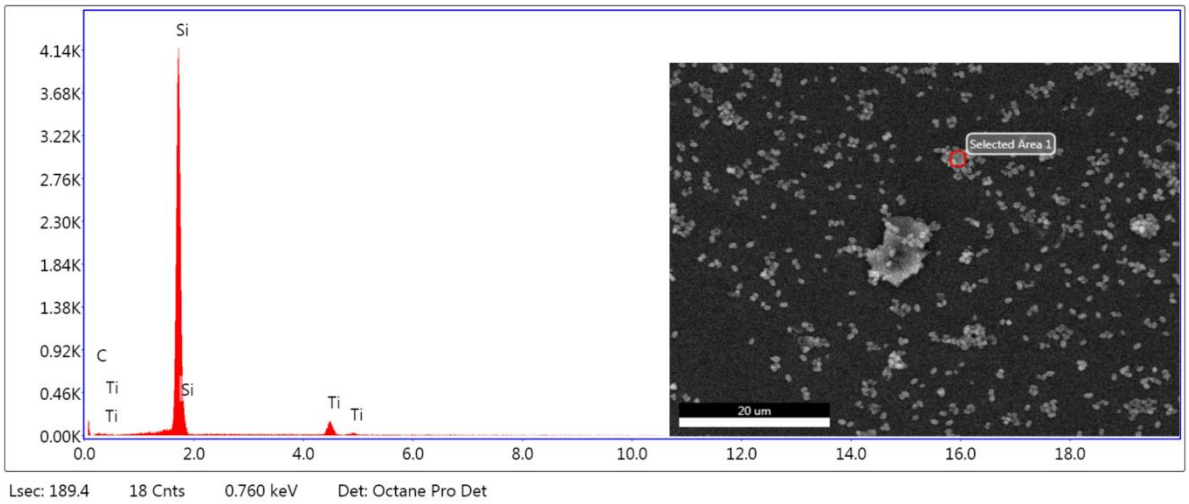

Appendix 3.14: EDX analysis of VanCitCD-TiO_2 (0.25 %)

	[50 % VanCitCD]		[6.25 % VanCitCD]		[0.25 % VanCitCD]	
hkl	**2θ°**	**d_{hkl} (Å)**	**2θ°**	**d_{hkl} (Å)**	**2θ°**	**d_{hkl} (Å)**
101	25.536	3.439	25.455	3.450	25.435	3.452
103	-	-	37.127	2.387	37.167	2.385
004	38.197	2.323	38.116	2.328	38.116	2.328
112	-	-	38.803	2.288	38.742	2.291
200	48.071	1.866	48.091	1.865	48.091	1.865
105	54.250	1.667	54.129	1.670	54.250	1.667
211	55.138	1.642	55.078	1.644	55.118	1.643
204	62.893	1.457	62.792	1.459	62.913	1.456
116	69.051	1.341	68.950	1.343	69.172	1.339
220	70.243	1.321	70.182	1.322	70.344	1.319
215	75.250	1.245	75.109	1.247	75.170	1.246

Appendix 3.15: Calculated d-spacings using $d_{hkl}=\lambda/(2\sin\theta)$, for TiO_2 with 50 %, 6.25 % and 0.25 % VanCitCD, where λ = 1.52 Å. 2θ values highlighted in red show > 0.1° deviation from pure TiO_2 equivalent.

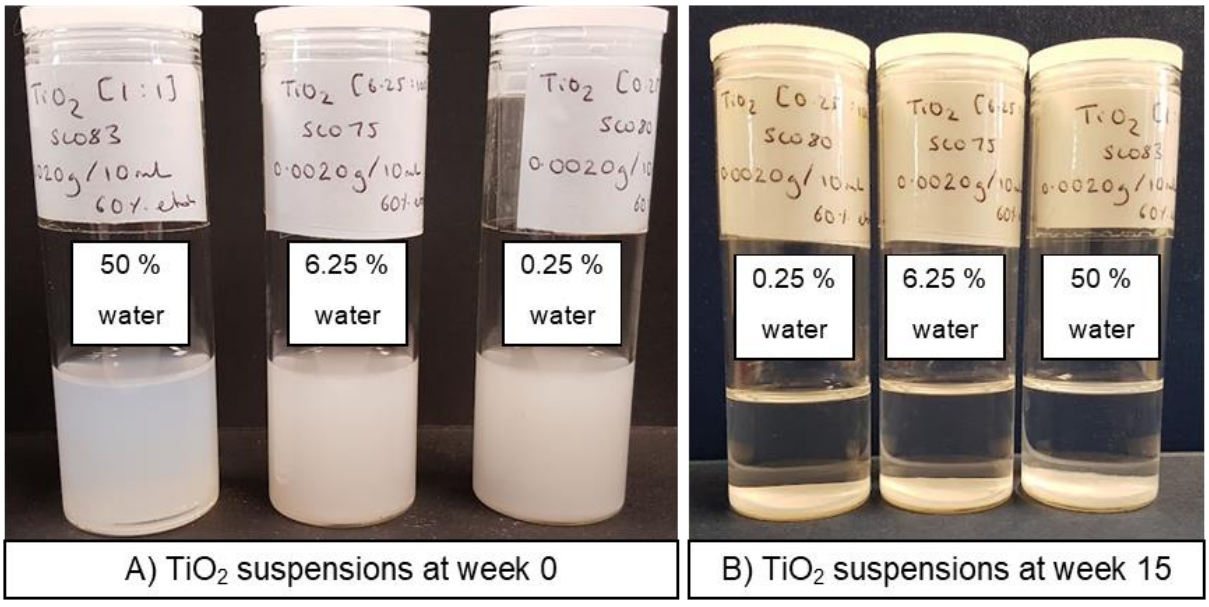

A) TiO_2 suspensions at week 0 B) TiO_2 suspensions at week 15

Appendix 3.16: Images of TiO_2 suspensions taken 15 weeks apart. Samples were kept at room temperature and were not agitated during this period.

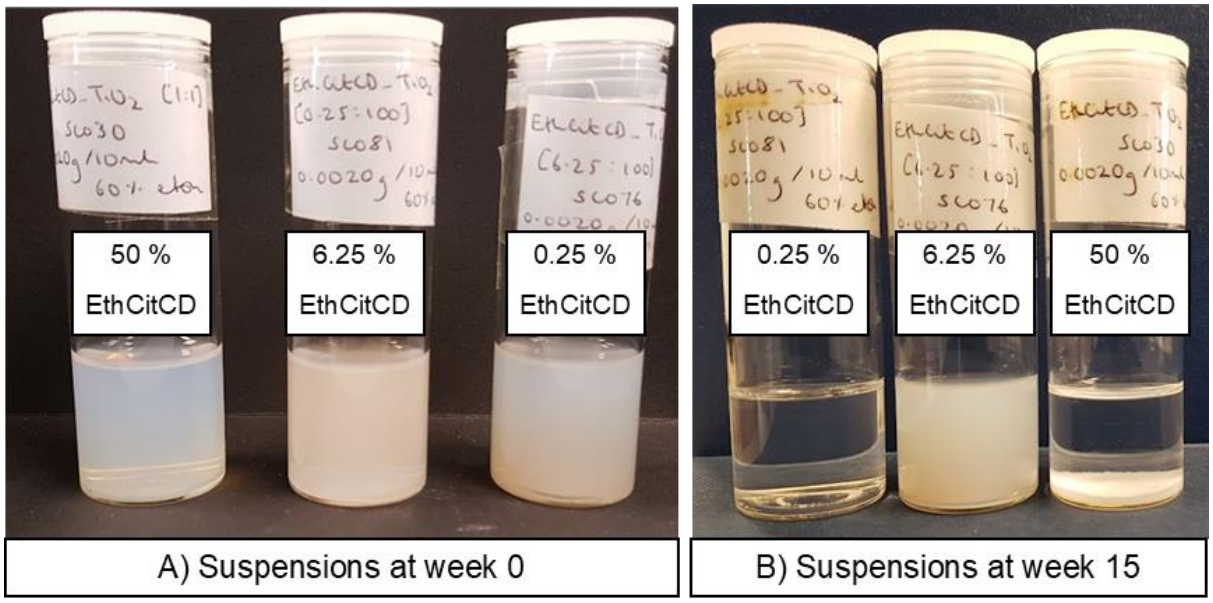

Appendix 3.17: Images of EthCitCD-TiO_2 suspensions taken 15 weeks apart. Samples were kept at room temperature and were not agitated during this period.

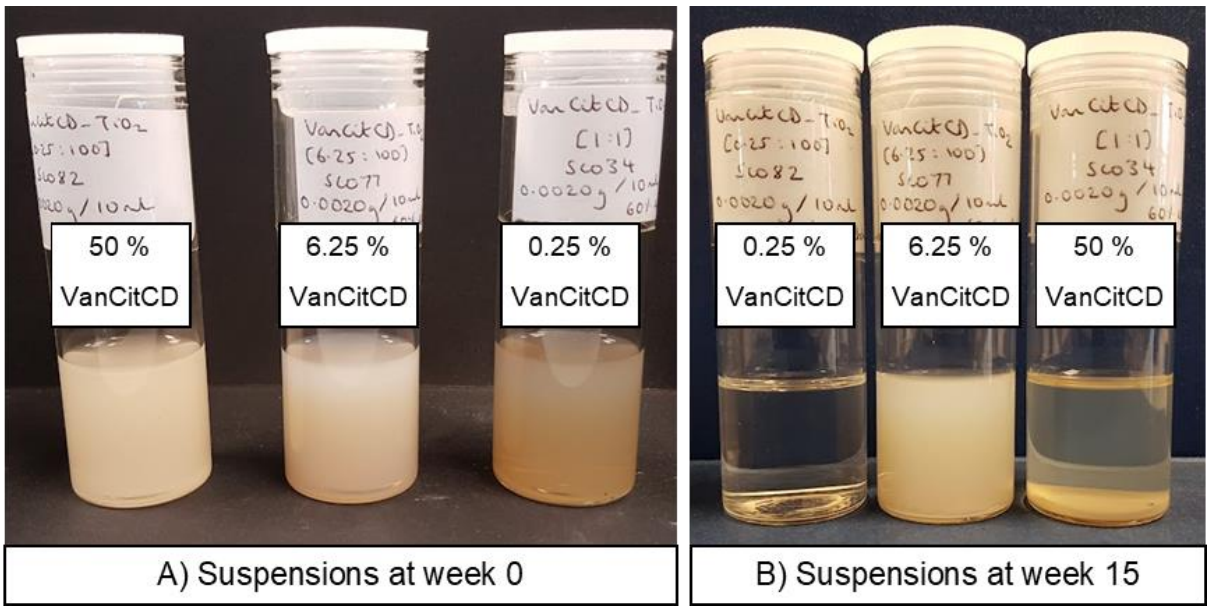

Appendix 3.18: Images of VanCitCD-TiO_2 suspensions taken 15 weeks apart. Samples were kept at room temperature and were not agitated during this period.

4. Investigations of zinc oxide

4.1. Introduction

Zinc oxide is a well-researched semiconductor with many desirable structural, mechanical, electrical, and optical properties that give it functionality in wide number of fields. For example, zinc oxide nanoparticles are highly desirable in biomedicine in applications such as anticancer, drug delivery, diabetes, and anti-inflammation (190, 191). ZnO nanoparticles with sufficient surface defects are also capable of luminescence, making them useful in bioimaging (192). Perhaps, its most well-known feature is its ability to attenuate broad-spectrum UVR, up to 450 nm, making it a frequent component in sunscreens as a physical filter. While it is a strong UVA filter, it is only weakly effective against High Energy Visible Light (HEVL)(193).

ZnO boasts the ability to be biocompatible to human cells while toxic to an array of bacteria and fungi, and so has been employed in antimicrobial applications, as biocides in paints and cosmetics (194). Biocidal nanostructures are sought after as their small size means a larger active surface area. Zinc oxide nanoparticles are thought to be particularly advantageous in this field, as they can withstand various temperatures and moisture levels, can be easily stored, and transported, and can be reused (195). The combination of their antibacterial, antimicrobial and UV-blocking capabilities also make them useful in finishing fabrics within the textile industry, providing UV light resistance as well as antibacterial and anti-odour qualities (191).

Zinc oxide has also been shown to be biodegradable under certain conditions (196). Zhou *et al.* showed ZnO wires to degrade into its corresponding ions (Zn^{2+} and O^{2-}) in deionised water (pH 4.5 - 5.0), ammonia (pH 7.0 - 7.1, 8.7 - 9.0) and NaOH solution (pH 7.0 - 7.1, 8.7 - 9.0) (196). The authors also investigated whether zinc oxide could survive in horse blood serum (pH 8.5), representative of biofluid, in which it degraded into Zn^{2+} and O^{2-} after a few hours (196). The biodegradability of nano-ZnO wires into biocompatible ions that can be reabsorbed by the body, means this material may show promise in bioscience applications, as a biosensor for example.

Additionally, ZnO has a direct and wide band gap of 3.37 eV at room temperature (197) which corresponds to the energy of UV light. A direct band gap is particularly advantageous because it means the valence and conduction bands exist at the same value of momentum, therefore an electron-hole pair can be produced by a photon with energy equal to the band gap as the electron does not require much momentum (198).

This feature allows it to be used in optoelectronic applications like light-emitting diodes, laser diodes and photodetectors (199).

4.1.1. Crystal structure & synthesis

There are three crystal structures of ZnO: wurtzite, zinc blende, and rock salt. Wurtzite is thermodynamically stable at ambient pressure and temperature, forming a hexagonal close-packed unit cell, and so is most common, as shown in the representation in Figure 4.1. Zinc blende has a face-centred cubic structure and can be stabilised through growth on cubic substrates, and rock salt is formed under high pressure (200). For wurtzite and zinc blende, each anion has four surrounding cations positioned to make a tetrahedron (201).

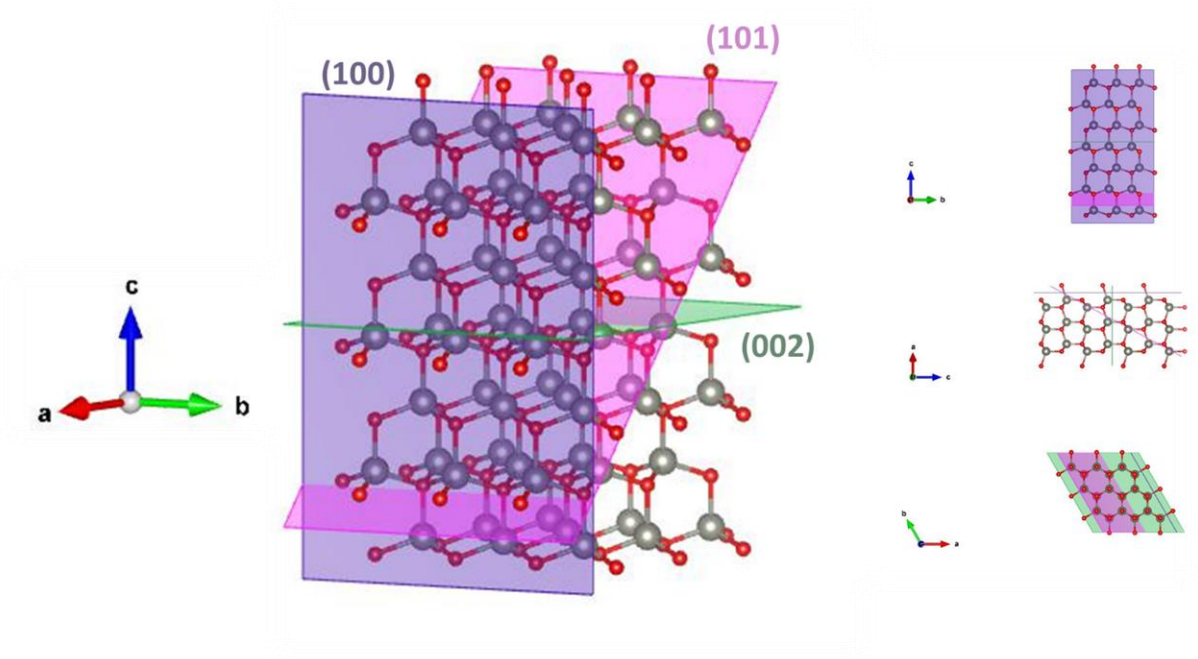

Figure 4.1: Representation of ZnO crystal lattice, featuring lattice planes (100), (002) and (101), as well as views along the a axis, b axis and c axis. Made with Vesta.

A variety of synthetic techniques can be employed to produce zinc oxide. Kołodziejczak-Radzimska *et al.* summarised some of the techniques (202) including:

the mechanochemical process (203-206), precipitation with and without surfactants present (207-211), sol-gel (212-214), solvothermal (215), hydrothermal (216-218), microwave assisted (219), emulsion (220) and microemulsion (221) techniques. In a review by Sadhasivam *et al.*, “green” synthetic routes for the production of ZnO were considered (222). These referred to those procedures that have been synthesised using plants and microbes which increased the efficiency of the reaction while reducing the cost (222).

With such a selection of synthetic routes, it is possible to obtain particles with a wide range of shapes, sizes, and properties. Some of the many morphologies that are achievable include: wires, rods, rings, and flowers, to name a few (223). The hydrothermal and solvothermal methods offer good control over features like shape, morphology, crystallinity, crystal size and orientation, typically achieving reproducible results. For example, Cai *et al.* fabricated zinc oxides with varying types of flower morphology, by altering the type of base (KOH (0.6 M), NH_3 (0.2 M) and NH_3 (0.3 M)), concentration, and time, using the hydrothermal technique (195). Other benefits of hydrothermal synthesis include lower reaction temperatures, they are typically one step processes and are relatively simple procedures (224).

As well as the synthetic route, the tuning of factors such as pH, temperature, reaction time and solvent, can also control the morphology of zinc oxide. As the optical properties of ZnO are dependent on its morphology (225), with good control of this, ZnO can be refined for the appropriate application.

4.1.2. Control of morphology with hydrothermal reaction conditions

Hydrothermal or solvothermal synthetic routes can produce crystalline zinc oxide, at low temperatures, in a relatively facile way. By changing the reaction conditions such as temperature, reaction time, pH and incorporating dopants, the morphology and subsequently the properties of ZnO can be modified. It is therefore a simple, yet highly effective, way of investigating how the properties of ZnO can be improved.

The research of Lu *et al.* is a good example of how the conditions of hydrothermal reactions can alter the shape and size of zinc oxide. Lu *et al.* reported the hydrothermal synthesis of ZnO using ammonia as the alkaline source and zinc nitrate as the Zn precursor. They investigated the effect of reaction temperature and time on the structure and particle size produced, as well as how the pH of starting solutions varied

the crystal structure. Reaction temperature varied between 100 °C, 150 °C and 200 °C for 2 h and all reactions produced crystalline ZnO, consistent with monophasic zincite with a hexagonal structure (226). The particles had ellipsoidal morphology, though smaller, rounded particles were observed for the reaction at 200 °C. The particle size decreased as the reaction temperature increased, and the yield of ZnO powder was also found to decrease from 82 % at lower temperatures to 57 % at 200 °C. Due to the high pressure of hydrothermal synthesis, combined with the higher temperature, it was thought that this could be as a result of partial dissolution of ZnO powder (226).

To study the effect of reaction time, Lu *et al.* fixed the temperature at 100 °C and varied the time from 0 h to 2 h. For 0 h, reaction was stopped and rapidly cooled when 100 °C was reached. The crystallinity was unaffected but the yield of ZnO slightly increased from 76 % to 83 %.

Finally, the influence of pH of the starting solutions were varied between 9 and 12, using ammonia. At pH > 9 the precursors dissolved more effectively and were completely in solution at pH 11 and above, which was thought to influence the formation of ZnO, significantly (226). At pH 9, the size of the particles was not uniform and ellipsoidal in shape. At pH 10, a mixture of ellipsoidal and rod-shaped particles was visible. A pH 11 and 12, the morphology was more homogenous and rod-like. The aspect ratio appears to increase with pH, which is reportedly due to preferential growth of ZnO in the a-axis at high pH (226).

At higher pH (11 and above), the amphoteric zinc hydroxide precursor was soluble, while at lower pH values it was only partially soluble. In these cases, nucleation of ZnO was occurring from a heterogenous system, while for those reactions in which the precursor was fully soluble, nucleation started from a homogenous system. This offers an explanation as to why, at a higher pH, the particles are more uniform in shape and size. Additionally, Lu *et al.* suggests in a homogenous solution, Zn^{2+} has greater freedom of movement to arrange itself in a more energetically favourable state, governing the production of rod-like structures (226). They also found that at a higher pH the yield was reduced, as ZnO can dissolve in strong alkaline conditions (as it is amphoteric). While the particle size increased, as more zinc hydroxide precursor was in solution, therefore the availability of Zn ions was greater (226).

Overall, the research of Lu *et al.* found pH of the starting materials to be instrumental in the characteristics of the resultant ZnO and it could alter the morphology, aspect ratio and yield. In contrast, the temperature slightly reduced the particle size and yield. It was found to be important to reach a temperature of 100 °C (which the author denoted as a 0 h reaction) but increasing the reaction time to 2 h had little impact except a slight increase in yield (226).

This is supported by Shang *et al.* who described the formation of ZnO flowers and nanoplates by varying the ratio of zinc sulfate heptahydrate and 5M NaOH (227). They stated that the size and morphology of ZnO is determined by competition between nucleation of crystals and crystal growth. With a higher concentration of NaOH in the precursor solution, flowers were formed, and plate-like structures formed at lower concentrations of NaOH as follows (227):

$$Zn^{2+} + 2OH^{-} \rightarrow ZnO + H_2O$$

They suggested that, at low concentrations of NaOH, there was a low driving force for growth in the (001) plane. In contrast, at higher concentrations flower-shaped ZnO made up of pencil-like rods formed. It was proposed that ZnO nuclei are formed at the start of the reaction, and act as seeds for the growth of the 3-dimensional branched structures (227). As the reaction progresses, the solution becomes supersaturated with the amount of ZnO nuclei which encourages the formation of branched structures. Shang *et al.* also reported the flower-like ZnO structures to have weak emission at 405 nm and 437 nm, and a broad green band at 500 nm and 573 nm, when excited at 325 nm. Suggested explanation of the broad green emission could result from recombination of electrons in singly ionised oxygen vacancies with photoexcited holes, giving this potential application in white light-emitting materials (227).

Similarly, Pal *et al.* controlled the structure of ZnO nanoparticles formed with zinc acetate dihydrate, using ethylenediamine as a “soft surfactant” and by varying the pH (228). They obtained nanorods at pH 11, with a broad emission band in the visible region, which corresponded to the overlap of green and yellow emissions likely due to recombination of electrons with photoexcited holes. Annealing the product appeared to reduce out of point defects and defect complexes, and the broad emission decreased (228).

Pariona *et al.* focussed on assessing the impact of morphology on the antifungal activity of ZnO particles, to control phytopathogenic fungi: *Fusarium solani, Fusarium oxysporum f.sp. lycopersici,* and *Colletotrichum gloeosporioides* (229). They evaluated three common morphologies: spheres, platelets, and rods (Figure 4.2). The latter two were produced hydrothermally while the first was synthesised by the colloidal method. In short, the ZnO particles were mixed with potato dextrose agar medium at various concentrations up to 1 mg/mL. A fresh spore sample was inoculated into the centre of the plates, that were then incubated for 6 days at 29 ± 1 °C. After which, the diameter of radial growth of fungi was measured and a growth inhibition percentage was calculated, relative to a control that used deionised water and no ZnO particles.

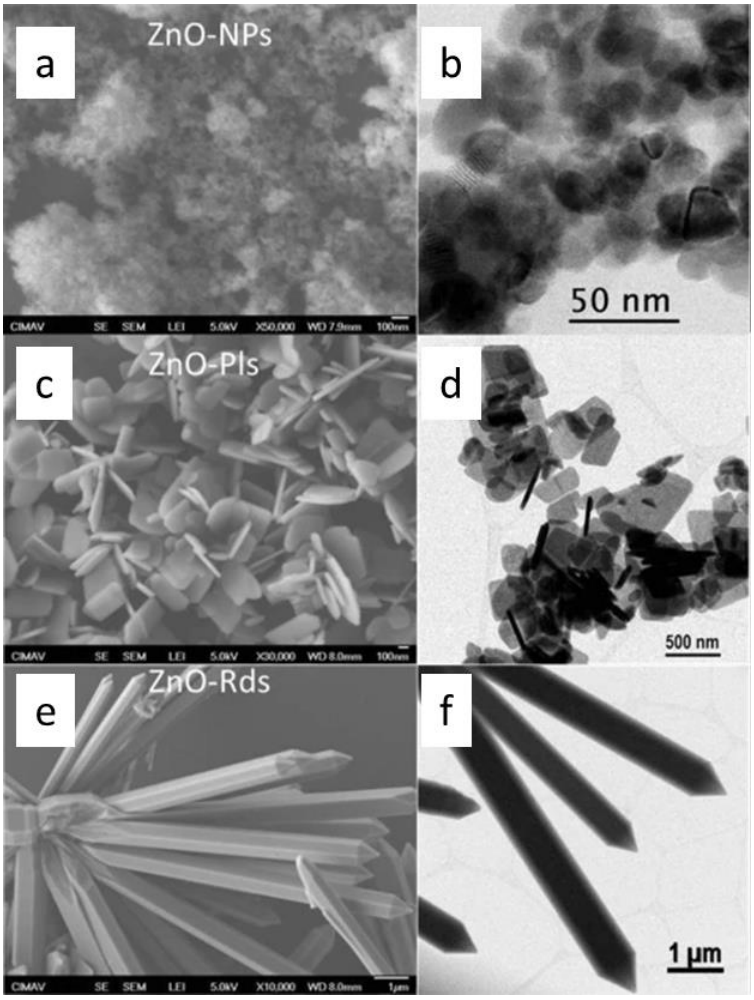

Figure 4.2: Pariona *et al.* showing three morphologies of ZnO by SEM and TEM for spheroidal (a-b), platelets (c-d) and rods (e-f). Reproduced with copyright permission.

The results indicated that although all ZnO particles were able to inhibit the mycelial growth of all three fungi, the platelet-shaped particles were most successful and required lower concentrations. The rods proved to have the lowest antifungal activity. It has been reported that antimicrobial activity is greater on crystalline planes (002) and this is also the preferred direction of growth for platelets which might be one of the reasons they were most effective (229). Pariona *et al.* propose that growth inhibition of the fungi is due to the generation of ROS by ZnO, which are capable of causing the membrane to dysfunction (229).

Using a one-step hydrothermal method, Marlinda *et al.* achieved different morphologies of ZnO nanostructures by adjusting between pH 9 and 12, with 0.1M NaOH (230). They formed batons, stars, flowers, and rod-shaped structures as shown in Figure 4.3 and attribute the variation in growth and morphologies to the abundance of OH^- in the reaction medium. Secondary nucleation because of ZnO baton structures colliding with heat, was a proposed mechanism for the formation of flowers and star shapes.

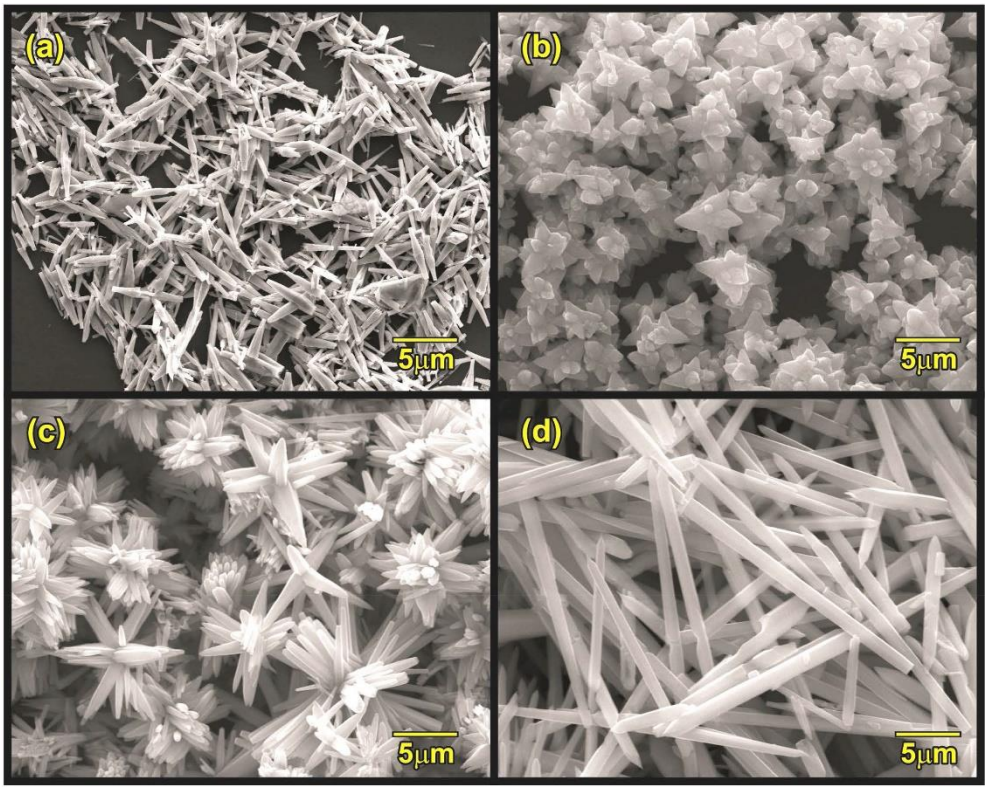

Figure 4.3: FESEM images of a) pH 9, batons b) pH 10, stars c) pH 11 flowers and d) pH 12, rods by Marlinda *et al.* (230). Reproduced with copyright permission.

4.1.3. Controlling properties of ZnO with organic additives

The addition of organic additives can affect the nucleation and growth of ZnO crystals, while some can be integrated into the structure itself (231). Dopants can be incorporated into ZnO to increase absorption of UV and HEV light. They can introduce optically active electronic states within the band gap of ZnO, allowing electrons to be promoted between these states and into or out of the conduction and valence bands (232). Additionally, the inclusion of dopants into the lattice can lead to strain as a result of the size difference between themselves and the original atoms (232). The nature of the strain (compressive or tensile) can increase or decrease the band gap of ZnO (232).

Cho *et al.* reported the use of ascorbic acid (vitamin C) as a carbon dopant in ZnO nanostructures, using a mild solution-based approach, as opposed to the hydrothermal technique (231). Zinc nitrate hexahydrate, hexamethylenetetramine and ascorbic acid were combined and kept at 95 °C for 1 h. The product was calcinated at 500 °C for 2 h as it was not crystalline, increasing the energy consumption of an otherwise low-energy reaction. Interestingly, vitamin C appeared to slow the growth rate in the [001] direction leading to a decrease in aspect ratio of the ZnO rods. It was proposed that the carboxylate anions and hydroxyl groups on vitamin C might adsorb onto the positively charged (001) surface of Zn^{2+} which would prevent the growth units from making contact. Instead, this encouraged crystal growth along the six symmetric directions, reducing the aspect ratio of the ZnO rods. The absorption profile of the carbon-doped nanostructures was red-shifted compared to undoped ZnO, and as a result they had superior photocatalytic activities at $\lambda \geq 420$ nm compared to their undoped equivalent (231). The extension of the absorption profile into the visible light region in this manner is also sought after in solar protection applications and could be investigated further for this purpose.

Another example is the work of Zhang *et al.* who used a homogenous solution of zinc acetate and urea (carbon source), which was calcinated at 450 °C for 2 h, to form carbon doped ZnO nanostructures (233). In line with the findings of Cho *et al.*, the addition of the carbon source interfered with the growth of regular ZnO nanorods, and the structures tended towards spheres as the concentration of urea increased. They proposed that urea condensed to form cyanuric acid at approximately 175 °C and the

resultant exposure of -OH groups encouraged adsorption on the positively charged (001) Zn^{2+} surface which inhibited growth in this direction. As a result, growth was promoted along the six symmetric directions leading to spheres (233). Zhang *et al.* found that the entrapment of carbon reduced the band gap of ZnO and prolonged the lifetime of electron-hole pairs, which improved the visible light photocatalytic activity as demonstrated by the degradation of methylene blue with visible light irradiation (233).

Using a hydrothermal method (180 °C, 12 h), Muthuchamy *et al.* synthesised ZnO nanoparticles on N-doped carbon nanosheets, using peach juice as the carbon source, in aqueous ammonia (nitrogen source) alongside zinc powder (234). A variety of techniques were used to study the physiochemical properties: XRD, Raman spectroscopy, FT-IR, FESEM and HRTEM. EDX elemental mapping showed even distribution of carbon, nitrogen, and zinc, which suggested ZnO had formed over the N-doped carbon sheets. By immobilising glucose oxidase onto the nanocomposite, they were able to create a biosensor with good selectivity for glucose, for the purpose of diabetic glucose monitoring (234).

Although there is some research dedicated to doping of ZnO with carbon species, few papers have investigated its potential from the perspective of solar protection. In 2016, Gershon *et al.* patented both the composition and technique of doping ZnO particles for sunscreen applications, with copper, chromium, cobalt, gallium, aluminium and/or tin (232). However, this work refers to the use of carbon-based species and does not infringe upon this patent. Though, it somewhat strengthens the argument that improving the technologies of ZnO in sunscreen application is sought after.

4.1.4. Aims and objectives

Hydrothermal synthesis is low cost and can be done on a large-scale. To date, a hydrothermally produced ZnO with broad-spectrum absorption that extends into the visible light region has not been investigated for the purpose of solar protection.

The basis of this study was two-fold. From the literature, the refinement of zinc oxide optical properties with organic additives is promising. The broad aim was to explore a simple way of controlling the properties of ZnO using two types of organic additives.

The first aim was to investigate a method of doping ZnO with carbon dots *in situ*, to explore whether this would extend the optical properties of ZnO into the visible region and enhance its broad-spectrum light attenuation, either through inclusion or by influencing the morphology (Section 4.2). The second aim was to introduce a naturally occurring polysaccharide into the solvothermal synthesis of ZnO and explore how this effected the morphology and resultant optical properties (Section 4.3).

4.2. Using nanoscale organic additives

This section investigates the use of carbon dots: EthCitCD and UreCitCD as organic additives in the preparation of zinc oxide. The *in-situ* incorporation aimed to improve visible light attenuation of zinc oxide through doping or by changing the morphology, ultimately to be evaluated for use in solar protection applications.

EthCitCD and UreCitCD are suspensions of carbon dots which have been characterised in Chapter 2. To briefly recap, EthCitCD was the result of the hydrothermal reaction of ethanolamine and citric acid, while UreCitCD was formed by the same reaction with urea and citric acid. Both reactions were carried out in a sealed autoclave, in a hydrothermal oven for 5 h at 200 °C. They were selected as they had the most desirable optical properties.

Following a method reported by Bozetine *et al.* (235) zinc acetate dihydrate was stirred into a solution of sodium hydroxide and carbon dots. Concentrated sodium hydroxide was added to attain pH 10 before the reactants were sealed in an autoclave and heated for 3 h at 80 °C in a pre-heated oven. The solid product was purified by washing and centrifugation and dried in an oven at 75 °C. A control experiment that used no carbon dots was also carried out, to produce pure ZnO. The same molarity of sodium hydroxide solution was used, and the starting pH was 10.

This procedure was chosen as it provided a good template for the preparation of crystalline ZnO alongside a carbon source and used mild reaction conditions of 80 °C, with a short reaction time of 3 h, and relatively mild reagents such as zinc acetate dihydrate, sodium hydroxide and water. It therefore seemed an appropriate method to apply carbon dots from Chapter 2 into ZnO preparation, and assess their impact on ZnO morphology, crystallinity, and optical properties.

The materials were analysed by FT-IR spectroscopy to determine the functional groups present, Scanning Electron Microscopy to analyse the morphology and homogeneity of the sample, X-Ray Diffraction to establish the crystallinity and crystal planes present, and finally UV-vis Spectroscopy to ascertain the product's attenuation of UV and visible light and therefore its usefulness in solar protection.

4.2.1. Analysis of morphology and crystallinity

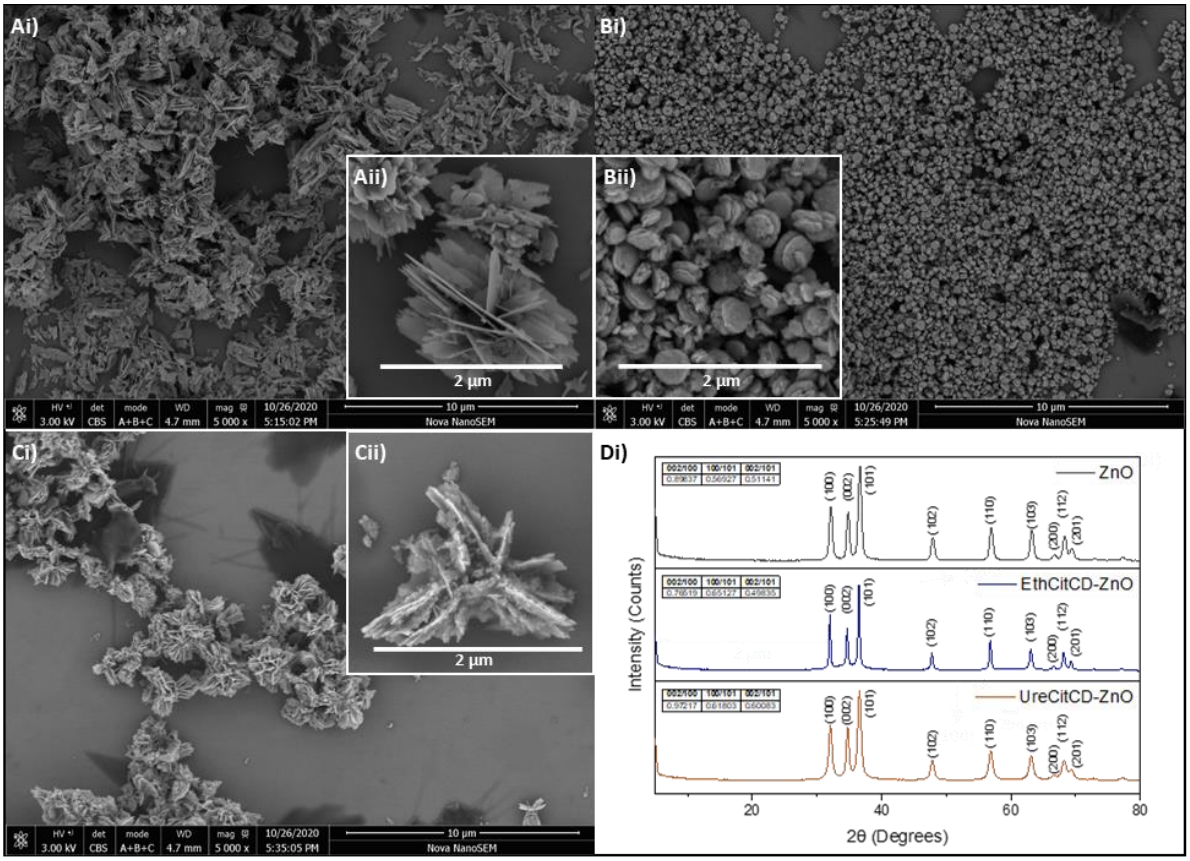

Figure 4.4: SEM images and XRD patterns of pure ZnO and ZnO grown with organic additives. Ai-ii) Pure ZnO, Bi-ii) EthCitCD-ZnO, Ci-ii) UreCitCD-ZnO and D) XRD of Pure ZnO, EthCitCD-ZnO and UreCitCD-ZnO.

Here, two different organic additives, EthCitCD and UreCitCD (as characterised in Chapter 2) were incorporated into ZnO. The pH of the solution containing precursors was maintained at pH 10 in order to control the morphology of the ZnO crystals. It is suggested that the formation of ZnO in aqueous solution is as follows (236):

$$Zn^{2+} + 2OH^- \leftrightarrow Zn(OH)_2$$

$$Zn(OH)_2 + 2OH^- \leftrightarrow Zn(OH)_4^{2-}$$

$$Zn(OH)_4^{2-} \xrightarrow{heat} ZnO + H_2O + 2OH^-$$

At pH 10, it is expected that $Zn(CH_3CO_2)_2 \cdot 2H_2O$ preferentially forms $Zn(OH)_2$, some of which decomposes with heat during the first stages of the solvothermal reaction, to form ZnO nuclei. Under these alkaline conditions, some $Zn(OH)_2$ can form growth units $[Zn(OH)_4]^{2-}$ which would usually adsorb onto the (001) plane of ZnO blocking it and promoting growth in the [001] direction (237).

With no additives, two-dimensional flakes formed which self-assembled into hollow spheres creating flower-like structures. Such formation of two-dimensional structures can occur when the rate of crystal growth along the lateral directions [100] and [120] is faster than growth rate in the [001] direction (238), as shown in Figure 4.5

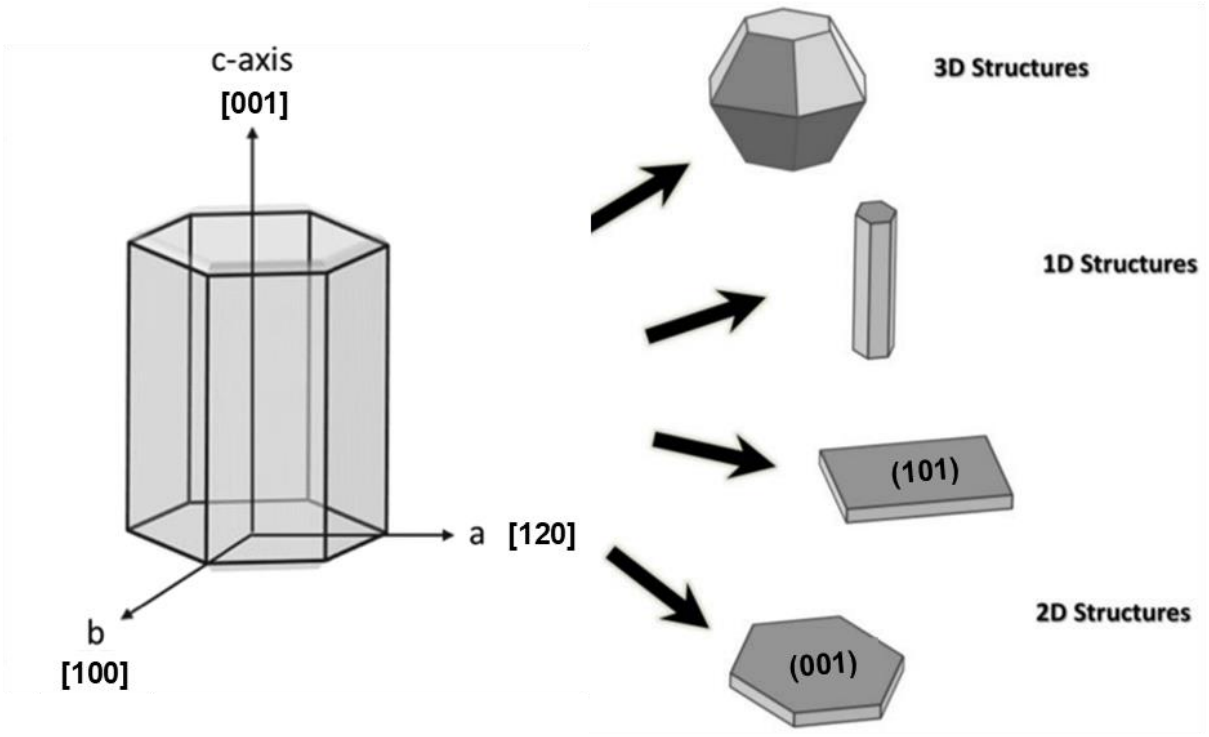

Figure 4.5: Growth directions of ZnO wurtzite crystals and probable structures. Copied and adapted from (238) (open access) (239) (with permission from Springer) to show the 3-axis Miller Index.

On addition of EthCitCD, layered nano-discs were formed. The structures had good uniformity and were approximately 200 nm in diameter. It is expected that EthCitCD is made up of negatively charged structures which may be capable of forming complexes with free Zn^{2+} ions. Therefore, it is postulated that these complexes may preferentially adsorb on the (001) plane in place of the $[Zn(OH)_4]^{2-}$ growth units, slowing growth in the [001] direction. As a result, smaller ZnO crystals with a disc-like morphology were formed. Zhang *et al.* observed a similar morphology when they used citric acid in the

solvothermal preparation of ZnO and suggested it acted as a capping agent, as it repelled the $[Zn(OH)_4]^{2-}$ growth units from adsorbing to (001) plane (237), much like what we have observed. The hydrothermal reaction reported by Zhang *et al.* took place at 200 °C for 20 h, while the preparation in our study occurred at the lower temperature of 80 °C and the shorter time of 3 h. Though the morphology was similar, the structures produced in this study were smaller (approximately 200 nm in diameter) while Zhang *et al.* achieved structures up to 2 µm in diameter. This may be because of the longer reaction time which allowed more time for growth. Additionally, Cao *et al.* produced layered nano-discs by inhibiting growth on the (001) surface of ZnO with didecyl benzene sulfonate (239). Theirs was a more energy-intensive, multi-step process, however, and involved refluxing for 24 h at the higher temperature of 139 °C (239).

The structures formed on addition of UreCitCD are more comparable to those of pure ZnO, and consist of thin flakes self-assembled into porous, flower-like structures. However, the surfaces of the flakes are more textured than the smooth ones on pure ZnO. This may indicate that UreCitCD facilitates the nucleation of secondary structures on the initial flakes, and it could be speculated that with a longer reaction time, these self-assembled structures may be significantly more complex.

There is one major change in the morphology on addition of EthCitCD and that is that the flower-like ZnO “superstructure” does not form. Instead, stacked discs were produced (Figure 4.4A and B). Flower structures can form because the primary ZnO nanosheets may contain more defects than other regions, and are therefore thermodynamically unstable (236). Surface reconstruction is one way that they can decrease their energy, and this tends to lead to site for secondary nucleation and growth. Therefore, it is possible that the discs are more thermodynamically stable and so do not aggregate in this manner.

The XRD patterns of pure ZnO, EthCitCD and UreCitCD are shown in Figure 4.4. The diffraction peaks in each of them corresponds to the hexagonal wurtzite structure of zinc oxide, as is consistent with JCPDS card 36-1451 (240), and the sharp signals indicate high levels of crystallinity. From the SEM images, the shape of zinc oxide varies between samples, and this is due to preferential growth of specific crystal planes during synthesis. Naturally, this is reflected in the XRD patterns as, in each sample, there will be a different population of each crystal plane as a result, leading to

variation in the intensities of the signals. This is what is seen in Figure 4.4D. For example, the (002) plane has the lowest intensity relative to (100) and (101) planes in EthCitCD-ZnO which may indicate lack of growth on this plane, resulting in the disc-like morphology with inhibited growth in the [001] direction. The relatively higher diffraction peak at (101) compared to (002) for all, suggests the nanosheets/flakes may be growing in the [210] direction.

4.2.2. FT-IR and UV-vis spectroscopic analysis

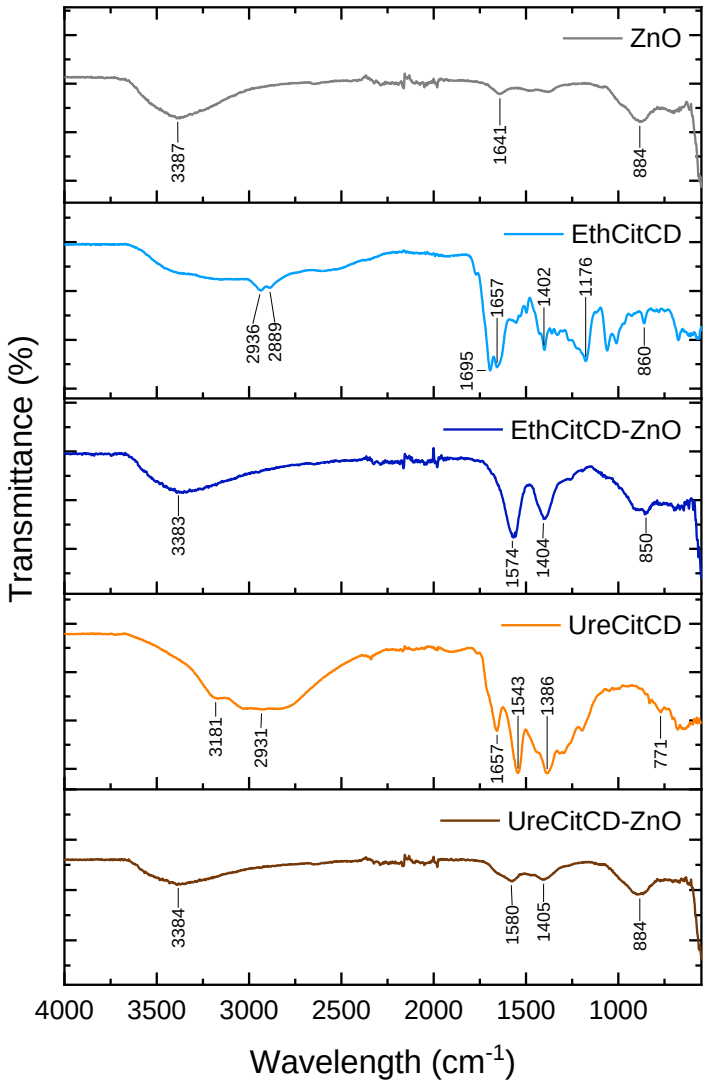

Figure 4.6: FT-IR spectra of pure ZnO and ZnO modified with organic additives (EthCitCD and UreCitCD).

FT-IR analysis gives an understanding of what interactions, if any, occur between ZnO and the organic additives. The FT-IR spectra of ZnO, ZnO modified with organic additives: EthCitCD and UreCitCD and the organic additives themselves, are shown

in Figure 4.6, in the range of 550 – 4000 cm^{-1}. There is evidence of a band forming at 550 cm^{-1} which appears to peak in a region beyond what the instrument can measure, which is the typical ZnO band (241). The peak at 884 cm^{-1} is reportedly due to carbonate moieties and can be observed when FT-IR measurements are carried out in air (241). A peak in this region is consistent in all spectra here. Additionally, absorption bands at 3387 cm^{-1} and 1641 cm^{-1} can be assigned to the stretching and bending modes of O-H in water, which may be on the surface of the ZnO crystals (241). EDX analysis is in alignment with FT-IR and confirms the purity of the sample, in which it detected only zinc and oxygen containing units (Appendix 4.1 - Appendix 4.5). The FT-IR spectra of EthCitCD-ZnO and UreCitCD-ZnO are comparable to pure ZnO, with the peak centred at 550 cm^{-1} present in all. Additionally, both spectra have peaks at 3383 cm^{-1} and 3384 cm^{-1} which correspond to stretching of O-H. Bands at 1574 cm^{-1} and 1580 cm^{-1} can be assigned to C=C stretch for polycyclic aromatic hydrocarbons. These correspond to bands visible in the FT-IR spectra of each respective organic additive. Absorption bands at 1404 cm^{-1} and 1405 cm^{-1} for EthCitCD-ZnO and UreCitCD-ZnO, respectively, can correspond to C-O vibrations (235). This is indicative of the presence of organic additives. A shift in the FT-IR absorption bands is noticeable for EthCitCD-ZnO and UreCitCD-ZnO compared to pure ZnO, which may be explained by interaction between the two components (235).

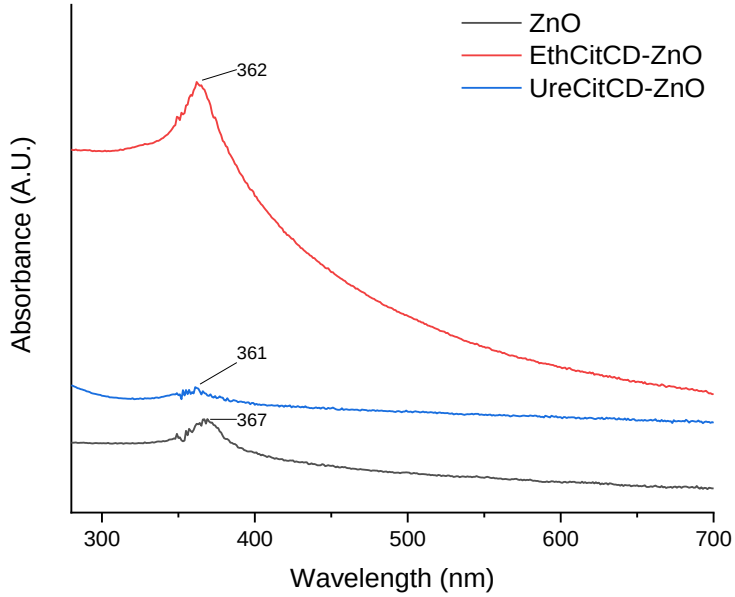

Figure 4.7: UV-vis spectra of pure ZnO and ZnO grown with organic additives. Measured at room temperature (0.05 mg/mL).

Figure 4.7 shows the UV and visible light attenuation of pure ZnO and the ZnO grown with organic additives (EthCitCD and UreCitCD), suspended in 60 % EtOH at 0.05 mg/mL. Of the three, EthCitCD-ZnO shows some broad attenuation of visible light. A single absorption peak of 367 nm is present for pure ZnO, which shows a blue shift compared to what is reported for ZnO bulk (375 nm) which may be due to the size of the nanocrystals. Sayari *et al.* reported a λ_{max} of 367 nm for nanocrystalline flakes of ZnO, very similar to the morphology seen here (241). There is a slight blue-shift in the spectra of EthCitCD-ZnO and UreCitCD-ZnO (λ_{max} = 362 nm and 361 nm, respectively), relative to pure ZnO, which may be as a result of the smaller size of the nanocrystals (242).

4.2.3. Summary

In this section, nanoscale organic additives from Chapter 2, namely EthCitCD and UreCitCD, have been incorporated into the hydrothermal synthesis of zinc oxide. Using FT-IR spectroscopy, the bands expected for zinc oxide were evident, alongside absorption bands for C=C and C-O. EDX confirmed the presence of Zn and O in all three samples (control included) and additionally detected C, N and O for modified ZnO. This would suggest the presence of organic moieties, which is also alluded to by the blue-shift of the FT-IR spectra. Furthermore, the X-Ray diffractograms are consistent with what is in the literature for zinc oxide. They showed that the result of each reaction was highly crystalline and did not contain any signals that would indicate impurities. As has been found in published literature, the small amounts of carbon present and its low crystallinity may give reason as to why its typical diffraction peaks at 10° and 20° (2θ) (243), are not detected (235).

The addition of EthCitCD altered the morphology from flowers made up of nano-sheets, to stacks of smaller nano-discs. It appears that the size may have led to the broad attenuation in the visible region, for this material. In contrast, smooth-surfaced flower-shaped ZnO and rough-surfaced flower-shaped UreCitCD-ZnO had similar UV-vis spectra, with low visible light attenuation.

Overall, the morphology of ZnO was successfully controlled using a simple, nanoscale organic additive and a low temperature reaction. The resultant UV-vis properties have been explored, and of the materials described here, EthCitCD-ZnO showed some visible light attenuation. The next section will discuss the incorporation of a

biopolymeric organic additive, to explore its impact on the morphology and properties of ZnO.

4.3. Using a biopolymeric organic additive

In this section, we investigated the use of chitosan, a natural biopolymer, as an organic additive in the preparation of ZnO[6]. Chitosan is derived from the partial deacetylation of chitin (244), which forms the basis of exoskeletons in insects, crustaceans and is used structurally in the cell walls of fungi (245). In industry, chitin is often sourced from waste from the food industry. For example, some factories remove the shells of crabs, shrimps, prawns and lobsters before canning, all of which are sources of chitin (246). Chitosan has greater than 7 % nitrogen content and a degree of acetylation lower than 0.4. It is biocompatible as it does not react adversely with human cells and is biodegradable as it can be degraded by enzymes in the body (246). It has previously been investigated for use in medicine and pharmaceuticals, as it is also advantageous in drug delivery (246). A review by H. Ababneh and B.H. Hameed (247), discussed the applications of chitosan-derived materials from hydrothermal methods which include use in: electrochemical sensors (248), catalysis (249) and water treatment such as the removal of Cr (VI) from wastewater (250).

4.3.1. Preparation of ZnO–chitosan materials

As outlined in Figure 4.8, chitosan was introduced into the solvothermal preparation of crystalline zinc oxide. The aim was to modify zinc oxide with chitosan during crystal growth, utilising the affinity of chitosan for Zn^{2+}, and investigate what impact this would have on the morphology and resultant properties of ZnO.

[6] In this section, reactions of ZnO with chitosan, UV-vis spectroscopy and FT-IR spectroscopy were carried out by MChem student Georgia McCluskey, under my supervision.

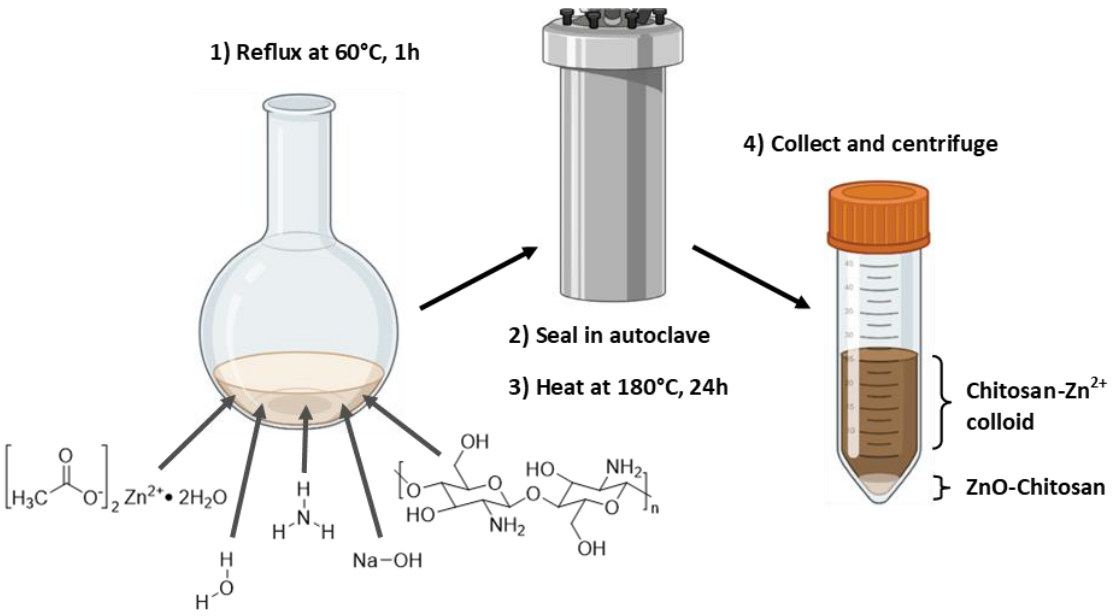

Figure 4.8: An illustration of the solvothermal preparation of ZnO with chitosan as an organic additive. Reactants were pH 12 after reflux.

Three ratios of zinc precursor (zinc acetate dihydrate) and chitosan were used: 1:1, 1:5 and 5:1, to determine their influence on the resultant properties of the materials. To further our understanding of the role of chitosan in this synthesis of ZnO, two additional experiments were undertaken: 1) solvothermal production of zinc oxide under the same reaction conditions but without the addition of chitosan and 2) a solvothermal reaction of chitosan and ammonium acetate in place of zinc acetate dihydrate. The reaction precursors were refluxed at 60 °C for 1 h, and then sealed in an autoclave and heated at 180 °C for 24 h. This solvothermal reaction was chosen as the conditions (180 °C, 24 h), closely resembled those used in Chapter 2, in the bottom-up synthesis of carbon dots. On completion of the reaction, the products were purified by centrifugation.

At 180 °C for 24 h, it was expected that chitosan might break down into smaller fragments and interfere with the crystalline formation of zinc oxide, by providing alternative nucleation sites or acting as a platform upon which to grow. Additionally, co-ordination bonds between the amine and hydroxyl groups, with Zn^{2+} might be expected, leading to the possible formation of complexes with the smaller fragments. A similar phenomenon occurred during a sol-gel preparation of chitosan and ZnO (251).

Overall, three varying shades of brown coloured, crystalline material were produced, for all three reactions that incorporated chitosan. In addition, a translucent, fluorescent colloid (when excited at 365 nm) was also formed with each reaction. Images of the solids and supernatants are shown in Figure 4.9. The powders and solutions were characterised by Fourier-transform Infrared Spectroscopy (FT-IR), Powder X-Ray Diffraction (PXRD), Scanning Electron Microscopy (SEM), Ultraviolet–visible spectroscopy (UV-vis) and Fluorescence spectroscopy.

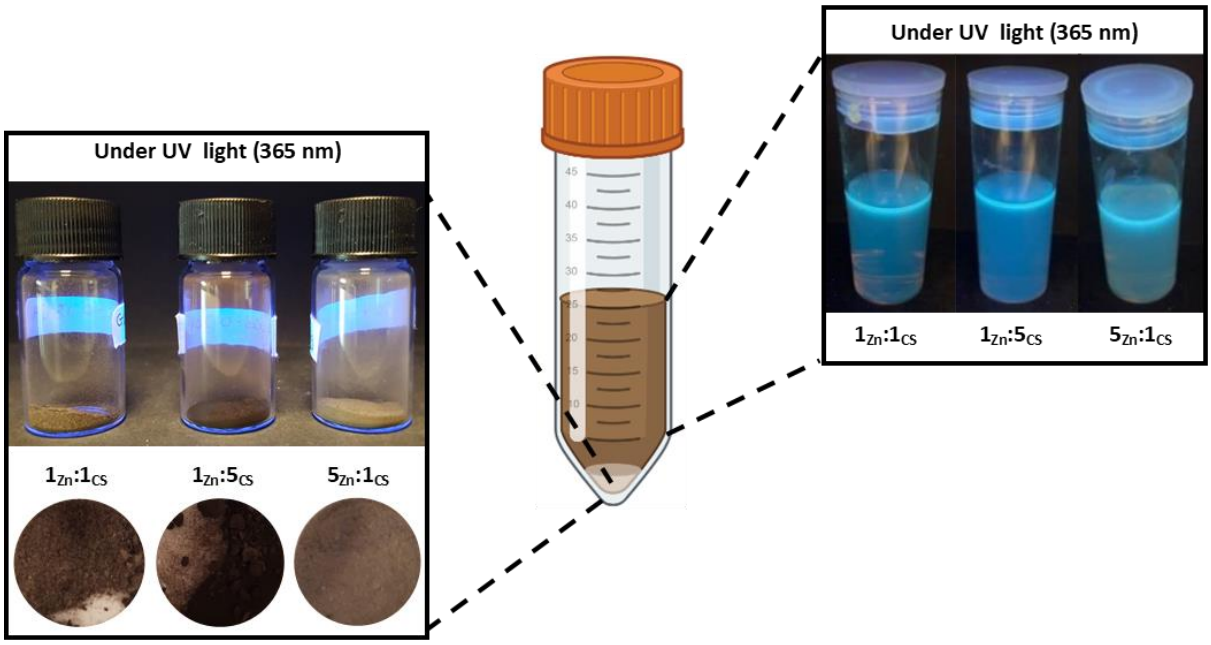

Figure 4.9: Images of modified brown coloured ZnO powders and their corresponding fluorescent supernatants (excited at 365 nm).

4.3.2. Characterisation by FT-IR

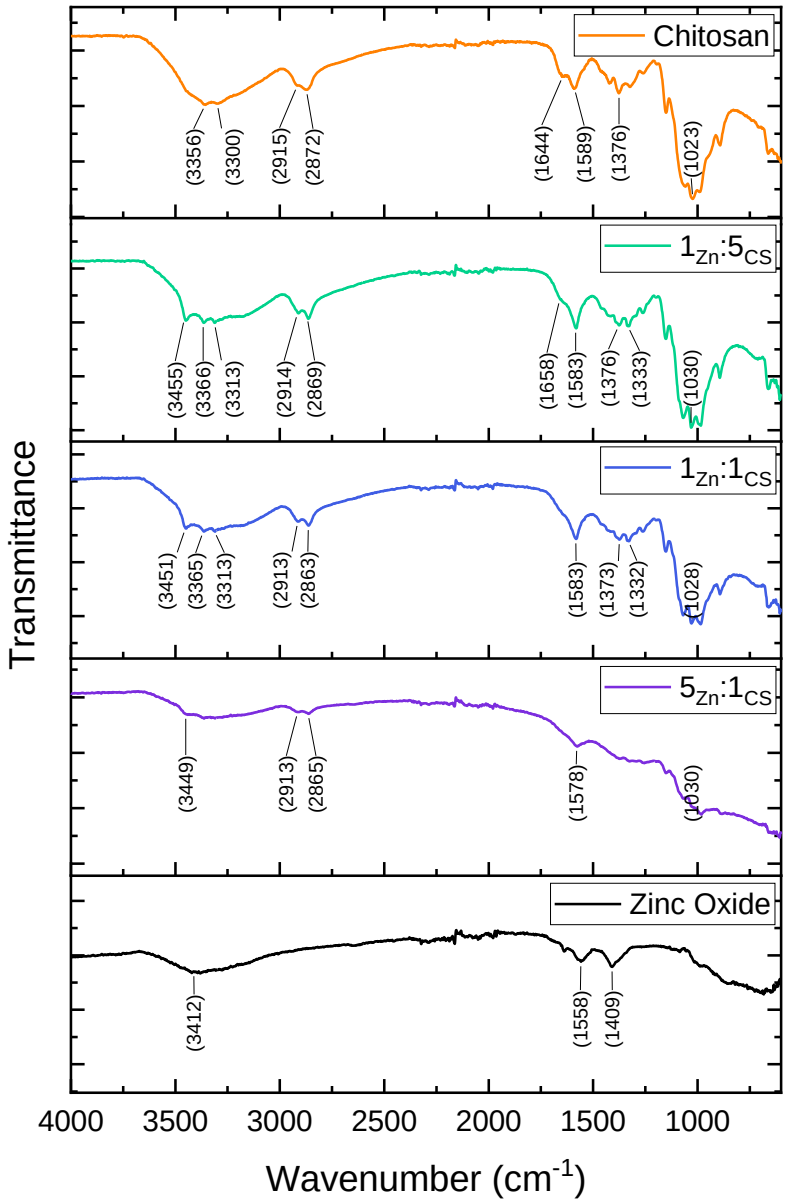

Figure 4.10: FT-IR spectra of chitosan (CS), unmodified zinc oxide, and zinc oxide modified with chitosan at ratios of 1:5; 5:1 and 1:1.

In the FT-IR spectrum of pure chitosan (Figure 4.10), the following characteristic bands include O-H stretching vibration and N-H stretching vibration (3339 cm^{-1}, broad) (251, 252), C-H stretching vibration for CH_2 and CH_3 (2872 and 2915 cm^{-1}, respectively) (251, 252), C=O vibration (1650 cm^{-1}) (252) of amide (i) group, protonated amino groups vibration (1589 cm^{-1}) (252), C-N stretching vibration (1376 cm^{-1}) (252) of amide (iii) and stretching band at (1062 cm^{-1}) indicate secondary -OH groups of chitosan are shown.

For unmodified zinc oxide, it typically has an absorption band between 460 and 700 cm^{-1} (252). Therefore, the broad absorption centring at 550 cm^{-1} can be assigned to pure ZnO (Figure 4.10). Due to the limitations of the spectrometer, absorption below 550 cm^{-1} cannot be measured. Vibrational bands of C=O (1558 cm^{-1}), C-O (1409 cm^{-1}) may be indicative of acetate groups and stretching bands of O-H (3412 cm^{-1}) are also evident, which can indicate moisture in the sample or evidence of H-bonding.

For ratios 1_{Zn}:5_{CS} and 1_{Zn}:1_{CS}, both FT-IR spectra show a broad, strong absorption band at 3342 cm^{-1} and 3339 cm^{-1}, respectively. These bands are in line with O-H and N-H stretching vibrations and suggest that these groups are present and available. There are further absorption bands overlaid with the broad band, which correspond to N-H stretching of primary amine (3455 cm^{-1}), aliphatic primary amine (3366 cm^{-1}) and secondary amine (3313 cm^{-1}) which are more defined in reactions 1_{Zn}:5_{CS} and 1_{Zn}:1_{CS}, than in pure chitosan. The higher intensity peak might indicate some co-ordination with Zn^{2+} in these two materials.

In contrast, the broad band (3450 cm^{-1}) associated with H bonding of O-H and N-H groups is weaker when Zn^{2+} is in excess. As Hammi *et al.* suggest, this might indicate a consumption of O-H and N-H groups, as Zn^{2+} is abundant, alluding to the possibility that ZnO is embedded in a carbonaceous scaffold interacting with O-H and N-H groups (253).

Overall, from FT-IR spectra, there is evidence to suggest a carbonaceous scaffold, functionalised with amino- and hydroxy groups is interacting with crystalline ZnO.

4.3.3. Analysis of crystallinity and morphology

Chitosan has two characteristic diffraction peaks that define its crystallinity: 10.6° (020) and 20.1° (110), evident in Figure 4.11A (254). Following the reaction, these are replaced by three new diffraction peaks: 15.3°, 21.1° and 24.1°, which are accentuated when chitosan is in excess and weakened in an excess of zinc acetate dihydrate. Their presence suggests that chitosan is no longer in its original form. It is possible that chitosan undergoes carbonisation during the reaction, and forms an ordered, carbonaceous template, leading to these new diffraction peaks. Hammi *et al.* investigated a similar hydrothermal treatment of chitosan and metal alkoxides (titanium (IV) diisopropoxide bis (acetylacetonate), iron (III) acetylacetonate, germanium (IV) ethoxide). They proposed that the resultant nanostructured metal oxides had grown

on a framework of carbonised chitosan, which supports our findings (253). It should be noted that their work was published in 2021, after this project began.

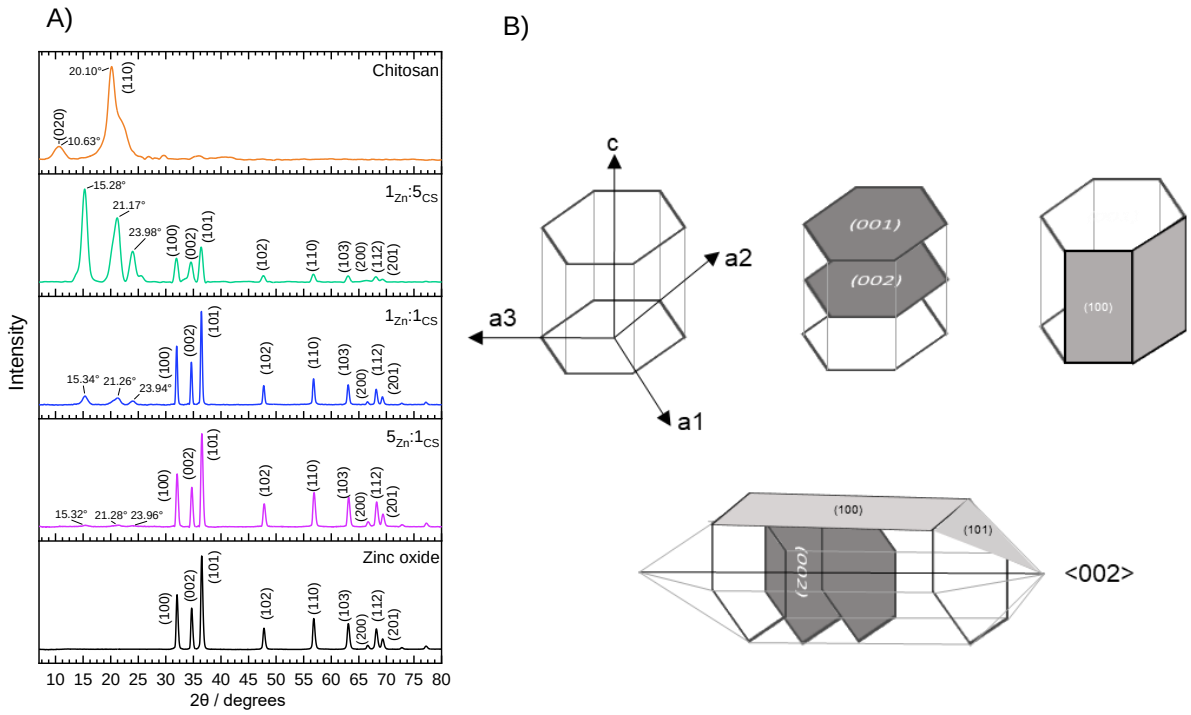

Figure 4.11: A) XRD patterns of chitosan (CS), unmodified zinc oxide, and zinc oxide modified with chitosan at ratios of 1:5; 5:1 and 1:1. B) Representation of zinc oxide hexagonal unit cell and microrod crystal structure, as copied from K. Urs and V. Kamble.

Additionally, N-doped graphene has been reported to form a diffraction peak at 25° (255). Therefore, the diffraction peak at 24.1° might be a result of the carbonaceous network described, doped with nitrogen. Furthermore, Safeera *et al.* formed chitosan-capped ZnO-sodium nanoparticles and reported minute peaks between 23° and 27° which they attributed to the diffraction of chitosan (256). Therefore, it is highly likely that these diffraction peaks (at 15.3°, 21.1° and 24.1°) are linked to functionalised carbonaceous material formed from chitosan during hydrothermal synthesis.

The XRD diffraction patterns in Figure 4.11, with the exception of pure chitosan, are consistent with crystalline ZnO, specifically the hexagonal wurtzite structure (JCPDS card 36-1451) (240). When chitosan is used in excess, the x-ray diffraction peaks are noticeably broadened. Literature states this phenomenon usually occurs when the crystallites are smaller than a micrometre or if lattice defects are abundant in the crystallite (257). If the former is true, it would indicate the formation of nanoparticles

which may provide better solubility, giving a reason as to why the material has enhanced fluorescence (described later in the chapter).

The crystallite size can be determined using the Scherrer equation (186):

$$D = \frac{k\lambda}{\beta_D \cos\theta}$$

where D is the crystallite size (nm), k is Scherrer's constant (0.90) (258), λ is the x-ray wavelength (0.152 nm), β_D is the full width at half-maximum intensity (radians) and θ is the peak position (radians).

Here, the crystallite size was calculated for three key peak positions: 32°, 34.5° and 36.5°, which correspond to lattice planes (100), (002) and (101), to enable comparison between them.

Table 4.1: Crystallite size (nm) of pure and modified ZnO, calculated using the Scherrer equation.

	Crystallite size D (nm)		
Ratio of Zn:CS	**(100)**	**(002)**	**(101)**
No chitosan	20.5	21.4	19.8
1:1	24.7	25.7	23.8
1:5	12.3	9.9	12.4
5:1	18.9	20.0	18.8

The crystallite size increased in this order: $1_{Zn}:5_{CS}$ < $5_{Zn}:1_{CS}$ < no chitosan <$1_{Zn}:1_{CS,}$ at all three peak positions 32°, 34.5° and 36.5° which correspond to lattice planes (100), (002) and (101). As D and β_D are reciprocals in the Scherrer equation, the broader the XRD peaks, the smaller the crystallite size. Here, peak broadening is most prominent for $1_{Zn}:5_{CS}$ and this is reflected in the crystallite size as a large excess of chitosan appears to reduce the crystallite size significantly compared to pure ZnO.

Peak broadening can also be caused by strain on the crystallite, which can affect the *d* spacings. Homogeneous strain typically reduces the *d* spacing while inhomogeneous strain can cause it to increase. From Table 4.2 it is evident that the d spacings are similar for the key peaks, therefore strain is unlikely to be altering the crystallite size.

Table 4.2: *d* spacings for d_{hkl} (100), (002) and (101)

	***d* spacing (Å)**		
Ratio of Zn:CS	**(100)**	**(002)**	**(101)**
No chitosan	2.75	2.55	2.43
1:1	2.76	2.55	2.43
1:5	2.76	2.56	2.43
5:1	2.75	2.55	2.42

The crystallinity of a material can be determined from the XRD pattern using the following equation:

$$Crystallinity = \frac{Area\ of\ crystalline\ peaks}{Area\ of\ all\ peaks\ (crystalline + amorphous)} \times 100$$

As shown in Figure 4.12, unmodified ZnO is > 99 % crystalline while for the modified materials, crystallinity decreases as the ratio of chitosan in the reaction increases, but by no more than 1 %. Overall, the materials maintain their crystallinity well when influenced by chitosan.

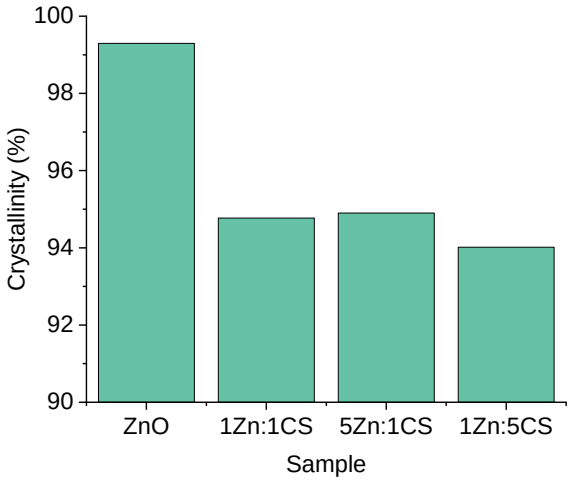

Figure 4.12: Percentage crystallinity of pure and modified zinc oxide

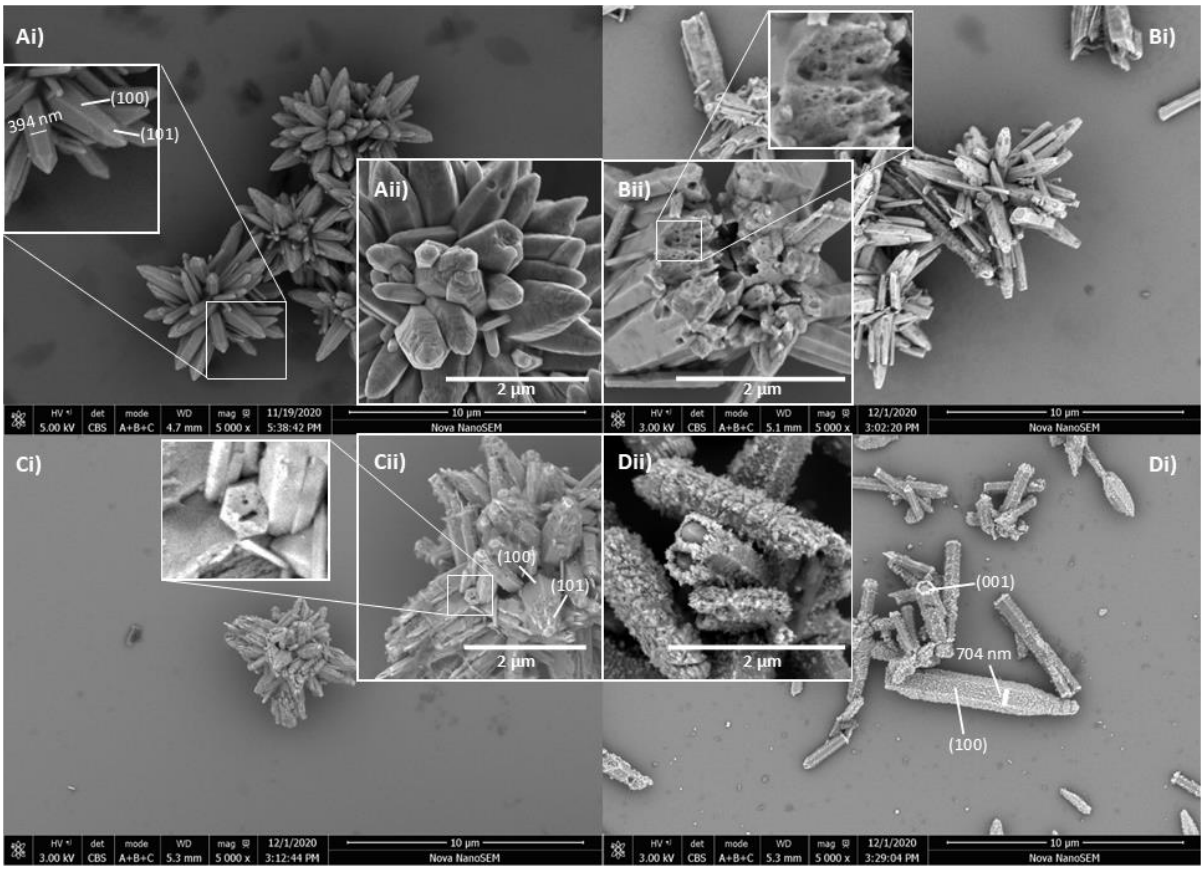

Figure 4.13: SEM images of pure and modified ZnO. Ai - Aii) ZnO; Bi - Bii) 1Zn:1CS, Ci - Cii) 1Zn:5CS, Di - Dii) 5Zn:1CS

Figure 4.11 depicts the hexagonal unit cell and microrod crystal of zinc oxide, taken from K. Urs and V. Kamble (259). Facets (100), (001) and (101) are indicated on the SEM images in Figure 4.13. Before the addition of zinc acetate dihydrate, the combination of 35 % ammonia, chitosan and sodium hydroxide created a highly basic mixture. As shown in the SEM images of pure ZnO, star-like ZnO structures were formed that are consistent with what Marlinda *et al.* achieved at pH 11 (230). Generally, the formation of ZnO occurs as follows (230):

$$NH_3.H_2O \leftrightarrow NH_4^+ + OH^-$$

$$Zn^{2+} + 2OH^- \leftrightarrow Zn(OH)_2$$

$$Zn(OH)_2 \leftrightarrow ZnO + H_2O$$

OH^- ions are abundant in the reaction and react with Zn^{2+} to form zinc hydroxide ($Zn(OH)_2$). On application of heat, a dehydration reaction forces zinc hydroxide to ZnO and water.

At a lower pH of 9, fewer OH^- ions mean the internal structure dictates the growth of ZnO and baton-like structures are formed (230). While, at pH 10-11 more OH^- ions are available to react with Zn^{2+}, this accelerates the production of baton-like structures which, on contact with one another, can spark secondary nucleation and lead to the star-like structures seen. The rate and direction of their growth varies which is in line with what the SEM images show for pure ZnO.

Now to turn the attention to the incorporation of chitosan. When chitosan and Zn precursor were used in a 1:1 ratio, collections of baton-like structures were formed. Much like the star-shaped structures that formed following secondary nucleation for unmodified ZnO, these structures branched off in various directions but in a less regular way. The batons are also of a smaller diameter with blunter ends, rather than the tapered points seen for pure ZnO. Chitosan may be inhibiting the dissolution of ZnO, which can disrupt growth and lead to crystals of a smaller diameter (230).

At a ratio of 5:1 for chitosan and Zn precursor, clusters like the star-like structure of unmodified ZnO, formed, built up of rods. In alignment with the XRD patterns, the ratio of planes 100/002, indicated that the crystals are getting shorter on increase of chitosan, while 100/101 and 002/101 suggested they are less sharp. Here, the crystals are not homogenous, although the familiar facets of ZnO are still apparent. It is expected that chitosan undergoes dehydration, among hydrolysis, decarboxylation and aromatisation during the solvothermal reaction (247). It may have broken down into much smaller fragments during reaction or formed carbonaceous networks which are acting as nucleation sites and leading to this irregular star shape as suggested by Hammi *et al.* (253) in sol-gel synthesis of ZnO.

In an excess of zinc precursor, the preferred structure was a rod/baton shape. This might be because the ratio of free OH^- ions to Zn^{2+} was too few, and so once again the internal structure dictated the growth of ZnO, leading to batons (230). The batons are coated in a nano-sized material which could be early secondary nucleation points.

Aside from the shape, structure, and size of the materials; one of the key observations in the SEM images is the presence of pores. Figure 4.13A shows unmodified ZnO has formed star-like structures with smooth surfaces. In comparison, following the introduction of chitosan in a 1:1 ratio with the Zn precursor, pores and channels are visible in the crystal structure which is evident in Figure 4.13Bii and its corresponding

inset image which shows the pores on an enlarged scale. From the images, the pore size varies (approx. 52.6 nm). Chitosan can form complexes with Zn^{2+} ions (260). With an established affinity for Zn^{2+}, it is possible that during the reaction, chitosan may act as nucleation sites for ZnO. With a melting point of 88°C, chitosan is expected to break down into smaller fragments over the course of the reaction and in doing so, channels might be created as the broken-down chitosan is solubilised.

Pores were also observed, but to a lesser degree, when chitosan was in excess (Figure 4.13Cii and inset). However, in an excess of Zn precursor, pores were not visible with SEM. It seems, that a 1:1 ratio of chitosan and Zn precursor provided the correct balance to produce regular pores and channels in the system, while an excess of either did not. It would be interesting to further explore less dramatic ratios of chitosan and Zn precursor, such as 3:2, and investigate how these factors govern the formation of the pores.

4.3.4. Evaluation of optical properties

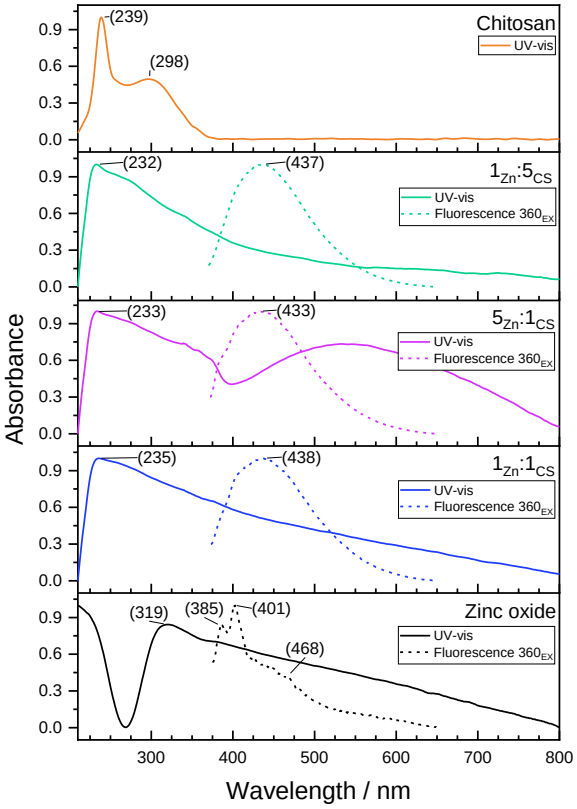

Figure 4.14: UV-vis spectra and fluorescence spectra of chitosan (CS), unmodified zinc oxide and zinc oxide modified with chitosan at ratios of 1:5; 5:1 and 1:1. UV-vis measured at 0.8 mg/mL in 60 % EtOH and normalised between 0 and 1. Fluorescence measured at 0.2 mg/mL in 60 % EtOH and normalised between 0 and 1.

Unmodified ZnO has a broad absorption band (300–800 nm) due to scattering of the particles in suspension, which peaks at 319 nm. Following the inclusion of chitosan into the solvothermal preparation of ZnO, each hybrid material absorbs strongly at approximately 235 nm which fits well with the absorption of pure chitosan (239 nm with a shoulder at 298 nm) and suggests the modified ZnO might share some of the functional groups of chitosan ($-NH_2$, -OH). The intensity of this peak does not change much with the variation of chitosan loading in the reaction. However, there are noticeable differences in the range of 400–800 nm, which suggests particle size is playing a part in the optical response. Additionally, each of the materials modified with chitosan show a fluorescence peak at approximately 435 nm, when excited at 360 nm. It is evident the intensity of emission has increased significantly on inclusion of the chitosan, which exceeds the capabilities of pure ZnO.

4.3.5. Characterisation of supernatants

Following the solvothermal reactions, the products were divided into their respective precipitates and supernatants. However, as the conditions of the reaction are very similar to those used in the preparation of carbon dots, which are characteristically fluorescent, further analysis of the supernatants was pursued. Interestingly, each supernatant showed blue fluorescence under a UV lamp when excited at 365 nm. These solutions were deemed worthy of further investigation and from now on will be labelled as: 1_{Zn}:1_{CS}_SUP, 1_{Zn}:5_{CS}_SUP and 5_{Zn}:1_{CS}_SUP corresponding to supernatants from the following reactions: 1_{Zn}:1_{CS}, 1_{Zn}:5_{CS} and 5_{Zn}:1_{CS}. It is possible that ammonia (from ammonia solution) and acetate (from zinc acetate dihydrate) were involved in the preparation of the suspected carbon nanoparticles in the supernatant. Therefore, an additional reaction was carried out where zinc acetate dihydrate was substituted for ammonium acetate to determine the impact of acetate, denoted as Chitosan CNPs.

The UV-vis spectra of the supernatants share some similarities such as a λ_{max} of 270 nm and a shoulder at 300 nm, which also correspond with the UV-vis profile of chitosan CNPs, albeit less intense shoulders at 267 nm and 302 nm (Figure 4.15). The absorption at 270 nm can be attributed to the $\pi \rightarrow \pi^*$ electronic transitions in the aromatic π system (presence of C=C), while the shoulder at 300 nm is consistent with $n \rightarrow \pi^*$ transitions of C=O groups (253, 261). There is an additional shoulder at 256 nm when chitosan is in excess that shifts hypsochromically as the amount of Zn precursor increases. This might indicate interactions between the aromatic π system and Zn^{2+}.

4.3.6. Summary

After analysis through XRD, SEM, UV-vis, and fluorescence spectroscopy it can be concluded that following the addition of chitosan to the solvothermal synthesis, three materials of crystalline ZnO, consistent with hexagonal wurtzite structure, were formed. Each material was a different shade of brown powder, and successfully extended the absorption profile of ZnO into the UVB region. Each material also showed fluorescence emission at approximately 435 nm, when excited at 360 nm, beyond the capability of pure ZnO. Also, through SEM analysis evidence of pores were found that could indicate that, alongside these enhanced properties, the surface area

of modified ZnO in reaction 1_{Zn}:1_{CS} also excelled. This could have uses in the biomedical field as well as in catalysis.

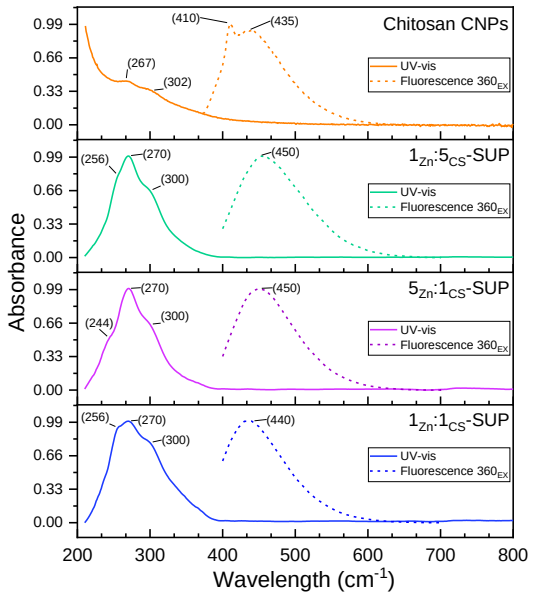

Figure 4.15: UV-vis spectra and corresponding fluorescence (λ_{ex} 360) for chitosan CNPs, and supernatants of unmodified and modified ZnO.

In Figure 4.15, the emission spectra when excited at 360 nm, are also shown. The chitosan CNPs fluoresced at 410 nm, with a broad shoulder at 435 nm. The emission was also measured at several excitation wavelengths between 300 and 400 nm and it was found that the resultant spectra were dependent on the excitation wavelength. A red shift in the emission maximum peak was evident as the excitation wavelength increased. This phenomenon is indicative of carbon dots, and has been reported in several studies, the cause of which may be varying size or functional groups on the surface of the carbon dots (262).

There are some parallels with the emission spectrum of pure chitosan and the supernatants. Firstly, when excited at 360 nm, the emission of the supernatants ranges from 440 – 450 nm, bathochromically shifted from 435 nm for chitosan CNPs. The presence of Zn^{2+} might be influencing this shift. The peak becomes broader as the amount of chitosan increases which might be due to greater abundance of functional groups (carboxylic acids and amines) which could be introducing various defects onto the surface of the carbon dots, affecting fluorescence, or simply more variation in particle size (263).

To conclude, the fluorescence properties of the supernatant are strikingly like those of the pure chitosan carbon dots which strongly suggests they are present in the supernatants and have been formed alongside ZnO in the solvothermal preparation. It also strengthens the idea that the ZnO may have formed around the chitosan-carbon template, which has later degraded into fluorescent carbon dots, in some cases leaving a pores and channels in the ZnO.

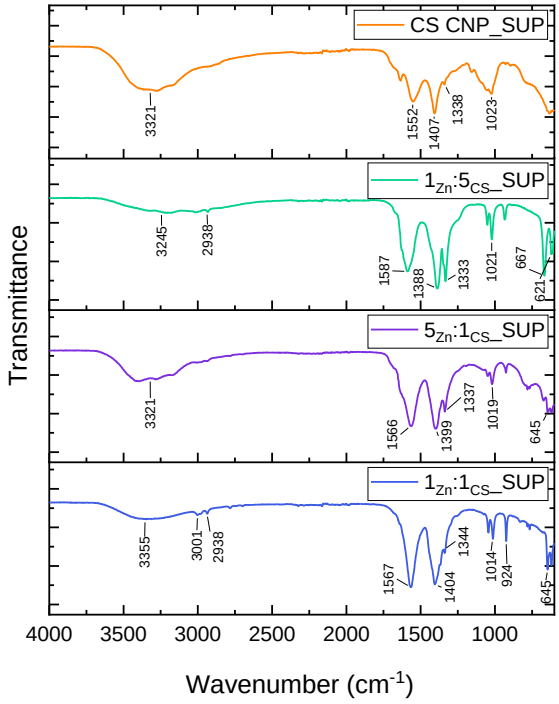

Figure 4.16: FT-IR of dried supernatants corresponding to reactions with no zinc acetate dihydrate, followed by 1:5, 5:1 and 1:1 ratios of zinc acetate dihydrate and chitosan (top to bottom).

The supernatants were dried in the oven at 75°C and then FT-IR analysis was carried out to investigate the chemical structure (Figure 4.16). For pure chitosan, the C-H stretch at approximately 2916 cm^{-1} is a broad peak of medium intensity. However, in all the supernatants including Chitosan CNP the C-H stretch is a much less significant peak, if discernible at all. This, coupled with the loss of intensity of the C-H bending vibrations (1165–992 cm^{-1}) might suggest degradation of the chitosan chain and pyranose ring, through dehydration. Additionally, it is evident that the amine peak (1550–1590 cm^{-1}) is prominent in all supernatants, although in some samples it is better defined than others. Overall, this is consistent with what has been found for amino-functionalised fluorescent CNPs in the literature (264). Additionally, Yang *et al.*

reported the reduction of intensity in the O-H/N-H stretch, which fits with our findings. As the ratio of chitosan to zinc precursor increased, this peak became even weaker.

4.4. Conclusion

To conclude, we have shown two facile methods of modifying the optical and morphological properties of ZnO with organic additives. First, we were able to successfully control the morphology of ZnO in a low temperature reaction, using biodegradable, nanoscale organic additives. Secondly, through preparation of ZnO alongside chitosan we have observed the formation of pores, which could improve the surface activity of ZnO from a catalysis perspective and have proposed a mechanism for the formation of pores and channels in ZnO which could be explored further by honing the ratio of Zn precursor and chitosan. Additionally, the modified ZnO was shown to exhibit some fluorescence which could be useful in biomedicine. Through extending the absorption of light into the UVB region, the material might also have application in skin protection and personal care.

In conjunction to this, we simultaneously produced a suspension of fluorescent nanomaterial which had similar optical properties to chitosan carbon nanoparticles. This material could be useful in bioimaging, for it is fluorescent, however further purification might be needed first.

4.5. Experimental

4.5.1. Characterisation techniques

Infrared spectra (IR) were obtained from solid phases using a Bruker Alpha Platinum ATR FTIR spectrometer with vibrational frequencies (cm^{-1}). The electronic absorption spectra were recorded using a Cary 100 UV-Vis scanning spectrophotometer. Samples for scanning electron microscopic (SEM) analysis were dispersed in ethanol, a drop of suspension was cast onto a silicon wafer attached to an SEM stub using copper films. The samples were viewed with a FEI Nova 450 FEG-SEM operating at 3 kV using a CBS detector at various magnifications. X-Ray diffraction (XRD) of the materials were recorded on Bruker D2-Phaser diffractometer using Cu Kα radiation, with a step size of θ = 0.01013° and x-ray wavelength (λ = 0.152 nm). Bragg's law was used to calculate lattice spacings, and Gaussian fitting was used to measure the full

width at half maximum (FWHM) of the diffraction peaks. The fluorescence spectra were recorded on a FluoroMax-3 spectrofluorometer.

4.5.2. Materials

Zinc acetate dihydrate (97+ %) was supplied by Alfa Aesar. Fischer Scientific provided ammonium acetate, sodium hydroxide pellets and ammonia solution (35 %).

4.5.3. Preparation of ZnO with nanoscale organic additives

4.5.3.1. Preparation of pure ZnO

Zinc acetate dihydrate (0.28 g) was dissolved in sodium hydroxide solution (0.25 M, 10 mL). This was stirred for 15 minutes at room temperature, recorded at pH 10. It was transferred to an autoclave and heated for 3 h at 80 °C, in a hydrothermal oven. The product was washed with water and centrifuged three times, then dried in an oven at 75 °C. Yield: 0.0928 g.

4.5.3.2. Preparation of EthCitCD-ZnO

EthCitCD suspended in water (5 mL) was added to sodium hydroxide solution (0.5 M, 5 mL). Zinc acetate dihydrate (0.28 g) was stirred in for 15 minutes, reading at pH 8. Sodium hydroxide solution (6 M) was added dropwise to attain pH 10. It was transferred to an autoclave and heated for 3 h at 80 °C, in a hydrothermal oven. The product was washed with water and centrifuged three times, then dried in an oven at 75 °C. Yield: 0.0912 g.

4.5.3.3. Preparation of UreCitCD-ZnO

UreCitCD suspended in water (5 mL) was added to sodium hydroxide solution (0.5 M, 5 mL). Zinc acetate dihydrate (0.28 g) was stirred in for 15 minutes, reading at pH 8. Sodium hydroxide solution (6 M) was added dropwise to attain pH 10. It was transferred to an autoclave and heated for 3 h at 80 °C, in a hydrothermal oven. The product was washed with water and centrifuged three times, then dried in an oven at 75 °C. Yield: 0.0960 g.

4.5.4. Preparation of ZnO with a biopolymeric organic additive

4.5.4.1. Preparation of pure ZnO

Zinc acetate dihydrate (0.2752 g) and sodium hydroxide (0.1456 g) were dissolved in 25 % ammonia solution (15 mL). The reactants were set to reflux with stirring, for 1 h at 60 °C, and reached pH 12. Water (5 mL) was added, no change in pH recorded, and the reactants were sealed in an autoclave and heated for 24 h at 180 °C. The product was centrifuged, and both the supernatant and residue solid were collected for analysis. The white solid product was washed with water and centrifuged three times, then dried in an oven at 75 °C.

4.5.4.2. Preparation of ZnO-Chitosan (1:1)

Chitosan (0.2797 g) was added to 25 % ammonia solution (15 mL) and sonicated for 5 minutes at 30 °C. Sodium hydroxide (0.1443 g) and zinc acetate dihydrate (0.2791 g) were added to the suspension, with stirring. The mixture was refluxed for 1 h at 60 °C, and pH 12 was recorded before it was sealed in an autoclave and heated for 24 h at 180 °C. The product was centrifuged, and both the supernatant (pH 10) and residue solid were collected for analysis. The solid product was washed with water and centrifuged three times, then dried in an oven at 75 °C.

4.5.4.3. Preparation of ZnO-Chitosan (1:5)

Chitosan (1.3743 g) was added to 25 % ammonia solution (15 mL) and sonicated for 5 minutes at 30 °C. Sodium hydroxide (0.1386 g) and zinc acetate dihydrate (0.2726 g) were added to the suspension, with stirring. The mixture was refluxed for 1 h at 60 °C, and pH 12 was recorded before it was sealed in an autoclave and heated for 24 h at 180 °C. The product was centrifuged, and both the supernatant (pH 10) and residue solid were collected for analysis. The solid product was washed with water and centrifuged three times, then dried in an oven at 75 °C.

4.5.4.4. Preparation of ZnO-Chitosan (5:1)

Chitosan (0.2796 g) was added to 25 % ammonia solution (15 mL) and sonicated for 5 minutes at 30 °C. Sodium hydroxide (0.1441 g) and zinc acetate dihydrate (1.3737 g) were added to the suspension, with stirring. The mixture was refluxed for 1 h at 60 °C, and pH 12 was recorded before it was sealed in an autoclave and heated for 24 h at 180 °C. The product was centrifuged, and both the supernatant (pH 10) and residue

solid were collected for analysis. The solid product was washed with water and centrifuged three times, then dried in an oven at 75 °C.

4.5.4.5. Preparation of chitosan CNPs

Chitosan (0.2319 g) was added to 25 % ammonia solution (15 mL) and sonicated for 5 minutes at 30 °C. Sodium hydroxide (0.1209 g) and ammonium acetate (0.2330 g) were added to the suspension, with stirring. The mixture was refluxed for 1 h at 60 °C, sealed in an autoclave and heated for 24 h at 180 °C. A suspension of black solid was centrifuged, and both the supernatant (pH 9) and residue solid were collected for analysis. The solid product was washed with water and centrifuged three times, then dried in an oven at 75 °C.

4.6. Appendices

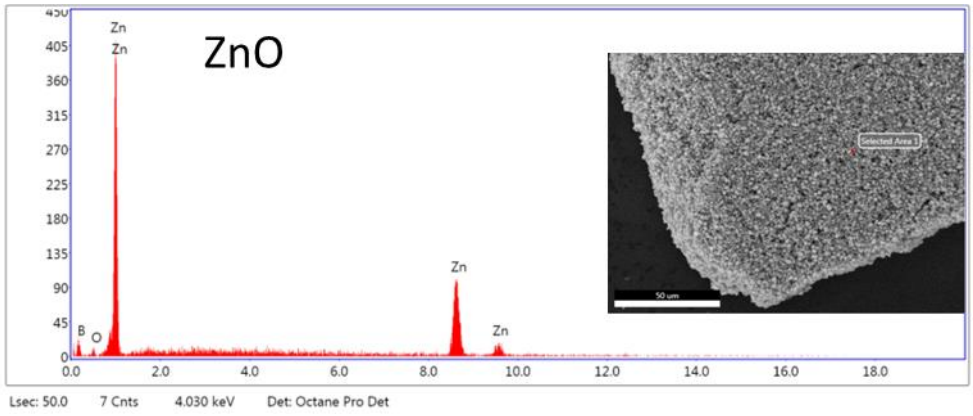

Appendix 4.1: EDX analysis of ZnO

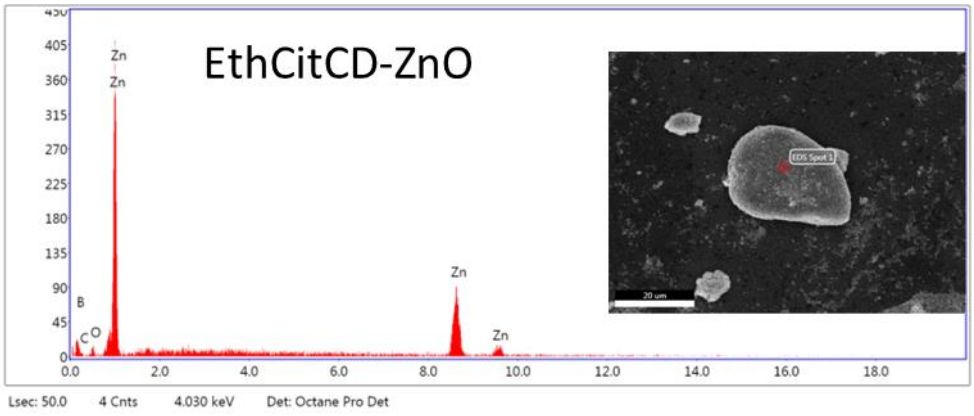

Appendix 4.2: EDX analysis of EthCitCD-ZnO (area 1)

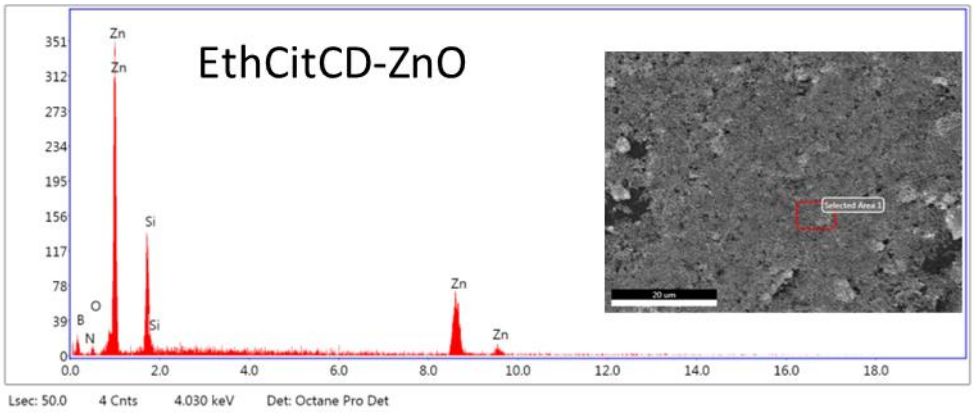

Appendix 4.3: EDX analysis of EthCitCD-ZnO (area 2)

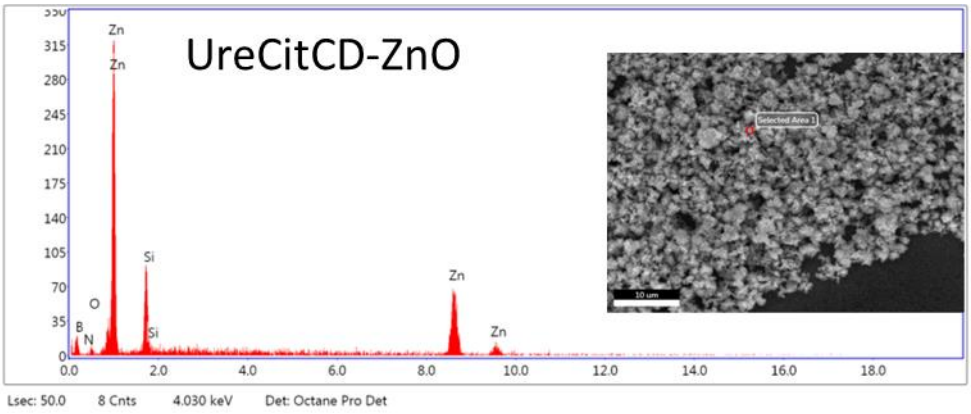

Appendix 4.4: EDX analysis of UreCitCD-ZnO (area 1)

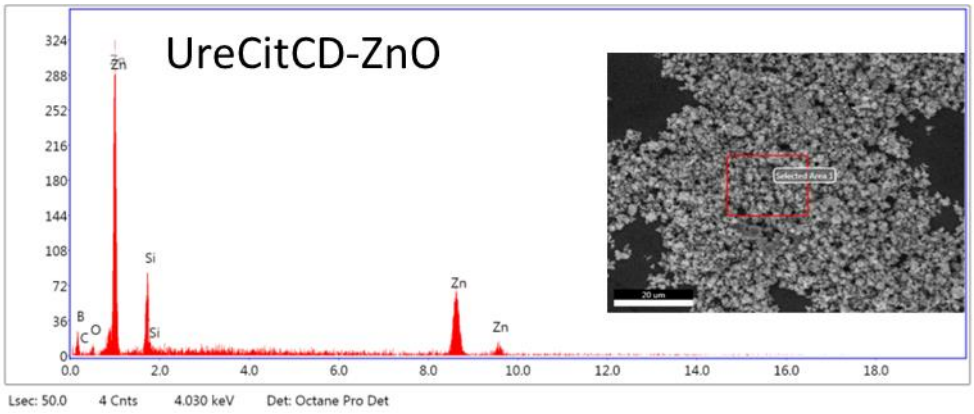

Appendix 4.5: EDX analysis of UreCitCD-ZnO (area 2)

5. Conclusion

A variety of carbon dots have been synthesised by a facile hydrothermal route and assessed for their UV-absorbing abilities, first and foremost. EthCitCD, UreCitCD and VanCitCD were the most promising and showed good potential as UV filters in sunscreen. The materials were characterised by FT-IR, TEM, and fluorescence spectroscopy to confirm the formation of carbon dots

As has been demonstrated, the carbon dots (EthCitCD and UreCitCD) have shown an improvement in the in vitro SPF of two of Croda's sunscreen formulations. Should the funding be acquired at a later stage, in vivo SPF analysis, which is measured by the erythemal response to UV radiation on the skin, would be necessary to confirm the SPF boosting quality induced by EthCitCD and UreCitCD. This is significant at very low loading of carbon dots therefore it would be interesting to investigate the impact of a higher loading, in the formulation. To do so, the carbon dots would need to be concentrated so as not to impact the overall water content of the formulation, which could be done by freeze-drying and redispersing them in less water. Aggregation of the carbon dots in these more concentrated samples may occur as a result, which may alter their optical properties, so this would need to be investigated. Further to this, the UVA blocking power in formulation, in addition to the SPF, could be studied. Cell toxicity must also be determined in order for the carbon dots to be appropriate for use within personal care products.

The carbon dots are shown to be multi-functional in a formulation. On account of their radical scavenging activities, they could be used as an antioxidant within sunscreen formulations or within other personal care products, that frequently contain antioxidants. The benefit here, is a material that can provide both UV filtering and antioxidant activity, simultaneously, produced by one simple reaction. Industry standard antioxidant testing would need to be carried out first.

From reactions with titanium dioxide, it was evident that the incorporation of carbon dots at 6.25 % improved the stability of the suspension over time, compared to pure TiO_2. This, in conjunction with its broad attenuation of UV-HEVL light, might give it dual purpose as an additive in personal care formulations. An assessment of cell toxicity, radical scavenging activity and scalability are the logical next steps for this research.

From the zinc oxide studies, the introduction of carbon dots as nanoscale organic additives, was able to control the morphology of ZnO in a low temperature reaction. However, using a biopolymeric organic additive (chitosan) in place of this formed fluorescent carbon nanomaterial in conjunction with crystalline ZnO with broad UVB attenuation. It would be interesting to explore the inclusion of other biopolymers into this reaction, for the dual formation of fluorescent carbon material and crystalline ZnO as both materials are functional and so the reaction is less wasteful.

This thesis has demonstrated the development of UV filters through facile hydrothermal synthesis reactions, with a focus on carbon dots in sunscreen formulations as well as their ability to enhance the UV attenuation of two metal oxides, through morphological changes. The findings may enable useful advancements in skincare applications, such as sunscreens.

6. References

1. Amsden, B.G. and Goosen, M.F.A. Transdermal delivery of peptide and protein drugs: An overview. *AIChE Journal.* 1995, **41**(8), pp.1972-1997.
2. Dellambra, E. and Dimri, G.P. Cellular Senescence and Skin Aging. In: *Skin Aging Handbook - An Integrated Approach to Biochemistry and Product Development*. William Andrew Publishing, pp.129-148.
3. Fitzpatrick, T.B. and Wolff, K. Fitzpatrick's dermatology in general medicine. In: 7th / Klaus Wolff . [et al.]. ed. New York: McGraw-Hill, 2008.
4. Freinkel, R.K. and Woodley, D. *The biology of the skin.* New York: Parthenon, 2001.
5. Hay, R.J., Augustin, M., Griffiths, C.E.M., Sterry, W., Abuabara, K., Airoldi, M., Ajose, F., Albert, S., Armstrong, A., Asgari, M., Bevan, G., Blume-Peytavi, U., Bohannon, B., Bolognia, J., Bordeaux, J., Boyers, L., Brewer, J., Camacho-Martinez, F., Ocampo-Candiani, J., Chen, S., Chren, M.M., Cohen, A., Dalgard, F., Dellavalle, B., Dommasch, E., Ehrlich, A., Eide, M., Estrada-Castaňon, R., Ettarp, L., Chul-Eun, H., Fuller, C., Gavin, A., Gelfand, J., Gottlieb, A., Grossmann, H., Henriksen, O., Ho, R., Hodin, M., Hong-Hu, C., Jerajani, H., Karimkhani, C., Katz, K., Ghani-Kibbi, A., Kroshinsky, D., Langan, S., Laumann, A., Lui, H., Maloney, M., Markova, A., Marks, R., Masenga, J., McKee, M., Miyachi, Y., Moertz, C., Moreau, J., Mostow, E., Naldi, L., Norton, S., Pariser, D., Poirier, V., Qureshi, A., Ramos-e-Silva, M., Reusch, M., Rhodes, A., Sadwani, D., Saurat, J.H., Seacrest, A., Severens, H., Shalom, G., Shapiro, J., Solomon, J., Svensson, A., Tan, J., Wienstock, M., Williams, H., Wu, J., Zhang, X., Board Int League Dermatological, S., Board Grand Challenges, C. and Board of the International League of Dermatological, S. The global challenge for skin health. *British Journal of Dermatology.* 2015, **172**(6), pp.1469-1472.
6. *Structure and Function of the Skin.* [Online]. 2018. [Accessed 20/02/18]. Available from:http://www.clinimed.co.uk/Wound-Care/Education/Wound-Essentials/Structure-and-Function-of-the-Skin.aspx
7. Thakur, R., Batheja, P., Kaushik, D. and Michniak, B. Chapter 4 - Structural and Biochemical Changes in Aging Skin and Their Impact on Skin Permeability Barrier. In: Dayan, N. ed. *Skin Aging Handbook*. Norwich, NY: William Andrew Publishing, 2009, pp.55-90.
8. Hwa, C., Bauer, E.A. and Cohen, D.E. Skin biology. *Dermatologic Therapy.* 2011, **24**(5), pp.464-470.
9. Menon, G.K. New insights into skin structure: scratching the surface. *Advanced Drug Delivery Reviews.* 2002, **54**, pp.S3-S17.
10. Burke, K.E. Prevention and Treatment of Aging Skin with Topical Antioxidants. In: *Skin Aging Handbook - An Integrated Approach to Biochemistry and Product Development*. William Andrew Publishing, pp.149-176.
11. Schroeder, P., Haendeler, J. and Krutmann, J. The role of near infrared radiation in photoaging of the skin. *Experimental Gerontology.* 2008, **43**(7), pp.629-632.
12. Mattson, B., Myers, J.D. and Newman, P. *The Electromagnetic Spectrum.* [Online]. 2014. [Accessed 03/03/22]. Available from: https://imagine.gsfc.nasa.gov/science/toolbox/emspectrum1.html
13. Atkins, P.W. and De Paula, J. *Elements of physical chemistry.* Fifth edition / Peter Atkins, Julio De Paula. ed. Oxford: Oxford University Press, 2009.

14. Dupont, E., Gomez, J. and Bilodeau, D. Beyond UV radiation: A skin under challenge. *International Journal of Cosmetic Science.* 2013, **35**(3), pp.224-232.
15. Romanhole, R.C., Ataide, J.A., Moriel, P. and Mazzola, P.G. Update on ultraviolet A and B radiation generated by the sun and artificial lamps and their effects on skin. *International Journal of Cosmetic Science.* 2015, **37**(4), pp.366-370.
16. Kaur, B. Sunscreens and their properties for skin protection from solar radiation. *Journal of Aesthetic Nursing.* 2017, **6**(2), pp.60-67.
17. Muller, R., Montzka, S.A., Salawitch, R., Harris, N., Tilmes, S., Garcia, R., Von Hobe, M., Stroh, F., Peter, T. and Crutzen, P. *Stratospheric Ozone Depletion and Climate Change.* 1 ed. Cambridge: Royal Society Of Chemistry, 2012.
18. Newman, P.A., Oman, L.D., Douglass, A.R., Fleming, E.L., Frith, S.M., Hurwitz, M.M., Kawa, S.R., Jackman, C.H., Krotkov, N.A., Nash, E.R., Nielsen, J.E., Pawson, S., Stolarski, R.S. and Velders, G.J.M. What would have happened to the ozone layer if chlorofluorocarbons (CFCs) had not been regulated? *Atmospheric Chemistry and Physics.* 2009, **9**(6), pp.2113-2128.
19. Rousseaux, M.C., Ballare, C.L., Giordano, C.V., Scopel, A.L., Zima, A.M., Szwarcberg-Bracchitta, M., Searles, P.S., Caldwell, M.M. and Diaz, S.B. Ozone Depletion and UVB Radiation: Impact on Plant DNA Damage in Southern South America. *Proceedings of the National Academy of Sciences of the United States of America.* 1999, **96**(26), pp.15310-15315.
20. European Commission. *Protection of the Ozone Layer.* [Online]. [Accessed 03/03/22]. Available from: https://ec.europa.eu/clima/eu-action/protection-ozone-layer_en
21. Cefali, L.C., Ataide, J.A., Moriel, P., Foglio, M.A. and Mazzola, P.G. Plant-based active photoprotectants for sunscreens. *International Journal of Cosmetic Science.* 2016, **38**(4), pp.346-353.
22. Kimlin, M.G. Geographic location and vitamin D synthesis. *Molecular Aspects of Medicine.* 2008, **29**(6), pp.453-461.
23. Hung, M.-W., Lin, Y.-H., Chang, H.-C. and Huang, K.-C. Spectral analysis of natural solar ultraviolet B to promote synthesis of vitamin D. *Optical Review.* 2016, **23**(5), pp.792-797.
24. Smith, E.L. and Holick, M.F. The skin: The site of vitamin D3 synthesis and a target tissue for its metabolite 1,25-dihydroxyvitamin D3. *Steroids.* 1987, **49**(1), pp.103-131.
25. Dmitrenko, O. and Reischl, W. *Previtamin D Photosynthesis In Vitro.* [Online]. [Accessed 23/02/2018]. Available from: http://www.photobiology.com/reviews/previtamin/index.html
26. Holick, M.F., Smith, E. and Pincus, S. Skin as the site of vitamin D synthesis and target tissue for 1,25-dihydroxyvitamin D3. Use of calcitriol (1,25-dihydroxyvitamin D3) for treatment of psoriasis. *Arch Dermatol.* 1987, **123**(12), pp.1677-1683a.
27. Lyons, A.B., Trullas, C., Kohli, I., Hamzavi, I.H. and Lim, H.W. Photoprotection beyond ultraviolet radiation: A review of tinted sunscreens. *Journal of the American Academy of Dermatology.* 2021, **84**(5), pp.1393-1397.
28. Schroeder, P., Lademann, J., Darvin, M.E., Stege, H., Marks, C., Bruhnke, S. and Krutmann, J. Infrared Radiation-Induced Matrix Metalloproteinase in Human Skin: Implications for Protection. *Journal of Investigative Dermatology.* 2008, **128**(10), pp.2491-2497.
29. Barolet, D., Christiaens, F. and Hamblin, M.R. Infrared and skin: Friend or foe. *Journal of Photochemistry and Photobiology B: Biology.* 2016, **155**, pp.78-85.

30. Danno, K., Mori, N., Toda, K., Kobayashi, T. and Utani, A. Near-infrared irradiation stimulates cutaneous wound repair: laboratory experiments on possible mechanisms. *Photodermatol Photoimmunol Photomed.* 2001, **17**(6), pp.261-265.
31. González, S., Fernández-Lorente, M. and Gilaberte-Calzada, Y. The latest on skin photoprotection. *Clinics in Dermatology.* 2008, **26**(6), pp.614-626.
32. Gallagher, R.P. and Lee, T.K. Adverse effects of ultraviolet radiation: A brief review. *Progress in Biophysics and Molecular Biology.* 2006, **92**(1), pp.119-131.
33. Flo, A., Calpena, A.C., Díez-Noguera, A., Pozo, A. and Cambras, T. Daily Variation of UV-induced Erythema and the Action of Solar Filters. *Photochemistry and Photobiology.* 2017, **93**(2), pp.632-635.
34. Poljšak, B. and Dahmane, R. Free Radicals and Extrinsic Skin Aging. *Dermatology Research and Practice.* 2012, **2012**, p.135206.
35. Klaunig, J.E. and Kamendulis, L.M. The role of oxidative stress in carcinogenesis. *Annu Rev Pharmacol Toxicol.* 2004, **44**, pp.239-267.
36. Pizzino, G., Irrera, N., Cucinotta, M., Pallio, G., Mannino, F., Arcoraci, V., Squadrito, F., Altavilla, D. and Bitto, A. Oxidative Stress: Harms and Benefits for Human Health. *Oxidative medicine and cellular longevity.* 2017, **2017**, pp.8416763-8416763.
37. Naylor, E.C., Watson, R.E.B. and Sherratt, M.J. Molecular aspects of skin ageing. *Maturitas.* 2011, **69**(3), pp.249-256.
38. Schaeffer, H.J. and Weber, M.J. Mitogen-activated protein kinases: specific messages from ubiquitous messengers. *Mol Cell Biol.* 1999, **19**(4), pp.2435-2444.
39. Schroeder, P., Pohl, C., Calles, C., Marks, C., Wild, S. and Krutmann, J. Cellular response to infrared radiation involves retrograde mitochondrial signaling. *Free Radical Biology and Medicine.* 2007, **43**(1), pp.128-135.
40. Krutmann, J. and Schroeder, P. Role of Mitochondria in Photoaging of Human Skin: The Defective Powerhouse Model. *Journal of Investigative Dermatology Symposium Proceedings.* 2009, **14**(1), pp.44-49.
41. Calles, C., Schneider, M., Macaluso, F., Benesova, T., Krutmann, J. and Schroeder, P. Infrared A Radiation Influences the Skin Fibroblast Transcriptome: Mechanisms and Consequences. *Journal of Investigative Dermatology.* 2010, **130**(6), pp.1524-1536.
42. Ritter, J.W., Berg, H. and Richter, K. *Entdeckungen zur Elektrochemie, Bioelektrochemie und Photochemie.* Leipzig: Geest & Portig, 1986.
43. Home, E. I. On the black rete mucosum of the Negro, being a defence against the scorching effect of the sun's rays. *Philosophical Transactions of the Royal Society of London.* 1820, **111**, pp.1-6.
44. Widmark, E.J. Über den Einfluss des Lichtes auf die Haut. . *Hygiea.* 1889, **3**, pp.1-22.
45. Santos, A.C., Marto, J., Chá-Chá, R., Martins, A.M., Pereira-Silva, M., Ribeiro, H.M. and Veiga, F. Nanotechnology-based sunscreens—a review. *Materials Today Chemistry.* 2022, **23**, p.100709.
46. Sambandan, D.R. and Ratner, D. Sunscreens: An overview and update. *Journal of the American Academy of Dermatology.* 2011, **64**(4), pp.748-758.
47. Vantage. *Liposhield TM.* [Online]. 2020. [Accessed 09/03/2022]. Available from: https://www.vantagegrp.com/en-US/Product/Page/d939f1f0-ffe3-4038-bf77-b108258858f5/Liposhield
48. Bernstein, E.F., Sarkas, H.W. and Boland, P. Iron oxides in novel skin care formulations attenuate blue light for enhanced protection against skin damage. *Journal of Cosmetic Dermatology.* 2021, **20**(2), pp.532-537.

49. Guan, L.L., Lim, H.W. and Mohammad, T.F. Sunscreens and Photoaging: A Review of Current Literature. *American Journal of Clinical Dermatology.* 2021, **22**(6), pp.819-828.
50. Schroeder, P., Calles, C. and Krutmann, J. Prevention of infrared-A radiation mediated detrimental effects in human skin. *Skin Therapy Lett.* 2009, **14**(5), pp.4-5.
51. Osterwalder, U. and Herzog, B. Chemistry and properties of organic and inorganic UV filters. In: *Clinical guide to sunscreens and photoprotection*. CRC Press, 2008, pp.27-54.
52. Irshad, M.A., Nawaz, R., Rehman, M.Z.u., Adrees, M., Rizwan, M., Ali, S., Ahmad, S. and Tasleem, S. Synthesis, characterization and advanced sustainable applications of titanium dioxide nanoparticles: A review. *Ecotoxicology and environmental safety.* 2021, **212**, p.111978.
53. *Opinion on titanium dioxide (nano form) as UV-filter in sprays 2019*.
54. Newman, M.D., Stotland, M. and Ellis, J.I. The safety of nanosized particles in titanium dioxide- and zinc oxide-based sunscreens. *Journal of the American Academy of Dermatology.* 2009, **61**(4), pp.685-692.
55. Fournier, K., Marina, N., Joshi, N., Berthiaume, V.R., Currie, S., Lanterna, A.E. and Scaiano, J.C. Scale-up of a photochemical flow reactor for the production of lignin-coated titanium dioxide as a sunscreen ingredient. *Journal of Photochemistry and Photobiology.* 2021, **7**, p.100040.
56. Brezová, V., Gabčová, S., Dvoranová, D. and Staško, A. Reactive oxygen species produced upon photoexcitation of sunscreens containing titanium dioxide (an EPR study). *Journal of Photochemistry and Photobiology B: Biology.* 2005, **79**(2), pp.121-134.
57. Yu, B., Ai, K.L. and Lu, L.H. Dual-protective nano-sunscreen enables high-efficient elimination of the self-derived hazards. *Applied Materials Today.* 2020, **18**.
58. European Commission. *Commission Regulation (EU) 2016/621 of 21 April 2016 amending Annex VI to Regulation (EC) No 1223/2009 of the European Parliament and of the Council on cosmetic products.* [Online]. 2016. [Accessed 10/03/22]. Available from: https://eur-lex.europa.eu/legalcontent/EN/TXT/PDF/?uri=CELEX:32016R0621&rid=1
59. Karlsson, I., Hillerström, L., Stenfeldt, A.-L., Mårtensson, J. and Börje, A. Photodegradation of Dibenzoylmethanes: Potential Cause of Photocontact Allergy to Sunscreens. *Chemical Research in Toxicology.* 2009, **22**(11), pp.1881-1892.
60. Safety, S.C.o.C. *Opinion of the Scientific Committee on Consumer Safety on Octocrylene.* [Online]. 2021. [Accessed 10/03/22]. Available from: https://ec.europa.eu/health/system/files/2021-04/sccs_o_249_0.pdf
61. Lim, H.W. and Draelos, Z.D. *Clinical Guide to Sunscreens and Photoprotection*. Wolters Kluwer Health, Inc. 2009, 10, p.279.
62. Afonso, S., Horita, K., Sousa e Silva, J.P., Almeida, I.F., Amaral, M.H., Lobão, P.A., Costa, P.C., Miranda, M.S., Esteves da Silva, J.C.G. and Sousa Lobo, J.M. Photodegradation of avobenzone: Stabilization effect of antioxidants. *Journal of Photochemistry and Photobiology B: Biology.* 2014, **140**, pp.36-40.
63. Burnett, M.E. and Wang, S.Q. Current sunscreen controversies: a critical review. Photodermatology Photoimmunology & Photomedicine. 2011, **27**(2), pp.58-67.
64. Jiang, R., Roberts, M.S., Collins, D.M. and Benson, H.A.E. Absorption of sunscreens across human skin: An evaluation of commercial products for children and adults. *British Journal of Clinical Pharmacology.* 1999, **48**(4), pp.635-637.

65. Schneider, S.L. and Lim, H.W. Review of environmental effects of oxybenzone and other sunscreen active ingredients. *Journal of the American Academy of Dermatology.* 2019, **80**(1), pp.266-271.
66. Danovaro, R., Bongiorni, L., Corinaldesi, C., Giovannelli, D., Damiani, E., Astolfi, P., Greci, L. and Pusceddu, A. Sunscreens Cause Coral Bleaching by Promoting Viral Infections. *Environmental Health Perspectives.* 2008, **116**(4), pp.441-447.
67. Downs, C.A., Bishop, E., Diaz-Cruz, M.S., Haghshenas, S.A., Stien, D., Rodrigues, A.M.S., Woodley, C.M., Sunyer-Caldú, A., Doust, S.N., Espero, W., Ward, G., Farhangmehr, A., Tabatabaee Samimi, S.M., Risk, M.J., Lebaron, P. and DiNardo, J.C. Oxybenzone contamination from sunscreen pollution and its ecological threat to Hanauma Bay, Oahu, Hawaii, U.S.A. *Chemosphere.* 2022, **291**, p.132880.
68. Fernández-García, E. Skin protection against UV light by dietary antioxidants. *FOOD & FUNCTION.* 2014, **5**(9), pp.1994-1923.
69. Yaar, M. and Gilchrest, B.A. Photoageing: mechanism, prevention and therapy. *British Journal of Dermatology.* 2007, **157**(5), pp.874-887.
70. Stahl, W. and Sies, H. Carotenoids and Flavonoids Contribute to Nutritional Protection against Skin Damage from Sunlight. *Molecular Biotechnology.* 2007, **37**(1), pp.26-30.
71. Pietta, P.G. Flavonoids as antioxidants. *Journal of Natural Products.* 2000, **63**(7), pp.1035-1042.
72. U.S. Food and Drug Administration. *What we do.* [Online]. 2018. [Accessed 10/03/22]. Available from: https://www.fda.gov/about-fda/what-we-do
73. European Chemicals Agency. *Cosmetic Products Regulation, Annex VI - Allowed UV Filters.* [Online]. [Accessed 19/02/22]. Available from: https://echa.europa.eu/cosmetics-uv-filters
74. European Chemicals Agency. *Understanding REACH.* [Online]. [Accessed 19/02/2022]. Available from: https://echa.europa.eu/regulations/reach/understanding-reach
75. *Regulation (EC) No 1272/2008 of the European Parliament and of the Council of 16 December 2008 on classification, labelling and packaging of substances and mixtures, amending and repealing Directives 67/548/EEC and 1999/45/EC, and amending Regulation (EC) No 1907/2006 2008*.
76. European Chemicals Agency. *Authorisation.* [Online]. [Accessed 19/02/22]. Available from: https://echa.europa.eu/substances-of-very-high-concern-identification-explained
77. *Commission Regulation (EU) 2021/850 of 26 May 2021 amending and correcting Annex II and amending Annexes III, IV and VI to Regulation (EC) No 1223/2009 of the European Parliament and of the Council on cosmetic products (Text with EEA relevance) 2021*.
78. Roelandts, R. Clinical Guide to Sunscreens and Photoprotection. In: Wolters Kluwer Health, Inc, 2009, p.279.
79. European Commission. *Commission Recommendation of 22 September 2006 on the efficacy of sunscreen products and the claims made relating thereto (notified under document number C(2006) 4089).* [Online]. 2006. [Accessed]. Available from: http://data.europa.eu/eli/reco/2006/647/oj
80. Boots. *UVA, UVB & SPF - what you need to know.* [Online]. 2022. [Accessed]. Available from: https://www.boots.com/inspiration-advice/sun-and-holiday-inspiration/suncare-advice/spf-factors-uva-and-uvb

81. Xu, X., Ray, R., Gu, Y., Ploehn, H.J., Gearheart, L., Raker, K. and Scrivens, W.A. Electrophoretic Analysis and Purification of Fluorescent Single-Walled Carbon Nanotube Fragments. *Journal of the American Chemical Society.* 2004, **126**(40), pp.12736-12737.
82. Bourlinos, A.B., Stassinopoulos, A., Anglos, D., Zboril, R., Georgakilas, V. and Giannelis, E.P. Photoluminescent Carbogenic Dots. *Chemistry of Materials.* 2008, **20**(14), pp.4539-4541.
83. Cao, L., Wang, X., Meziani, M.J., Lu, F., Wang, H., Luo, P.G., Lin, Y., Harruff, B.A., Veca, L.M., Murray, D., Xie, S.-Y. and Sun, Y.-P. Carbon Dots for Multiphoton Bioimaging. *Journal of the American Chemical Society.* 2007, **129**(37), pp.11318-11319.
84. Baker, S.N. and Baker, G.A. Luminescent Carbon Nanodots: Emergent Nanolights. Angewandte Chemie-International Edition. 2010, **49**(38), pp.6726-6744.
85. Lim, S.Y., Shen, W. and Gao, Z.Q. Carbon quantum dots and their applications. *Chemical Society Reviews.* 2015, **44**(1), pp.362-381.
86. Yao, B., Huang, H., Liu, Y. and Kang, Z. Carbon Dots: A Small Conundrum. *Trends in Chemistry.* 2019, **1**(2), pp.235-246.
87. Hu, S.L., Niu, K.Y., Sun, J., Yang, J., Zhao, N.Q. and Du, X.W. One-step synthesis of fluorescent carbon nanoparticles by laser irradiation. *Journal of Materials Chemistry.* 2009, **19**(4), pp.484-488.
88. Sharma, V., Tiwari, P. and Mobin, S.M. Sustainable carbon-dots: recent advances in green carbon dots for sensing and bioimaging. *Journal of Materials Chemistry B.* 2017, **5**(45), pp.8904-8924.
89. Sun, Y.-P., Zhou, B., Lin, Y., Wang, W., Fernando, K.A.S., Pathak, P., Meziani, M.J., Harruff, B.A., Wang, X., Wang, H., Luo, P.G., Yang, H., Kose, M.E., Chen, B., Veca, L.M. and Xie, S.-Y. Quantum-Sized Carbon Dots for Bright and Colorful Photoluminescence. *Journal of the American Chemical Society.* 2006, **128**(24), pp.7756-7757.
90. Yang, H., Yang, L., Yuan, Y.S., Pan, S., Yang, J.D., Yan, J.J., Zhang, H., Sun, Q.Q. and Hu, X.L. A portable synthesis of water-soluble carbon dots for highly sensitive and selective detection of chlorogenic acid based on inner filter effect. *Spectrochimica Acta Part A - Molecular and Biomolecular Spectroscopy.* 2018, **189**, pp.139-146.
91. Namdari, P., Negahdari, B. and Eatemadi, A. Synthesis, properties and biomedical applications of carbon-based quantum dots: An updated review. *Biomedicine & Pharmacotherapy.* 2017, **87**, pp.209-222.
92. Cui, L., Ren, X., Sun, M., Liu, H. and Xia, L. Carbon Dots: Synthesis, Properties and Applications. *Nanomaterials.* 2021, **11**(12).
93. Wang, Y.F. and Hu, A.G. Carbon quantum dots: synthesis, properties and applications. *Journal of Materials Chemistry C.* 2014, **2**(34), pp.6921-6939.
94. Deng, J., Lu, Q., Mi, N., Li, H., Liu, M., Xu, M., Tan, L., Xie, Q., Zhang, Y. and Yao, S. Electrochemical Synthesis of Carbon Nanodots Directly from Alcohols. *Chemistry – A European Journal.* 2014, **20**(17), pp.4993-4999.
95. Hu, S.-L., Niu, K.-Y., Sun, J., Yang, J., Zhao, N.-Q. and Du, X.-W. One-step synthesis of fluorescent carbon nanoparticles by laser irradiation. *Journal of Materials Chemistry.* 2009, **19**(4), pp.484-488.
96. Liu, Y., Xiao, N., Gong, N., Wang, H., Shi, X., Gu, W. and Ye, L. One-step microwave-assisted polyol synthesis of green luminescent carbon dots as optical nanoprobes. *Carbon.* 2014, **68**, pp.258-264.

97. Pires, N.R., Santos, C.M., Sousa, R.R., Paula, R., Cunha, P.L. and Feitosa, J.J.J.o.t.B.C.S. Novel and fast microwave-assisted synthesis of carbon quantum dots from raw cashew gum. 2015, **26**, pp.1274-1282.
98. Bandi, R., Gangapuram, B.R., Dadigala, R., Eslavath, R., Singh, S.S. and Guttena, V. Facile and green synthesis of fluorescent carbon dots from onion waste and their potential applications as sensor and multicolour imaging agents. *RSC Advances.* 2016, **6**(34), pp.28633-28639.
99. Mewada, A., Pandey, S., Shinde, S., Mishra, N., Oza, G., Thakur, M., Sharon, M. and Sharon, M. Green synthesis of biocompatible carbon dots using aqueous extract of Trapa bispinosa peel. *Materials Science and Engineering: C.* 2013, **33**(5), pp.2914-2917.
100. Zhu, L., Yin, Y., Wang, C.-F. and Chen, S. Plant leaf-derived fluorescent carbon dots for sensing, patterning and coding. *Journal of Materials Chemistry C.* 2013, **1**(32), pp.4925-4932.
101. Sahu, S., Behera, B., Maiti, T.K. and Mohapatra, S. Simple one-step synthesis of highly luminescent carbon dots from orange juice: application as excellent bio-imaging agents. *Chemical Communications.* 2012, **48**(70), pp.8835-8837.
102. Shi, L., Li, X., Li, Y., Wen, X., Li, J., Choi, M.M.F., Dong, C. and Shuang, S. Naked oats-derived dual-emission carbon nanodots for ratiometric sensing and cellular imaging. *Sensors and Actuators B: Chemical.* 2015, **210**, pp.533-541.
103. Mehta, V.N., Jha, S., Singhal, R.K. and Kailasa, S.K. Preparation of multicolor emitting carbon dots for HeLa cell imaging. *New Journal of Chemistry.* 2014, **38**(12), pp.6152-6160.
104. Wang, L. and Zhou, H.S. Green Synthesis of Luminescent Nitrogen-Doped Carbon Dots from Milk and Its Imaging Application. *Analytical Chemistry.* 2014, **86**(18), pp.8902-8905.
105. Wareing, T.C., Gentile, P. and Phan, A.N. Biomass-Based Carbon Dots: Current Development and Future Perspectives. *ACS Nano.* 2021, **15**(10), pp.15471-15501.
106. Wu, X., Zhang, B. and Hu, Z. Large-scale and additive-free hydrothermal synthesis of lamellar morphology boehmite. *Powder Technology.* 2013, **239**, pp.155-161.
107. Pajewska-Szmyt, M., Buszewski, B. and Gadzała-Kopciuch, R. Sulphur and nitrogen doped carbon dots synthesis by microwave assisted method as quantitative analytical nano-tool for mercury ion sensing. *Materials Chemistry and Physics.* 2020, **242**, p.122484.
108. Jiang, C., Wu, H., Song, X., Ma, X., Wang, J. and Tan, M. Presence of photoluminescent carbon dots in Nescafe® original instant coffee: Applications to bioimaging. *Talanta.* 2014, **127**, pp.68-74.
109. Gholinejad, M., Najera, C., Hamed, F., Seyedhamzeh, M., Bahrami, M. and Kompany-Zareh, M. Green synthesis of carbon quantum dots from vanillin for modification of magnetite nanoparticles and formation of palladium nanoparticles: Efficient catalyst for Suzuki reaction. *Tetrahedron.* 2017, **73**(38), pp.5585-5592.
110. Shan, D.Y., Hsieh, J.T., Bai, X.C. and Yang, J. Citrate-Based Fluorescent Biomaterials. *Advanced Healthcare Materials.* 2018, **7**(18).
111. Song, Y., Zhu, S., Zhang, S., Fu, Y., Wang, L., Zhao, X. and Yang, B. Investigation from chemical structure to photoluminescent mechanism: a type of carbon dots from the pyrolysis of citric acid and an amine. *Journal of Materials Chemistry C.* 2015, **3**(23), pp.5976-5984.

112. Li, H., Yan, X., Kong, D., Jin, R., Sun, C., Du, D., Lin, Y. and Lu, G. Recent advances in carbon dots for bioimaging applications. *Nanoscale Horizons.* 2020, **5**(2), pp.218-234.
113. Hsu, P.-C., Shih, Z.-Y., Lee, C.-H. and Chang, H.-T. Synthesis and analytical applications of photoluminescent carbon nanodots. *Green Chemistry.* 2012, **14**(4), pp.917-920.
114. Dong, Y., Pang, H., Yang, H.B., Guo, C., Shao, J., Chi, Y., Li, C.M. and Yu, T. Carbon-Based Dots Co-doped with Nitrogen and Sulfur for High Quantum Yield and Excitation-Independent Emission. *Angewandte Chemie-International Edition.* 2013, **52**(30), pp.7800-7804.
115. Tetsuka, H., Asahi, R., Nagoya, A., Okamoto, K., Tajima, I., Ohta, R. and Okamoto, A. Optically Tunable Amino-Functionalized Graphene Quantum Dots. *Advanced Materials.* 2012, **24**(39), pp.5333-5338.
116. Sam, D.M. and Vergheese, M. Fluorescent N-doped Carbon Dot-Copper and Silver Nanocomposite - An effective uric acid sensor. *Indian Journal of Biochemistry & Biophysics.* 2021, **58**(6), pp.590-601.
117. Abbasi, A. and Shakir, M. Simple One-step Solid-state Synthesis of Highly Crystalline N Doped Carbon Dots As Selective Turn Off-sensor for Picric Acid and Metanil Yellow. *Journal of Fluorescence.* 2022, **32**(3), pp.1239-1246.
118. Zhou, N., Shi, Y.P., Sun, C., Zhang, X.W. and Zhao, W. Carbon quantum dot-AgOH colloid fluorescent probe for selective detection of biothiols based on the inner filter effect. *Sprectrochimica Acta Part A - Molecular and Biomolecular Spectroscopy.* 2020, **228**.
119. Gan, J., Wu, Y., Yang, F., Wu, X., Wang, Y. and Wang, J. UV-Filtering Cellulose Nanocrystal/Carbon Quantum Dot Composite Films for Light Conversion in Glass Windows. *ACS Applied Nano Materials.* 2021, **4**(11), pp.12552-12560.
120. Xie, Z., Du, Q.Q., Wu, Y.Z., Hao, X.P. and Liu, C.Y. Full-band UV shielding and highly daylight luminescent silane-functionalized graphene quantum dot nanofluids and their arbitrary polymerized hybrid gel glasses. *Journal of Materials Chemistry C.* 2016, **4**(41), pp.9879-9886.
121. Park, S.J., Yang, H.K. and Moon, B.K. Ultraviolet to blue blocking and wavelength convertible films using carbon dots for interrupting eye damage caused by general lighting. *Nano Energy.* 2019, **60**, pp.87-94.
122. Hu, G., Lei, B., Jiao, X., Wu, S., Zhang, X., Zhuang, J., Liu, X., Hu, C. and Liu, Y. Synthesis of modified carbon dots with performance of ultraviolet absorption used in sunscreen. *Optics Express.* 2019, **27**(5), pp.7629-7641.
123. Chatzimitakos, T.G., Kasouni, A., Troganis, A., Leonardos, I., Tzovenis, I., Ntzouvaras, A. and Stalikas, C. Carbon Nanodots Synthesized from Dunaliella salina as Sun Protection Filters. *C-Journal of Carbon Research.* 2020, **6**(4).
124. Jian, H.-J., Wu, R.-S., Lin, T.-Y., Li, Y.-J., Lin, H.-J., Harroun, S.G., Lai, J.-Y. and Huang, C.-C. Super-Cationic Carbon Quantum Dots Synthesized from Spermidine as an Eye Drop Formulation for Topical Treatment of Bacterial Keratitis. *ACS Nano.* 2017, **11**(7), pp.6703-6716.
125. Wang, W., Cheng, L. and Liu, W.G. Biological applications of carbon dots. *Science China-Chemistry.* 2014, **57**(4), pp.522-539.
126. Ding, H., Cheng, L.-W., Ma, Y.-Y., Kong, J.-L. and Xiong, H.-M. Luminescent carbon quantum dots and their application in cell imaging. *New Journal of Chemistry.* 2013, **37**(8), pp.2515-2520.

127. Wang, X., Cao, L., Lu, F., Meziani, M.J., Li, H., Qi, G., Zhou, B., Harruff, B.A., Kermarrec, F. and Sun, Y.-P. Photoinduced electron transfers with carbon dots. *Chemical Communications.* 2009, (25), pp.3774-3776.
128. Yao, Y., Zhang, H.Y., Hu, K.S., Nie, G., Yang, Y.Y., Wang, Y.X., Duan, X.G. and Wang, S.B. Carbon dots based photocatalysis for environmental applications. *Journal of Environmental Chemical Engineering.* 2022, **10**(2).
129. Qu, S., Wang, X., Lu, Q., Liu, X. and Wang, L.J.A.C.i.e. A biocompatible fluorescent ink based on water-soluble luminescent carbon nanodots. *Angewandte Chemie International Edition.* 2012, **51**(49), pp.12215-12218.
130. Liu, J., Li, R. and Yang, B. Carbon Dots: A New Type of Carbon-Based Nanomaterial with Wide Applications. *ACS Central Science.* 2020, **6**(12), pp.2179-2195.
131. LibreTexts. *The Effect of Conjugation on λmax.* [Online]. 2014. [Accessed]. Available from: https://chem.libretexts.org/@go/page/16353
132. Zhu, S., Meng, Q., Wang, L., Zhang, J., Song, Y., Jin, H., Zhang, K., Sun, H., Wang, H. and Yang, B. Highly Photoluminescent Carbon Dots for Multicolor Patterning, Sensors, and Bioimaging. *Angewandte Chemie International Edition.* 2013, **52**(14), pp.3953-3957.
133. Sigma Aldrich. *Introduction to Yeast Media.* [Online]. 2022. [Accessed 22/05/22]. Available from: https://www.sigmaaldrich.com/GB/en/technical-documents/technical-article/microbiological-testing/microbial-culture-media-preparation/Introduction-yeast-media
134. Peng, J., Gao, W., Gupta, B.K., Liu, Z., Romero-Aburto, R., Ge, L., Song, L., Alemany, L.B., Zhan, X., Gao, G., Vithayathil, S.A., Kaipparettu, B.A., Marti, A.A., Hayashi, T., Zhu, J.-J. and Ajayan, P.M. Graphene Quantum Dots Derived from Carbon Fibers. *Nano Letters.* 2012, **12**(2), pp.844-849.
135. Kim, Y., Park, Y., Han, S., Park, W., Kim, M., Kim, K., Joo, J., Hahn, S.K. and Kwon, W. Radiative and Non-Radiative Decay Pathways in Carbon Nanodots toward Bioimaging and Photodynamic Therapy. *Nanomaterials (Basel, Switzerland).* 2021, **12**(1), p.70.
136. Sinclair, L., Brown, J., Salim, M.G., May, D., Guilvaiee, B., Hawkins, A. and Cathles, L. Optimization of fluorescence and surface adsorption of citric acid/ethanolamine carbon nanoparticles for subsurface tracers. *Carbon.* 2020, **169**, pp.395-402.
137. Wu, P., Li, W., Wu, Q., Liu, Y. and Liu, S. Hydrothermal synthesis of nitrogen-doped carbon quantum dots from microcrystalline cellulose for the detection of Fe3+ ions in an acidic environment. *RSC Advances.* 2017, **7**(70), pp.44144-44153.
138. Chun, L., Liu, W., Sun, X., Pan, W., Yu, G. and Wang, J. Excitation dependent emission combined with different quenching manners supports carbon dots to achieve multi-mode sensing. *Sensors and Actuators B: Chemical.* 2018, **263**, pp.1-9.
139. Dager, A., Uchida, T., Maekawa, T. and Tachibana, M. Synthesis and characterization of Mono-disperse Carbon Quantum Dots from Fennel Seeds: Photoluminescence analysis using Machine Learning. *Scientific Reports.* 2019, **9**(1), p.14004.
140. Li, X., Zhang, S., Kulinich, S.A., Liu, Y. and Zeng, H. Engineering surface states of carbon dots to achieve controllable luminescence for solid-luminescent composites and sensitive Be2+ detection. *Scientific Reports.* 2014, **4**(1), p.4976.
141. Wang, B., Song, H., Tang, Z., Yang, B. and Lu, S. Ethanol-derived white emissive carbon dots: the formation process investigation and multi-color/white LEDs preparation. *Nano Research.* 2022, **15**(2), pp.942-949.

142. Huang, C., Dong, H., Su, Y., Wu, Y., Narron, R. and Yong, Q. Synthesis of Carbon Quantum Dot Nanoparticles Derived from Byproducts in Bio-Refinery Process for Cell Imaging and In Vivo Bioimaging. *Nanomaterials.* 2019, **9**(3).
143. Szabo, M.R., Idiţoiu, C., Chambre, D. and Lupea, A.X. Improved DPPH determination for antioxidant activity spectrophotometric assay. *Chemical Papers.* 2007, **61**(3), pp.214-216.
144. Sharma, O.P. and Bhat, T.K. DPPH antioxidant assay revisited. *Food Chemistry.* 2009, **113**(4), pp.1202-1205.
145. Chen, J., Dong, X., Zhao, J. and Tang, G. In vivo acute toxicity of titanium dioxide nanoparticles to mice after intraperitioneal injection. *Journal of Applied Toxicology.* 2009, **29**(4), pp.330-337.
146. Morishige, T., Yoshioka, Y., Tanabe, A., Yao, X., Tsunoda, S.-i., Tsutsumi, Y., Mukai, Y., Okada, N. and Nakagawa, S. Titanium dioxide induces different levels of IL-1β production dependent on its particle characteristics through caspase-1 activation mediated by reactive oxygen species and cathepsin B. *Biochemical and Biophysical Research Communications.* 2010, **392**(2), pp.160-165.
147. Sysoltseva, M., Winterhalter, R., Wochnik, A.S., Scheu, C. and Fromme, H. Electron microscopic investigation and elemental analysis of titanium dioxide in sun lotion. *International Journal of Cosmetic Science.* 2017, **39**(3), pp.292-300.
148. Weir, A., Westerhoff, P., Fabricius, L., Hristovski, K. and von Goetz, N. Titanium Dioxide Nanoparticles in Food and Personal Care Products. *Environmental Science & Technology.* 2012, **46**(4), pp.2242-2250.
149. Pfaff, G. and Reynders, P. Angle-Dependent Optical Effects Deriving from Submicron Structures of Films and Pigments. *Chemical Reviews.* 1999, **99**(7), pp.1963-1982.
150. Peters, R.J.B., van Bemmel, G., Herrera-Rivera, Z., Helsper, H.P.F.G., Marvin, H.J.P., Weigel, S., Tromp, P.C., Oomen, A.G., Rietveld, A.G. and Bouwmeester, H. Characterization of Titanium Dioxide Nanoparticles in Food Products: Analytical Methods To Define Nanoparticles. *Journal of Agricultural and Food Chemistry.* 2014, **62**(27), pp.6285-6293.
151. Rompelberg, C., Heringa, M.B., van Donkersgoed, G., Drijvers, J., Roos, A., Westenbrink, S., Peters, R., van Bemmel, G., Brand, W. and Oomen, A.G. Oral intake of added titanium dioxide and its nanofraction from food products, food supplements and toothpaste by the Dutch population. *Nanotoxicology.* 2016, **10**(10), pp.1404-1414.
152. Salvador, A., Pascual-Martí, M.C., Adell, J.R., Requeni, A. and March, J.G. Analytical methodologies for atomic spectrometric determination of metallic oxides in UV sunscreen creams. *Journal of Pharmaceutical and Biomedical Analysis.* 2000, **22**(2), pp.301-306.
153. Ali, I., Suhail, M., Alothman, Z.A. and Alwarthan, A. Recent advances in syntheses, properties and applications of TiO_2 nanostructures. *RSC Advances.* 2018, **8**(53), pp.30125-30147.
154. Shi, H., Magaye, R., Castranova, V. and Zhao, J. Titanium dioxide nanoparticles: a review of current toxicological data. *Particle and Fibre Toxicology.* 2013, **10**(1), p.15.
155. Sharma, S., Sharma, R.K., Gaur, K., Cátala Torres, J.F., Loza-Rosas, S.A., Torres, A., Saxena, M., Julin, M. and Tinoco, A.D. Fueling a Hot Debate on the Application of TiO_2 Nanoparticles in Sunscreen. *Materials (Basel, Switzerland).* 2019, **12**(14), p.2317.

156. Tanvir, S., Pulvin, S. and Anderson, W. Toxicity associated with the photo catalytic and photo stable forms of titanium dioxide nanoparticles used in sunscreen. *MOJ Toxicology.* 2015, **1**(00011).
157. T. Downs, R. and Hall-Wallace, M. The American Mineralogist crystal structure database. *American Mineralogist.* 2003, **88**, pp.547-250.
158. Fujishima, A., Zhang, X.T. and Tryk, D.A. TiO2 photocatalysis and related surface phenomena. *Surface Science Reports.* 2008, **63**(12), pp.515-582.
159. Chen, X. and Mao, S.S. Titanium Dioxide Nanomaterials: Synthesis, Properties, Modifications, and Applications. *Chemical Reviews.* 2007, **107**(7), pp.2891-2959.
160. Su, C., Tseng, C.M., Chen, L.F., You, B.H., Hsu, B.C. and Chen, S.S. Sol-hydrothermal preparation and photocatalysis of titanium dioxide. *Thin Solid Films.* 2006, **498**(1-2), pp.259-265.
161. Wu, M., Lin, G., Chen, D., Wang, G., He, D., Feng, S. and Xu, R. Sol-Hydrothermal Synthesis and Hydrothermally Structural Evolution of Nanocrystal Titanium Dioxide. *Chemistry of Materials.* 2002, **14**(5), pp.1974-1980.
162. Yang, X., Yang, Y., Hou, H., Zhang, Y., Fang, L., Chen, J. and Ji, X. Size-Tunable Single-Crystalline Anatase TiO2 Cubes as Anode Materials for Lithium Ion Batteries. *The Journal of Physical Chemistry C.* 2015, **119**(8), pp.3923-3930.
163. Yu, J., Fan, J. and Lv, K. Anatase TiO2 nanosheets with exposed (001) facets: improved photoelectric conversion efficiency in dye-sensitized solar cells. *Nanoscale.* 2010, **2**(10), pp.2144-2149.
164. Prathan, A., Sanglao, J., Wang, T., Bhoomanee, C., Ruankham, P., Gardchareon, A. and Wongratanaphisan, D. Controlled Structure and Growth Mechanism behind Hydrothermal Growth of TiO2 Nanorods. *Scientific Reports.* 2020, **10**(1), p.8065.
165. Yin, H., Wada, Y., Kitamura, T., Kambe, S., Murasawa, S., Mori, H., Sakata, T. and Yanagida, S. Hydrothermal synthesis of nanosized anatase and rutile TiO2 using amorphous phase TiO2. *Journal of Materials Chemistry.* 2001, **11**(6), pp.1694-1703.
166. Yang, H.G., Sun, C.H., Qiao, S.Z., Zou, J., Liu, G., Smith, S.C., Cheng, H.M. and Lu, G.Q. Anatase TiO2 single crystals with a large percentage of reactive facets. *Nature.* 2008, **453**(7195), pp.638-641.
167. Pan, J., Liu, G., Lu, G.Q. and Cheng, H.-M. On the True Photoreactivity Order of {001}, {010}, and {101} Facets of Anatase TiO2 Crystals. *Angewandte Chemie International Edition.* 2011, **50**(9), pp.2133-2137.
168. Zhao, X., Jin, W., Cai, J., Ye, J., Li, Z., Ma, Y., Xie, J. and Qi, L. Shape- and Size-Controlled Synthesis of Uniform Anatase TiO2 Nanocuboids Enclosed by Active {100} and {001} Facets. *Advanced Functional Materials.* 2011, **21**(18), pp.3554-3563.
169. Roy, N., Sohn, Y. and Pradhan, D. Synergy of Low-Energy {101} and High-Energy {001} TiO2 Crystal Facets for Enhanced Photocatalysis. *ACS Nano.* 2013, **7**(3), pp.2532-2540.
170. Han, X., Kuang, Q., Jin, M., Xie, Z. and Zheng, L. Synthesis of Titania Nanosheets with a High Percentage of Exposed (001) Facets and Related Photocatalytic Properties. *Journal of the American Chemical Society.* 2009, **131**(9), pp.3152-3153.
171. Wang, L., Zang, L., Zhao, J. and Wang, C. Green synthesis of shape-defined anatase TiO_2 nanocrystals wholly exposed with {001} and {100} facets. *Chemical Communications.* 2012, **48**(96), pp.11736-11738.
172. Gamage McEvoy, J., Cui, W. and Zhang, Z. Degradative and disinfective properties of carbon-doped anatase–rutile TiO_2 mixtures under visible light irradiation. *Catalysis Today.* 2013, **207**, pp.191-199.

173. Leary, R. and Westwood, A. Carbonaceous nanomaterials for the enhancement of TiO_2 photocatalysis. *Carbon.* 2011, **49**(3), pp.741-772.
174. Low, J.X., Cheng, B. and Yu, J.G. Surface modification and enhanced photocatalytic CO2 reduction performance of TiO_2: a review. *Applied Surface Science.* 2017, **392**, pp.658-686.
175. Ghosh, S. and Das, A.P. Modified titanium oxide (TiO_2) nanocomposites and its array of applications: a review. *Toxicological and Environmental Chemistry.* 2015, **97**(5), pp.491-514.
176. Dai, L., Sun, F., Fan, Q., Li, H., Yang, K., Guo, T., Zheng, L. and Fu, P. Carbon-based titanium dioxide materials for hydrogen production in water-methanol reforming: A review. *Journal of Environmental Chemical Engineering.* 2022, **10**(2), p.107326.
177. Daghrir, R., Drogui, P. and Robert, D. Modified TiO_2 For Environmental Photocatalytic Applications: A Review. *Industrial & Engineering Chemistry Research.* 2013, **52**(10), pp.3581-3599.
178. Shen, M., Wu, Z., Huang, H., Du, Y., Zou, Z. and Yang, P. Carbon-doped anatase TiO_2 obtained from TiC for photocatalysis under visible light irradiation. *Materials Letters.* 2006, **60**(5), pp.693-697.
179. Yan, Y., Kuang, W., Shi, L., Ye, X., Yang, Y., Xie, X., Shi, Q. and Tan, S. Carbon quantum dot-decorated TiO_2 for fast and sustainable antibacterial properties under visible-light. *Journal of Alloys and Compounds.* 2019, **777**, pp.234-243.
180. Safardoust-Hojaghan, H. and Salavati-Niasari, M. Degradation of methylene blue as a pollutant with N-doped graphene quantum dot/titanium dioxide nanocomposite. *Journal of Cleaner Production.* 2017, **148**, pp.31-36.
181. Parashar, M., Shukla, V.K. and Singh, R. Metal oxides nanoparticles via sol–gel method: a review on synthesis, characterization and applications. *Journal of Materials Science: Materials in Electronics.* 2020, **31**(5), pp.3729-3749.
182. Ananth, S., Arumanayagam, T., Vivek, P. and Murugakoothan, P. Direct synthesis of natural dye mixed titanium dioxide nano particles by sol–gel method for dye sensitized solar cell applications. *Optik.* 2014, **125**(1), pp.495-498.
183. Praveen, P., Viruthagiri, G., Mugundan, S. and Shanmugam, N. Structural, optical and morphological analyses of pristine titanium di-oxide nanoparticles – Synthesized via sol–gel route. *Spectrochimica Acta Part A: Molecular and Biomolecular Spectroscopy.* 2014, **117**, pp.622-629.
184. Lu, X., Lv, X., Sun, Z. and Zheng, Y. Nanocomposites of poly(l-lactide) and surface-grafted TiO2 nanoparticles: Synthesis and characterization. *European Polymer Journal.* 2008, **44**(8), pp.2476-2481.
185. Hashimoto, M., Takadama, H., Mizuno, M. and Kokubo, T. Enhancement of mechanical strength of TiO2/high-density polyethylene composites for bone repair with silane-coupling treatment. *Materials Research Bulletin.* 2006, **41**(3), pp.515-524.
186. Talam, S., Karumuri, S.R. and Gunnam, N. Synthesis, Characterization, and Spectroscopic Properties of ZnO Nanoparticles. *ISRN Nanotechnology.* 2012, **2012**, p.372505.
187. Warkhade, S.K., Gaikwad, G.S., Zodape, S.P., Pratap, U., Maldhure, A.V. and Wankhade, A.V. Low temperature synthesis of pure anatase carbon doped titanium dioxide: An efficient visible light active photocatalyst. *Materials Science in Semiconductor Processing.* 2017, **63**, pp.18-24.

188. Dolabella, S., Borzì, A., Dommann, A. and Neels, A. Lattice Strain and Defects Analysis in Nanostructured Semiconductor Materials and Devices by High-Resolution X-Ray Diffraction: Theoretical and Practical Aspects. *Small Methods.* 2022, **6**(2), p.2100932.
189. Maletić, M., Vukčević, M., Kalijadis, A., Janković-Častvan, I., Dapčević, A., Laušević, Z. and Laušević, M. Hydrothermal synthesis of TiO_2/carbon composites and their application for removal of organic pollutants. *Arabian Journal of Chemistry.* 2019, **12**(8), pp.4388-4397.
190. Mishra, P.K., Mishra, H., Ekielski, A., Talegaonkar, S. and Vaidya, B. Zinc oxide nanoparticles: a promising nanomaterial for biomedical applications. *Drug Discovery Today.* 2017, **22**(12), pp.1825-1834.
191. Jiang, J., Pi, J. and Cai, J. The Advancing of Zinc Oxide Nanoparticles for Biomedical Applications. *Bioinorganic chemistry and applications.* 2018, **2018**, pp.1062562-1062518.
192. Zhang, Z.-Y. and Xiong, H.-M. Photoluminescent ZnO Nanoparticles and Their Biological Applications. *Materials.* 2015, **8**(6), pp.3101-3127.
193. Smijs, T.G. and Pavel, S. Titanium dioxide and zinc oxide nanoparticles in sunscreens: focus on their safety and effectiveness. *Nanotechnol Sci Appl.* 2011, **4**, pp.95-112.
194. S, S., H, L.J.K., K, R. and M, S. Antimicrobial and antioxidant potentials of biosynthesized colloidal zinc oxide nanoparticles for a fortified cold cream formulation: A potent nanocosmeceutical application. *Materials Science & Engineering C.* 2017, **79**, pp.581-589.
195. Cai, Q., Gao, Y., Gao, T., Lan, S., Simalou, O., Zhou, X., Zhang, Y., Harnoode, C., Gao, G. and Dong, A. Insight into Biological Effects of Zinc Oxide Nanoflowers on Bacteria: Why Morphology Matters. *ACS Applied Materials & Interfaces.* 2016, **8**(16), pp.10109-10120.
196. Zhou, J., Xu, N.S. and Wang, Z.L. Dissolving Behavior and Stability of ZnO Wires in Biofluids: A Study on Biodegradability and Biocompatibility of ZnO Nanostructures. *Advanced Materials.* 2006, **18**(18), pp.2432-2435.
197. Zhang, Y., Ram, M.K., Stefanakos, E.K. and Goswami, D.Y. Synthesis, Characterization, and Applications of ZnO Nanowires. *Journal of Nanomaterials.* 2012, **2012**, p.624520.
198. Direct and Indirect Band Gap Semiconductors.
199. Janotti, A. and Van de Walle, C.G. Fundamentals of zinc oxide as a semiconductor. *Reports on Progress in Physics.* 2009, **72**(12), p.126501.
200. Ding, M., Guo, Z., Zhou, L., Fang, X., Zhang, L., Zeng, L., Xie, L. and Zhao, H. One-Dimensional Zinc Oxide Nanomaterials for Application in High-Performance Advanced Optoelectronic Devices. *Crystals.* 2018, **8**(5).
201. Morkoç, H. and Özgür, Ü. *Zinc oxide: fundamentals, materials and device technology.* John Wiley & Sons, 2008.
202. Kołodziejczak-Radzimska, A. and Jesionowski, T. Zinc Oxide-From Synthesis to Application: A Review. *Materials (Basel, Switzerland).* 2014, **7**(4), pp.2833-2881.
203. Ao, W., Li, J., Yang, H., Zeng, X. and Ma, X.J.P.T. Mechanochemical synthesis of zinc oxide nanocrystalline. 2006, **168**(3), pp.148-151.
204. Stanković, A., Veselinović, L., Škapin, S., Marković, S. and Uskoković, D.J.J.o.m.s. Controlled mechanochemically assisted synthesis of ZnO nanopowders in the presence of oxalic acid. 2011, **46**(11), pp.3716-3724.
205. Tsuzuki, T. and McCormick, P.G.J.S.M. ZnO nanoparticles synthesised by mechanochemical processing. 2001, **44**(8-9), pp.1731-1734.

206. Moballegh, A., Shahverdi, H., Aghababazadeh, R. and Mirhabibi, A.J.S.S. ZnO nanoparticles obtained by mechanochemical technique and the optical properties. 2007, **601**(13), pp.2850-2854.
207. Kołodziejczak-Radzimska, A., Jesionowski, T. and Krysztafkiewicz, A.J.P.P.o.M.P. Obtaining zinc oxide from aqueous solutions of KOH and Zn (CH3COO) 2. 2010, **44**, pp.93-102.
208. Hong, R., Pan, T., Qian, J. and Li, H.J.C.E.J. Synthesis and surface modification of ZnO nanoparticles. 2006, **119**(2-3), pp.71-81.
209. Cao, Z., Zhang, Z., Wang, F., Wang, G.J.C., physicochemical, s.A. and aspects, e. Synthesis and UV shielding properties of zinc oxide ultrafine particles modified with silica and trimethyl siloxane. 2009, **340**(1-3), pp.161-167.
210. Li, P., Wei, Y., Liu, H. and Wang, X.-k.J.J.o.s.s.c. Growth of well-defined ZnO microparticles with additives from aqueous solution. 2005, **178**(3), pp.855-860.
211. Ma, C.-l. and Sun, X.-d.J.I.C.C. Preparation of nanocrystalline metal oxide powders with the surfactant-mediated method. 2002, **5**(10), pp.751-755.
212. Mahato, T., Prasad, G., Singh, B., Acharya, J., Srivastava, A. and Vijayaraghavan, R.J.J.o.h.m. Nanocrystalline zinc oxide for the decontamination of sarin. 2009, **165**(1-3), pp.928-932.
213. Benhebal, H., Chaib, M., Salmon, T., Geens, J., Leonard, A., Lambert, S.D., Crine, M. and Heinrichs, B.J.A.E.J. Photocatalytic degradation of phenol and benzoic acid using zinc oxide powders prepared by the sol–gel process. 2013, **52**(3), pp.517-523.
214. Ristić, M., Musić, S., Ivanda, M., Popović, S.J.J.o.A. and Compounds. Sol–gel synthesis and characterization of nanocrystalline ZnO powders. 2005, **397**(1-2), pp.L1-L4.
215. Chen, S.-J., Li, L.-H., Chen, X.-T., Xue, Z., Hong, J.-M. and You, X.-Z. Preparation and characterization of nanocrystalline zinc oxide by a novel solvothermal oxidation route. *Journal of crystal growth.* 2003, **252**(1), pp.184-189.
216. Chen, D., Jiao, X. and Cheng, G.J.S.S.C. Hydrothermal synthesis of zinc oxide powders with different morphologies. 1999, **113**(6), pp.363-366.
217. Ismail, A.A., El-Midany, A., Abdel-Aal, E.A. and El-Shall, H. Application of statistical design to optimize the preparation of ZnO nanoparticles via hydrothermal technique. *Materials Letters.* 2005, **59**(14), pp.1924-1928.
218. Dem'Yanets, L., Li, L. and Uvarova, T.J.J.o.m.s. Zinc oxide: hydrothermal growth of nano-and bulk crystals and their luminescent properties. 2006, **41**(5), pp.1439-1444.
219. Schneider, J.r.J., Hoffmann, R.C., Engstler, J.r., Klyszcz, A., Erdem, E., Jakes, P., Eichel, R.d.-A., Pitta-Bauermann, L. and Bill, J.J.C.o.M. Synthesis, characterization, defect chemistry, and FET properties of microwave-derived nanoscaled zinc oxide. 2010, **22**(7), pp.2203-2212.
220. Lu, C.-H. and Yeh, C.-H.J.M.L. Emulsion precipitation of submicron zinc oxide powder. 1997, **33**(3-4), pp.129-132.
221. Li, X., He, G., Xiao, G., Liu, H., Wang, M.J.J.o.C. and Science, I. Synthesis and morphology control of ZnO nanostructures in microemulsions. 2009, **333**(2), pp.465-473.
222. Sadhasivam, S., Shanmugam, M., Umamaheswaran, P.D., Venkattappan, A. and Shanmugam, A. Zinc Oxide Nanoparticles: Green Synthesis and Biomedical Applications. *Journal of Cluster Science.* 2021, **32**(6), pp.1441-1455.
223. Schmidt-Mende, L. and MacManus-Driscoll, J.L. ZnO – nanostructures, defects, and devices. *Materials Today.* 2007, **10**(5), pp.40-48.

224. Türkyılmaz, Ş.Ş., Güy, N. and Özacar, M. Photocatalytic efficiencies of Ni, Mn, Fe and Ag doped ZnO nanostructures synthesized by hydrothermal method: The synergistic/antagonistic effect between ZnO and metals. *Journal of Photochemistry and Photobiology A: Chemistry.* 2017, **341**, pp.39-50.
225. Wu, W.-Y., Kung, W.-Y. and Ting, J.-M. Effect of pH Values on the Morphology of Zinc Oxide Nanostructures and their Photoluminescence Spectra. *Journal of the American Ceramic Society.* 2011, **94**(3), pp.699-703.
226. Lu, C.H. and Yeh, C.H. Influence of hydrothermal conditions on the morphology and particle size of zinc oxide powder. *Ceramics International.* 2000, **26**(4), pp.351-357.
227. Shang, T.-M., Sun, J.-H., Zhou, Q.-F. and Guan, M.-Y. Controlled synthesis of various morphologies of nanostructured zinc oxide: flower, nanoplate, and urchin. *Crystal Research and Technology.* 2007, **42**(10), pp.1002-1006.
228. Pal, U. and Santiago, P. Controlling the Morphology of ZnO Nanostructures in a Low-Temperature Hydrothermal Process. *The Journal of Physical Chemistry B.* 2005, **109**(32), pp.15317-15321.
229. Pariona, N., Paraguay-Delgado, F., Basurto-Cereceda, S., Morales-Mendoza, J.E., Hermida-Montero, L.A. and Mtz-Enriquez, A.I. Shape-dependent antifungal activity of ZnO particles against phytopathogenic fungi. *Applied Nanoscience.* 2020, **10**(2), pp.435-443.
230. Marlinda, A.R., Yusoff, N., Pandikumar, A., Huang, N.M., Akbarzadeh, O., Sagadevan, S., Wahab, Y.A. and Johan, M.R. Tailoring morphological characteristics of zinc oxide using a one-step hydrothermal method for photoelectrochemical water splitting application. *International Journal of Hydrogen Energy.* 2019, **44**(33), pp.17535-17543.
231. Cho, S., Jang, J.-W., Lee, J.S. and Lee, K.-H. Carbon-doped ZnO nanostructures synthesized using vitamin C for visible light photocatalysis. *CrystEngComm.* 2010, **12**(11), pp.3929-3935.
232. Gershon, T.S., Li, N., Sadana, D.K. and Todorov, T.K. *Doping of zinc oxide particles for sunscreen applications*. Google Patents. 2019.
233. Zhang, X., Qin, J., Hao, R., Wang, L., Shen, X., Yu, R., Limpanart, S., Ma, M. and Liu, R. Carbon-Doped ZnO Nanostructures: Facile Synthesis and Visible Light Photocatalytic Applications. *Journal of physical chemistry. C.* 2015, **119**(35), pp.20544-20554.
234. Muthuchamy, N., Atchudan, R., Edison, T.N.J.I., Perumal, S. and Lee, Y.R. High-performance glucose biosensor based on green synthesized zinc oxide nanoparticle embedded nitrogen-doped carbon sheet. *Journal of Electroanalytical Chemistry.* 2018, **816**, pp.195-204.
235. Bozetine, H., Wang, Q., Barras, A., Li, M., Hadjersi, T., Szunerits, S. and Boukherroub, R. Green chemistry approach for the synthesis of ZnO–carbon dots nanocomposites with good photocatalytic properties under visible light. *Journal of Colloid and Interface Science.* 2016, **465**, pp.286-294.
236. Sun, Y., Wang, L., Yu, X. and Chen, K. Facile synthesis of flower-like 3D ZnO superstructures via solution route. *CrystEngComm.* 2012, **14**(9), pp.3199-3204.
237. Zhang, H., Yang, D., Li, D., Ma, X., Li, S. and Que, D. Controllable Growth of ZnO Microcrystals by a Capping-Molecule-Assisted Hydrothermal Process. *Crystal Growth & Design.* 2005, **5**(2), pp.547-550.
238. Leonardi, S.G. Two-Dimensional Zinc Oxide Nanostructures for Gas Sensor Applications. *Chemosensors.* 2017, **5**(2).

239. Cao, X., Wang, N., Huang, X., Feng, Q., Wang, L., Zhou, K., Gao, X. and Lee, J.-H. Layered ZnO microcrystals with intense stimulated emission. *CrystEngComm.* 2013, **15**(9), pp.1715-1720.
240. Guo, M., Diao, P. and Cai, S. Hydrothermal growth of well-aligned ZnO nanorod arrays: Dependence of morphology and alignment ordering upon preparing conditions. *Journal of Solid State Chemistry.* 2005, **178**(6), pp.1864-1873.
241. Sayari, A. Characterization of Nanocrystalline ZnO Flakes Synthesized by a Simple Reaction Process. *KONA Powder and Particle Journal.* 2013, **30**, pp.119-124.
242. Ashtaputre, S.S., Deshpande, A., Marathe, S., Wankhede, M., Chimanpure, J., Pasricha, R., Urban, J., Haram, S., Gosavi, S. and Kulkarni, S.J.P. Synthesis and analysis of ZnO and CdSe nanoparticles. 2005, **65**(4), pp.615-620.
243. Julkapli, N.M., Ahmad, Z. and Akil, H.M. X-Ray Diffraction Studies of Cross Linked Chitosan With Different Cross Linking Agents For Waste Water Treatment Application. *AIP Conference Proceedings.* 2010, **1202**(1), pp.106-111.
244. Chandy, T. and Sharma, C.P. Chitosan-as a Biomaterial. *Biomaterials, Artificial Cells and Artificial Organs.* 1990, **18**(1), pp.1-24.
245. Cheung, R.C.F., Ng, T.B., Wong, J.H. and Chan, W.Y. Chitosan: An Update on Potential Biomedical and Pharmaceutical Applications. *Marine drugs.* 2015, **13**(8), pp.5156-5186.
246. Kumar, M.N.V.R., Muzzarelli, R.A.A., Muzzarelli, C., Sashiwa, H. and Domb, A.J. Chitosan Chemistry and Pharmaceutical Perspectives. *Chemical Reviews.* 2004, **104**(12), pp.6017-6084.
247. Ababneh, H. and Hameed, B.H. Chitosan-derived hydrothermally carbonized materials and its applications: A review of recent literature. *International Journal of Biological Macromolecules.* 2021, **186**, pp.314-327.
248. Raja, A.N. Recent development in chitosan-based electrochemical sensors and its sensing application. 2020, **164**, pp.4231-4244.
249. Hammi, N., Chen, S., Dumeignil, F., Royer, S. and El Kadib, A.J.M.T.S. Chitosan as a sustainable precursor for nitrogen-containing carbon nanomaterials: synthesis and uses. 2020, **10**, p.100053.
250. Rimu, S.H. and Rahman, M.M. Insight of chitosan-based nanocomposite for removal of hexavalent chromium from wastewater-a review. 2020, pp.1-18.
251. AbdElhady, M.M. Preparation and Characterization of Chitosan/Zinc Oxide Nanoparticles for Imparting Antimicrobial and UV Protection to Cotton Fabric. *International Journal of Carbohydrate Chemistry.* 2012, **2012**, p.840591.
252. Aadnan, I., Zegaoui, O., Daou, I. and Esteves da Silva, J.C.G. Synthesis and physicochemical characterization of a ZnO-Chitosan hybrid-biocomposite used as an environmentally friendly photocatalyst under UV-A and visible light irradiations. *Journal of Environmental Chemical Engineering.* 2020, **8**(5), p.104260.
253. Hammi, N., Marcotte, N., Marinova, M., Draoui, K., Royer, S. and El Kadib, A. Nanostructured metal oxide@carbon dots through sequential chitosan templating and carbonisation route. *Carbohydrate Polymer Technologies and Applications.* 2021, **2**, p.100043.
254. Jampafuang, Y., Tongta, A. and Waiprib, Y. Impact of Crystalline Structural Differences Between α- and β-Chitosan on Their Nanoparticle Formation Via Ionic Gelation and Superoxide Radical Scavenging Activities. *Polymers.* 2019, **11**(12), p.2010.

255. Zhang, Y., Wang, Q., Wang, B., Mei, Y. and Lian, P. N-doped graphene/Bi nanocomposite with excellent electrochemical properties for lithium–ion batteries. *Ionics.* 2017, **23**(6), pp.1407-1415.
256. Safeera, T.A. and Anila, E.I. Wet chemical synthesis of chitosan capped ZnO:Na nanoparticles for luminescence applications. *International Journal of Biological Macromolecules.* 2017, **104**, pp.1833-1836.
257. Ungár, T. Microstructural parameters from X-ray diffraction peak broadening. *Scripta Materialia.* 2004, **51**(8), pp.777-781.
258. Bindu, P. and Thomas, S. Estimation of lattice strain in ZnO nanoparticles: X-ray peak profile analysis. *Journal of Theoretical and Applied Physics.* 2014, **8**(4), pp.123-134.
259. Urs, K.M.B. and Kamble, V. Surface photovoltage response of zinc oxide microrods on prismatic planes: effect of UV, temperature and oxygen ambience. *Journal of Materials Science: Materials in Electronics.* 2021, **32**(5), pp.6414-6424.
260. Hon, D.N.S. and Tang, L.-G. Chelation of chitosan derivatives with zinc ions. I. O,N-carboxymethyl chitosan. *Journal of Applied Polymer Science.* 2000, **77**(10), pp.2246-2253.
261. Janus, Ł., Piątkowski, M., Radwan-Pragłowska, J., Bogdał, D. and Matysek, D. Chitosan-Based Carbon Quantum Dots for Biomedical Applications: Synthesis and Characterization. *Nanomaterials (Basel, Switzerland).* 2019, **9**(2), p.274.
262. Sun, L.L., Zhang, H.M., Wang, Y.S., Xiong, Z., Zhao, X.H. and Xia, Y.Z. Chitosan-derived N-doped carbon dots for fluorescent determination of nitrite and bacteria imaging. *Spectrochimica Acta Part A - Molecular and Biomolecular Spectroscopy.* 2021, **251**.
263. Xiao, D., Yuan, D., He, H. and Lu, J. Microwave-assisted one-step green synthesis of amino-functionalized fluorescent carbon nitride dots from chitosan. *Luminescence.* 2013, **28**(4), pp.612-615.
264. Yang, Y., Cui, J., Zheng, M., Hu, C., Tan, S., Xiao, Y., Yang, Q. and Liu, Y. One-step synthesis of amino-functionalized fluorescent carbon nanoparticles by hydrothermal carbonization of chitosan. *Chemical Communications.* 2012, **48**(3), pp.380-382.